



**HAL**  
open science

# Monte Carlo analysis of heterogeneity and core decoupling effects on reactor kinetics : Application to the EOLE critical facility

Vito Vitali

► **To cite this version:**

Vito Vitali. Monte Carlo analysis of heterogeneity and core decoupling effects on reactor kinetics : Application to the EOLE critical facility. Nuclear Theory [nucl-th]. Université Paris-Saclay, 2020. English. NNT : 2020UPASP045 . tel-03164857

**HAL Id: tel-03164857**

**<https://theses.hal.science/tel-03164857>**

Submitted on 10 Mar 2021

**HAL** is a multi-disciplinary open access archive for the deposit and dissemination of scientific research documents, whether they are published or not. The documents may come from teaching and research institutions in France or abroad, or from public or private research centers.

L'archive ouverte pluridisciplinaire **HAL**, est destinée au dépôt et à la diffusion de documents scientifiques de niveau recherche, publiés ou non, émanant des établissements d'enseignement et de recherche français ou étrangers, des laboratoires publics ou privés.

# Monte Carlo analysis of heterogeneity and core decoupling effects on reactor kinetics: Application to the EOLE critical facility

Thèse de doctorat de l'Université Paris-Saclay  
École doctorale n°576 Particules, Hadrons, Énergie, Noyau, Instrumentation, Imagerie,  
Cosmos et Simulation (PHENIICS)  
Spécialité de doctorat: Énergie nucléaire  
Unité de recherche: Université Paris-Saclay, CEA, Service d'Études des Réacteurs et de Mathématiques  
Appliquées, 91191, Gif-sur-Yvette, France  
Réfèrent : Faculté des sciences d'Orsay

Thèse présentée et soutenue à Saclay, le 23 octobre 2020, par

**VITO VITALI**

## Composition du Jury :

Sylvain David Directeur de recherche CNRS, Université Paris-Saclay	Président
Christophe Demazière Professeur, Chalmers University	Rapporteur
Gert Van den Eynde Docteur, SCK-CEN	Rapporteur
Sandra Dulla Professeure, Politecnico di Torino	Examineur
Patrick Blaise Directeur de recherche (HDR), CEA Cadarache	Directeur de thèse
Andrea Zoia Ingénieur-chercheur (HDR), CEA Saclay	Directeur de thèse
Alexis Jinaphanh Ingénieur-chercheur, CEA Saclay	Encadrant
Florent Chevallier Ingénieur-chercheur, CEA Saclay	Encadrant



*This dissertation is dedicated to my Ph.D. director Andrea and my Ph.D. supervisor Alexis for their efforts in this work and for everything they taught me during these years.*



# Acknowledgements

I write these lines on a happy day after my thesis defense. As a student, as a friend and as a relative I am proud to dedicate these acknowledgements to all those who have contributed to achieve this goal.

My first thanks go to the commission in charge of verifying and judging this manuscript: thanks to the reporters Gert Van den Eynde and Christophe Demazière for their constructive critics and to the examiners Sandra Dulla and Sylvain David for their reviews. I want to emphasize these thanks for your efforts in analyzing the thesis and participating to the defense despite the critical sanitary situation.

A huge thank you goes to those who have followed me professionally from the beginning until the end of this adventure: my thesis directors Andrea and Patrick, and my advisors Alexis and Florent. During these years you have been great guides on both professional and human levels and I hope with all my heart to always value all your teachings. I promised that I would dedicate a statue to you, Andrea and Alexis, for the commitment, perseverance, helpfulness and expertise shown during every single day. For the time being this is not possible for me, but to you I dedicate this work and the efforts I have made to complete it. I know that it has not always been easy for you to follow me and that I have often tested your patience: thank you for always continuing to believe in my abilities and for everything you have taught me!

I thank the CEA, and especially the whole SERMA, for giving me the opportunity to work on neutronics and to improve professionally in a dynamic and active research environment. Among the people with whom I have had the opportunity to share a lot during these years I want to sincerely thank all the friends I met during my internship and PhD: I don't have the courage to write all your names for fear of forgetting some, but you know very well who you are and how much each one of you has been a friend to me. I sincerely thank the Italian team composed by Alberto, Alessandro, Andrea, Antonio, Daniele, Dominic, Laurent, Francesco, Matteo, Moira, Paolo, Simone Bleynat, Simone Guiso and Tony. You were the most beautiful piece of Italy I could hope to meet here in France. A big hug to those who are today more distant than anyone else: Gregory and Nicoleta. I will always wish you the best and I will never have the chance to thank you enough for all the good you have spread. Thanks also to those who have been both professional guides and kind friends: Davide, Fausto, Simone and Igor. To all of you, I ask you to prepare the spoons for the next tiramisù!

With great pride, I want to thank the professors who inspired me in the choice of neutronics during my studies at the Polytechnic of Turin and who remain a model to always follow: Professor Sandra Dulla and Professor Piero Ravetto. From my university experience I would like to thank my dear friends Giuseppe, Andrea, Vincenzo, Ortensia, Silvia, Simone and Damiano for their great support and for all the moments shared together. A special thanks also goes to my dear friends Giuseppe and Stefano with the sincere wish to see you again soon.

Tengo a ringraziare gli amici e i luoghi in cui sono cresciuto perché credo fermamente che abbiano formato la persona che sono oggi e che abbiano quindi contribuito a farmi arrivare così lontano. Grazie Presicce per avermi trasmesso in egual misura il desiderio di partire e quello di tornare. Grazie a voi, amici e compagni di tante avventure: il gruppo dell'estate, i buoni compagni liceali, le nuove conoscenze e l'inseparabile compagnia incontrata in oratorio. Voglio infine dire grazie al trio Chiara, Giorgia e Giulia per tutto il sostegno e l'affetto condiviso in questi anni, nella speranza di riabbracciarvi presto.

---

Il ringraziamento più grande v'è a tutta la mia famiglia. A mio padre Luciano e a mia madre Speranza, i primi e i più importanti maestri che continuano ad insegnarmi ad essere felice. A mio fratello Simone e mia sorella Grazia, fiero della strada che hanno saputo costruirsi per il loro futuro e dei loro insegnamenti di vita. Ai miei carissimi nonni Vito, Carmelo, Lidia e Donata, e a mia zia Maria, prove concrete di amore incondizionato e puro. Tutti voi, siete, e sempre sarete, il mio orgoglio più grande.

Per ultimo, imparo in quest'occasione e per la prima volta nella mia vita, a ringraziare me stesso per non essermi mai arreso anche nei momenti più difficili. L'augurio è che questo traguardo mi aiuti a credere nelle mie capacità e a continuare sempre a migliorare facendo ciò che amo.

Excelsior!

# Contents

<b>1</b>	<b>Introduction</b>	<b>4</b>
1.1	Plan of the thesis . . . . .	8
1.2	List of published material . . . . .	9
<b>2</b>	<b>Overview of time-dependent transport and spectral analysis in reactor physics</b>	<b>11</b>
2.1	Neutron interactions with matter . . . . .	11
2.2	General form of the transport equation . . . . .	12
2.3	The integro-differential transport equations . . . . .	16
2.4	The integral formulation of the transport equations . . . . .	17
2.5	The adjoint transport equations . . . . .	18
2.6	Eigenvalue problems for the transport equations . . . . .	20
2.7	Point kinetics . . . . .	24
<b>3</b>	<b>Monte Carlo methods for reactor physics</b>	<b>27</b>
3.1	Monte Carlo estimation: average and variance . . . . .	27
3.2	Neutron random walks . . . . .	28
3.3	Non-analog neutron random walk . . . . .	29
3.4	Estimators for neutron histories . . . . .	31
3.5	Kinetic Monte Carlo methods . . . . .	32
3.6	Monte Carlo methods for eigenvalue problems . . . . .	33
3.7	Numerical simulation tools developed and used in this work . . . . .	35
<b>4</b>	<b>Analysis of forward and adjoint fundamental <math>k</math> and <math>\alpha</math>-eigenfunctions</b>	<b>37</b>
4.1	Introduction . . . . .	37
4.2	Monte Carlo power iteration for $k$ -eigenvalue problems . . . . .	38

---

4.3	Determining the fundamental adjoint mode: the IFP method . . . . .	39
4.4	The fundamental $\alpha$ -eigenmode . . . . .	41
4.5	Adjoint $\alpha$ -eigenvalue equations . . . . .	44
4.6	Analysis of Godiva-like benchmark configurations . . . . .	45
4.7	An application to the CROCUS reactor . . . . .	55
4.8	Conclusions . . . . .	61
<b>5</b>	<b>A new matrix-filling Monte Carlo method for <math>\alpha</math>-spectral analysis</b>	<b>63</b>
5.1	Matrix-filling methods: the fission matrix approach . . . . .	64
5.2	A new matrix-filling method for $\alpha$ -eigenvalues . . . . .	67
5.3	Numerical simulations . . . . .	73
5.4	Discussion . . . . .	82
5.5	Conclusions . . . . .	83
<b>6</b>	<b>Eigenvalue separation: a numerical investigation</b>	<b>85</b>
6.1	Introduction . . . . .	85
6.2	Choice of the benchmark configurations . . . . .	86
6.3	Simulation settings . . . . .	87
6.4	Homogeneous benchmark configurations . . . . .	88
6.5	Heterogeneous benchmark configurations . . . . .	105
6.6	Conclusions . . . . .	110
<b>7</b>	<b>Spectral analysis of the EOLE reactor: the EPILOGUE experimental program</b>	<b>113</b>
7.1	Introduction . . . . .	113
7.2	The EPILOGUE program and the EOLE configurations . . . . .	114
7.3	Analysis of multi-instrumented rod-drop measurements: investigation of spatial kinetics effects . .	118
7.4	Spectral analysis of the water blade configurations . . . . .	124
7.5	Conclusions . . . . .	139
<b>8</b>	<b>Conclusions</b>	<b>143</b>
<b>A</b>	<b>The transient fission matrix method</b>	<b>147</b>
<b>B</b>	<b>Derivation of the point kinetics equations</b>	<b>149</b>

**C Résumé en français**

**151**

# Chapter 1

## Introduction

Within the framework of the safety of nuclear installations, the development of predictive, reliable and fast simulation tools enabling the multi-physics simulation of nuclear reactor cores (including thermal-hydraulics feedbacks, in stationary and transient conditions) is the subject of a very extensive research program [106, 93, 94, 61, 30, 151]. The design of new reactor configurations, which are possibly highly heterogeneous and/or decoupled, also calls for a numerical characterization, which might complement or even replace the need for experimental facilities, especially in view of the characterization of the non-stationary neutron population behavior during operational and accidental transients. These efforts have been capitalized in the form of the innovation agendas SNETP, NUGENIA and H2020. Several European projects have risen, such as NURESIM (2005-2008), NURISP (2009-2012), NURESAFE (2013-2015), HPMC (2011-2014), McSAFE (2017-2020) and its successor McSAFER (2020)<sup>1</sup>. Similar strategies have been proposed in the USA (for instance, the CESAR project<sup>2</sup> or the CASL consortium<sup>3</sup>) and in China. The final goal of these efforts is to pave the way towards a “numerical reactor”, allowing even extreme (i.e., inaccessible to experimental evidence) conditions to be probed and the associated uncertainties to be quantified by simulation.

The investigation of neutron kinetics, i.e., the time-dependent behavior of neutron transport, is predominantly founded on deterministic methods, ranging from extremely simplified (point kinetics) to sophisticated (transport theory) approaches [32, 36, 31, 48, 85, 77]. For non-stationary problems, the state of the art of the current generation of numerical simulation codes using deterministic methods typically relies on a “two-step” approach: a fine calculation of the neutron distribution at the lattice level in stationary conditions and in two dimensions, followed by a calculation of the time evolution of the neutron flux based on the cross sections determined in the first step and introducing simplified models for transport (for example diffusion or  $SP_N$ ) with energy discretization having a small number of groups [81]. These approximations being specific to each type of reactor, the validity of the obtained results, as well as the quantification of the uncertainties associated with the physical quantities of interest, therefore depends on the configuration under analysis. In order to overcome these issues and to be able to validate deterministic codes in a non-stationary regime, it is primordial to develop reference calculation tools capable of alleviating the paucity of experimental data related to transient regimes.

The Monte Carlo simulation is based on the realization of a very large number of random neutron trajectories, whose probability laws are determined in agreement with the underlying physical laws: the probability of particle-matter interaction, post-collision angle and energy distributions, etc. Contrary to deterministic methods, no approximations are introduced for the energy variable, which is explicitly dealt with during the particle flights and collisions; furthermore, an exact treatment of the reactor geometry is in principle possible, without resorting to discretization [96]. Therefore, the Monte Carlo simulation has been always considered as the reference method for neutron transport [4]. Until very recently, Monte Carlo simulation has been almost exclusively devoted to the solution of stationary transport problems, mainly due to the large computation cost (expressed in terms of CPU and memory burden) required by the realization of the particle trajectories. This is also the case for the TRIPOLI-4<sup>®</sup>

---

<sup>1</sup><https://cordis.europa.eu/projects>. McSAFER is an European project scheduled on September 2020.

<sup>2</sup><https://cesar.mcs.anl.gov>

<sup>3</sup><https://www.casl.gov>

code [20], developed at CEA/Saclay.

Thanks to the increasing performances of computer clusters, the availability of super-computers for scientific calculation in the last decade and the intrinsic parallelism of Monte Carlo simulation, this stochastic method has begun to be applied to the investigation of non-stationary problems [88, 140, 79, 141, 142]. For this purpose, two formidable obstacles have been identified. The first concerns the simultaneous presence of two very different time scales for particle transport, the one of neutrons and the one of delayed neutron precursors [72], which are separated by a factor of  $10^4$  for typical light water reactors and might thus induce serious under-sampling issues [41]. The second concerns the need of taking into account the effects of physical feedbacks during the transient, since the energy released by the fissions generates changes in temperature and density, which in turn modify the cross sections and therefore the probability of neutron collisions. This calls for coupling the Monte Carlo codes with external tools such as thermal-hydraulics [61] and/or thermo-mechanics solvers [83]. Such challenges have been met by first developing specific and highly non-trivial variance-reduction techniques for the time variable (the so-called “kinetic” Monte Carlo methods) and then coupling schemes capable of exchanging information back and forth between the Monte Carlo simulation and the external feedback solvers, by taking into account subtle stability and convergence issues due to the stochastic nature of the Monte Carlo simulation (the so-called “dynamic” Monte Carlo methods [63, 146]). Despite having been the subject of a major research effort in recent years, kinetic and dynamic Monte Carlo methods are still in their infancy and require such massive computer resources that their daily use for reactor design is still beyond reach. Intensive work will be still required in the next future in order to establish these methods as a practical tool for reactor physicists, as witnessed e.g. by the McSAFER project.

A somewhat complementary approach to reactor kinetics consists in transforming the original time-dependent neutron transport equations into a stationary form, by introducing a set of eigenvalue equations associated to the Boltzmann operator [34]. For this purpose, two main eigenbases have been historically proposed in the literature: the  $k$ -eigenpairs [28], which physically correspond to decomposing the system evolution with respect to the successive fission generations, and the  $\alpha$ -eigenpairs [82], which physically correspond to decomposing the system evolution with respect to time. For this reason, the  $\alpha$ -eigenbasis is in particular ideally suited for time-dependent problems. Once determined, the eigenvalues and eigenfunctions associated with each basis can be used to perform the spectral analysis of the Boltzmann operator and reconstruct the transient behaviour by convoluting the eigenbasis with the source.

The analysis of the operator eigenvalues and eigenfunctions (i.e. spectral analysis) can provide such information as the shape of the fundamental mode, which represents the asymptotic behaviour of the neutron density with respect to time or fission generations, depending on whether the  $\alpha$ - or  $k$ - eigenbasis are adopted [28, 4]. Moreover, it can be used to assess the eigenvalue separation and in particular the dominance ratio between the fundamental and the following eigenvalue, which is a measure of the degree of “tightness” of a core and thus of the response to external perturbations: the system is said to be tightly coupled if the first two eigenvalues are separated, and loosely coupled otherwise [144, 120, 54, 113]. Finally, it can estimate the space and energy behaviour of higher eigenmodes, which will shed light on the way perturbations will propagate through the reactor core [128, 126].

In this respect, a fundamental observable is provided by the *eigenvalue separation* E.S. [144], which for  $k$ -eigenvalue problems is defined as follows:

$$\text{E.S.}_n(k) = \frac{1}{k_n} - \frac{1}{k_0} \geq 0, \quad (1.1)$$

for  $n > 0$ . Here  $k_n$  are the  $n$ -th order  $k$ -eigenvalues <sup>4</sup>,  $k_0$  being the fundamental eigenvalue (i.e., the multiplication factor). The case  $n = 1$  plays a special role, and is frequently referred to without using the index [120], namely,

$$\text{E.S.}(k) = \text{E.S.}_1(k) = \frac{1}{k_1} - \frac{1}{k_0} \geq 0. \quad (1.2)$$

A closely related quantity is the dominance ratio

$$\text{DR} = \frac{k_1}{k_0} \leq 1, \quad (1.3)$$

---

<sup>4</sup>We are implicitly assuming here that the  $k$ -eigenvalues can be ordered, with  $k_0 > k_1 \geq k_2, \dots$ .

which can be monotonically mapped onto the E.S., thus sharing the same information content [37, 73]. Although in the mathematical literature the analogous notion of *spectral gap*<sup>5</sup> is widely used for eigenvalue problems sharing some similarity to the  $\alpha$ -eigenvalue formulation (for instance in the context of the time-dependent diffusion equation [84, 125, 26, 2, 44]), the concept of eigenvalue separation or dominance ratio do not seem to have been drawn much attention for  $\alpha$ -eigenvalue, to the best of our knowledge.

Experimental and numerical investigations have shown that a small E.S. would increase the probability for a system to propagate instabilities, thus enhancing complex space-time patterns (as opposed to systems displaying a large E.S., which behave as point-kinetics) [120]. This is especially relevant for loosely coupled cores, such as breeders having alternating regions of highly enriched fuel and depleted blankets. By virtue of its key role in understanding the system kinetics, and in particular the reactor response due to external actions such as perturbations and tilts, the eigenvalue separation has been extensively investigated [128, 38, 3, 54, 113, 78].

For the  $k$ -eigenvalue formulation, Monte Carlo methods can determine (without approximations) the fundamental (direct) mode and eigenvalue by the power iteration method, which will yield the asymptotic neutron flux within the core [96, 95]. The stochastic version of the power iteration has a long history, and has been in use almost since the beginning of the Monte Carlo methods [47]. The calculation of the fundamental adjoint mode, on the contrary, has been out of reach for many years<sup>6</sup> and has been recently made possible by a major breakthrough: the rediscovery that the fundamental adjoint mode is proportional to the neutron importance function (which can be estimated by running a regular power iteration and recording the genealogy of each ancestor neutron) has been key to the development of the Iterated Fission Probability (IFP) method [42, 43, 110, 75]. By resorting to the IFP, most modern production Monte Carlo codes (including TRIPOLI-4<sup>®</sup>) can now provide an unbiased estimate of the fundamental adjoint mode for  $k$ -eigenvalue problems [147, 138].

The  $\alpha$ -eigenvalue problems, although their formulation is as old as (or maybe older than) that of  $k$ -eigenvalues, has been cast in a stochastic algorithm adapted to Monte Carlo methods in later times [18]. The original method was flawed for sub-critical configurations (the eigenvalue search led to numerical instabilities and to abnormal terminations [57]) and did not include the contributions of delayed neutron precursors [115, 28, 169, 166, 162]. Since then, several improvements (most notably, concerning the stability for sub-critical systems) and generalizations have been proposed and successfully tested in production Monte Carlo codes [8, 94, 170]. The most widely used algorithm for the fundamental (direct)  $\alpha$ -eigenmode is based on an extension of the traditional power iteration, where the dominant  $\alpha$ -eigenvalue is treated as a parameter and progressively adjusted until a fictitious  $k$  eigenvalue converges to one. The characterization of the adjoint fundamental mode for the  $\alpha$ -eigenvalue problem has been achieved quite recently, based on a slight modification of the IFP method [147].

Once the direct and adjoint fundamental modes have been computed by Monte Carlo, the effective (i.e., adjoint-weighted) kinetics parameters of the core can be easily determined [75]: the time evolution of the reactor can then be expressed by solving the approximated point-kinetics equations, whose coefficients are precisely the kinetics parameters. Point-kinetics equations, whose derivation is intrinsically based on collapsing the full phase-space of the Boltzmann equation into a few effective parameters (representing the whole reactor as a “point”, provided that the entire neutron population obeys the fundamental eigenmode with respect to space, angle and energy variable), are widely used in the reactor physics community as a reliable and fast tool for the analysis of core kinetics [72, 55, 4]. However, their use is deemed to be appropriate only when *i*) the core is sufficiently homogeneous (for the collapsing to a point to be a realistic approximation), and when *ii*) the fundamental mode of the neutron population is sufficiently separated from higher harmonics (for the reduction to the fundamental mode to be meaningful). If these conditions cannot be ensured, the analysis of higher-order eigenvalues and eigenfunctions becomes mandatory [21].

Monte Carlo methods have been also applied to the estimation of higher-order eigenvalues and eigenfunctions, both for  $k$ - and  $\alpha$ -eigenvalue problems [35, 68, 22, 8]. Contrary to the fundamental mode, which can be assessed by simulating particles carrying positive statistical weights, the exact determination of higher eigenmodes in principle requires weights with alternating signs, which is a daunting task for Monte Carlo methods: for  $k$ -eigenvalue problems, some ingenious strategies have been proposed in recent years, but most are hindered by convergence issues and none has led so far to a practical implementation that can be transposed to production codes [12, 153].

---

<sup>5</sup>I.e., the distance between two consecutive eigenvalues, and most often the first and the second.

<sup>6</sup>The propagation of adjoint particles is notoriously unstable [96].

---

For  $\alpha$ -eigenvalue problems, the number of attempts is even smaller [164].

Nonetheless, a viable strategy for higher-order  $k$ -eigenvalues and eigenfunctions has been developed: the idea is to discretize the operators appearing in the eigenvalue equations and to obtain finite-size matrices, whose elements can be filled in the course of a regular Monte Carlo power iteration [22]. It is important to stress that the resulting eigenvalues and eigenvectors are approximations, for two concurrent reasons: the matrix has a finite size, and the neutron distribution used in order to fill the matrix element can preserve <sup>7</sup> at most the fundamental mode and eigenvalue. By increasing the matrix size, the eigenvalues and eigenvectors are supposed to converge to those of the original equation. The so-called "fission matrix method" [152] belongs to this class of approaches and has been in use for a long time, although it has been made popular only in recent years, when increased computer power has become available, and thanks to the use of sparse-matrix storage techniques [22]. Based on a similar strategy, a matrix-filling approach has been also proposed for  $\alpha$ -eigenvalue problems, which poses specific challenges [8].

By building upon these considerations, the goal of this thesis is two-fold: on one hand, we will thoroughly compare the Monte Carlo methods for eigenvalue problems and propose novel computational strategies for the  $\alpha$ -eigenvalues; on the other hand, we will apply these methods to the investigation of a few relevant reactor configurations, in order to show how pertinent information can be extracted and used in order to better grasp the features of the nuclear systems.

On the methodological side, in the first part of this manuscript we will begin by addressing the case of the direct and adjoint fundamental eigenmodes, and show that discrepancies might arise between the  $k$ - and  $\alpha$ -eigenbasis close to the critical point (i.e.,  $k = 1$  and  $\alpha = 0$ ). At criticality, the two fundamental modes coincide by definition, whereas for an increasing departure from criticality deviations should appear, which are enhanced by the presence of decoupling effects and/or heterogeneities in the cores. These spatial and spectral differences in the fundamental modes are mirrored in the kinetics parameters (which are expressed as bilinear forms involving both the direct and adjoint modes), and thus also on the system reactivity (via the in-hour equation). It is thus of utmost importance to ascertain whether and to which extent the estimation of the kinetics parameters is affected by the system heterogeneities, which are conveyed in the shapes of the eigenmodes. Special attention will be paid to the contribution of the delayed neutron precursors, which has been neglected so far in previous investigations.

Concerning higher eigenmodes and eigenvalues, we will focus on the case of matrix-filling methods for  $\alpha$ -eigenvalue problems, in view of their relevance for the time response of nuclear systems, and provide a novel Monte Carlo strategy that can overcome some of the limitations of the existing approaches. These methods, conceived and tested in a Monte Carlo code built from scratch for the purpose of exploring new algorithms, will be implemented in TRIPOLI-4<sup>®</sup> to be deployed for the analysis of realistic reactor configurations.

In the second part of this manuscript, we will probe the impact of system geometry and material compositions on the reactor kinetics, via an eigenmode decomposition computed by Monte Carlo methods, in view of interpreting experimental data coming from the EPILOGUE experiments carried out at the EOLE critical facility (formerly operated CEA Cadarache) [50, 51, 49]. We will first examine some simplified benchmark configurations, which will allow us to understand how the mechanisms of heterogeneities (and other decoupling effects, such as the system size) manifest themselves in the eigenvalues and eigenvectors of the  $k$ - and  $\alpha$ -matrices. Then, we will consider the EPILOGUE experiments, where special reactor configurations with an increased moderator fraction at selected locations (under the form of a "water blade") have been tested. Unfortunately, the experiments for a single water blade were not conclusive, possibly due to a poor choice of the detector locations within the core. Our numerical simulations, carried out by using the TRIPOLI-4<sup>®</sup> model of the EPILOGUE configuration and the newly developed  $\alpha$ -matrix capabilities, will allow exploring details that were inaccessible in the experimental campaign. In particular, we will also consider a modified configuration where additional water blades are added: we will thus investigate the effects of increasing the presence of a localised moderator region on the shape of the eigenmodes and on the eigenvalues, which might shed light on the system response to perturbations such as control rods or external sources. In this respect, the proposed approach plays the role of a "fully numerical experiment" and might help in designing new experimental campaigns in research reactors.

---

<sup>7</sup>i.e., yield an unbiased estimate for.

## 1.1 Plan of the thesis

This manuscript is organized as follows.

In Chapter 2 we will begin by providing a general overview of neutron transport problems in the context of reactor physics. We will establish the basic notation and introduce the key quantities of interest. We will focus in particular on time-dependent transport and present the integro-differential and integral forms of the Boltzmann equations satisfied by the neutron density. The peculiar role of the delayed neutron precursors will be recalled. The adjoint transport equations will be introduced as well. We will then show how a class of eigenvalue problem formulations can be established based on the transport equation: two main classes of eigenvalue problems, namely  $k$ -eigenvalues and  $\alpha$ -eigenvalues, will be discussed, and their physical meaning will be emphasized. The spectral analysis of such eigenvalue equations can provide useful information on the asymptotic behavior of the neutron population, which can complement the full description stemming from the time-dependent transport equations. We will conclude this chapter by considering the point-kinetics approach, which provides a fast, albeit approximated, way of characterizing the time evolution of the nuclear systems.

In Chapter 3 we will recall the role and the principles of Monte Carlo simulation in the domain of reactor physics. The basic methods will be briefly mentioned. We will in particular focus on the special role of Monte Carlo simulation as a numerical tool capable of producing reference (i.e., unbiased) solutions for nuclear systems: almost no approximations are introduced, since the energy, angle and space do not need to be discretized. We will briefly illustrate how Monte Carlo simulation has been recently extended to kinetic (i.e., time-dependent) systems, which demands even longer computing times. The remaining part of the chapter is devoted to introducing the Monte Carlo methods specifically devoted to eigenvalue problems, which will be at the heart of the following parts of the manuscript. A short description of the Monte Carlo codes used in this thesis will be provided: TRIPOLI-4<sup>®</sup>, the general-purpose code developed at CEA [20], and a mock-up simplified code that was built from scratch in order to test the algorithms, probe their stability and numerical convergence, and verify them against analytical solutions (where possible).

Chapter 4 will be devoted to the analysis of the behavior of the fundamental modes, both forward and adjoint, of the  $k$ - and  $\alpha$ -eigenvalue formulations. We start by recalling the algorithms implemented in TRIPOLI-4<sup>®</sup> that allow the fundamental modes to be estimated without approximations. The Iterated Fission Probability [150] and the Generalized Iterated Fission Probability [147] methods, which have recently paved the way to the calculation of the adjoint eigenmodes, will be described at length. Our *first original* contribution is the investigation of the discrepancies between the  $k$ - and  $\alpha$ -fundamental modes close to the critical point (where the two are known to coincide): contrary to previous works [28], we will explicitly take into account the presence of the precursor contributions and we will also focus on the adjoint eigenmodes. Slight, yet systematic differences will be highlighted for a chosen set of reactor configurations, including two benchmarks based on spherical multiplying systems and the CROCUS facility operated at the EPFL, Switzerland. The discrepancies observed for the fundamental modes might have an impact on the calculation of derived reactor parameters, such as the effective kinetics parameters and the reactivity: a thorough discussion will be presented.

In Chapter 5 we will examine how Monte Carlo methods can be successfully used for the calculation of higher-order  $k$ - and  $\alpha$ -eigenmodes and eigenvalues. We will first recall the basics of the fission matrix approach, a matrix-filling Monte Carlo method that can be used in order to estimate the elements of a finite-size matrix whose eigenvectors and eigenvalues converge to those of the  $k$ - eigenvalue problem in the limit of an infinite size. Contrary to the methods used for the fundamental eigenmode and eigenvalue, the estimation of the higher eigenmodes and eigenvalues via the fission matrix is affected by a bias. Inspired by this approach, our *second original* contribution will consist in conceiving a new technique designed to estimate the elements of a distinct matrix whose eigenvectors and eigenvalues converge to those of the  $\alpha$ -eigenvalue problem. This novel matrix-filling Monte Carlo method lays the bases for  $\alpha$ -spectral analysis. A thorough description of the algorithm and its practical implementation will be discussed. A few relevant applications will be analyzed and the discrepancies between the higher  $\alpha$ - and  $k$ -higher-order eigenmodes will be illustrated.

Chapter 6 will present some significant applications of the Monte Carlo methods for the determination of  $k$ - and  $\alpha$ -eigenmodes and eigenvalues. The *third original* contribution will be to examine whether the two modal expansions may convey different information content concerning the behavior of the systems under analysis, with special focus on the eigenvalue separation as defined above. In particular, we will examine how the fundamental

and higher eigenmodes and eigenvalues behave in the presence of decoupling factors: starting from (homogeneous or heterogeneous) tightly coupled reactor configurations, we will progressively modify these systems by introducing an increasingly stronger decoupling effect, either due to the system size or to the spatial heterogeneity. For this purpose, we will select some simple benchmark configurations where these effects can be exacerbated. The eigenvalue separation and the shape of the eigenfunctions will be carefully examined and commented. We will examine on the discrepancies between the  $k$ - and  $\alpha$ -basis and show how both eigenpairs react to the presence of the decoupling effects.

Finally, in Chapter 7 our *fourth original* contribution will be to revisit the EPILOGUE experiment, carried out in the EOLE critical facility of CEA Cadarache. The EPILOGUE experiment was aimed at exploring – among others – the effects of the presence of a water blade with respect to the reactor response. By building on the knowledge and numerical simulation tools developed in the previous chapters, we will first run the TRIPOLI-4® model corresponding to the EPILOGUE experiment and compare the effects of the water blades on the fundamental and higher eigenmodes and eigenvalues of the  $k$  and  $\alpha$ -bases. Then, as a way of conceiving a “thought experiment”, we will explore the effects of adding several other water blades into the core, thus increasing the decoupling effect. A physical interpretation based on the Monte Carlo simulations will be provided. The obtained results might suggest a better way of arranging the detector positions within the core, so as to emphasize their response, and might thus help in conceiving a future experimental campaign in a dedicated research reactor, in view of assessing the effects of heterogeneities with respect to the system behavior.

Conclusions will be finally drawn in Chapter 8.

## 1.2 List of published material

Part of the contents of this manuscript has appeared or will appear in the following peer-reviewed journals and proceedings of international conferences:

- Vitali, V., Blaise, P., Chevallier, F., Jinaphanh, A., Zoia, A., 2019. Spectral analysis by direct and adjoint Monte Carlo methods. *Ann. Nucl. Energy* **137**, 107033.
- Vitali, V., Blaise, P., Chevallier, F., Jinaphanh, A., Zoia, A., 2019. Direct and adjoint Monte Carlo methods for  $\alpha$ -eigenvalue spectral analysis In Proceedings of the ICTT 2019 conference. Paris, France.
- Vitali, V., Blaise, P., Chevallier, F., Jinaphanh, A., Zoia, A., 2020. Comparison of direct and adjoint  $k$ - and  $\alpha$ -eigenfunctions In Proceedings of the PHYSOR 2020 conference. Cambridge, UK.
- Vitali, V., Blaise, P., Chevallier, F., Jinaphanh, A., Zoia, A., 2020. Monte Carlo analysis of spectral effects: application to the EPILOGUE experiments, to be submitted to *Ann. Nucl. Energy*



## Chapter 2

# Overview of time-dependent transport and spectral analysis in reactor physics

The behaviour of the neutron population within a nuclear system is ruled by the Boltzmann equation, possibly coupled with the equations describing the evolution of the delayed neutron precursors [4]. Since these equations are key to the discussions and the development of the Monte Carlo methods presented in the following of this manuscript, in this chapter we first provide an overview of the physical principles and the mathematical description of non-stationary neutron transport, and successively show how complementary information can be extracted from the associated eigenvalue equations.

### 2.1 Neutron interactions with matter

For the energy range considered in this work, neutrons are assumed to be distinct point particles, and wave properties are neglected [34]. Under these assumptions, neutrons freely travel through media and interact with the background, which is the primary source of randomness for particle transport. In the applications of interest in nuclear reactor physics, the neutron population is much more diluted ( $10^8$  n/cm<sup>3</sup> for a full power reactor) than the one of the nuclei composing the traversed medium (roughly  $10^{23}$  at/cm<sup>3</sup>) [4]. For this reason, the probability of a neutron undergoing a collision at a generic point in phase-space is not related to the probability of encountering other neutrons in the same position [23].

Neutron interactions are characterized by the *total macroscopic cross section*  $\Sigma_t(\mathbf{r}, E)$ , which represents the probability per unit length for a neutron to undergo a collision event, at given position  $\mathbf{r}$  and energy  $E$  [34, 23, 157]. This quantity does not depend on the direction of the particle, provided that the traversed medium is isotropic. In the following we will assume that the physical properties of the medium are time-independent. Moreover, for a generic nuclide  $A$ , the cross section can be expressed as the product

$$\Sigma_A(\mathbf{r}, E) = \rho_A(\mathbf{r})\sigma_A(E), \quad (2.1)$$

where  $\rho_A(\mathbf{r})$  is the *nuclide density* and has units of the inverse of a volume,  $\sigma_A(E)$  is the *microscopic cross section* and has units of a surface. The inverse of the total macroscopic cross section is defined as the *mean free path* and represents the mean distance travelled by the neutron between any two successive collisions. This typical length is considerably larger than both the particle wavelength and the interaction range, so that we can consider collisions as localized events in the phase-space.

The interactions between neutrons and the medium occur during a negligible period of time, hence particles freely stream up to the next collision site, where their state is randomly modified [34, 23, 24, 157]. The hypothesis of an instantaneous collision is valid for short-range interaction forces and if the emission of the particle after such collision occurs in a time interval considerably shorter than the time from one collision to another. These conditions are typically satisfied if the particle mean free paths are much larger than the characteristic space scale

over which collision events occur.

The collisions between neutrons and nuclei occur in about  $10^{-14}$  s, with a correlation length of about  $10^{-13}$  cm. The neutrons streaming in nuclear systems are characterized by a typical lifetime of about  $(10^{-6} - 10^{-4})$  s and the inter-collision distance exhibits values of the order of some cm [24, 157, 34]. As an example, the neutron wavelength  $\lambda$  expressed in cm for energy value  $E$  expressed in MeV is given by

$$\lambda = \frac{h}{m_n v} \approx \frac{2.86 \times 10^{-9}}{\sqrt{E}}, \quad (2.2)$$

where the neutron mass  $m_n$  is around 939.56 MeV,  $h$  represents the Planck constant and  $v$  is the speed of the neutron. By considering the typical linear size of an atom ( $10^{-10}$  cm), interference or diffraction phenomena for neutrons related to the wave-particle duality will only occur for energy values smaller than  $10^{-2}$  eV [117].

The stochastic motion of neutrons due to their interactions with the background medium suggests a *probabilistic approach* [34, 157, 158]. Since it is not possible to predict the exact number of particles at a given position in the phase-space, physical observables will be thus averaged over multiple particle histories in order to describe the main properties of the system.

We will assume that the phase-space is entirely defined in terms of two variables, namely the vector position  $\mathbf{r}$  and the vector velocity  $\mathbf{v}$  of the particles at a given time  $t$ . In other words, we will follow a classical approach, and neglect the contributions of quantum variables (such as spin, for instance). A key physical observable is the *phase-space density function*  $n(\mathbf{r}, \mathbf{v}, t)$ , here defined as

$$n(\mathbf{r}, \mathbf{v}, t) d\mathbf{r} d\mathbf{v}, \quad (2.3)$$

representing the average number of particles in the infinitesimal phase-space volume  $d\mathbf{r} d\mathbf{v}$  located around  $(\mathbf{r}, \mathbf{v})$  at time  $t$  [34, 157].

The *phase-space current density*  $\mathbf{J}(\mathbf{r}, \mathbf{v}, t)$  can be formulated as the product of the velocity  $\mathbf{v}$  times the phase-space density function  $n(\mathbf{r}, \mathbf{v}, t)$ . The average number of particles that cross the infinitesimal surface  $d\mathbf{S}$  per unit time having velocity  $d\mathbf{v}$  around  $\mathbf{v}$  at time  $t$  [34] is finally defined as

$$\mathbf{J}(\mathbf{r}, \mathbf{v}, t) \cdot d\mathbf{S} d\mathbf{v}. \quad (2.4)$$

## 2.2 General form of the transport equation

The transport equation for the particle density can be derived from a balance for the phase-space density function  $n(\mathbf{r}, \mathbf{v}, t)$  [34, 157, 24]. Given a generic volume  $V$  in the phase-space, the variation of particles in the system can be obtained by considering the leakage rate through the surface  $S = \partial V$  of  $V$ , the collision rate which randomly modifies the velocity vector and the external source rate from a generic function  $Q(\mathbf{r}, \mathbf{v}, t)$ . This yields the following equation

$$\frac{\partial}{\partial t} \int_V d\mathbf{r} d\mathbf{v} n(\mathbf{r}, \mathbf{v}, t) = - \int_S d\mathbf{S} \cdot \mathbf{J}(\mathbf{r}, \mathbf{v}, t) d\mathbf{v} + \int_V d\mathbf{r} d\mathbf{v} \left( \frac{\partial n}{\partial t} \right)_{coll} + \int_V d\mathbf{r} d\mathbf{v} Q(\mathbf{r}, \mathbf{v}, t), \quad (2.5)$$

where the term  $(\partial_t n)_{coll}$  is the rate of change of  $n$  due to collisions of a generic particle with the medium. The region  $V$  does not depend on time. Hence, it is possible to move the time derivative inside the integral operator. Then, Gauss' theorem can be applied in order to rewrite the leakage rate as

$$\int_S d\mathbf{S} \cdot \mathbf{J}(\mathbf{r}, \mathbf{v}, t) = \int_V d\mathbf{r} \nabla_{\mathbf{r}} \cdot \mathbf{J}(\mathbf{r}, \mathbf{v}, t) = \int_V d\mathbf{r} \mathbf{v} \cdot \nabla_{\mathbf{r}} n(\mathbf{r}, \mathbf{v}, t), \quad (2.6)$$

where we have used  $\nabla_{\mathbf{r}} \cdot \mathbf{v} n = \mathbf{v} \cdot \nabla_{\mathbf{r}} n$ , since  $\mathbf{r}$  and  $\mathbf{v}$  are independent variables. Equation (2.5) has to be valid for any volume, hence the integrand has to be null, which yields

$$\frac{\partial n(\mathbf{r}, \mathbf{v}, t)}{\partial t} + \mathbf{v} \cdot \nabla_{\mathbf{r}} n(\mathbf{r}, \mathbf{v}, t) = \left( \frac{\partial n}{\partial t} \right)_{coll} + Q(\mathbf{r}, \mathbf{v}, t). \quad (2.7)$$

Equation (2.7) is the *general form of the transport equation* for the phase-space density  $n(\mathbf{r}, \mathbf{v}, t)$ .

### 2.2.1 Collision phenomena

For neutron transport, we can justify the *linearity* of the collision kernel  $(\partial_t n)_{coll}$  in view of the fact that the neutron population is highly diluted, which implies no interactions among neutrons [34, 23].

It is customary to introduce the collision kernel  $C(\mathbf{r}, \mathbf{v}' \rightarrow \mathbf{v})$  [24]

$$C(\mathbf{r}, \mathbf{v}' \rightarrow \mathbf{v}) d\mathbf{v}, \quad (2.8)$$

which represents the average number of particles emitted at  $\mathbf{r}$  with velocity in  $d\mathbf{v}$  around  $\mathbf{v}$ , given an incoming particle having a collision at  $\mathbf{r}$  with velocity  $\mathbf{v}'$  [157]. The general form of the collision kernel is

$$C(\mathbf{r}, \mathbf{v}' \rightarrow \mathbf{v}) = \sum_A \frac{\Sigma_{A,t}(\mathbf{r}, v')}{\Sigma_t(\mathbf{r}, v')} \sum_j \frac{\sigma_{A,j}(\mathbf{r}, v')}{\sigma_{A,t}(\mathbf{r}, v')} \bar{v}_{A,j}(v') f_{A,j}(\mathbf{v}' \rightarrow \mathbf{v}), \quad (2.9)$$

where  $v = |\mathbf{v}|$  (recall that the cross sections do not depend on the direction of the particle). The first sum of Eq. (2.9) considers all the nuclides  $A$  composing a given material, and the second considers all possible reactions  $j$  for a given nuclide  $A$ . Among the most common reactions we mention capture (the neutron is absorbed and no particles are emitted), scattering (the energy and direction of the particle are modified according to the corresponding diffusion law) and fission (the neutron is absorbed and a random number of fission neutrons is emitted with energy and direction obeying the emission laws). The macroscopic cross section  $\Sigma_{A,t}(\mathbf{r}, v')$  is the total cross section of nuclide  $A$  and  $\Sigma_t(\mathbf{r}, v')$  is the cross section of the entire material. Furthermore, the microscopic cross section  $\sigma_{A,j}(\mathbf{r}, v')$  is associated to the reaction  $j$  and nuclide  $A$  and  $\sigma_{A,t}(\mathbf{r}, v')$  is the total cross section of nuclide  $A$  [82].

From inspection of this kernel, three different components can be singled out. The first is expressed by the probability for a neutron to interact with nuclide  $A$ :

$$p_A = \frac{\Sigma_{A,t}(\mathbf{r}, v')}{\Sigma_t(\mathbf{r}, v')}. \quad (2.10)$$

The second is the probability for a neutron to have a collision of type  $j$  with nuclide  $A$

$$p_{A,j} = \frac{\sigma_{A,j}(\mathbf{r}, v')}{\sigma_{A,t}(\mathbf{r}, v')}. \quad (2.11)$$

The third is given by the product of the multiplicity factor  $\bar{v}_{A,j}(v')$  and the probability density function  $f_{A,j}(\mathbf{v}' \rightarrow \mathbf{v})$ . These quantities represent the yield associated to the emitted neutrons after the collision and the distribution for the energy and direction of such particles for collision  $j$ .

Recalling the previous definitions, the collision rate density  $v\Sigma_t(\mathbf{r}, \mathbf{v})n(\mathbf{r}, \mathbf{v}, t)$  represents the rate of any possible interaction per unit volume. Neutrons travelling with velocity  $\mathbf{v}'$  and creating secondary particles with velocity  $\mathbf{v}$  are described by the collision rate density  $v'\Sigma_t(\mathbf{r}, v')C(\mathbf{r}, \mathbf{v}' \rightarrow \mathbf{v})n(\mathbf{r}, \mathbf{v}', t)$ .

The collision term  $(\partial_t n)_{coll}$  can then be expressed as

$$\left(\frac{\partial n}{\partial t}\right)_{coll} = \int_{4\pi} \int_0^\infty d\mathbf{v}' v'\Sigma_t(\mathbf{r}, v')C(\mathbf{r}, \mathbf{v}' \rightarrow \mathbf{v})n(\mathbf{r}, \mathbf{v}', t) - v\Sigma_t(\mathbf{r}, v)n(\mathbf{r}, \mathbf{v}, t). \quad (2.12)$$

The linear transport equation for the phase-space density  $n(\mathbf{r}, \mathbf{v}, t)$  is finally expressed by coupling Eq. (2.12) with the balance from Eq. (2.7)

$$\frac{\partial n}{\partial t} + \mathbf{v} \cdot \nabla_{\mathbf{r}} n + v\Sigma_t(\mathbf{r}, v)n = \int_{4\pi} \int_0^\infty d\mathbf{v}' v'\Sigma_t(\mathbf{r}, v')C(\mathbf{r}, \mathbf{v}' \rightarrow \mathbf{v})n(\mathbf{r}, \mathbf{v}', t) + Q(\mathbf{r}, \mathbf{v}, t). \quad (2.13)$$

Equation (2.13) is the *linear Boltzmann equation* [34, 23, 24]. This is a linear integro-differential equation for the phase-space density  $n$ , where linearity stems from assuming that cross sections do not depend on  $n(\mathbf{r}, \mathbf{v}, t)$  and from

the absence of collisions between neutrons.

The collision term can be split in order to separately consider the scattering and the fission contributions:

$$\Sigma_t(\mathbf{r}, \mathbf{v}')C(\mathbf{r}, \mathbf{v}' \rightarrow \mathbf{v}) = \Sigma_t(\mathbf{r}, \mathbf{v}')C_s(\mathbf{r}, \mathbf{v}' \rightarrow \mathbf{v}) + \Sigma_t(\mathbf{r}, \mathbf{v}')C_f(\mathbf{r}, \mathbf{v}' \rightarrow \mathbf{v}), \quad (2.14)$$

with

$$C_s(\mathbf{r}, \mathbf{v}' \rightarrow \mathbf{v}) = \frac{\Sigma_s(\mathbf{r}, \mathbf{v}')}{\Sigma_t(\mathbf{r}, \mathbf{v}')} \bar{\nu}_s(v') f_s(\mathbf{v}' \rightarrow \mathbf{v}), \quad (2.15)$$

and

$$C_f(\mathbf{r}, \mathbf{v}' \rightarrow \mathbf{v}) = \frac{\Sigma_f(\mathbf{r}, \mathbf{v}')}{\Sigma_t(\mathbf{r}, \mathbf{v}')} \bar{\nu}_f(v') \chi_f(\mathbf{v}' \rightarrow \mathbf{v}). \quad (2.16)$$

The quantity  $\bar{\nu}_s(v')$  is the multiplicity of the scattering interactions (as in  $(n, xn)$  reactions), whereas  $\bar{\nu}_f(v')$  is the multiplicity of the fission events. The average number of fission neutrons is denoted by  $\bar{\nu}_f(v')$  (of the order of 2.5 for  $^{235}\text{U}$  [72]), and the associated (normalized) fission spectrum is denoted by  $\chi_f(\mathbf{v}' \rightarrow \mathbf{v})$ .

## 2.2.2 Precursors and delayed neutrons

In the previous paragraphs, we have implicitly assumed that there is no delay between the collision time and the emission time at collision events. Upon collision with a fissile nucleus, the neutron is absorbed, and the nucleus becomes unstable. After a very short time lapse, the unstable nucleus may split into several fragments (typically two), and sets free a variable number of other neutrons, each following an energy and angle distribution [72]. These neutrons are conventionally labelled as *prompt*. It is a good approximation to assume that fission neutrons are emitted isotropically in the laboratory system, and the energy spectrum is only weakly dependent on the incident neutron energy, in which case we have

$$\chi_p(\mathbf{v}' \rightarrow \mathbf{v}) = \frac{\chi_p(v)}{4\pi}, \quad (2.17)$$

where  $4\pi$  is the normalization factor of the isotropic distribution [4]. The fission spectrum can be reasonably well approximated by a Maxwellian distribution

$$\chi_p(E) \approx \chi_{p,\text{Maxwell}}(E), \quad (2.18)$$

where

$$\chi_{p,\text{Maxwell}}(E) = \frac{2}{\sqrt{\pi}} \frac{1}{kT} \sqrt{\frac{E}{kT}} e^{-E/kT}, \quad (2.19)$$

with parameter  $kT = 1.29$ . Watt has also published an analytical formula based on data fitting, which reads

$$\chi_{p,\text{Watt}}(E) = c_w e^{-E} \sinh(\sqrt{E}), \quad (2.20)$$

with  $E$  expressed in MeV and parameter  $c_w = 0.484$ .

The fission fragments are in an excited state and decay to their fundamental state via  $\beta^-$  nuclear reactions by emitting supplementary neutrons. Each fissile isotope leads to wide range of possible fission fragments, which are customarily grouped in so-called *families*, according to the value of their average decay times [4]. The corresponding decay rates are usually denoted  $\lambda_j$ , in units of  $\text{s}^{-1}$ , whereas the average decay time is defined as  $1/\lambda_j$  with  $j$  the index of the family. The extra neutrons emitted after the decay time of the  $\beta^-$  nuclear reactions are conventionally labelled as *delayed*, as opposed to prompt neutrons. Between the fission event and the actual emission from the fission fragments by  $\beta^-$  decay, the delayed neutrons are named *precursors* [72]. The average number of precursors of family  $j$  created per fission event is denoted by  $\bar{\nu}_d^j(v')$ , and we typically have  $\bar{\nu}_d^j(v') \ll \bar{\nu}_p(v')$ . The emitted delayed neutrons hold the same position as the associated precursors, and are emitted isotropically with an energy spectrum  $\chi_d^j(v)$ .

For a typical light-water reactor, the average decay time of precursors is about  $\lambda^{-1} \approx 10$  s, which is to be compared with the average mean generation time (i.e., the time between a birth from fission and a death by absorption) in the reactor, which is of the order of  $\Lambda \approx 20$   $\mu\text{s}$ . This difference is crucial for nuclear reactor control, since the contribution due to delayed neutrons allows the time evolution of the system due to a change in reactivity to

be slowed down by a considerable amount [72]. Table 2.1 collects the values of delayed neutron yields, decay constants and emission energies for the six precursor families associated to the  $^{235}\text{U}$  isotope, according to the ENDF/B-VI nuclear data library [102].

family	$\bar{\nu}_d^j[-]$	$\lambda_j [\text{s}^{-1}]$	$E_j [\text{MeV}]$
1	$5.85 \times 10^{-4}$	$1.33 \times 10^{-2}$	$4.05 \times 10^{-1}$
2	$3.02 \times 10^{-3}$	$3.27 \times 10^{-2}$	$4.72 \times 10^{-1}$
3	$2.88 \times 10^{-3}$	$1.21 \times 10^{-1}$	$4.43 \times 10^{-1}$
4	$6.46 \times 10^{-3}$	$3.03 \times 10^{-1}$	$5.57 \times 10^{-1}$
5	$2.65 \times 10^{-3}$	$8.49 \times 10^{-1}$	$5.18 \times 10^{-1}$
6	$1.11 \times 10^{-3}$	$2.85 \times 10^0$	$5.40 \times 10^{-1}$

Table 2.1:  $^{235}\text{U}$  data from ENDF/B-VI nuclear data library: average values of delayed yields  $\bar{\nu}_d^j$ , decay constants  $\lambda_j$  and emission energies  $E_j$  of the six precursor families.

As apparent from Tab. 2.1, another major difference in the properties of prompt and delayed neutrons concerns their kinetic energy. In light-water reactors, fission events occur mostly at energies below 1 eV, so neutrons have to slow down to thermal energies in order to maximise the probability of undergoing a fission event. However, prompt neutrons are emitted at a mean energy of about 2 MeV, whereas delayed neutrons are generated at energies around 500 keV. Thus, delayed neutrons have a larger probability of avoiding leakage and absorption during the slow-down process and are more likely to induce thermal fissions than prompt neutrons [33].

As for the transport equation, precursors are considered separately. Recalling the fission collision kernel from Eq. (2.16), the prompt fission component is expressed as

$$\Sigma_t(\mathbf{r}, v') C_{f,p}(\mathbf{r}, \mathbf{v}' \rightarrow \mathbf{v}) = \bar{\nu}_p(v') \Sigma_f(\mathbf{r}, v') \frac{\chi_p(v)}{4\pi}, \quad (2.21)$$

where  $\Sigma_f(\mathbf{r}, v')$  is the fission cross section. By taking into account the concentration of precursors  $c_j(\mathbf{r}, t)$  for family  $j$ , it is possible to define a balance equation as it follows:

$$\frac{\partial c_j(\mathbf{r}, t)}{\partial t} = \int_{4\pi} \int_0^\infty d\mathbf{v}' \bar{\nu}_d^j(v') v' \Sigma_f(\mathbf{r}, v') n(\mathbf{r}, \mathbf{v}', t) - \lambda_j c_j(\mathbf{r}, t). \quad (2.22)$$

Delayed neutrons are created from the decay of the precursor belonging to family  $j$  with a rate equal to  $\lambda_j c_j(\mathbf{r}, t)$ . This quantity can be derived by solving Eq. (2.22)

$$c_j(\mathbf{r}, t) = e^{-\lambda_j(t-t_0)} c_j(\mathbf{r}, t_0) + \int_{4\pi} \int_0^\infty d\mathbf{v}' \int_{t_0}^t dt' \bar{\nu}_d^j(v') v' \Sigma_f(\mathbf{r}, v') e^{-\lambda_j(t-t')} n(\mathbf{r}, \mathbf{v}', t'), \quad (2.23)$$

where  $t_0$  is the initial time.

The total fission contribution to the collision kernel is then

$$\int_{4\pi} \int_0^\infty d\mathbf{v}' \Sigma_t(\mathbf{r}, v') C_f(\mathbf{r}, \mathbf{v}' \rightarrow \mathbf{v}) v' n(\mathbf{r}, \mathbf{v}', t) = \frac{\chi_p(v)}{4\pi} \int_{4\pi} \int_0^\infty d\mathbf{v}' \bar{\nu}_p(v') \Sigma_f(\mathbf{r}, v') v' n(\mathbf{r}, \mathbf{v}', t) + \sum_j \lambda_j \frac{\chi_d^j(v)}{4\pi} c_j(\mathbf{r}, t). \quad (2.24)$$

For *stationary* problems (implying that precursors have reached equilibrium),

$$\lambda_j c_j(\mathbf{r}) = \int_{4\pi} \int_0^\infty d\mathbf{v}' \bar{\nu}_d^j(v') v' \Sigma_f(\mathbf{r}, v') n(\mathbf{r}, \mathbf{v}'). \quad (2.25)$$

The total fission contribution to the collision kernel for the stationary case is then

$$\Sigma_t(\mathbf{r}, v') C_f(\mathbf{r}, \mathbf{v}' \rightarrow \mathbf{v}) = \frac{\chi_p(v)}{4\pi} \bar{\nu}_p(v') \Sigma_f(\mathbf{r}, v') + \sum_j \frac{\chi_d^j(v)}{4\pi} \bar{\nu}_d^j(v') v' \Sigma_f(\mathbf{r}, v'). \quad (2.26)$$

### 2.2.3 Boundary and initial conditions

In order to compute solutions for the evolution of the phase-space density  $n(\mathbf{r}, \mathbf{v}, t)$  from Eq. (2.13), proper initial and boundary conditions are required [34, 157]. It is customary to define the initial phase-space distribution  $n_0(\mathbf{r}, \mathbf{v})$  as

$$n(\mathbf{r}, \mathbf{v}, t = t_0) = n_0(\mathbf{r}, \mathbf{v}). \quad (2.27)$$

Different types of boundary conditions can be applied at the frontiers of the analyzed system. In particular, in the context of the simulations investigated in the following, leakage and reflective boundary conditions will be considered. In the former case, particles cannot re-enter the system and are lost for the simulation domain. Conversely, neutrons bounce on the reflected surface, continuing their walks in the system.

## 2.3 The integro-differential transport equations

In transport theory, it is customary to introduce the *angular neutron flux*  $\varphi(\mathbf{r}, \mathbf{v}, t)$  [34, 157], defined as

$$\varphi(\mathbf{r}, \mathbf{v}, t) = v n(\mathbf{r}, \mathbf{v}, t). \quad (2.28)$$

This function can be related to the current previously defined in Eq. (2.4):  $\mathbf{J}(\mathbf{r}, \mathbf{v}, t) = \boldsymbol{\Omega} \varphi(\mathbf{r}, \mathbf{v}, t)$ , where the unit vector  $\boldsymbol{\Omega} = \mathbf{v}/v$  denotes the neutron direction. The velocity vector can be equivalently expressed in terms of the direction  $\boldsymbol{\Omega}$  and the energy  $E$ . In view of the derivation detailed in the previous sections, the angular flux  $\varphi(\mathbf{r}, \boldsymbol{\Omega}, E, t)$  obeys the Boltzmann equation, coupled with the equations for the precursor concentrations  $c_j(\mathbf{r}, t)$ . The integro-differential form of this problem reads [4, 23, 24]

$$\begin{aligned} \frac{1}{v(E)} \frac{\partial \varphi(\mathbf{r}, \boldsymbol{\Omega}, E, t)}{\partial t} + \boldsymbol{\Omega} \cdot \nabla \varphi(\mathbf{r}, \boldsymbol{\Omega}, E, t) + \Sigma_t(\mathbf{r}, E) \varphi(\mathbf{r}, \boldsymbol{\Omega}, E, t) - \int_{4\pi} d\boldsymbol{\Omega}' \int_0^\infty dE' \Sigma_s(\mathbf{r}, \boldsymbol{\Omega}' \rightarrow \boldsymbol{\Omega}, E' \rightarrow E) \varphi(\mathbf{r}, \boldsymbol{\Omega}', E', t) = \\ \frac{\chi_p(E)}{4\pi} \int_{4\pi} d\boldsymbol{\Omega}' \int_0^\infty dE' \bar{v}_p(E') \Sigma_f(\mathbf{r}, E') \varphi(\mathbf{r}, \boldsymbol{\Omega}', E', t) + \sum_j \frac{\chi_d^j(E)}{4\pi} \lambda_j c_j(\mathbf{r}, t) + Q(\mathbf{r}, \boldsymbol{\Omega}, E, t), \end{aligned} \quad (2.29)$$

$$\frac{\partial c_j(\mathbf{r}, t)}{\partial t} = \int_{4\pi} d\boldsymbol{\Omega}' \int_0^\infty dE' \bar{v}_d^j(E') \Sigma_f(\mathbf{r}, E') \varphi(\mathbf{r}, \boldsymbol{\Omega}', E', t) - \lambda_j c_j(\mathbf{r}, t). \quad (2.30)$$

The term  $\Sigma_s(\mathbf{r}, \boldsymbol{\Omega}' \rightarrow \boldsymbol{\Omega}, E' \rightarrow E)$  is a short-hand for the scattering kernel

$$\Sigma_s(\mathbf{r}, \boldsymbol{\Omega}' \rightarrow \boldsymbol{\Omega}, E' \rightarrow E) = \bar{v}_s(E') \Sigma_s(\mathbf{r}, E') f_s(\boldsymbol{\Omega}' \rightarrow \boldsymbol{\Omega}, E' \rightarrow E), \quad (2.31)$$

and the other notations have been previously introduced.

The system of coupled Eqs. (2.29) and (2.30) can be rewritten in a more compact form by introducing some appropriate linear transport operators. In particular, at the left-hand side of the neutron equation it is possible to define the *net disappearance operator*  $\mathcal{M}$  as

$$\mathcal{M} = \mathcal{L} + \mathcal{R} - \mathcal{S}, \quad (2.32)$$

where the *streaming operator*  $\mathcal{L}$ , the *collisional operator*  $\mathcal{R}$  and the *scattering operator*  $\mathcal{S}$  are respectively defined as

$$\mathcal{L} = \boldsymbol{\Omega} \cdot \nabla, \quad (2.33)$$

$$\mathcal{R} = \Sigma_t(\mathbf{r}, E), \quad (2.34)$$

$$\mathcal{S} = \int_{4\pi} d\boldsymbol{\Omega}' \int_0^\infty dE' \Sigma_s(\mathbf{r}, \boldsymbol{\Omega}' \rightarrow \boldsymbol{\Omega}, E' \rightarrow E). \quad (2.35)$$

The *prompt fission operator*  $\mathcal{F}_p$  and the *precursor production operator*  $\mathcal{F}_d^j$  are defined as

$$\mathcal{F}_p = \frac{\chi_p(E)}{4\pi} \int_{4\pi} d\boldsymbol{\Omega}' \int_0^\infty dE' \bar{v}_p(E') \Sigma_f(\mathbf{r}, E'), \quad (2.36)$$

$$\mathcal{F}_d^j = \int_{4\pi} d\Omega' \int_0^\infty dE' \bar{v}_d^j(E') \Sigma_f(\mathbf{r}, E'). \quad (2.37)$$

In order to keep the notation compact, we can use a matrix form for this set of equations. First, we consider a vector for the neutron flux and the precursor concentrations defined as  $\Psi = \{\varphi, c_1, \dots, c_J\}^T$ . Then, we combine the transport operators as

$$\begin{pmatrix} \frac{1}{v} & 0 & \cdots & 0 \\ 0 & 1 & \cdots & 0 \\ \vdots & \vdots & \ddots & \vdots \\ 0 & 0 & \cdots & 1 \end{pmatrix} \frac{\partial \Psi}{\partial t} = \begin{pmatrix} \mathcal{F}_p - \mathcal{M} & \lambda_1 \frac{\chi_d^1}{4\pi} & \cdots & \lambda_J \frac{\chi_d^J}{4\pi} \\ \mathcal{F}_d^1 & -\lambda_1 & \cdots & 0 \\ \vdots & \vdots & \ddots & \vdots \\ \mathcal{F}_d^J & 0 & \cdots & -\lambda_J \end{pmatrix} \Psi + \begin{pmatrix} Q \\ 0 \\ \vdots \\ 0 \end{pmatrix}, \quad (2.38)$$

where  $J$  denotes the number of precursors families for the problem at hand. Finally, by introducing the linear operators

$$\mathcal{A} = \begin{pmatrix} \mathcal{F}_p - \mathcal{M} & \lambda_1 \frac{\chi_d^1}{4\pi} & \cdots & \lambda_J \frac{\chi_d^J}{4\pi} \\ \mathcal{F}_d^1 & -\lambda_1 & \cdots & 0 \\ \vdots & \vdots & \ddots & \vdots \\ \mathcal{F}_d^J & 0 & \cdots & -\lambda_J \end{pmatrix}, \quad (2.39)$$

and

$$\mathcal{V}^{-1} = \begin{pmatrix} \frac{1}{v} & 0 & \cdots & 0 \\ 0 & 1 & \cdots & 0 \\ \vdots & \vdots & \ddots & \vdots \\ 0 & 0 & \cdots & 1 \end{pmatrix}, \quad (2.40)$$

Eq. (2.38) can be written as

$$\mathcal{V}^{-1} \frac{\partial \Psi}{\partial t} = \mathcal{A} \Psi + Q, \quad (2.41)$$

where  $Q = \{Q, 0, \dots, 0\}^T$  is a vector representing the external source distributions for neutrons and precursors. For the sake of simplicity, in the following we neglect external precursor sources. The set of Eqs. (2.41) is well-posed for suitable external source distribution, initial and boundary conditions [4, 82, 70, 157].

In general, one is interested in determining a response  $R$  at a given detector, which we express as a linear functional of the neutron flux:

$$R = \int_V d\mathbf{r} \int_{4\pi} d\Omega \int_0^\infty dE \int_{t_0}^{t_f} dt \varphi(\mathbf{r}, \Omega, E, t) \eta_\varphi(\mathbf{r}, \Omega, E, t), \quad (2.42)$$

where  $\eta_\varphi$  is the response function of the detector to the neutron flux (with  $\eta_\varphi = 0$  outside the detector region in the phase-space),  $t_0$  and  $t_f$  are the initial and the final time, respectively. It is assumed that precursors do not directly contribute to the detector response.

## 2.4 The integral formulation of the transport equations

It is possible to express Eqs. (2.29) and (2.30) in a more compact form by formally solving Eq. (2.30) to yield

$$c_j(t) = c_{j,0} e^{-\lambda_j(t-t_0)} + \int_{t_0}^t dt' \mathcal{F}_d^j \varphi(t') e^{-\lambda_j(t-t')},$$

where  $c_{j,0}$  corresponds to precursors concentration for family  $j$  at initial time  $t_0$ .

Substituting this expression for  $c_j(\mathbf{r}, t)$  in Eq. (2.29) and using the formalisms introduced from Eq. (2.32) to Eq. (2.41), we obtain

$$\frac{1}{v} \frac{\partial \varphi}{\partial t} + \mathcal{M} \varphi = \mathcal{F}_p \varphi + \sum_j \frac{\chi_d^j}{4\pi} \lambda_j \int_{t_0}^t dt' \mathcal{F}_d^j \varphi(t') e^{-\lambda_j(t-t')} + Q. \quad (2.43)$$

Equation (2.43) is amenable to an integral formulation, which is the natural framework for Monte Carlo, as discussed in the next chapter. First, let  $P = (\mathbf{r}, \boldsymbol{\Omega}, E, t)$  denote the coordinates of a generic point in the extended phase-space (including time). It can be shown [100] that Eq. (2.43) can be rewritten as

$$\psi(P) = \mathbb{T}\chi(P), \quad (2.44)$$

$$\chi(P) = \mathbb{C}\psi(P) + Q(P). \quad (2.45)$$

Here  $\psi(P) = \Sigma_t(\mathbf{r}, E)\varphi(P)$  is the *collision density* and  $\chi(P)$  is the *emission density* in  $P$ . The *flight operator*  $\mathbb{T}$  reads

$$\mathbb{T}g(P) = \int dP' T(P' \rightarrow P)g(P'),$$

where the integration over  $dP'$  is short-hand for integration over all the coordinates of the phase-space and  $g(P)$  is any suitable function:

$$\int dP' T(P' \rightarrow P)g(P') = \int d\mathbf{r}' \int d\boldsymbol{\Omega}' \int dE' \int dt' T(\mathbf{r}' \rightarrow \mathbf{r}, \boldsymbol{\Omega}' \rightarrow \boldsymbol{\Omega}, E' \rightarrow E, t' \rightarrow t)g(\mathbf{r}', \boldsymbol{\Omega}', E', t').$$

The flight kernel reads

$$T(P' \rightarrow P) = \Sigma_t(\mathbf{r}, E) \exp\left(-\int_0^{|\mathbf{r}-\mathbf{r}'|} d\ell \Sigma_t(\mathbf{r} + \ell \cdot \boldsymbol{\Omega}, E)\right) \cdot \frac{\delta\left(\boldsymbol{\Omega} - \frac{\mathbf{r}-\mathbf{r}'}{|\mathbf{r}-\mathbf{r}'|}\right)}{(\mathbf{r}-\mathbf{r}')^2} \cdot \delta\left(t-t' - \frac{|\mathbf{r}-\mathbf{r}'|}{v}\right) \cdot \delta(\boldsymbol{\Omega}-\boldsymbol{\Omega}') \cdot \delta(E-E'), \quad (2.46)$$

where  $\delta$  is a Dirac delta function.

Similarly, the *collision operator*  $\mathbb{C}$  reads

$$\mathbb{C}g(P) = \int dP' C(P' \rightarrow P)g(P'),$$

where the kernel  $C(P' \rightarrow P)$  consists of a prompt and a delayed term as discussed in Section 2.2.2:

$$C(P' \rightarrow P) = C_p(P' \rightarrow P) + C_d(P' \rightarrow P), \quad (2.47)$$

with

$$C_p(P' \rightarrow P) = \left[ \bar{v}_s(E') \frac{\Sigma_s(\mathbf{r}, E')}{\Sigma_t(\mathbf{r}, E')} f_s(\boldsymbol{\Omega}' \rightarrow \boldsymbol{\Omega}, E' \rightarrow E) + \bar{v}_p(E') \frac{\Sigma_f(\mathbf{r}, E')}{\Sigma_t(\mathbf{r}, E')} \cdot \frac{\chi_p(E)}{4\pi} \right] \cdot \delta(t-t') \cdot \delta(\mathbf{r}-\mathbf{r}'), \quad (2.48)$$

$$C_d(P' \rightarrow P) = \sum_j \bar{v}_d^j(E') \frac{\Sigma_f(\mathbf{r}, E')}{\Sigma_t(\mathbf{r}, E')} \cdot \frac{\chi_d^j(E)}{4\pi} \cdot \lambda_j e^{-\lambda_j(t-t')} \cdot \delta(\mathbf{r}-\mathbf{r}'). \quad (2.49)$$

## 2.5 The adjoint transport equations

For a well-defined operator  $K$  associated to a kernel  $\mathcal{K}(z' \rightarrow z)$ , the adjoint operator  $K^\dagger$  associated to the kernel  $\mathcal{K}^\dagger$  is defined by the scalar product

$$\int dz u(z) \int dz' \mathcal{K}(z' \rightarrow z)v(z') = \int dz v(z) \int dz' \mathcal{K}^\dagger(z' \rightarrow z)u(z'), \quad (2.50)$$

for every set of suitable integrable functions  $u(z)$  and  $v(z)$ . By interchanging the integration variables in Eq. (2.50), we have thus the definition of the adjoint kernel in terms of forward kernel, namely  $\mathcal{K}^\dagger(z' \rightarrow z) = \mathcal{K}(z \rightarrow z')$ .

The adjoint formulation of the time-dependent transport equations reads [4, 62]

$$-\frac{1}{v(E)} \frac{\partial \varphi^\dagger(\mathbf{r}, \boldsymbol{\Omega}, E, t)}{\partial t} - \boldsymbol{\Omega} \cdot \nabla \varphi^\dagger(\mathbf{r}, \boldsymbol{\Omega}, E, t) + \Sigma_t(\mathbf{r}, E) \varphi^\dagger(\mathbf{r}, \boldsymbol{\Omega}, E, t) - \int_{4\pi} d\boldsymbol{\Omega}' \int_0^\infty dE' \Sigma_s(\mathbf{r}, \boldsymbol{\Omega} \rightarrow \boldsymbol{\Omega}', E \rightarrow E') \varphi^\dagger(\mathbf{r}, \boldsymbol{\Omega}', E', t) = \bar{v}_p(E) \Sigma_f(\mathbf{r}, E) \int_{4\pi} d\boldsymbol{\Omega}' \int_0^\infty dE' \frac{\chi_p(E')}{4\pi} \varphi^\dagger(\mathbf{r}, \boldsymbol{\Omega}', E', t) + \sum_j \bar{v}_d^j(E) \Sigma_f(\mathbf{r}, E) \lambda_j c_j^\dagger(\mathbf{r}, t) + Q^\dagger(\mathbf{r}, \boldsymbol{\Omega}, E, t), \quad (2.51)$$

$$-\frac{\partial c_j^\dagger(\mathbf{r}, t)}{\partial t} = \int_{4\pi} d\boldsymbol{\Omega}' \int_0^\infty dE' \frac{\chi_d^j(E')}{4\pi} \varphi^\dagger(\mathbf{r}, \boldsymbol{\Omega}', E', t) - \lambda_j c_j^\dagger(\mathbf{r}, t), \quad (2.52)$$

where  $\varphi^\dagger(\mathbf{r}, \boldsymbol{\Omega}, E, t)$  and  $c_j^\dagger(\mathbf{r}, t)$  are the *adjoint neutron flux* and the *adjoint precursors concentration*, respectively, and  $Q^\dagger(\mathbf{r}, \boldsymbol{\Omega}, E, t)$  is an arbitrary adjoint source. The physical interpretation of the adjoint flux and the precursor concentrations will be thoroughly discussed in the next chapters. The adjoint transport operators appearing in Eqs. (2.51) and (2.52) for the net disappearance, streaming, scattering and fission contributions are defined as:

$$\mathcal{M}^\dagger = \mathcal{L}^\dagger + \mathcal{R}^\dagger - \mathcal{S}^\dagger, \quad (2.53)$$

$$\mathcal{L}^\dagger = -\boldsymbol{\Omega} \cdot \nabla, \quad (2.54)$$

$$\mathcal{R}^\dagger = \Sigma_t(\mathbf{r}, E), \quad (2.55)$$

$$\mathcal{S}^\dagger = \int_{4\pi} d\boldsymbol{\Omega}' \int_0^\infty dE' \Sigma_s(\mathbf{r}, \boldsymbol{\Omega} \rightarrow \boldsymbol{\Omega}', E \rightarrow E'), \quad (2.56)$$

$$\mathcal{F}_p^\dagger = \bar{v}_p(E) \Sigma_f(\mathbf{r}, E) \int_{4\pi} d\boldsymbol{\Omega}' \int_0^\infty dE' \frac{\chi_p(E')}{4\pi}, \quad (2.57)$$

$$\mathcal{F}_{d,j}^\dagger = \int_{4\pi} d\boldsymbol{\Omega}' \int_0^\infty dE' \frac{\chi_d^j(E')}{4\pi}. \quad (2.58)$$

In analogy with Eq. (2.38), it is convenient to introduce the adjoint vector  $\Psi^\dagger = \{\varphi^\dagger, c_1^\dagger, \dots, c_J^\dagger\}^T$  and the adjoint matrix form of the transport equations as

$$\begin{pmatrix} \frac{1}{v} & 0 & \dots & 0 \\ 0 & 1 & \dots & 0 \\ \vdots & \vdots & \ddots & \vdots \\ 0 & 0 & \dots & 1 \end{pmatrix} \frac{\partial \Psi^\dagger}{\partial t} = \begin{pmatrix} \mathcal{F}_p^\dagger - \mathcal{M}^\dagger & \bar{v}_d^1 \Sigma_f & \dots & \bar{v}_d^J \Sigma_f \\ \lambda_1 \mathcal{F}_{d,1}^\dagger & -\lambda_1 & \dots & 0 \\ \vdots & \vdots & \ddots & \vdots \\ \lambda_J \mathcal{F}_{d,J}^\dagger & 0 & \dots & -\lambda_J \end{pmatrix} \Psi^\dagger + \begin{pmatrix} Q^\dagger \\ 0 \\ \vdots \\ 0 \end{pmatrix}. \quad (2.59)$$

The final formulation of the adjoint transport equations is

$$\mathcal{V}^{-1} \frac{\partial \Psi^\dagger}{\partial t} = \mathcal{A}^\dagger \Psi^\dagger + \mathcal{Q}^\dagger, \quad (2.60)$$

where we have introduced the adjoint matrix operator

$$\mathcal{A}^\dagger = \begin{pmatrix} \mathcal{F}_p^\dagger - \mathcal{M}^\dagger & \bar{v}_d^1 \Sigma_f & \dots & \bar{v}_d^J \Sigma_f \\ \lambda_1 \mathcal{F}_{d,1}^\dagger & -\lambda_1 & \dots & 0 \\ \vdots & \vdots & \ddots & \vdots \\ \lambda_J \mathcal{F}_{d,J}^\dagger & 0 & \dots & -\lambda_J \end{pmatrix}, \quad (2.61)$$

and the vector  $Q^\dagger = \{Q^\dagger, 0, \dots, 0\}^T$  representing the adjoint external source for neutrons and precursors.

## 2.6 Eigenvalue problems for the transport equations

The coupled system of Eqs. (2.38) fully describes the time evolution of the neutron and precursor populations within the reactor. However, one may be interested in the solution of the stationary problem, which is tantamount to determining the *asymptotic* state of the system [4, 34]. Let us introduce the time-independent neutron transport equation in integro-differential form:

$$\boldsymbol{\Omega} \cdot \nabla \varphi(\mathbf{r}, \boldsymbol{\Omega}, E) + \Sigma_t(\mathbf{r}, E)\varphi(\mathbf{r}, \boldsymbol{\Omega}, E) = \int_{4\pi} d\boldsymbol{\Omega}' \int_0^\infty dE' \Sigma_t(\mathbf{r}, E')C(\mathbf{r}, \boldsymbol{\Omega}' \rightarrow \boldsymbol{\Omega}, E' \rightarrow E)\varphi(\mathbf{r}, \boldsymbol{\Omega}', E') + Q(\mathbf{r}, \boldsymbol{\Omega}, E). \quad (2.62)$$

To simplify notation, we introduce the total fission operator  $\mathcal{F}$  as

$$\mathcal{F} = \frac{\chi_p(E)}{4\pi} \int_{4\pi} d\boldsymbol{\Omega}' \int_0^\infty dE' \bar{v}_p(E')\Sigma_f(\mathbf{r}, E') + \sum_j \frac{\chi_d^j(E)}{4\pi} \int_{4\pi} d\boldsymbol{\Omega}' \int_0^\infty dE' \bar{v}_d^j(E')\Sigma_f(\mathbf{r}, E') = \mathcal{F}_p + \sum_j \frac{\chi_d^j(E)}{4\pi} \mathcal{F}_d^j. \quad (2.63)$$

In this way, Eq. (2.62) can be rewritten in a more compact form as

$$\mathcal{M}\varphi = \mathcal{F}\varphi + Q. \quad (2.64)$$

One of the main challenges in reactor physics is to determine whether Eq. (2.64) admits stationary bounded, non-negative and non-trivial solutions. In this context, the spectral analysis based on the eigenvalue formulation of the neutron and precursor transport problem can provide useful information [4]. The spectral properties of the Boltzmann operator  $\mathcal{B} = \mathcal{F} - \mathcal{M}$  allow characterizing the asymptotic state of the reactor, as well as assessing how this state is reached and whether the asymptotic state is stable with respect to external perturbations [34]. To have an idea of the extent of this subject, we briefly list a series of applications: start-up of commercial reactors [123], analysis of accelerator-driven systems [122], material control and accountability in critical assemblies [131], and pulsed neutron reactivity measurements [21]. By imposing proper assumptions, it is possible to conceive different eigenvalue problems associated to the transport operator [154]. In the following, we detail the main eigenvalue formulations related to neutron transport.

### 2.6.1 The $k$ -eigenvalue problem

Historically, the  $k$ -eigenvalue formulation stands as the possibly best-known formulation for criticality analysis [34]. We assume the absence of external sources (i.e. independent source-driven problem), and we seek a stationary solution. For this to happen, one needs to find a combination of geometry and materials for which a stationary solution is possible. Therefore, one introduces a "fictitious" factor  $k$  that artificially reduces ( $k > 1$ ) or increases ( $k < 1$ ) the fission contribution to match the losses.

We seek then a value of  $k$  that makes the operator  $\mathcal{M} - \mathcal{F}/k$  singular, such that the homogeneous problem will allow a non-trivial solution (defined up to a multiplicative constant). This strategy transforms the original time-dependent problem into an eigenvalue problem. Recalling Eq. (2.64) and applying these hypotheses leads to the generalized eigenvalue problem

$$\mathcal{M}\varphi_k = \frac{1}{k}\mathcal{F}\varphi_k, \quad (2.65)$$

where  $(k, \varphi_k)$  are the  $k$ -eigenpairs, composed of the eigenvalues  $k$  and the corresponding eigenmodes  $\varphi_k(\mathbf{r}, \boldsymbol{\Omega}, E)$ . From a physical point of view, this eigenvalue problem corresponds to following the evolution of particles through fission generations [55]. Neutrons emitted after  $g$  successive fission events are said to belong to *generation*  $g$ , hence Eq. (2.65) can also be interpreted as a balance through generations. By inspection of Eq. (2.63), this operator carries the contributions of prompt and delayed neutrons.

Equation (2.65) can be reformulated by introducing the fission emission density  $S_{f,k} = \mathcal{F}\varphi_k$ , and the operator  $\mathcal{K}$  as

$$\mathcal{K} = \mathcal{M}^{-1}\mathcal{F}, \quad (2.66)$$

where  $\mathcal{M}^{-1}$  is the inverse of the net disappearance operator  $\mathcal{M}$ , provided that it exists. The  $k$ -eigenvalue problem

for the  $S_{f,k}$  distribution can be thus defined by the following equation

$$\mathcal{K}S_{f,k} = kS_{f,k}. \quad (2.67)$$

In relation with the eigenvalues, there exists an eigenvalue  $k_0$ , positive and simple such that  $k_0 > |k_n|$  for  $n \neq 0$ , associated to the real eigenfunction  $\varphi_{k_0}$  [1, 154].

Equation (2.65) represents a balance between the production and the disappearance of neutrons from the system. A physical interpretation of the dominant eigenvalue  $k_0$  can be obtained by integrating over the phase-space

$$k_0 = \frac{\langle \mathcal{F}\varphi_{k_0} \rangle}{\langle \mathcal{M}\varphi_{k_0} \rangle}, \quad (2.68)$$

where  $\langle \dots \rangle$  represents integration over the whole phase space.

The value  $k_0$ , also known as the *multiplication factor*, represents the ratio between the rate of neutrons produced by fission events and the rate of neutrons absorbed or leaked from the system. A critical system would be identified by a perfect balance between production and disappearance, hence, a ratio  $k_0$  equal to 1. For  $k_0 < 1$  the system is sub-critical, whereas for  $k_0 > 1$  the system is super-critical. The corresponding eigenmode  $\varphi_{k_0}$  is the dominant eigenfunction, assumed to be real and non-negative [34]. The ratio  $k_1/k_0$  is defined as the *dominance ratio* and expresses the influence of the first excited eigenmode on the fundamental distribution [55]. The eigenvalue separation related to the the fundamental and the first order eigenvalues is a key parameter for the stability of the system. In particular, it has been proved that it strongly influences the response of the system to a perturbation [46, 135]. Moreover, it can also be considered as an indicator of decoupling effects present in the system [98].

This eigenvalue problem can be reformulated by following the adjoint approach, under the same assumptions previously introduced, which yields

$$\mathcal{M}^\dagger \varphi_k^\dagger = \frac{1}{k^\dagger} \mathcal{F}^\dagger \varphi_k^\dagger, \quad (2.69)$$

where  $\mathcal{F}^\dagger$  is the adjoint total fission operator defined as

$$\mathcal{F}^\dagger = \bar{\nu}_p(E)\Sigma_f(\mathbf{r}, E) \int_{4\pi} d\Omega' \int_0^\infty dE' \frac{\chi_p(E')}{4\pi} + \sum_j \bar{\nu}_d^j(E)\Sigma_f(\mathbf{r}, E) \int_{4\pi} d\Omega' \int_0^\infty dE' \frac{\chi_d^j(E')}{4\pi}. \quad (2.70)$$

It can be shown that  $k^\dagger = k$  [34].

### 2.6.2 The $\alpha$ -eigenvalue problem

The  $k$ -eigenvalue formulation is intrinsically based on a decomposition of the system evolution through fission generations. Although this approach is very useful in quickly ascertaining whether the system is critical, sub- or super-critical, one might in general be interested also in determining the asymptotic reactor behaviour with respect to time [25, 4, 34].

Assuming no delayed neutrons in the system, the most common hypotheses for the analysis of the time behaviour of the reactor are the separation of the phase-space variables and an exponential evolution of the neutron flux with respect to time, namely

$$\varphi(\mathbf{r}, \mathbf{\Omega}, E, t) = \varphi_\alpha(\mathbf{r}, \mathbf{\Omega}, E)e^{\alpha t}, \quad (2.71)$$

where  $\alpha$  is a suitable constant carrying the units of the inverse of a time.

In this way the so-called *prompt  $\alpha$ -eigenvalue problem* is defined as

$$\mathcal{B}_p \varphi_\alpha = \alpha \varphi_\alpha, \quad (2.72)$$

where the operator  $\mathcal{B}_p = \mathcal{V}(\mathcal{F}_p - \mathcal{M})$  [34], the speed operator  $\mathcal{V}$  is defined as the inverse of  $\mathcal{V}^{-1}$  from Eq. (2.40) and we assumed the absence of the source term  $Q$ .

The spectrum associated to this operator has been thoroughly investigated [82, 80, 34]. Pioneering work in this

field has concerned mono-kinetic transport in slab geometries [89, 90, 124]. In general, the eigenvalues associated to Eq. (2.72) are complex and include discrete points, lines and possibly a continuum portion of the complex plane. The discrete and the continuum spectrum are separated into two half-planes by the so-called *Corngold limit*, defined as the smallest value of  $v\Sigma_t$  [27]. For more complex geometries and multi-group problems [67], it has been shown that the continuum region of the spectrum disappears. In particular, if neutrons travel through the system with a velocity such that no wave phenomena occur, the spectrum presents a collection of distinct points in the phase-space. A broader overview related to the  $\alpha$ -spectrum can be found in the references [130, 129].

Assuming the presence of a discrete set of  $\alpha$ -eigenvalues, it has been demonstrated that this part of the spectrum can be ordered as

$$\operatorname{Re}(\alpha_\infty) \cdots \leq \operatorname{Re}(\alpha_i) \cdots \leq \operatorname{Re}(\alpha_2) \leq \operatorname{Re}(\alpha_1) < \alpha_0, \quad (2.73)$$

where the fundamental eigenvalue  $\alpha_0$  exists and the corresponding fundamental eigenfunction  $\varphi_{\alpha_0}$  is non-negative and real [82, 80]. From a physical point of view, the absolute value of  $\alpha_0$  represents the *inverse of the asymptotic reactor period*, which is the time required by the neutron flux to scale by a factor  $e$  when all the transients related to time constants  $\alpha_i$  shorter than  $\alpha_0$  are over (this can be understood by inspection of the time-dependence of the flux after introducing the variable separation in Eq. (2.71)) [159]. If particle populations do not evolve during time, a value  $\alpha_0 = 0$  is found and the system is critical. Conversely, a sub-critical system is characterized by  $\alpha_0 < 0$ , whereas a super-critical configuration is defined by  $\alpha_0 > 0$ . Moreover, since the operator  $\mathcal{B}_p$  is real, each complex eigenvalue comes as a pair of complex conjugate values.

Let us now take into account also the delayed neutrons. If the hypothesis of separation of phase-space variables and exponential time behaviour is now applied to the precursor concentrations [25, 4, 34], the vector  $\Psi = \{\varphi, c_1, \dots, c_J\}^T$  reads

$$\Psi(P) = \Psi_\alpha(\mathbf{r}, \boldsymbol{\Omega}, E)e^{\alpha t}. \quad (2.74)$$

By replacing Eq. (2.74) inside Eq. (2.38) the time derivative applied to the  $\Psi$  vector is equal to  $\alpha\Psi_\alpha e^{\alpha t}$ . Dividing both sides of Eq. (2.38) by  $e^{\alpha t}$  and in the absence of the source term  $\mathcal{Q}$ , the  $\alpha$ -eigenvalue problem is obtained as

$$\alpha \begin{pmatrix} \frac{1}{v} & 0 & \cdots & 0 \\ 0 & 1 & \cdots & 0 \\ \vdots & \vdots & \ddots & \vdots \\ 0 & 0 & \cdots & 1 \end{pmatrix} \Psi_\alpha = \begin{pmatrix} \mathcal{F}_p - \mathcal{M} & \lambda \frac{\chi_d^1}{4\pi} & \cdots & \lambda_J \frac{\chi_d^J}{4\pi} \\ \mathcal{F}_d^1 & -\lambda_1 & \cdots & 0 \\ \vdots & \vdots & \ddots & \vdots \\ \mathcal{F}_d^J & 0 & \cdots & -\lambda_J \end{pmatrix} \Psi_\alpha, \quad (2.75)$$

which can also be expressed in a compact form as

$$\mathcal{A}\Psi_\alpha = \alpha\mathcal{V}^{-1}\Psi_\alpha, \quad (2.76)$$

where the direct operators  $\mathcal{A}$  and  $\mathcal{V}^{-1}$  have been introduced in Eqs. (2.39) and (2.40), respectively. The fundamental eigenpair  $(\alpha_0, \Psi_{\alpha_0})$  physically represents the inverse of the asymptotic period of the reactor (including delayed contributions), and the asymptotic particle distribution. The spectral properties of the full system (2.76), including precursor contributions, have received comparatively less attention with respect to the prompt case (see for instance [25, 55, 70] for a survey); however, these properties have recently attracted renewed attention in view of the practical applications in reactor kinetics [139, 108, 5].

Contrary to the  $k$ -eigenvalue formulation, the delay of fission neutrons emitted from precursor decay is explicitly taken into account, and the distributions for precursor concentrations are additional unknowns for Eq. (2.76). It is possible to recast Eq. (2.76) as an eigenvalue problem for the neutron flux alone by formally solving the precursor distribution as

$$c_\alpha^j = \frac{1}{\lambda_j + \alpha} \mathcal{F}_d^j \varphi_\alpha, \quad (2.77)$$

and substituting this formulation in the neutron equation. A new operator for the fission events is then defined as

$$\mathcal{F}_\alpha = \mathcal{F}_p + \sum_j \frac{\lambda_j}{\lambda_j + \alpha} \frac{\chi_d^j}{4\pi} \mathcal{F}_d^j, \quad (2.78)$$

which yields

$$\mathcal{V}[\mathcal{F}_\alpha - \mathcal{M}]\varphi_\alpha = \alpha\varphi_\alpha. \quad (2.79)$$

Equation (2.79) is now non-linear with respect to the eigenvalues [155, 25, 55].

The adjoint formulation of the  $\alpha$ -eigenvalue problem can be obtained recalling the definition of adjoint transport operators. In particular, the adjoint versions of Eqs. (2.76) and (2.79) can be respectively obtained as

$$\mathcal{A}^\dagger \Psi_\alpha^\dagger = \alpha^\dagger \mathcal{V}^{-1} \Psi_\alpha^\dagger, \quad (2.80)$$

$$\mathcal{V}[\mathcal{F}_\alpha^\dagger - \mathcal{M}^\dagger]\varphi_\alpha^\dagger = \alpha\varphi_\alpha^\dagger, \quad (2.81)$$

where the adjoint operator  $\mathcal{F}_\alpha^\dagger$  is defined as

$$\mathcal{F}_\alpha^\dagger = \mathcal{F}_p^\dagger + \sum_j \frac{\lambda_j}{\lambda_j + \alpha} \bar{v}_d^j \Sigma_f \mathcal{F}_{d,j}^\dagger. \quad (2.82)$$

It can be proved that  $\alpha^\dagger = \alpha$  [34].

### Time expansion on a modal basis

Assuming the access to all eigenmodes, and that the spectrum is purely discrete, the complete temporal evolution of a system can be determined by expanding over a complete modal basis:

$$\Psi(P) = \sum_m^M w_{\alpha_m}(t) \Psi_{\alpha_m}(\mathbf{r}, \mathbf{\Omega}, E), \quad (2.83)$$

where  $w_{\alpha_m}$  and  $\Psi_{\alpha_m}$  are the coefficients of the expansion and the direct eigenmode of the  $m$  order according to the  $\alpha$ -eigenvalue problem, respectively. If this expression is applied in the compact version of the transport Eq. (2.41), we obtain

$$\sum_m w_{\alpha_m} \mathcal{A} \Psi_{\alpha_m} + \mathcal{Q} = \sum_m \frac{dw_{\alpha_m}}{dt} \mathcal{V}^{-1} \Psi_{\alpha_m}. \quad (2.84)$$

It can be proven that the  $\alpha$ -eigenmodes are a complete set of functions for the modal expansion [34].

The speed operator  $\mathcal{V}$  can be applied to both sides of Eq. (2.76) in order to recast the  $\alpha$ -eigenvalue problem as

$$\mathcal{V} \mathcal{A} \Psi_{\alpha_m} = \alpha_m \Psi_{\alpha_m}. \quad (2.85)$$

This relation can be exploited by multiplying the operator  $\mathcal{A}$  of Eq. (2.84) by the direct and the inverse of the speed operator and introducing the eigenvalue  $\alpha_m$  of the generic  $m$  order. Then each term of this equation is multiplied by the sum of the adjoint eigenmodes  $\Psi_{\alpha_n}^\dagger$ , where the index  $n$  denotes the generic order of these functions. Finally, an integration over the phase-space is performed in order to obtain the following expression

$$\sum_n \sum_m \left[ \alpha_m w_{\alpha_m}(t) \langle \Psi_{\alpha_n}^\dagger, \mathcal{V}^{-1} \Psi_{\alpha_m} \rangle + \langle \Psi_{\alpha_n}^\dagger, \mathcal{Q} \rangle \right] = \sum_n \sum_m \frac{dw_{\alpha_m}}{dt} \langle \Psi_{\alpha_n}^\dagger, \mathcal{V}^{-1} \Psi_{\alpha_m} \rangle. \quad (2.86)$$

The scalar products between the adjoint eigenmodes and the inverse matrix operator applied to the direct eigenmodes can be simplified by applying a bi-orthogonality condition [34]. For the  $\alpha$ -eigenvalue problem, such product is null in the case where the two functions have different order ( $m \neq n$ ), hence

$$\langle \Psi_{\alpha_n}^\dagger, \mathcal{V}^{-1} \Psi_{\alpha_m} \rangle = 0. \quad (2.87)$$

Due to this property, only one summation over the modes is kept and, by dividing both sides of Eq. (2.86) by the bi-orthogonality condition, the coefficient  $w_{\alpha_m}$  is computed as solution of the following differential equation in time [34, 21]

$$\frac{dw_{\alpha_m}}{dt} = \alpha_m w_{\alpha_m} + \frac{\langle \Psi_{\alpha_m}^\dagger, \mathcal{Q} \rangle}{\langle \Psi_{\alpha_m}^\dagger, \mathcal{V}^{-1} \Psi_{\alpha_m} \rangle}, \quad (2.88)$$

given an initial value of  $w_{\alpha_m}$ .

An important property coming from such expression is that the behaviour of the  $m$ -th order coefficient describing the evolution of particle populations depends on the source function  $Q$ , but also on the adjoint eigenmode of the same order  $\Psi_{\alpha_m}^\dagger$ .

In reality, as discussed in Section 2.6.2, a possible continuum spectrum can arise and the number of discrete eigen-modes can be finite, say  $M$ . Therefore a residual term  $\zeta(\mathbf{r}, \boldsymbol{\Omega}, E)$  is introduced

$$\Psi(P) = \sum_m^M w_{\alpha_m}(t) \Psi_{\alpha_m}(\mathbf{r}, \boldsymbol{\Omega}, E) + \zeta(\mathbf{r}, \boldsymbol{\Omega}, E). \quad (2.89)$$

For  $t \rightarrow \infty$ ,  $\zeta$  goes to zero and the influence of higher order harmonics will die out due to the negative real part of the eigenvalues. If this is the case, the temporal behaviour of the flux is only ruled by the fundamental order. The residual associated to the continuum is smaller as compared to the other contributions of the modal expansion: even for the cases where the basis is incomplete, viable expansions can still be computed [90].

## 2.7 Point kinetics

The computation of the time-dependent neutron distribution requires the resolution of the Boltzmann equation: a system of coupled integro-differential equations, depending on seven physical variables. However, if we are only interested in the evolution of neutron and precursor populations with respect to time, it is possible to obtain a simplified formulation of this problem. In order to apply this methodology, the main assumption is to split the neutron flux distribution into a *shape function*  $\phi(P)$ , and an *amplitude function*  $A(t)$  [4, 55]:

$$\varphi(P) = A(t)\phi(P). \quad (2.90)$$

In order to ensure the uniqueness of the solution of this problem, an additional assumption for the shape function is required. Often, it is assumed that such function has to fulfill the following property

$$\frac{\partial}{\partial t} \left\langle \varphi_0^\dagger, \frac{1}{v} \phi \right\rangle = 0, \quad (2.91)$$

where  $\varphi_0^\dagger$  is the adjoint fundamental mode of the  $k$ -eigenvalue problem and the scalar product is applied over the whole phase-space. The normalization is arbitrary, but this particular expression satisfies the following relation

$$\frac{\partial}{\partial t} \left\langle \varphi_0^\dagger(\mathbf{r}, \boldsymbol{\Omega}, E), \frac{1}{v(E)} \varphi(P) \right\rangle = \frac{\partial}{\partial t} \left( A(t) \left\langle \varphi_0^\dagger(\mathbf{r}, \boldsymbol{\Omega}, E), \frac{1}{v(E)} \phi(P) \right\rangle \right). \quad (2.92)$$

The flux factorization from Eq. (2.90) can be applied to the Boltzmann Eq. (2.41). Then, the transport operators are rearranged, multiplied by the weighting function  $\varphi_0^\dagger$  and integrated over the phase-space. The final formulation for the *exact point kinetics equations* is expressed by

$$\begin{aligned} \frac{dA(t)}{dt} &= \frac{\rho(t) - \beta(t)}{\Lambda(t)} A(t) + \sum_j \lambda_j \tilde{c}_j(t) + q(t) \\ \frac{d\tilde{c}_j(t)}{dt} &= \frac{\beta(t)}{\Lambda(t)} A(t) - \lambda_j \tilde{c}_j(t), \end{aligned} \quad (2.93)$$

$$\begin{aligned} \frac{dA(t)}{dt} &= \frac{\rho - \beta}{\Lambda} A(t) + \sum_j \lambda_j \tilde{c}_j(t) + q(t) \\ \frac{d\tilde{c}_j(t)}{dt} &= \frac{\beta}{\Lambda} A(t) - \lambda_j \tilde{c}_j(t), \end{aligned} \quad (2.94)$$

A detailed derivation for Eq. (2.93) is given in Appendix B.

The solutions of this system are the amplitude function  $A$  and the amplitude of the rescaled precursor concen-

trations  $\tilde{c}_j$  defined as

$$\tilde{c}_j(t) = \frac{1}{F(t)\Lambda(t)} \left\langle \varphi_0^\dagger(\mathbf{r}, \boldsymbol{\Omega}, E), \chi_d^j c_j(\mathbf{r}, t) \right\rangle, \quad (2.95)$$

depending on the initial conditions of the problem and the source distribution  $q$ , defined as

$$q(t) = \frac{1}{F(t)\Lambda(t)} \left\langle \varphi_0^\dagger(\mathbf{r}, \boldsymbol{\Omega}, E), Q(P) \right\rangle, \quad (2.96)$$

where  $F$  is a normalization function defined as

$$F(t) = \left\langle \varphi_0^\dagger(\mathbf{r}, \boldsymbol{\Omega}, E), \mathcal{F}\phi(P) \right\rangle. \quad (2.97)$$

From a mathematical point of view, the function  $F$  has no effect on the resolution of Eqs. (2.93) and its definition is arbitrary. Nevertheless, the specific expression in Eq. (2.97) gives a physical meaning to the other quantities describing the evolution of particles in the system: the *point kinetics parameters*. The *reactivity*  $\rho$ , the *effective delayed fraction*  $\beta_{\text{eff}}$ , and the *effective mean generation lifetime*  $\Lambda_{\text{eff}}$  are defined as

$$\rho(t) = \frac{1}{F(t)} \left\langle \varphi_0^\dagger(\mathbf{r}, \boldsymbol{\Omega}, E), [-\mathcal{M} + \mathcal{F}]\phi(P) \right\rangle, \quad (2.98)$$

$$\beta_{\text{eff}}^j(t) = \frac{1}{F(t)} \left\langle \varphi_0^\dagger(\mathbf{r}, \boldsymbol{\Omega}, E), \mathcal{F}_d^j \phi(P) \right\rangle, \quad (2.99)$$

$$\beta_{\text{eff}}(t) = \sum_j \beta_{\text{eff}}^j(t), \quad (2.100)$$

$$\Lambda_{\text{eff}}(t) = \frac{1}{F(t)} \left\langle \varphi_0^\dagger(\mathbf{r}, \boldsymbol{\Omega}, E), \frac{1}{v(E)} \phi(P) \right\rangle, \quad (2.101)$$

where *effective* refers to the fact that these quantities have been weighted by the adjoint eigenmode  $\varphi_0^\dagger$  [4, 72].

The effective mean generation time  $\Lambda_{\text{eff}}$  is the ratio between the adjoint-weighted neutron population and the adjoint-weighted rate of emission of fission neutrons, the total effective neutron fraction  $\beta_{\text{eff}}$  represents the adjoint-weighted fraction of delayed neutrons in the system.

### 2.7.1 Simplified $k$ - and $\alpha$ -point kinetics equations

The exact point kinetics equations introduced in Section 2.7 provide a complete solution for the time-dependence of the system. Since the real shape function  $\phi(P)$  is usually not accessible, it is customary to approximate  $\phi(P)$  with the direct fundamental eigenfunction from both the  $k$ - and the  $\alpha$ -formulations, which does not depend on time [34]. This assumption can be considered as valid if the shape function does not change significantly with respect to time, which is the case for a system close to the critical condition, and in the absence of very localized perturbations [55]. If the fundamental  $\alpha$  eigenmode is chosen for the flux factorization, the weighting function is correspondingly taken to be the adjoint fundamental  $\alpha$  eigenmode.

Under these hypotheses, the kinetics parameters do not depend on time and can be rewritten as

$$\rho_{(\alpha,k)} = \frac{1}{F_{(\alpha,k)}} \left\langle \varphi_{(\alpha,k)}^\dagger(\mathbf{r}, \boldsymbol{\Omega}, E), [-\mathcal{M} + \mathcal{F}]\varphi_{(\alpha,k)}(\mathbf{r}, \boldsymbol{\Omega}, E) \right\rangle, \quad (2.102)$$

$$\beta_{\text{eff}(\alpha,k)}^j = \frac{1}{F_{(\alpha,k)}} \left\langle \varphi_{(\alpha,k)}^\dagger(\mathbf{r}, \boldsymbol{\Omega}, E), \chi_d^j \mathcal{F}_d^j \varphi_{(\alpha,k)}(\mathbf{r}, \boldsymbol{\Omega}, E) \right\rangle, \quad (2.103)$$

$$\Lambda_{\text{eff}(\alpha,k)} = \frac{1}{F_{(\alpha,k)}} \left\langle \varphi_{(\alpha,k)}^\dagger(\mathbf{r}, \boldsymbol{\Omega}, E), \frac{1}{v} \varphi_{(\alpha,k)}(\mathbf{r}, \boldsymbol{\Omega}, E) \right\rangle, \quad (2.104)$$

where the function  $F_{(\alpha,k)}$  again gives a physical meaning to these quantities and is defined as

$$F_{(\alpha,k)} = \left\langle \varphi_{(\alpha,k)}^\dagger(\mathbf{r}, \boldsymbol{\Omega}, E), \mathcal{F}\varphi_{(\alpha,k)}(\mathbf{r}, \boldsymbol{\Omega}, E) \right\rangle. \quad (2.105)$$

In particular, by taking into account the  $k$ -eigenvalue problem, the *static reactivity*  $\rho_k$  represents the relative change in the effective multiplication factor  $k_0$ . This can be proved by recalling Eq. (2.65) and substituting the net disappearance operator  $\mathcal{M}$  applied to the direct eigenfunction  $\varphi_{k_0}$ , leading to

$$\rho_k = \frac{k_0 - 1}{k_0}. \quad (2.106)$$

In a similar fashion, the *dynamic reactivity*  $\rho_\alpha$  [55] is obtained by considering the non-linear form of the  $\alpha$ -eigenvalue problem

$$\frac{\alpha}{v(E)}\varphi_\alpha(\mathbf{r}, \boldsymbol{\Omega}, E) = \left[ \mathcal{F}_p + \sum_j \frac{\lambda_j}{\lambda_j + \alpha} \chi_d^j \mathcal{F}_d^j - \mathcal{M} \right] \varphi_\alpha(\mathbf{r}, \boldsymbol{\Omega}, E). \quad (2.107)$$

A new term is added to both sides of equation in order to recall the total fission operator  $\mathcal{F}$  from Eq. (2.63), which yields

$$\left[ \frac{\alpha}{v(E)} + \sum_j \frac{\alpha}{\lambda_j + \alpha} \chi_d^j \mathcal{F}_d^j \right] \varphi_\alpha(\mathbf{r}, \boldsymbol{\Omega}, E) = \left[ \mathcal{F} - \mathcal{M} \right] \varphi_\alpha(\mathbf{r}, \boldsymbol{\Omega}, E), \quad (2.108)$$

which can be integrated over the phase-space in order to retrieve the so called *inhour equation* as [148, 110]

$$\rho_\alpha = \alpha \Lambda_{\text{eff}, \alpha} + \sum \frac{\alpha \beta_{\text{eff}, \alpha}^j}{\alpha + \lambda_j}. \quad (2.109)$$

These definitions of reactivity depend on the approach used for the approximation of the shape function.

The kinetic parameters provide qualitative information on the time evolution of the neutron flux. In the case where the shape function does not change significantly over time, the kinetics parameters are considered as constant and solutions of the system (2.93) can be determined [4]. However, this could not always be the case. Moreover, the kinetics parameters are integrated over the phase-space region. If the shape function is integrated over some very heterogeneous domain, the system could be not considered as a "point", hence the assumption of variable separation between space, energy, direction and time is no longer valid. If on the contrary the system is close to the critical condition and in the absence of very localized perturbations), the shape function can be replaced by the asymptotic distributions.

## Chapter 3

# Monte Carlo methods for reactor physics

The resolution of the Boltzmann transport equation for neutral particles requires the implementation of specific numerical methods. In this regard, two approaches can be adopted: *deterministic methods* and *stochastic methods* [95]. The first category introduces a discretization of the phase-space in order to obtain a matrix formulation of the problem, which implies an error related to the approximations of continuous variables and functions [4, 34]. Furthermore, additional hypotheses are required for each specific configuration under analysis. Under these conditions, the main advantage related to these methods is the "smaller" computational time for the simulations with respect to other approaches.

The *Monte Carlo method* is based on a stochastic approach, involving sampling techniques for the simulation of the physical processes governing particle transport [96]. Unlike deterministic methods, Monte Carlo methods for particle transport do not discretize the Boltzmann equations introduced in the previous sections, but sample the underlying physical phenomena described in nuclear data. The ensemble average of the sampled quantities tends to the solution of the Boltzmann equation. In Monte Carlo methods, almost no approximations are introduced: the physical laws defining particles transport and the cross sections for different materials are retrieved from the nuclear data libraries [134, 102] and are directly used for the sampling process during the simulation. The probabilistic nature of this approach implies a statistical error carried by the estimation. In order to reduce these uncertainties, a larger number of particle histories must be sampled, typically implying long simulation times. Despite the computational cost, Monte Carlo method stands as the "golden standard" for the simulation of neutron transport [4].

### 3.1 Monte Carlo estimation: average and variance

The main algorithm related to Monte Carlo simulation for particle transport concerns the sampling process. A large set of random samples is collected in order to compute scores of physical observables. To ensure the convergence of these results to the quantities of interest, a sufficiently large number of samples is required. The final goal of a Monte Carlo simulation is the estimation of average quantities and the associated error [143]. The *mean value*  $m$  and the *variance*  $\sigma^2$  associated to the generic random variable  $X$  are defined as

$$m = \mathbb{E}[X] = \int_a^b dx x f_X(x) = \int_a^b dF_X(x) x, \quad (3.1)$$

$$\sigma^2 = \mathbb{E}[(X - m)^2] = \int_a^b dx (x - m)^2 f_X(x) = \int_a^b dF_X(x) (x - m)^2, \quad (3.2)$$

where  $f_X(x)$  and  $F_X(x)$  are the corresponding probability density function and cumulative distribution associated to the random variable  $X$ , respectively [96]. In general, the mean value is obtained as the *sample average* of a set of  $N$  random variables:

$$m = \frac{1}{N} \sum_{i=1}^N x_i, \quad (3.3)$$

and the variance is consequently obtained as

$$\sigma^2 = \frac{1}{(N-1)} \sum_{i=1}^N (m - x_i)^2. \quad (3.4)$$

The variance of the distribution  $\sigma^2$  measures the dispersion of the realizations, whereas the variance of the mean value  $\bar{\sigma}^2$

$$\bar{\sigma}^2 = \frac{1}{N(N-1)} \sum_{i=1}^N (m - x_i)^2. \quad (3.5)$$

provides an estimation of the error associated to  $m$  with respect to its exact value, based on the Central Limit Theorem [143]. The two variances can be related since  $\bar{\sigma}^2 = \sigma^2/N$ .

The performance of a simulation is quantified by the so-called *figure of merit* (FOM)

$$\text{FOM} = \frac{1}{\bar{\sigma}^2 \tau_c}, \quad (3.6)$$

where  $\tau_c$  is the required computation time, proportional to the total number of sampled variables  $N$  [143]. This quantity is a commonly used metric for evaluating the efficiency of a Monte Carlo calculation: the FOM increases for decreasing computer time and decreasing statistical uncertainty [96].

The main drawback of Monte Carlo methods is related to the fact that the uncertainty of the average results decreases with the square root of the number  $N$  of sampled histories [96]. The convergence rate for deterministic methods is typically proportional to the inverse of  $N^{2/d}$ , where  $d$  is the dimensionality of the problem [118]. By inspection of these rates for the two approaches, if  $d > 4$  Monte Carlo methods allow a faster convergence to the exact solution. *Variance reduction methods* can be applied during a non-analog Monte Carlo simulation in order to reduce the uncertainties related to the score of interest (see Section 3.3).

## 3.2 Neutron random walks

In the previous section we have briefly recalled the basics of probability distributions and sampling techniques applied for a generic Monte Carlo problem. In this section, we detail the implementation of such techniques for neutron transport, which is formulated in terms of *random walk processes*. Particle histories start according to source distributions and propagate through the media following the transport kernels. The steps presented in the following paragraphs define the rules of an *analog* Monte Carlo game, in the sense that the simulated neutrons obey the physical laws encoded in the transport equation [143].

### 3.2.1 Sampling source neutrons

Each neutron random walk starts from a generic source distribution defined as a function  $Q(P)$ . An initial time  $t_0$  is set and the position of particles in the phase-space is sampled from the normalized probability density function

$$\frac{Q(P_0)}{\int_{\mathcal{P}} dP_0 Q(P_0)}, \quad (3.7)$$

where  $P_0$  represents the original coordinates and  $\mathcal{P}$  is a phase-space region. Whenever the walker crosses the scoring region, a normalization factor equal to  $\int_{\mathcal{P}} dP_0 Q(P_0)$  is applied to the final score of the random walk.

### 3.2.2 Sampling the particle flights

The transition kernel  $T(P' \rightarrow P)$  from Eq. (2.46) is applied in order to sample particle flights. In general, neutrons move through heterogeneous media composed of different materials, characterized by distinct total macroscopic cross sections  $\Sigma_t(\mathbf{r}, E)$ . We make the hypothesis that the system is thus composed of a collection of material regions of arbitrary shapes, each being homogeneous in its interior. Moreover, different boundary conditions can be applied to the geometrical domain.

Given the initial flight position  $\mathbf{r}$ , direction  $\mathbf{\Omega}$  and energy  $E$ , the distance  $l_{max}$  to the next intersection with the boundaries of the traversed material region is computed. It is possible that particles collide before reaching this frontier according to the following probability density function

$$P(l|\mathbf{r}, \mathbf{\Omega}, E) = \Sigma_t(\mathbf{r} + l\mathbf{\Omega}, E) e^{-\int_0^l dt' \Sigma_t(\mathbf{r} + t'\mathbf{\Omega}, E)}, \quad (3.8)$$

which can be integrated by applying the inverse transform in order to obtain the sampled distance  $l$  as

$$l = -\frac{1}{\Sigma_t(\mathbf{r}, E)} \ln(1 - u_i), \quad (3.9)$$

where  $u_i$  is a uniform sampled number in the interval  $[0, 1]$ .

If  $l < l_{max}$ , the neutron is moved to the collision site at position  $\mathbf{r} + l\mathbf{\Omega}$ . Otherwise, the particle is transported to the frontier at position  $\mathbf{r} + l_{max}\mathbf{\Omega}$ . In the case where a different material region has been reached, a new distance  $l$  is sampled by using the new total macroscopic cross section [96], which is in order to be compared with an updated value for  $l_{max}$ . If instead the particle has arrived at the boundary of the system, boundary conditions are applied and, if it has not leaked, new distances  $l$  and  $l_{max}$  are computed.

### 3.2.3 Interactions

At the end of the flight, particles may undergo collision events, which are ruled by the collision kernel  $C(P \rightarrow P')$  from Eq. (2.9). In particular, the interacting nuclide  $A$ , and the nuclear reaction  $j$ , are chosen with probabilities  $p_A(\mathbf{r}, E')$  and  $p_{A,j}(\mathbf{r}, E')$  from Eqs. (2.10) and (2.11) respectively. Then, the number of emitted particles from the collision and the corresponding energy and direction coordinates are sampled by considering the multiplicity factor  $\nu_{A,j}(E')$  and the distribution  $f_{A,j}(\mathbf{\Omega}' \rightarrow \mathbf{\Omega}, E' \rightarrow E)$ , respectively.

### 3.2.4 Sampling from fission

As introduced in Section 2.2.2, neutrons are absorbed during fission events and the unstable nucleus splits into fission fragments and a random number of fission neutrons with average  $\bar{\nu}_f(E)$ . During analog simulations, neutrons undergo fission events at collision site with probability

$$p_{fission} = \frac{\Sigma_f(\mathbf{r}, E)}{\Sigma_t(\mathbf{r}, E)}. \quad (3.10)$$

The directions of the emitted neutrons are isotropically sampled according to a uniform distribution over the solid angle  $4\pi$ . Moreover, the energy related to these particles are sampled from the Maxwellian or the Watt distributions introduced in Eqs. (2.19) and (2.20) respectively. These distributions are representative for the emission spectrum of the prompt neutrons  $\chi_p(E)$ . The same functions can be implemented for the energy sampling of the specific  $j$  delayed family according to the spectrum  $\chi_d^j(E)$  by using different constant values for  $kT$  and  $c_w$  [72].

## 3.3 Non-analog neutron random walk

Despite Monte Carlo being suitable for parallel computing, since each history can in principle be processed by an independent computing unit, strategies aimed at reducing the computational time for a given target statistical uncertainty have been under development since the inception of this simulation method, and go generally under the name of *non-analog* Monte Carlo methods [96, 143]. The main idea is to sample particles from modified distributions in order to increase the number of events that contribute to the score of interest. To preserve the unbiasedness of the score estimation, particles carry a *statistical weight* that can be different from unity.

In particular, particles sampled from a modified generic distribution or kernel  $\tilde{f}(P' \rightarrow P)$  carry a correction weight  $\tilde{w}(P' \rightarrow P)$  equal to

$$\tilde{w}(P' \rightarrow P) = \frac{f(P' \rightarrow P)}{\tilde{f}(P' \rightarrow P)}, \quad (3.11)$$

where  $\tilde{f}(P' \rightarrow P)$  is the original distribution for sampling neutrons from  $P'$  to  $P$  in the phase-space. Such modifi-

cations can be applied to the source function  $Q(P)$ , the flight kernel  $T(P' \rightarrow P)$  or the collision kernel  $C(P' \rightarrow P)$ . In the following paragraphs, further details will be given concerning the weight correction for specific variance reduction methods.

### 3.3.1 Implicit capture

In the case where particles are captured due to physical reactions, their histories are terminated, possibly before they could contribute to a detector. The *implicit capture* routine allows neutrons to survive captures in order to increase the probability for the particle to reach the detector region. In order to compensate for the absence of this capture event, the statistical weight of the particle is reduced by the survival probability after the collision:

$$w' = w \frac{\Sigma_s(\mathbf{r}, E)}{\Sigma_t(\mathbf{r}, E)}, \quad (3.12)$$

where  $w$  and  $w'$  are the statistical weights of the particle before and after the collision, respectively.

### 3.3.2 Forced fission

For multiplying systems, fission events can be enhanced by implementation of *forced fission*: if a collision with a fissile nuclide occurs, fission is systematically sampled. In order to ensure an unbiased simulation, it is necessary to either modify the number of particles emitted from fission or adjust their statistical weights. In the first case, the number of emitted particles  $n_{fission}$  is computed as

$$n_{fission} = \left\lceil \xi + \bar{\nu}_f(E) \frac{\Sigma_f(\mathbf{r}, E)}{\Sigma_t(\mathbf{r}, E)} \right\rceil, \quad (3.13)$$

where  $\xi$  is a uniform random number in the interval  $[0, 1]$ ,  $\bar{\nu}_f(E)$  is the mean number of fission neutrons,  $\frac{\Sigma_f(\mathbf{r}, E)}{\Sigma_t(\mathbf{r}, E)}$  is the probability to undergo a fission reaction.

### 3.3.3 Population control techniques

The implementation of the implicit capture implies that particles cannot terminate their histories at collision sites: if an infinite system is analyzed, the simulation would never end. Population control techniques are therefore introduced in order to avoid extreme values for the statistical weights of the particles and ensure that the histories are terminated when needed [96, 143]. The coexistence of particles with very small and very large statistical weights leads to a variance increase due to statistical dispersion and/or fluctuations. *Population control techniques* are applied in order to balance the number of particles reaching the detector region. Specific techniques can be further applied in order to resize a collection of particles in the simulation. Overall, these routines must preserve the average statistical weight after their application and the unbiasedness of the simulation. In the following we will provide a brief overview.

#### Russian roulette

This population control technique allows terminating particle histories with small statistical weights [96, 143]. Due to the implicit capture routine, the statistical weight of the particle after the collision is reduced by a factor  $\Sigma_s(\mathbf{r}, E)/\Sigma_t(\mathbf{r}, E)$ . If the weight is below a fixed threshold  $w_r$ , the *Russian roulette* is activated: a random number  $\xi$  is uniformly sampled in the interval  $[0, 1]$ , if the weight of the particle is such that  $w < \xi$ , the particle survives and a new weight  $w' = 1$  is attributed, otherwise it is killed. This population control technique is usually applied after each collision. A typical value for the threshold is  $w_r = 0.8$ .

#### Splitting

Contrary to the previous procedure, the *splitting* is implemented in order to avoid the presence of particles with large statistical weights [96, 143]. The main idea is to split the original particle into  $n_c$  copies with weight  $w' = w/n_c$ . If the weight of the particle increases beyond a general threshold  $w_s > 1$ , the splitting is activated generating an additional number of particles with smaller weights. Again, this technique is applied after a collision event. The threshold value is typically set at  $w_s = 2$ .

### Combing

The following technique is applied in order to change the population of  $K$  particles to  $M$  particles by preserving the total statistical weight [11]. In particular, a set of  $K$  particles can be arranged as shown in Fig. 3.1 with corresponding initial weights  $w_i$ , with total weight:

$$W = \sum_{i=1}^K w_i. \quad (3.14)$$

A random number  $u_i$  is uniformly sampled in the interval  $[0,1]$  and multiplied by  $W/M$ , where  $M$  is the total number of particles after the combing. The obtained quantity is defined as the first tooth of the comb. All the following teeth  $T_m$  will be located with a step equal to  $W/M$ . These considerations can be summarized by the following formula

$$T_m = \xi \frac{W}{M} + (m-1) \frac{W}{M}, \quad m = 1, 2, \dots, M. \quad (3.15)$$

In the end, a new set of  $M$  particles will be copied from the original population, each with a statistical weight equal to  $W/M$ . The uniform random number  $\xi$  determines if  $j$  or  $j+1$  teeth are related to the interval of length  $w_i$ , given

$$j \leq w_i \frac{M}{W} \leq j+1. \quad (3.16)$$

$j$  teeth fall in the  $i$ -th interval with probability

$$p_{i,j} = j+1 - w_i \frac{M}{W}, \quad (3.17)$$

whereas  $j+1$  teeth fall in the  $i$ -th interval with probability

$$p_{i,j+1} = w_i \frac{M}{W} - j. \quad (3.18)$$

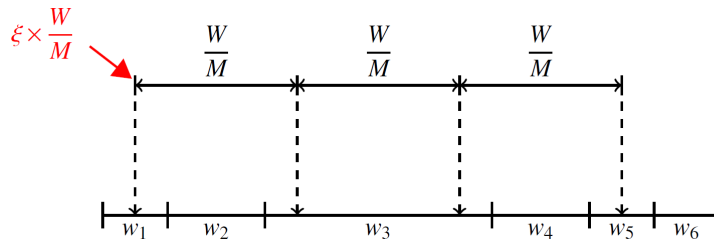


Figure 3.1: Scheme for the weight distribution of 6 particles according to the combing technique [11].

## 3.4 Estimators for neutron histories

Random contributions are computed in order to relate the realization of a physical process to the average value of the quantity of interest. As previously introduced in Eq. (2.42), it is possible to estimate a response  $R$  in a defined detector region in the phase-space as the following integral

$$R = \int_{\mathcal{P}} dP \varphi(P) \eta_{\varphi}(P), \quad (3.19)$$

where  $\varphi(P)$  is the neutron flux and  $\eta_{\varphi}(P)$  is the corresponding response function. In the following, we consider estimators related to the neutron flux, but additional estimators can also be applied by considering the emission density  $\chi(P)$  and the collision density  $\psi(P)$  from Eq. (2.45).

The response  $R$  is computed as the sample average

$$R = \frac{1}{N} \sum_{i=1}^N \omega_i, \quad (3.20)$$

where  $\omega_i$  is the estimator for the  $i$ -th random walks, over a total number of  $N$  random walks. Now, we introduce two estimators as the *collision estimator*  $\omega_{coll}$  and the *track-length estimator*  $\omega_{track}$

$$\omega_{coll} = \sum_m^M \frac{w_m}{\Sigma_t(P_m)}, \quad (3.21)$$

$$\omega_{track} = \sum_m^M w_m l_m, \quad (3.22)$$

over  $M$  total particle tracks, where  $w_m$  is the relative statistical weight and  $l_m$  defined is the corresponding track-length in the detector volume. These quantities are estimated for each neutron random walk. The first estimator is updated at each collision in the detector region, whereas the second estimator scores a realization each time a particle travels through the region of interest.

Similarly, the current  $\mathbf{J}(P) = \varphi(P)\mathbf{\Omega}$  can be estimated with *surface estimators* for each particle crossing of the detector surface  $S = \partial D$

$$\omega_{surf} = \sum_m^M w_m. \quad (3.23)$$

### 3.5 Kinetic Monte Carlo methods

The Monte Carlo methods described so far do not explicitly take into account time-dependent problems. Recently, thanks to the increasing computational capabilities and many efforts on this field [140, 141, 88, 41, 92, 107], it has become possible to perform *kinetic Monte Carlo* simulations of realistic nuclear systems. However, such simulations are extremely expensive from a computational point of view. The major challenges related to time-dependent Monte Carlo methods concern the presence of two different time scales for neutron and precursor particles, and the influence of feedback effects during transients. The simulation of such physical problem is tantamount to solving the time-dependent Boltzmann system coupled to the equations defining the thermal-hydraulics effects.

The times associated to particles during their histories need to be computed, so that a score can be averaged over a proper time grid. The rate by which neutrons are converted into precursors is defined by the ratio  $\beta_{eff}/\Lambda_{eff}$ ; conversely, precursors decay into delayed neutrons following the mean decay constant  $\bar{\lambda}$ . By considering a general system at equilibrium and the ratio of these two rates ( $\beta_{eff}/(\bar{\lambda} \times \Lambda_{eff}) \simeq 10^4$ ), precursors would be much more abundant with respect to neutrons due to their longer lifetime. In order to properly fill each time bin, specific techniques must be then applied for variance reduction and population control.

From the beginning of the simulation, each particle stores its local time and adds each partial contribution during flights as the ratio between the distance travelled before the next collision and the speed at the given energy. Prompt and delayed neutrons can be simulated in the same transport: the former are immediately emitted after a fission and inherit the time of the parent neutron, the latter addition to their local time an additional delay related to the precursor decay. If a critical configuration is considered, the difference in the time scales of these two particles would prohibit an analog Monte Carlo simulation [88].

A possible solution to this problem is to apply additional population control techniques to the population of precursors [88, 59]. These particles will not be transported, but will provide a "buffer" for delayed neutrons that can contribute to Monte Carlo scores. In particular, it is convenient to introduce a single representative (averaged) precursor, carrying the total statistical weight of all possible precursors [41]. Its decay rate is defined according to the following function

$$P(t|t_0) = \sum_j \lambda_j \frac{\beta_j}{\beta} e^{-\lambda_j(t-t_0)}, \quad (3.24)$$

given the fraction  $\beta_j/\beta$  of delayed neutrons belonging to family  $j$ , and the relative generation time  $t_0$ . Then, the weight of the precursor at a generic time  $t$  is estimated as

$$\mathcal{W}(t|t_0) = w_c \sum_j \frac{\beta_j}{\beta} e^{-\lambda_j(t-t_0)}, \quad (3.25)$$

where  $w_c$  is its original weight. In order to improve the sampling of particles during the decay of the precursors, it is possible to force the decay in order to ensure a larger number of neutrons during the fission chain, leading to an overall variance reduction [142]. In particular, it has been proposed to force this decay uniformly in each time bin of a specified temporal mesh from the initial time  $t_0$  up to the final time  $t_f$ . Particle trajectories are Markovian (i.e., they depend only on the particle state at the current time, and not on the past history) and thus can be stopped and restarted at each bound of this grid preserving the ensemble averages for the physical quantities to be computed [141].

The forced decay can be sampled uniformly over the chosen time mesh, following the distribution

$$p_{decay} = \frac{1}{t_{q+1} - t_q} \chi(t_q, t_{q+1}), \quad (3.26)$$

where  $\chi(t_q, t_{q+1})$  is a step function applied over the time interval  $[t_q, t_{q+1}]$ . The unbiased Monte Carlo simulation is preserved by considering

$$\mathcal{W}_{decay}(t|t_0) = (t_{q+1} - t_q) \sum_j \lambda_j \frac{\beta_j}{\beta} e^{-\lambda_j(t-t_0)} w_c, \quad (3.27)$$

as the statistical weight for the emitted delayed neutron [41, 142]. Energy and direction for the emitted delayed neutron are sampled from the specific spectrum of family  $j$ , which can be chosen with probability  $p(j, t|t_0)$  [141], namely:

$$p(j, t|t_0) = \frac{\lambda_j \frac{\beta_j}{\beta} e^{-\lambda_j(t-t_0)}}{\sum_k \lambda_k \frac{\beta_k}{\beta} e^{-\lambda_k(t-t_0)}}. \quad (3.28)$$

The delayed neutron follows its history during the simulation, whereas, the precursor will be again forced to decay in the next time bin.

Regardless of the refinement chosen for the temporal mesh, the Monte Carlo score performed over a time bin is a fair estimate of the integral of a generic observable averaged over the phase-space in that time interval. Even though the average scores are preserved for any arbitrary mesh, the variances associated to them are intimately related to the size of the bin. Moreover, population control techniques must be applied at the end of each time bin, in order to avoid a large CPU overhead caused by the application of such routines at each population size variation.

### 3.6 Monte Carlo methods for eigenvalue problems

Beside kinetic simulations, the assessment of the evolution of the neutron population can be usefully complemented by the spectral analysis of the Boltzmann operator [34]. For this purpose, in the following, direct and adjoint formulations of  $k$ - and  $\alpha$ -eigenvalue problems will be briefly recalled and related to specific Monte Carlo methods. A thorough description of these procedures will be further provided in Chapter 4.

#### The direct $k$ -eigenvalue problem calculation

For direct  $k$ -eigenvalue calculations, the fundamental mode  $\varphi_{k_0}$  satisfying Eq. (2.65) is computed by using the standard *power iteration* method [20]. The idea is to iteratively solve Eq. (2.67)

$$\mathcal{K}S_{f,k} = kS_{f,k}, \quad (3.29)$$

by following the distribution  $S_{f,k}$  at each generation  $g$ . Neutrons are transported from the initial guess source distribution  $S_{f,k}^{(0)}$  until their deaths by leakage or absorption. Each fission event is considered as a promotion of the particle to the next generation that will be sampled according to  $S_{f,k}^{(1)} = \mathcal{F}\varphi_k^{(0)}$ . At the beginning of each cycle, a

proper normalization factor  $k^{(g)}$  is applied in order to bound the particle population, computed as the ratio of two successive fission emission density

$$k^{(g)} = \frac{S_{f,k}^{(g+1)}}{S_{f,k}^{(g)}}. \quad (3.30)$$

This factor provides an estimation for the fundamental eigenvalue  $k_0$  at each iteration. For these reasons, this procedure is also known as the *successive generations* method [96].

### The adjoint $k$ -eigenvalue problem calculation

Concerning the adjoint  $k$ -eigenmodes  $\varphi_k^\dagger$ , which satisfy Eq. (2.69)

$$\mathcal{M}^\dagger \varphi_k^\dagger = \frac{1}{k} \mathcal{F}^\dagger \varphi_k^\dagger, \quad (3.31)$$

the Iterated Fission Probability (IFP) method has been recently proposed in [111, 75, 149]. The introduction of the IFP method has paved the way to obtaining the fundamental adjoint flux  $\varphi_{k_0}^\dagger$  for  $k$ -eigenvalue problems in continuous-energy Monte Carlo simulations: the adjoint flux  $\varphi_{k_0}^\dagger$  is equated to the neutron importance  $I_k$ , which can be then estimated by running a direct calculation. The neutron importance  $I_k$  is obtained by recording the descendants after  $M$  latent generations for an ancestor injected into the system at coordinates  $\mathbf{r}, \mathbf{\Omega}, E$  (neutrons are promoted to the next generation by fission events).

### The direct $\alpha$ -eigenvalue problem calculation

For  $\alpha$ -eigenvalue problems, in the form of Eq. (2.79)

$$\mathcal{V}[\mathcal{F}_\alpha - \mathcal{M}]\varphi_\alpha = \alpha\varphi_\alpha. \quad (3.32)$$

the fundamental mode  $\varphi_{\alpha_0}$  can be determined by using the  $\alpha$ - $k$  power iteration [170]. The  $\alpha$ - $k$  method was originally proposed for prompt eigenvalues [18] and later extended to the general case with neutrons and precursors [108]. The basic idea is to iteratively search for the dominant  $\alpha$  value that makes the  $\alpha$ -eigenvalue equation exactly critical with respect to a fictitious  $k$ -eigenvalue applied to the production terms. For positive  $\alpha$ , a ‘‘capture’’ cross section  $\alpha/\nu$  is taken into account while applying a modified power iteration [28]. For negative  $\alpha$ , the contribution  $-\alpha/\nu$  was originally interpreted as a ‘‘production’’ term. Improved algorithms have been proposed in order to overcome the numerical instabilities of the original method and to take into account the presence of delayed neutrons in the system [99].

### The adjoint $\alpha$ -eigenvalue problem calculation

By building upon these ideas, a novel method has been introduced in order to compute the fundamental adjoint flux  $\varphi_{\alpha_0}^\dagger$  for  $\alpha$ -eigenvalue problems, which solves Eq. (2.81)

$$\mathcal{V}[\mathcal{F}_\alpha^\dagger - \mathcal{M}^\dagger]\varphi_\alpha^\dagger = \alpha\varphi_\alpha^\dagger, \quad (3.33)$$

by resorting to a generalized version of IFP (Generalized-IFP) [147]. The fundamental adjoint flux  $\varphi_{\alpha_0}^\dagger$  can be again equated to the neutron importance  $I_\alpha$ , i.e., can be estimated by recording the descendants after  $M$  latent generations for an ancestor injected into the system at coordinates  $\mathbf{r}, \mathbf{\Omega}, E$ . The only difference with respect to the regular IFP method is that for  $\alpha$ -eigenvalue problems additional events, other than fissions, contribute to promoting the neutrons to the next generation. For positive  $\alpha$ , the additional term  $\alpha/\nu$  acts as a sterile capture: neutrons can thus contribute to the importance only being promoted to the next generation by prompt and delayed fission. For negative  $\alpha$ , neutrons can contribute to importance also via the  $\alpha$ -production term, associated to the copy operator with cross section  $-\alpha/\nu$ . In both cases, the weight of the delayed neutrons is assigned a correction factor  $\lambda_j/(\lambda_j + \alpha)$ .

To sum up, the methodologies introduced in this section allow the computation of both direct and adjoint fundamental eigenpairs, according to the  $k$ - and the  $\alpha$ -eigenvalue formulations. A detailed investigation on the comparison of these eigenpairs will be provided in Chapter 4. Regarding higher-order modes, the  $k$ -eigenvalue

problem has been extensively analyzed in literature [105, 71, 53, 152, 76, 35, 156, 22]. In particular, matrix-filling Monte Carlo methods can be applied in order to obtain a discrete version of the operator  $\mathcal{K}$  from Eq. (2.66) and will be described in Chapter 5. Standard algebraic methods are then applied for the computation of the spectrum and the associated eigenfunctions. Similarly, a recent method [6, 7, 8] has suggested a similar procedure for the estimation of the  $\alpha$ -eigenvalue problem. In view of their importance in the context of reactor physics, a major part of this thesis will be devoted to the implementation and investigation of matrix-filling Monte Carlo methods for spectral analysis. In particular, we will investigate the performance and the accuracy of these methods as applied to benchmark and realistic core configurations.

### 3.7 Numerical simulation tools developed and used in this work

The Monte Carlo simulations performed for this work have been carried out by using two distinct codes.

On one hand, we have *developed a stand-alone test-bed Monte Carlo code* with simplified physics, in order to probe, verify and analyse the proposed algorithms. This code will be extensively used in Chapters 5 (development and applications of the new alpha matrix method) and 6 (spectral analysis of benchmark configurations).

On the other hand, we have resorted to the production code TRIPOLI-4<sup>®</sup>, developed at CEA[20], in order to explore more realistic configurations with continuous-energy transport and state-of-the art nuclear data. At the time of the thesis, the code was already endowed with the possibility of computing  $k$ -weighted and  $\alpha$ -weighted quantities, both in forward and adjoint simulations. These functionalities have been used, with minor modifications and improvements, in Chapter 4 for the analysis of fundamental modes. For the purpose of the spectral analysis of the EOLE critical facility, carried out in Chapter 7, we have *implemented and verified the  $\alpha$ -matrix method in the development version of the code*.

In the following, we provide a succinct description of both codes.

#### 3.7.1 Test-bed Monte Carlo code

In order to test the methodologies analyzed in this work, *a test-bed Monte Carlo code has been developed from scratch*.

This code allows particle navigation in heterogeneous geometries with multigroup cross sections in dimension 1, 2 and 3. The geometries are described as a Cartesian mesh, where each cell can be associated to a different material. In order to simulate multiple materials in the same mesh, a delta-tracking method has been implemented on a mesh basis [160]. Leakage and reflective boundary conditions can be applied at the frontiers of the system. The code allows the transport of both prompt and delayed neutrons.

Criticality calculations can be performed with  $k$ - or  $\alpha$ -eigenvalue formulations. All of these calculations rely on the algorithms introduced in Section 2.6. It is worth noting that an additional method is also implemented to solve the  $\alpha$ -formulation: the  $\alpha$ -tally method [69]. Further details will be provided in Section 4.4.1. Adjoint criticality calculations can be performed for both  $k$ - and  $\alpha$ - eigenvalue problems via the implemented IFP and G-IFP methods, respectively, described in Section 4.3 and 4.5.

During particle transport, matrix-filling methods are applied in order to score the discretized version of the linear transport operators. The idea is to obtain the matrix operators associated to the analyzed eigenvalue problem, as explained in Chapter 5. Standard linear algebra methods are then applied in order to compute the associated eigenpairs with MATLAB<sup>®</sup> [101] by the implementation of the QZ algorithm [103]. The fission matrix method is applied for the estimation of the  $k$ -eigenpairs during direct particle transport. An improved version of matrix-filling method for  $\alpha$ -eigenpairs calculation is also implemented. This version allows the estimation of direct and adjoint transport operators during the Monte Carlo simulation of an eigenvalue problem, as described in Chapter 5. Moreover, it allows the estimation of both direct and adjoint  $\alpha$ -eigenmodes from both direct ( $\alpha$ - $k$  power iteration,  $\alpha$ -tally method) and adjoint (G-IFP method) calculations. The code has been applied to the investigation of the benchmark configurations presented in Chapter 4 and of the novel  $\alpha$  matrix-filling method discussed in Chapter 5.

### 3.7.2 TRIPOLI-4<sup>®</sup> Monte Carlo code

TRIPOLI-4<sup>®</sup> is the fourth generation of a transport Monte Carlo code developed by the Service d'Études des Réacteurs et de Mathématiques Appliquées (SERMA) at CEA/Saclay [20]. TRIPOLI-4<sup>®</sup> simulates 3D continuous-energy problems and is devoted to shielding, reactor physics with depletion, criticality safety and nuclear instrumentation for both fission and fusion systems. The code has been under development at CEA since the mid-60s, at the Fontenay-aux-Roses center first, then at the Saclay center. Version 4 has been developed starting from the mid 90s in C++ [16, 15].

For the purpose of this work, TRIPOLI-4<sup>®</sup> has been used for the simulations of 3D continuous-energy problems by considering the transport of both prompt and delayed neutrons: the Godiva-like sphere geometry (Section 4.6), the CROCUS reactor (Section 4.7) and the EOLE research reactor (Section 7.4).

TRIPOLI-4<sup>®</sup> allows computing the direct and the adjoint fundamental eigenmode according to the  $k$ - and the  $\alpha$ -eigenvalue formulation [150, 147, 169, 170], following the procedure introduced in Section 3.6 and detailed in the Chapter 4. Moreover, a recently developed critical boron research allows iteratively adjusting the configurations at a critical state, when needed. Such calculations allow the estimation of the fundamental eigenvalues  $k_0$  and  $\alpha_0$ , as well as the effective kinetic parameters introduced in Section 2.7.

In order to access to the higher-order modes of the eigenvalue problems, matrix filling methods are used for the estimation of the discretized linear operators. In particular, TRIPOLI-4<sup>®</sup> is capable of filling the elements of the fission matrix during a  $k$  power iteration in order to compute the eigenpairs  $(S_f, k)$  related to the direct  $k$ -eigenvalue problem. For the purpose of applying the  $\alpha$  matrix-filling method to continuous-energy transport problems, *we have implemented new routines* in order to score the matrix elements for the evaluation of the discretized linear operators during a  $\alpha$ - $k$  power iteration, as shown in Chapter 7. This paves the way for the estimation of the direct eigenpairs  $(\Psi_{\alpha}, \alpha)$  of arbitrary order for realistic configurations, as illustrated in Chapter 7 for the EOLE reactor.

## Chapter 4

# Analysis of forward and adjoint fundamental $k$ and $\alpha$ -eigenfunctions

### 4.1 Introduction

Assessing the asymptotic behaviour of a nuclear system is intimately related to computing the dominant (direct, i.e., forward) eigenmode and the associated dominant eigenvalue of the configuration under analysis, which is central in several applications in reactor physics, including pulsed neutron reactivity measurements [121] and reactor period analysis [108, 167, 171]. Furthermore, for several key reactor coefficients, such as kinetics parameters, sensitivities to nuclear and material data, or perturbations, bilinear forms involving both the direct and the adjoint fundamental eigenfunctions are required [111, 75, 150, 148, 39, 66].

The most common bases for eigenfunction expansions are those related to the  $k$ -eigenvalues and to the  $\alpha$ -eigenvalues, respectively [34]. Calculations of dominant  $k$ - or  $\alpha$ - eigenvalues/eigenfunctions try to assess the asymptotic reactor behaviour, each with a distinct point of view: the former basically determines the shape of the neutron population after a large number of fission generations, whereas the latter after a sufficiently long time. When the reactor is exactly critical, i.e., for  $k_0 = 1$  or equivalently  $\alpha_0 = 0$ , the fundamental modes of both eigenfunction bases coincide, as expected on physical grounds. However, for systems far from criticality the fundamental  $k$ - and  $\alpha$ -eigenmodes show discrepancies and (with the possible exception of very simple cases involving single-speed transport) are not related to each other in any trivial manner [28]. Such discrepancies have been observed even for very small deviations from criticality [147]. Since both direct and adjoint eigenmodes are involved in the calculation of key reactor parameters, the investigation of the behaviour of the eigenfunctions might shed some light on the behaviour of such parameters at and close to the critical point.

In the context of Monte Carlo simulation, the analysis of the prompt direct fundamental  $k$ - and  $\alpha$ -eigenmodes (neglecting delayed neutron contributions) has been previously carried out by D. E. Cullen in a seminal work concerning a set of sub- and super-critical systems based on homogeneous and heterogeneous Godiva-like cores with rapid and thermal spectra [28], recently reconsidered by [153]. In this chapter, we will revisit and extend these findings on some benchmark configurations, with a twofold aim. First, we will explicitly include the effects of *delayed neutrons*, which had been originally neglected. We will thus determine whether the presence of delayed contributions has an impact on the shape of the eigenfunctions, and in particular whether the discrepancies between  $k$ - and  $\alpha$ -eigenmodes increase or decrease. Then, we will examine the behaviour of the *fundamental adjoint eigenmodes* for both  $k$ - and  $\alpha$ -eigenvalue problems, whose comparison has not been addressed so far, to the best of our knowledge. For the numerical simulations presented in the following, we have used the development version of TRIPOLI-4<sup>®</sup> [20].

## 4.2 Monte Carlo power iteration for $k$ -eigenvalue problems

The fundamental distribution  $\varphi_{k_0}$  and the corresponding eigenvalue  $k_0$ , solutions of the  $k$ -eigenvalue problem in Eq. (2.65), can be estimated by the *power iteration* technique [95]. This procedure, originally implemented for deterministic methods, has been adapted to Monte Carlo simulation.

The  $k$ -eigenvalue problem can be expressed in integral form recalling the collision density  $\psi(P)$ , obtained by replacing the emission density  $\chi(P)$  from Eq. (2.45) in Eq. (2.44)

$$\psi(P) = \mathbb{K}\psi(P) + \mathbb{T}Q(P), \quad (4.1)$$

where the *transport operator*  $\mathbb{K}$  is defined as a combination of the flight operator  $\mathbb{T}$  from Eq. (2.4) and the collision operator  $\mathbb{C}$  from Eq. (2.4), namely,

$$\mathbb{K}g(P) = \int_{\mathcal{P}'} dP' \int_{\mathcal{P}''} dP'' C(P' \rightarrow P'') T(P'' \rightarrow P) g(P') = \int_{\mathcal{P}'} dP' K(P' \rightarrow P) g(P').$$

The transport kernel  $K(P' \rightarrow P)$  can be split into a scattering contribution  $K_s(P' \rightarrow P)$  and a fission contribution  $K_f(P' \rightarrow P)$ , defined as

$$K_s(P' \rightarrow P) = \bar{v}_s(E') \frac{\Sigma_s(\mathbf{r}, E')}{\Sigma_t(\mathbf{r}, E')} f_s(\mathbf{\Omega}' \rightarrow \mathbf{\Omega}'', E' \rightarrow E'') \cdot \delta(\mathbf{r} - \mathbf{r}'') T(P'' \rightarrow P), \quad (4.2)$$

$$K_f(P' \rightarrow P) = \bar{v}_f(E') \frac{\Sigma_f(\mathbf{r}, E')}{\Sigma_t(\mathbf{r}, E')} \cdot \frac{\chi_f(E'')}{4\pi} \cdot \delta(\mathbf{r} - \mathbf{r}'') T(P'' \rightarrow P). \quad (4.3)$$

By using the results derived in Section 2.6.1, the collision density is expressed as

$$\psi_k(\mathbf{r}, \mathbf{\Omega}, E) = \mathbb{K}_s \psi_k(\mathbf{r}, \mathbf{\Omega}, E) + \frac{1}{k} \mathbb{K}_f \psi_k(\mathbf{r}, \mathbf{\Omega}, E). \quad (4.4)$$

A new function  $\zeta(\mathbf{r} \rightarrow \mathbf{r}', \mathbf{\Omega}', E')$  is now introduced [96] as

$$\zeta(\mathbf{r} \rightarrow \mathbf{r}', \mathbf{\Omega}', E') = \int_{\mathcal{P}} dP'' \zeta(\mathbf{r} \rightarrow \mathbf{r}'', \mathbf{\Omega}'', E'') K_s(P'' \rightarrow P') + \frac{\chi_f(E')}{4\pi} T(\mathbf{r} \rightarrow \mathbf{r}', \mathbf{\Omega}', E'), \quad (4.5)$$

which expresses the collision density at coordinates  $\mathbf{r}', \mathbf{\Omega}', E'$  given a fission neutron generated at position  $\mathbf{r}$ .

Moreover, the *fission density*  $S_f(\mathbf{r})$  is defined as

$$S_f(\mathbf{r}) = \frac{1}{k} \int_{4\pi} d\mathbf{\Omega} \int_0^\infty dE \bar{v}_f(E) \frac{\Sigma_f(\mathbf{r}, E)}{\Sigma_t(\mathbf{r}, E)} \psi_k(\mathbf{r}, \mathbf{\Omega}, E), \quad (4.6)$$

representing the density of neutrons emerged from fission at position  $\mathbf{r}$ . If Eq. (4.5) is multiplied by the fission density  $S_f(\mathbf{r})$  and integrated over the spatial coordinates, Eq. (4.1) is retrieved, provided that

$$\psi_k(\mathbf{r}, \mathbf{\Omega}, E) = \int_V d\mathbf{r}' \zeta(\mathbf{r}' \rightarrow \mathbf{r}, \mathbf{\Omega}, E) S_f(\mathbf{r}'). \quad (4.7)$$

The kernel  $Z(\mathbf{r}' \rightarrow \mathbf{r})$  is then introduced as

$$Z(\mathbf{r}' \rightarrow \mathbf{r}) = \int_{4\pi} d\mathbf{\Omega} \int_0^\infty dE \bar{v}_f(E) \frac{\Sigma_f(\mathbf{r}, E)}{\Sigma_t(\mathbf{r}, E)} \zeta(\mathbf{r}' \rightarrow \mathbf{r}, \mathbf{\Omega}, E), \quad (4.8)$$

representing the density of neutrons emitted from fission at position  $\mathbf{r}$  given an initial fission neutron generated at position  $\mathbf{r}'$  [96]. These last three definitions can be combined in order to obtain the formulation of the  $k$ -eigenvalue problem as a function of  $S_f(\mathbf{r})$ , namely,

$$\int_V d\mathbf{r}' Z(\mathbf{r}' \rightarrow \mathbf{r}) S_f(\mathbf{r}') = k S_f(\mathbf{r}). \quad (4.9)$$

Two main properties can be derived from Eq. (4.9): it is expressed as an eigenvalue problem and it can be solved by iteration. Fission density at iteration  $g + 1$  can be defined as

$$S_f^{(g+1)}(\mathbf{r}) = \int_V d\mathbf{r}' Z(\mathbf{r}' \rightarrow \mathbf{r}) S_f^{(g)}(\mathbf{r}'), \quad (4.10)$$

and, by integrating over the spatial domain, the multiplication factor can be expressed as the ratio between two successive iterations

$$k^{(g)} = \frac{\int_V d\mathbf{r} S_f^{(g+1)}(\mathbf{r})}{\int_V d\mathbf{r} S_f^{(g)}(\mathbf{r})}. \quad (4.11)$$

An initial distribution  $S_f^{(0)}(\mathbf{r})$  is introduced and transported up to the next iteration according to Eq. (4.10). Particle histories are followed during the simulation from fission events to the next ones, which suggests that each iteration (or cycle) can be interpreted as a fission *generation*. For this reason, this procedure is also known as the *method of successive generations* [96].

For a sufficient number of generations, it has been shown that this method will converge to the asymptotic distribution. However, population control techniques are required in order to bound the particle number during the simulation. As an example, if a super-critical system is considered, neutron population could diverge after few generations, whereas particles transported in a sub-critical system could quickly disappear if not properly normalized. For this purpose, the statistical weights of fission neutrons are divided by a factor  $k^{(g)}$  at the end of each generation in order to ensure a balanced number of particles in the system at each iteration.

The method discussed here could require a large number of iterations to achieve convergence. The initial source distribution is introduced as a guess function in the power iteration process and will thus influence the particle distribution during the following generations. The effect of this initial function, generally affected by the higher-order eigenfunctions, can be quantified by the dominance ratio  $DR^{(g)} = k_1^{(g)}/k_0^{(g)}$ . In particular, the closer this value is to unit, the more the initial distribution will influence the successive generations, hence, a larger number of iterations will be required to ensure convergence.

The fission density can be expanded over the eigenfunctions as follows [19]:

$$S_f^{(g+1)}(\mathbf{r}) = S_{f,0}(\mathbf{r}) + c_s (DR)^{(g+1)} S_{f,1}(\mathbf{r}) + \dots, \quad (4.12)$$

where  $c_s$  are normalization constants defined by the modal expansion. The corresponding eigenvalue is equivalently expressed as

$$k^{(g+1)} = k_0 - c_k (DR)^{(g)} (1 - (DR)^{(g)}) + \dots \quad (4.13)$$

This expansion states that the high-order eigemodes and eigenvalues are proportional to  $(DR)^{(g+1)}$  and  $(DR)^{(g)}(1 - (DR)^{(g)})$ , respectively. Additionally, it shows that convergence needs to be achieved with respect to both quantities: eigenvalues and eigenfunctions. For this reason, the dominance ratio plays a fundamental role in determining the convergence rate of this method.

### 4.3 Determining the fundamental adjoint mode: the IFP method

The computation of bilinear-form quantities is required in several applications, such as the estimation of the kinetics parameters, perturbation theory and sensitivity analysis. The aim of these problems is to determine a general quantity  $R$  defined as

$$R = \frac{\langle \varphi_k^\dagger, A\varphi_k \rangle}{\langle \varphi_k^\dagger, B\varphi_k \rangle}, \quad (4.14)$$

where  $A$  and  $B$  are given operators,  $\varphi_k$  and  $\varphi_k^\dagger$  are the solutions of the direct and adjoint  $k$ -eigenvalue problems introduced by Eqs. (2.65) and (2.69) respectively [4].

The  $k$ -power iteration method allows the computation of the fundamental direct distribution  $\varphi_{k_0}$  during forward random walks. On the other hand, the estimation of the fundamental adjoint function  $\varphi_{k_0}^\dagger$  by Monte Carlo methods

requires in principle the simulation of backward transport according to the adjoint operators [96]. In this respect, a first attempt has been performed via the simulation of fixed-source problems by defining backward random walks of a new class of particle: the *adjunctons* [58]. However, serious flaws and obstacles have been found in the simulation of continuous-energy transport problems and the normalization of the adjoint eigenmode. For this reason, methods involving the forward transport of particles for the estimation of the adjoint flux have been recently proposed. In particular, the rediscovery of the *Iterated Fission Probability method* has provided an exact computation tool for this distribution by equating it with the importance function [42, 43, 110, 75].

The importance function  $I(\mathbf{r}, \boldsymbol{\Omega}, E)$  represents the average number of neutrons generated at an asymptotic generation by an *ancestor* neutron introduced in the system at coordinates  $\mathbf{r}, \boldsymbol{\Omega}, E$  [56]. All neutrons belonging to a distant generation are defined as *descendants* (the name progeny can also be found in literature).

By imposing a backward balance equation, it can be shown that the neutron importance at a generic point in the phase-space satisfies [110].

$$I_k(\mathbf{r}, \boldsymbol{\Omega}, E) = p_{nc}I(\mathbf{r} + \boldsymbol{\Omega}ds, \boldsymbol{\Omega}, E) + Q_k(\mathbf{r} + \boldsymbol{\Omega}ds, \boldsymbol{\Omega}, E), \quad (4.15)$$

where  $p_{nc} = 1 - \Sigma_t ds$  is the probability of non-collision during the infinitesimal path  $ds$  and  $Q_k$  is the average number of descendants for neutrons having a collision in  $d\mathbf{s} = \mathbf{r} - \mathbf{r}' = \boldsymbol{\Omega}ds$ .

Given the kernel  $q_k(\mathbf{r} + \boldsymbol{\Omega}ds, \boldsymbol{\Omega} \rightarrow \boldsymbol{\Omega}', E \rightarrow E')$  as the average number of neutrons undergoing a collision during the flight  $ds$  and the with incoming coordinates  $\boldsymbol{\Omega}', E'$  and defined as

$$q_k(\mathbf{r} + \boldsymbol{\Omega}ds, \boldsymbol{\Omega} \rightarrow \boldsymbol{\Omega}', E \rightarrow E') = \Sigma_s(\mathbf{r} + \boldsymbol{\Omega}ds, \boldsymbol{\Omega} \rightarrow \boldsymbol{\Omega}', E \rightarrow E')ds + \frac{1}{k} \bar{v}_p(E) \Sigma_f(\mathbf{r} + \boldsymbol{\Omega}ds, E) \frac{\chi_p(E')}{4\pi} ds + \frac{1}{k} \sum_j \bar{v}_d^j(E) \Sigma_f(\mathbf{r} + \boldsymbol{\Omega}ds, E) \frac{\chi_d^j(E')}{4\pi} ds, \quad (4.16)$$

the term  $Q_k$  can be expressed as

$$Q_k(\mathbf{r}, \boldsymbol{\Omega}, E) = \int_{4\pi} d\boldsymbol{\Omega}' \int_0^\infty dE' q_k(\mathbf{r}, \boldsymbol{\Omega} \rightarrow \boldsymbol{\Omega}', E \rightarrow E') I_k(\mathbf{r}, \boldsymbol{\Omega}', E'). \quad (4.17)$$

Equation (4.15) can be divided by  $ds$  with  $ds \rightarrow 0$ , which yields

$$0 = \frac{dI_k(\mathbf{r}, \boldsymbol{\Omega}, E)}{ds} - \Sigma_t(\mathbf{r}, E) I_k(\mathbf{r}, \boldsymbol{\Omega}, E) + \frac{Q_k(\mathbf{r} + \boldsymbol{\Omega}ds, \boldsymbol{\Omega}, E)}{ds}. \quad (4.18)$$

By developing the total derivative along  $ds$ , Eq. (4.18) can be rewritten as

$$0 = \boldsymbol{\Omega} \cdot \nabla I_k(\mathbf{r}, \boldsymbol{\Omega}, E) - \Sigma_t(\mathbf{r}, E) I_k(\mathbf{r}, \boldsymbol{\Omega}, E) + \int_{4\pi} d\boldsymbol{\Omega}' \int_0^\infty dE' \Sigma_s(\mathbf{r}, \boldsymbol{\Omega} \rightarrow \boldsymbol{\Omega}', E \rightarrow E') I_k(\mathbf{r}, \boldsymbol{\Omega}', E') + \frac{1}{k} \bar{v}_p(E) \Sigma_f(\mathbf{r}, E) \int_{4\pi} d\boldsymbol{\Omega}' \int_0^\infty dE' \frac{\chi_p(E')}{4\pi} I_k(\mathbf{r}, \boldsymbol{\Omega}', E') + \frac{1}{k} \sum_j \bar{v}_d^j(E) \Sigma_f(\mathbf{r}, E) \int_{4\pi} d\boldsymbol{\Omega}' \int_0^\infty dE' \frac{\chi_d^j(E')}{4\pi} I_k(\mathbf{r}, \boldsymbol{\Omega}', E'). \quad (4.19)$$

By inspection of Eq. (4.19), the importance  $I_k$  satisfies Eq. (2.69) defined for the adjoint eigenfunction  $\varphi_k^\dagger$

$$\mathcal{M}^\dagger I_k = \frac{1}{k} \mathcal{F}^\dagger I_k, \quad (4.20)$$

where we have used the definitions of the adjoint operators  $\mathcal{M}^\dagger$  and  $\mathcal{F}^\dagger$  from Eqs. (2.53) and (2.70) respectively.

The next step is to obtain the number of descendants during a Monte Carlo simulation, in order to estimate the neutron importance. First, a classic  $k$ -power iteration is performed in order to obtain the effective multiplication factor  $k$  and to distribute the particles according to the fundamental mode  $\varphi_{k_0}$ . Once convergence has been reached, neutrons belonging to each successive generation  $g$  are tagged as ancestors. Then, a fixed-source calculation is performed by simulating independent replicas and collecting the total statistical weight of the fission neutrons after  $M + 1$  generations, produced by a common ancestor generated at coordinates  $\mathbf{r}_0, \boldsymbol{\Omega}_0, E_0$ . The  $M$  generations are

defined as *latent generations*. In order to control the particle population, at the end of each generation a factor  $1/k$  is applied for the normalization of the total statistical weights of the new generation. In this way, the adjoint flux  $\varphi_{k_0}^\dagger(\mathbf{r}_0, \mathbf{\Omega}_0, E_0)$  is estimated as being proportional to the importance function  $I(\mathbf{r}_0, \mathbf{\Omega}_0, E_0)$  after  $g + M + 1$  generations.

The choice of the number of latent generations  $M$  used for this calculation is not trivial. In principle, a large value of  $M$  provides a better accuracy for the convergence of the results. On the other hand, a large value of  $M$  could terminate particle histories before reaching the scoring generation. Thorough considerations concerning the optimization of the choice of the parameter  $M$  can be found in [150]. In practice, an asymptotic distribution is usually reached for values of  $M$  between 10 and 20.

The results obtained by the IFP method can be used in order to estimate the kinetics parameters as the effective mean generation time  $\Lambda_{\text{eff},k}$  from Eq. (2.104) and the effective delayed fraction  $\beta_{\text{eff},k}^j$  from Eq. (2.103). These quantities are computed by using the fundamental direct mode  $\varphi_{k_0}$ , which is calculated during the  $k$ -power iteration, and the fundamental adjoint mode  $\varphi_{k_0}^\dagger$ , which is proportional to the importance  $I$  computed during a fixed-source simulation over the cycles of the power iteration. An index  $i$  is attributed to each fission neutron at generation  $g$  and it will be associated to all fission neutrons emitted at the following  $g + M + 1$  generations from the same ancestor. The IFP cycle is defined as the generations in the interval  $[g, g + M + 1]$  and  $M + 1$  is the cycle length. During this cycle, the importance of the ancestor  $i$  is defined as  $(\pi)_i$  and it is decomposed into  $(\pi_p)_i$  and  $(\pi_d)_i$  depending on the prompt or delayed nature of the fission event creating the ancestor.

The adjoint-weighted fission score for a given history can be estimated as

$$\frac{1}{k} \langle \varphi_k^\dagger, \mathcal{F} \varphi_k \rangle_{\text{history}} = \varphi_{k,1}^\dagger w_{f1} + \varphi_{k,2}^\dagger w_{f2} + \dots \propto \sum_i \frac{(\pi)_i}{w_{fi}} w_{fi} = \sum (\pi)_i, \quad (4.21)$$

where  $w_{fi}$  is the simulation weight of the fission neutron. Moreover, a factor  $1/k$  is applied in order to take into account the normalization of the particle at the end of each generation [75, 74]. Prompt and delayed contributions can be obtained by extending the sum for  $(\pi_p)_i$  and  $(\pi_d)_i$  respectively. In a similar way, the adjoint-weighted neutron lifetime is estimated as

$$\langle \varphi_k^\dagger, \frac{1}{v} \varphi_k \rangle_{\text{history}} = \sum (\pi)_i t_i, \quad (4.22)$$

where  $t_i$  is the lifetime of the ancestor  $i$  created at generation  $g$ .

## 4.4 The fundamental $\alpha$ -eigenmode

### 4.4.1 The $\alpha$ -k power iteration method

The power iteration introduced in Section 4.2 for the  $k$ -eigenvalue formulation can be generalized to solve the direct  $\alpha$ -eigenvalue: the  $\alpha$ - $k$  power iteration method [18] is usually performed by considering separately sub-critical and super-critical cases.

For both cases, the iterative procedure solves the following equation

$$\mathcal{M}_\alpha^{(g+1)} \varphi_\alpha^{(g+1)} = \frac{1}{k^{(g)}} S_{f,\alpha}^{(g)}, \quad (4.23)$$

where the definitions of the operator  $\mathcal{M}_\alpha^{(g+1)}$  and the emission density  $S_{f,\alpha}^{(g)}(\mathbf{r})$  depend on the critical state of the problem. For super-critical systems, Eq. (4.23) can be balanced by considering an additional capture reaction with macroscopic cross section

$$\Sigma_\alpha(E) = \frac{\alpha}{v(E)}, \quad (4.24)$$

defined as *time absorption cross section* and applied to the net disappearance operator  $\mathcal{M}$  in order to obtain

$$\mathcal{M}_\alpha = \Sigma_\alpha + \mathcal{M}. \quad (4.25)$$

The emission density  $S_{f,\alpha}(\mathbf{r})$  is defined by the contribution of prompt and delayed fission neutrons and reads

$$S_{f,\alpha} = \mathcal{F}_p \varphi_\alpha + \sum_j w_j(\alpha) \chi_d^j \mathcal{F}_d^j \varphi_\alpha, \quad (4.26)$$

where  $w_j(\alpha)$  is

$$w_j(\alpha) = \frac{\lambda_j}{\lambda_j + \alpha}. \quad (4.27)$$

The aim of this procedure is to find the value of  $\alpha$  such that the system is critical with respect to  $k$ , i.e.,  $k_0 = 1$ . For this purpose, a positive initial guess of  $\alpha^{(0)}$  is defined and neutrons are generated according to an arbitrary source distribution  $S_{f,\alpha}^{(0)}$ . Particle histories continue until their absorption: the resulting fission particles are recorded and moved to the next generation. At the end of each cycle, a value  $k^{(0)}$  can be estimated by taking the ratio of the current and the produced total weight of neutrons. This factor is used to balance the system for the next generation, according to:

$$\alpha^{(g+1)} = \alpha^{(g)} k^{(g)}. \quad (4.28)$$

These steps will be repeated until convergence is achieved. In particular,  $k$  will converge to unity and the fundamental eigenpair  $(\alpha_0, \varphi_{\alpha_0})$  will converge to the asymptotic values [99].

For sub-critical cases,  $\alpha$  is negative and we cannot introduce a corresponding capture cross section. A possible option to overcome this problem is to promote neutrons to the next generation by a new reaction, expressed by the "copy" operator [169, 170]

$$\mathcal{F}_{\alpha,\eta} = \int_{4\pi} d\Omega' \int_0^\infty dE' v_\eta \Sigma_{\alpha,\eta}(E') \delta(\Omega - \Omega') \delta(E - E'), \quad (4.29)$$

where  $\Sigma_{\alpha,\eta}(E)$  is a macroscopic cross section defined as

$$\Sigma_{\alpha,\eta}(E) = -\frac{\eta\alpha}{v(E)}, \quad (4.30)$$

and the associated yield  $v_\eta$  is equal to

$$v_\eta = \frac{\eta + 1}{\eta} > 0, \quad (4.31)$$

for arbitrary  $\eta > 0$ .

The so called  $\alpha$ -production term acts as a copy operator, applied in order to balance the promotion of neutrons to the next batch [169]. The expressions for  $\mathcal{M}_\alpha$  and  $S_{f,\alpha}(\mathbf{r})$  are then respectively reformulated as

$$\mathcal{M}_\alpha = \Sigma_{\alpha,\eta} + \mathcal{M}, \quad (4.32)$$

$$S_{f,\alpha} = \mathcal{F}_{\alpha,\eta} \varphi_\alpha + \mathcal{F}_p \varphi_\alpha + \sum_j w_j(\alpha) \chi_d^j \mathcal{F}_d^j \varphi_\alpha. \quad (4.33)$$

The special interactions needed in the  $\alpha$ - $k$  algorithm can be interpreted as an absorption in the  $\mathcal{M}_\alpha$  kernel, and as a copy in the emission density  $S_{f,\alpha}$ . The simulation of non-multiplying media is allowed, since particles are promoted by this  $\alpha$ -copy operation. The eigenvalue  $\alpha$  is finally updated as

$$\alpha^{(g+1)} = \frac{\alpha^{(g)}}{k^{(g+1)}}. \quad (4.34)$$

The  $\alpha$ - $k$  power iteration method is considered as a reference for the evaluation of the fundamental eigenpairs of the  $\alpha$ -eigenvalue problem by Monte Carlo simulation [18, 169, 170]. Nevertheless, the implementation of this procedure implies some drawbacks as well as limitations in the reliability of the results obtained. Singling out sub-critical and super-critical cases forces the sign of the initial guess  $\alpha^{(0)}$  to be constant during the simulation. This property could possibly lead to a bias if systems very close to the critical state are considered. Moreover, for deeply sub-critical systems, the  $\alpha$  estimated at the end of each iteration could be smaller than  $-\min(\lambda_j)$ . Even though specific routines can be applied in order to force  $\alpha$  so that this physical limit is preserved, these operations

are somewhat delicate and could lead to wrong predictions. Finally, the variances of the results obtained by power iteration tend to be underestimated. This is due to the correlation between generations: the update of  $\alpha$  is obtained by either multiplying or dividing by  $k$ . When this factor is close to unity, the generic  $\alpha^{(g+1)}$  can only slightly change with respect to  $\alpha^{(g)}$ .

### The $\alpha$ -tally method

Some of the limitations of the traditional  $\alpha$ - $k$  method can be removed by a recently proposed algorithm named  *$\alpha$ -tally method*, which provides an estimation of  $\alpha^{(g)}$  at the end of each generation  $g$  [69]. The main idea is to collapse the transport operators as integrals over the entire phase-space and to search for the largest real root of a non-linear equation, which is representative of the fundamental eigenvalue  $\alpha_0$ .

The  $\alpha$ -eigenvalue problem from Eq. (2.79) is recast as

$$\alpha \mathcal{V}^{-1} \varphi_\alpha + \mathcal{M} \varphi_\alpha = \mathcal{F}_p \varphi_\alpha + \sum_j \frac{\lambda_j}{\lambda_j + \alpha} \frac{\chi_d^j}{4\pi} \mathcal{F}_d^j \varphi_\alpha. \quad (4.35)$$

By expanding the net disappearance operator  $\mathcal{M}$  into the combination of the streaming term  $\mathcal{L}$ , the collisional term  $\mathcal{R}$  and the scattering term  $\mathcal{S}$ , the previous equation is integrated over the phase-space, which yields

$$\alpha \langle \mathcal{V}^{-1} \varphi_\alpha \rangle + \langle \mathcal{L} \varphi_\alpha \rangle + \langle \mathcal{R} \varphi_\alpha \rangle - \langle \mathcal{S} \varphi_\alpha \rangle = \langle \mathcal{F}_p \varphi_\alpha \rangle + \sum_j \frac{\lambda_j}{\lambda_j + \alpha} \left\langle \frac{\chi_d^j}{4\pi} \mathcal{F}_d^j \varphi_\alpha \right\rangle. \quad (4.36)$$

These integrated quantities represent reaction rates that can be scored during a Monte Carlo simulation and Eq. (4.36) is formally a polynomial as a function of  $\alpha$ , once the coefficients appearing in the equation have been estimated. Table 4.1 shows the distinct contributions and the physical interpretation associated to each score.

Equation (4.36) can then be solved with respect to the unknown  $\alpha$ , obtained by bisection method as the largest real root of the polynomial [69]. The  $\alpha$ -tally method yields smaller correlations between successive generations due to the estimation of  $\alpha$  from a polynomial equation at each cycle. Moreover,  $\alpha$  values estimated during the simulation can cross the critical boundary at  $\alpha = 0$ , allowing a more precise estimation with respect to the  $\alpha$ - $k$  power iteration for systems very close to criticality.

rate	contribution	physical interpretation
$\langle \mathcal{V}^{-1} \varphi_\alpha \rangle$	$w \frac{l}{v}$	time of flight
$\langle \mathcal{L} \varphi_\alpha \rangle$	$w$	leakage from the system
$\langle \mathcal{R} \varphi_\alpha \rangle$	$w \frac{\Sigma_t}{\Sigma_t^*}$	collision rate
$\langle \mathcal{S} \varphi_\alpha \rangle$	$w \frac{\Sigma_s}{\Sigma_t^*}$	scattering rate
$\langle \mathcal{F}_p \varphi_\alpha \rangle$	$w \frac{v_p \Sigma_f}{\Sigma_t^*}$	prompt fission rate
$\left\langle \frac{\chi_d^j}{4\pi} \mathcal{F}_d^j \varphi_\alpha \right\rangle$	$w \frac{v_d \Sigma_f}{\Sigma_t^*}$	delayed fission rate

Table 4.1: Estimation of the integrated transport operators for the  $\alpha$ -tally method [69]. In particular,  $w$  is the statistical weight,  $l$  is the length travelled by the particle and  $\Sigma_t^*(\mathbf{r}, E)$  is the macroscopic cross section obtained as  $\Sigma_t(\mathbf{r}, E) + \Sigma_\alpha(E)$  if  $\alpha$  is positive or  $\Sigma_t(\mathbf{r}, E) + \Sigma_{\alpha, \eta}(E)$  if  $\alpha$  is negative. The virtual cross sections  $\Sigma_\alpha(E)$  and  $\Sigma_{\eta, \alpha}(E)$ , defined in Eqs. (4.24) and (4.30) respectively, take into account the additional reactions for time absorption and  $\alpha$ -copy.

## 4.5 Adjoint $\alpha$ -eigenvalue equations

The IFP method discussed in Section 4.3 can be generalized in order to estimate adjoint-weighted quantities according to the  $\alpha$ -eigenvalue formulation. The main idea of the *Generalized Iterated Fission probability method* is to basically follow the same procedure presented in Section 4.3 and adapt it to the equations introduced for the description of the  $\alpha$ - $k$  power iteration in Section 4.4.1. For this reason, the procedure is different for positive and negative  $\alpha_0$ . The idea is again to first relate the adjoint fundamental eigenfunction  $\varphi_{\alpha_0}^\dagger$  to the importance function  $I_\alpha$ , and then to estimate such observable as the total contributions of descendants from a given ancestor.

For super-critical systems, the probability of non-collision during the infinitesimal path  $ds$  is  $p_{nc,\alpha} = 1 - (\Sigma_t + \Sigma_\alpha)ds$ , with  $\Sigma_\alpha$  defined in Eq. (4.24). The kernel  $q_\alpha$  takes into account the modifications of the delayed fission operators by an addition factor  $\lambda_j/(\lambda_j + \alpha)$ , namely

$$q_\alpha(\mathbf{r} + \mathbf{\Omega}ds, \mathbf{\Omega} \rightarrow \mathbf{\Omega}', E \rightarrow E') = \Sigma_s(\mathbf{r} + \mathbf{\Omega}ds, \mathbf{\Omega} \rightarrow \mathbf{\Omega}', E \rightarrow E')ds + \frac{1}{k} \bar{v}_p(E) \Sigma_f(\mathbf{r} + \mathbf{\Omega}ds, E) \frac{\chi_p(E')}{4\pi} ds + \frac{1}{k} \sum_j \frac{\lambda_j}{\lambda_j + \alpha} \bar{v}_d^j(E) \Sigma_f(\mathbf{r} + \mathbf{\Omega}ds, E) \frac{\chi_d^j(E')}{4\pi} ds, \quad (4.37)$$

with  $k$  defined as the ratio between two successive population sizes. Recalling the same procedure described in Section 4.3, the importance balance equation for sub-critical systems according to the  $\alpha$ -eigenvalue formulation yields

$$0 = \mathbf{\Omega} \cdot \nabla I_\alpha(\mathbf{r}, \mathbf{\Omega}, E) - (\Sigma_t(\mathbf{r}, E) + \Sigma_\alpha(E)) I_\alpha(\mathbf{r}, \mathbf{\Omega}, E) + \int_{4\pi} d\mathbf{\Omega}' \int_0^\infty dE' \Sigma_s(\mathbf{r}, \mathbf{\Omega} \rightarrow \mathbf{\Omega}', E \rightarrow E') I_\alpha(\mathbf{r}, \mathbf{\Omega}', E') + \frac{1}{k} \bar{v}_p(E) \Sigma_f(\mathbf{r}, E) \int_{4\pi} d\mathbf{\Omega}' \int_0^\infty dE' \frac{\chi_p(E')}{4\pi} I_\alpha(\mathbf{r}, \mathbf{\Omega}', E') + \frac{1}{k} \sum_j \frac{\lambda_j}{\lambda_j + \alpha} \bar{v}_d^j(E) \Sigma_f(\mathbf{r}, E) \int_{4\pi} d\mathbf{\Omega}' \int_0^\infty dE' \frac{\chi_d^j(E')}{4\pi} I_\alpha(\mathbf{r}, \mathbf{\Omega}', E'). \quad (4.38)$$

For sub-critical systems, the probability of non-collision during the infinitesimal path  $ds$  is  $p_{nc,\alpha,\eta} = 1 - (\Sigma_t + \Sigma_{\alpha,\eta})ds$ , with  $\Sigma_{\alpha,\eta}$  defined in Eq. (4.30). The kernel  $q_{\alpha,\eta}$  includes the  $\alpha$ -copy operator from Eq. (4.29), which yields

$$q_{\alpha,\eta}(\mathbf{r} + \mathbf{\Omega}ds, \mathbf{\Omega} \rightarrow \mathbf{\Omega}', E \rightarrow E') = \Sigma_s(\mathbf{r} + \mathbf{\Omega}ds, \mathbf{\Omega} \rightarrow \mathbf{\Omega}', E \rightarrow E')ds + \frac{1}{k} \bar{v}_p(E) \Sigma_f(\mathbf{r} + \mathbf{\Omega}ds, E) \frac{\chi_p(E')}{4\pi} ds + \frac{1}{k} \sum_j \frac{\lambda_j}{\lambda_j + \alpha} \bar{v}_d^j(E) \Sigma_f(\mathbf{r} + \mathbf{\Omega}ds, E) \frac{\chi_d^j(E')}{4\pi} ds + \frac{1}{k} \bar{v}_\eta \Sigma_{\alpha,\eta}(E) \delta(\mathbf{\Omega} - \mathbf{\Omega}') \delta(E - E') ds. \quad (4.39)$$

The importance balance equation for super-critical systems according to the  $\alpha$ -eigenvalue formulation is expressed as

$$0 = \mathbf{\Omega} \cdot \nabla I_\alpha(\mathbf{r}, \mathbf{\Omega}, E) - (\Sigma_t(\mathbf{r}, E) + \Sigma_{\alpha,\eta}(E)) I_\alpha(\mathbf{r}, \mathbf{\Omega}, E) + \int_{4\pi} d\mathbf{\Omega}' \int_0^\infty dE' \Sigma_s(\mathbf{r}, \mathbf{\Omega} \rightarrow \mathbf{\Omega}', E \rightarrow E') I_\alpha(\mathbf{r}, \mathbf{\Omega}', E') + \frac{1}{k} \bar{v}_p(E) \Sigma_f(\mathbf{r}, E) \int_{4\pi} d\mathbf{\Omega}' \int_0^\infty dE' \frac{\chi_p(E')}{4\pi} I_\alpha(\mathbf{r}, \mathbf{\Omega}', E') + \frac{1}{k} \sum_j \frac{\lambda_j}{\lambda_j + \alpha} \bar{v}_d^j(E) \Sigma_f(\mathbf{r}, E) \int_{4\pi} d\mathbf{\Omega}' \int_0^\infty dE' \frac{\chi_d^j(E')}{4\pi} I_\alpha(\mathbf{r}, \mathbf{\Omega}', E') + \frac{1}{k} \bar{v}_\eta \Sigma_{\alpha,\eta}(E) \int_{4\pi} d\mathbf{\Omega}' \int_0^\infty dE' \delta(\mathbf{\Omega} - \mathbf{\Omega}') \delta(E - E') I_\alpha(\mathbf{r}, \mathbf{\Omega}', E'). \quad (4.40)$$

The relation between the neutron importance  $I_\alpha$  and the adjoint fundamental mode  $\varphi_{\alpha_0}^\dagger$  yields

$$\mathcal{M}_{\alpha,\eta}^\dagger I_\alpha = \frac{1}{k} \left[ \mathcal{F}_{\alpha,\eta}^\dagger + \mathcal{F}_\alpha^\dagger \right] I_\alpha, \quad (4.41)$$

where the operators  $\mathcal{M}_{\alpha,\eta}^\dagger$  and  $\mathcal{F}_{\alpha,\eta}^\dagger$  are respectively defined as

$$\mathcal{M}_{\alpha,\eta}^\dagger = \mathcal{M}^\dagger + \Sigma_{\alpha,\eta}, \quad (4.42)$$

$$\mathcal{F}_{\alpha,\eta}^\dagger = \nu_\eta \Sigma_{\alpha,\eta}. \quad (4.43)$$

For sub-critical configurations, the  $\alpha$ -copy operation acts as an additional promotion of particles to the next generation.

Similarly as for the standard IFP method, the adjoint fundamental function  $\varphi_{\alpha_0}^\dagger$  is then estimated by collecting all statistical weights of the descendants at generation  $M + 1$ , given an ancestor born at coordinate  $\mathbf{r}_0, \mathbf{\Omega}_0, E_0$ . Contrary to the case of the  $k$ -eigenvalue problem, the eigenvalue  $\alpha_0$  obtained from the direct simulation explicitly appears in the transport operators for the importance function  $I_\alpha$ . The general strategy is thus to first perform an  $\alpha$ - $k$  power iteration in order to estimate  $\alpha_0$ , and then to start a fixed-source calculations according to the kernels previously defined.

The generalized IFP method allows computing general bilinear forms of the kind  $\langle \varphi_\alpha^\dagger, A\varphi_\alpha \rangle$ . At the end of the  $\alpha$ - $k$  power iteration, the particle population is distributed according to the direct fundamental mode  $\varphi_{\alpha_0}$ . Then, the ancestors are defined for the successive  $g$  generations in order to compute the importance  $I_\alpha$  up to the end of the IFP cycle at generation  $g + M + 1$ . The bilinear form is then estimated by multiplying the score related to the ancestor by its importance.

## 4.6 Analysis of Godiva-like benchmark configurations

As a preliminary step in view of characterizing the behaviour of the direct and adjoint fundamental modes for  $k$ - and  $\alpha$ -eigenvalue problems, we have selected two simple benchmark configurations, both inspired from Godiva-like test-cases previously considered in the literature [28]. The first configuration consists in a bare sphere of uranium, whose specifications are taken from [28] (Problem I) and are very close to those of the standard Godiva benchmark [60]. In particular, the radius of the sphere is equal to 8.7407 cm and the uranium isotopic composition (normalized with respect to the uranium density) consists of 93.7695% atoms of  $U^{235}$ , 5.2053% atoms of  $U^{238}$  and 1.0252% atoms of  $U^{234}$ . The system is spatially homogeneous, and the neutron spectrum is fast. The second configuration is also taken from [28] (Problem III) and corresponds to a sphere of uranium with equal radius and uranium isotopic composition, surrounded by a thick water reflector: the system is spatially heterogeneous with a total radius of 38.7407 cm and a strong thermal component. The water density is equal to 1 g/cm<sup>3</sup> with 2 atoms of  $H^1$  and 1 atom of  $O^{16}$ . For the sake of simplicity, we will call these configurations Problem I and Problem III.

### 4.6.1 Description of the benchmark configurations

For both cases, starting from the specifications given in [28], we have adjusted the uranium density in order to obtain slightly sub-critical and slightly super-critical configurations, with the aim of examining the effects of slight deviations from criticality on the shape of the direct and adjoint eigenmodes. The chosen values of uranium density for each configuration are shown in Tab. 4.2.

configuration	$\rho_U$ [g/cm <sup>3</sup> ]
I sub-critical	18.6836
I super-critical	18.9085
III sub-critical	13.5676
III super-critical	13.8600

Table 4.2: Uranium densities for benchmark configurations. Uranium isotopic mass fractions and water properties are equal to those described in the reference [28].

The simulation results displayed in the following have been obtained by resorting to TRIPOLI-4<sup>®</sup>. The forward simulations are performed via the power iteration method for the  $k$ -eigenvalue problem, and the  $\alpha$ - $k$  power iteration method for the  $\alpha$ -eigenvalue problem. The corresponding numerical simulation parameters are presented in Tab. 4.3. The adjoint simulations are performed via the IFP method for the  $k$ -eigenvalue problem, and the G-IFP method for the  $\alpha$ -eigenvalue problem. The corresponding numerical simulation parameters are presented in Tab. 4.4. All flux distributions have been scored into 281 energy meshes. Nuclear data for our calculations have been taken from the JEFF3.1.1 library, where all fissile isotopes have 8 families of precursors. [134].

configuration	active cycles	inactive cycles	particles
I sub-critical	$5 \times 10^3$	$10^3$	$10^5$
I super-critical	$5 \times 10^3$	$10^3$	$10^5$
III sub-critical	$2 \times 10^3$	$2 \times 10^3$	$10^4$
III super-critical	$2 \times 10^3(*)$	$2 \times 10^3$	$10^4$

(\*)  $5 \times 10^3$  for the  $\alpha$ -simulation including delayed neutron contributions

Table 4.3: Numerical simulation parameters for benchmark configurations: forward simulations.

configuration	particles	latent generations
I sub-critical	$5 \times 10^7$	20
I super-critical	$5 \times 10^7$	20
III sub-critical	$5 \times 10^9$	5
III super-critical	$5 \times 10^9$	5

Table 4.4: Numerical simulation parameters for benchmark configurations: adjoint simulations.

## 4.6.2 Analysis of the fundamental eigenmodes

### Problem I

The fundamental eigenvalues  $k_0$  and  $\alpha_0$  computed in the corresponding simulations for Problem I by including and neglecting the delayed neutron contributions are given in Tabs. 4.5 and 4.6, respectively. It is worth noting that the super-critical configuration in Problem I becomes sub-critical when delayed neutron contributions are neglected in the calculations. Moreover, the fundamental eigenvalue  $k_0$  is reduced by approximately 650 pcm when the delayed contribution is not considered. Concerning the  $\alpha$ -eigenvalue formulation, the absolute value of  $\alpha_0$  is smaller than  $1 \text{ s}^{-1}$  by including delayed neutrons, whereas the absolute value of this eigenvalue is larger than  $10^5 \text{ s}^{-1}$  when neglecting delayed neutrons. Neglecting the presence of the delayed neutrons in this fast spectrum system implies thus a decrease of the reactor period of approximately 5 orders of magnitude.

configuration	$k_0[-]$ , with delayed contributions	$k_0[-]$ , prompt fission only
I sub-critical	$0.99396 \pm 5 \times 10^{-5}$	$0.98750 \pm 4 \times 10^{-5}$
I super-critical	$1.00389 \pm 6 \times 10^{-5}$	$0.99740 \pm 6 \times 10^{-5}$

 Table 4.5: Fundamental eigenvalues  $k_0$  for Problem I.

configuration	$\alpha_0[\text{s}^{-1}]$ , including precursors	$\alpha_0[\text{s}^{-1}]$ , without precursors
I sub-critical	$-1.1880 \times 10^{-2} \pm 2 \times 10^{-6}$	$-1.379 \times 10^6 \pm 1 \times 10^3$
I super-critical	$3.025 \times 10^{-1} \pm 3 \times 10^{-4}$	$-4.339 \times 10^5 \pm 4 \times 10^2$

 Table 4.6: Fundamental eigenvalues  $\alpha_0$  for Problem I.

For illustration, the shapes of direct and adjoint eigenmodes  $\varphi_{k_0}^{(\dagger)}$  and  $\varphi_{\alpha_0}^{(\dagger)}$  (with and without delayed neutron contributions) for the sub-critical configuration and the super-critical configuration of Problem I are shown in Figs. 4.1 and 4.2, respectively. For comparison, all curves have been normalized. Deviations due to the kind of eigenfunction (either  $k$  or  $\alpha$ ) and to the presence of delayed contributions are clearly visible in the adjoint distributions.

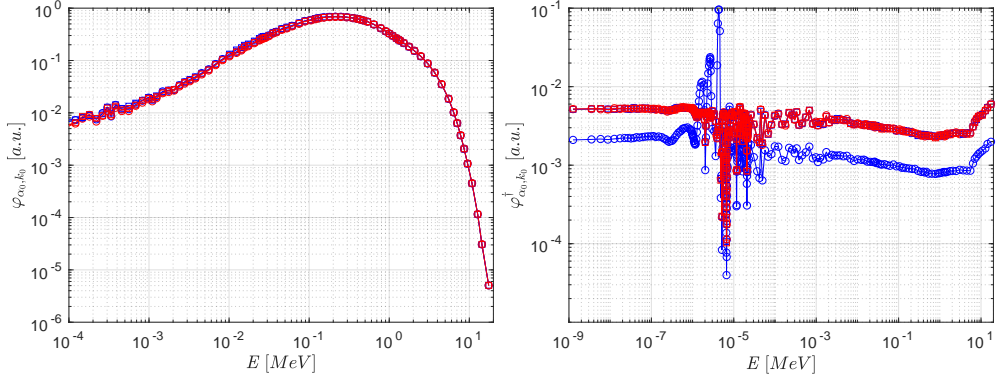


Figure 4.1: Problem I, sub-critical configuration, direct (left) and adjoint (right) fundamental distributions according to the  $\alpha$ - (blue) and  $k$ - (red) eigenvalue formulations, with (squares) and without (circles) delayed contributions.

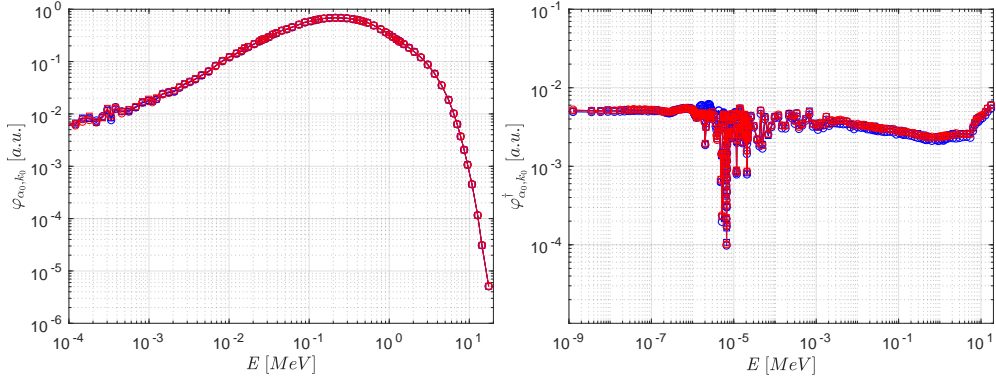


Figure 4.2: Problem I, super-critical configuration, direct (left) and adjoint (right) fundamental distributions according to the  $\alpha$ - (blue) and  $k$ - (red) eigenvalue formulations, with (squares) and without (circles) delayed contributions.

In order to quantitatively assess these differences, in Figs. 4.3 and 4.4 we show the ratios between  $\alpha$ - and  $k$ -eigenfunctions for the direct and adjoint problem, respectively. For the direct eigenfunctions, deviations are overall rather small (see Fig. 4.3). In the sub-critical configuration, we have  $\varphi_{\alpha_0} < \varphi_{k_0}$  in the fast region and vice-versa in the epithermal region, both with and without delayed neutrons (Fig. 4.3 left). For the super-critical configuration, the situation is different: in the fast region, we have  $\varphi_{\alpha_0} < \varphi_{k_0}$  without delayed neutrons and  $\varphi_{\alpha_0} > \varphi_{k_0}$  with delayed neutrons; in the epithermal region the behaviour is inverted. This is possibly due to the fact that in the super-critical configuration the sign of  $\alpha_0$  changes with or without delayed neutrons. In the thermal region, very few neutrons contribute to the direct eigenfunctions (as expected from a fast neutron spectrum system), although statistical uncertainty prevents from drawing solid conclusions.

As for the adjoint eigenfunctions, deviations are somewhat stronger when delayed neutrons are not considered (see Fig. 4.4), especially in the resonance region. On the contrary, when delayed neutron contributions are taken into account deviations of  $\varphi_{k_0}^\dagger$  from  $\varphi_{\alpha_0}^\dagger$  become much smaller. Overall, neglecting the presence of delayed neutrons leads to  $\varphi_{\alpha_0}^\dagger < \varphi_{k_0}^\dagger$  outside the resonance region and the difference between the two distributions is larger for the more sub-critical configuration.

Direct and adjoint eigenmodes computed by including delayed neutrons show similar distributions. In principle, the absolute value of  $\alpha_0$  drops around  $10^{-1} \text{ s}^{-1}$ , therefore the term  $\alpha_0/v\varphi_{\alpha_0}$  is significantly reduced. Moreover, the weight multiplier for both the  $k$ -delayed fission operator ( $1/k_0$ ) and the  $\alpha$ -delayed fission operator ( $\lambda_j/(\lambda_j + \alpha_0)$ ) are both around the unit value. For this reason, the  $k$ - and the  $\alpha$ - eigenvalue problems presented in Eqs. (2.65), (2.79) for the direct formulation and in Eqs. (2.69), (2.81) for the adjoint formulation would be close to each other.

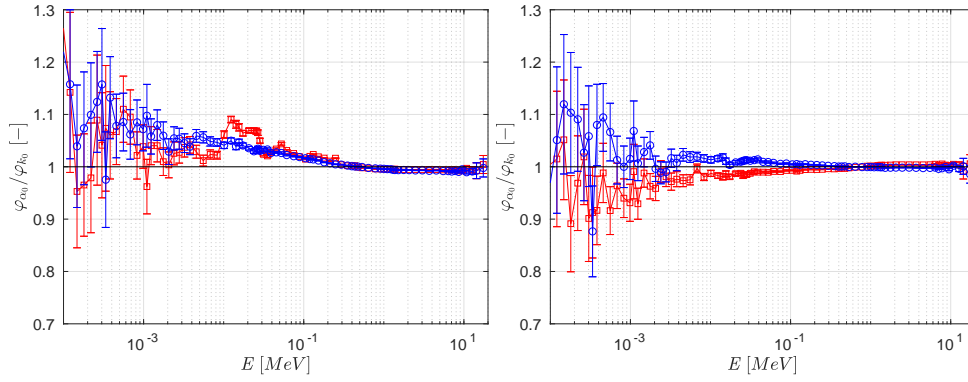


Figure 4.3: Problem I, ratios  $\varphi_{\alpha_0}/\varphi_{k_0}$  of the direct fundamental distributions, for sub-critical (left) and super-critical (right) configuration, with (red squares) and without (blue circles) delayed contributions.

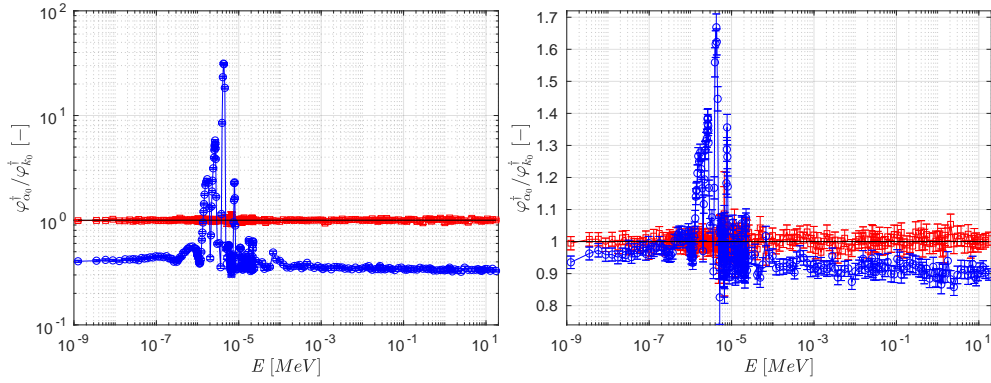


Figure 4.4: Problem I, ratios  $\varphi_{\alpha_0}^\dagger/\varphi_{k_0}^\dagger$  of the adjoint fundamental distributions, for sub-critical (left) and super-critical (right) configuration, with (red squares) and without (blue circles) delayed contributions.

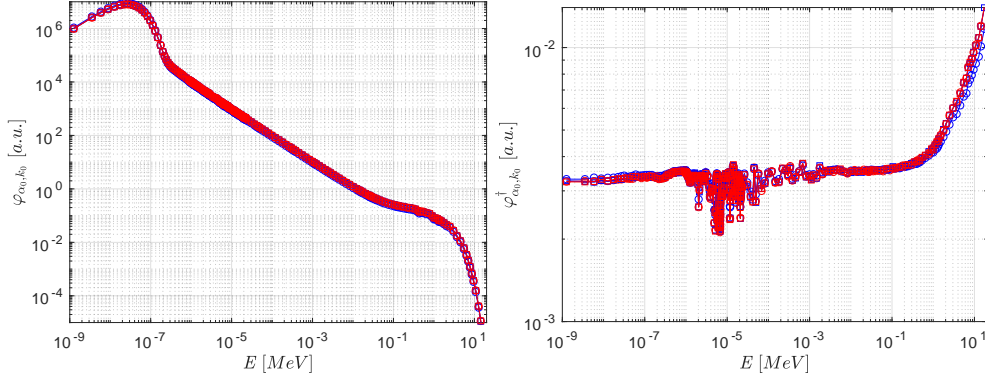
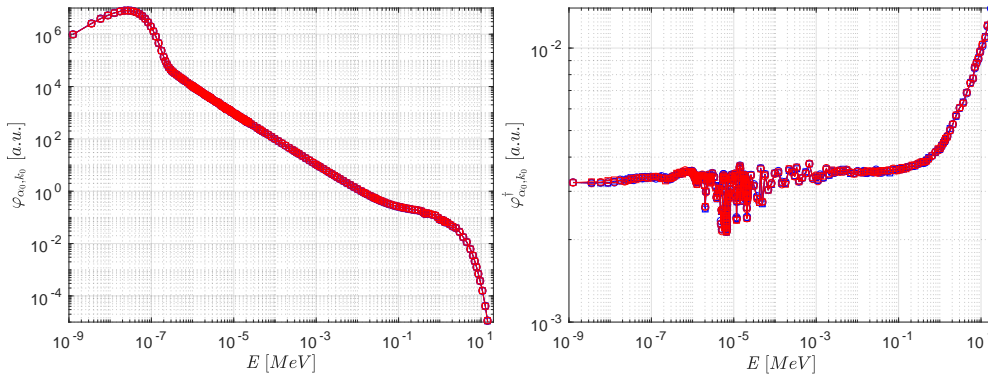
### Problem III

The fundamental eigenvalues  $k_0$  and  $\alpha_0$  computed in the corresponding simulations for Problem III with and without the delayed neutron contributions are given in Tabs. 4.7 and 4.8, respectively. It is worth noting that similarly to Problem I the system described in Problem III is sub-critical if delayed neutron contributions are neglected in the calculations. Moreover, the fundamental eigenvalue  $k_0$  is reduced by approximately 700 pcm when the delayed contribution is not considered. Concerning the  $\alpha$ -eigenvalue formulation, the absolute value of  $\alpha_0$  is again smaller than  $1 \text{ s}^{-1}$  by including delayed neutrons, whereas the absolute value of this eigenvalue is between  $10^2 \text{ s}^{-1}$  and  $10^3 \text{ s}^{-1}$  when neglecting delayed neutrons. Neglecting the presence of the delayed neutrons in this thermal system implies a decrease of the reactor period of approximately 3 orders of magnitude.

configuration	$k_0[-]$ , with delayed contributions	$k_0[-]$ , prompt fission only
III sub-critical	$0.9927 \pm 2 \times 10^{-4}$	$0.9858 \pm 2 \times 10^{-4}$
III super-critical	$1.0050 \pm 2 \times 10^{-4}$	$0.9979 \pm 2 \times 10^{-4}$

Table 4.7: Fundamental eigenvalues  $k_0$  for Problem III.

configuration	$\alpha_0[s^{-1}]$ , including precursors	$\alpha_0[s^{-1}]$ , without precursors
III sub-critical	$-1.1686 \times 10^{-2} \pm 7 \times 10^{-6}$	$-9.820 \times 10^2 \pm 9 \times 10^{-1}$
III super-critical	$4.71 \times 10^{-1} \pm 1 \times 10^{-3}$	$-1.945 \times 10^2 \pm 4 \times 10^{-1}$

 Table 4.8: Fundamental eigenvalues  $\alpha_0$  for Problem III.

 Figure 4.5: Problem III, sub-critical configuration, direct (left) and adjoint (right) fundamental distributions according to the  $\alpha$ - (blue) and  $k$ - (red) eigenvalue formulations, with (squares) and without (circles) delayed contributions.

 Figure 4.6: Problem III, super-critical configuration, direct (left) and adjoint (right) fundamental distributions according to the  $\alpha$ - (blue) and  $k$ - (red) eigenvalue formulations, with (squares) and without (circles) delayed contributions.

The shapes of the direct eigenmodes  $\varphi_{k_0}$  and  $\varphi_{\alpha_0}$  (with and without delayed neutron contributions) for the sub-critical configuration of Problem III are shown in Fig. 4.5 (left); the adjoint eigenmodes are also shown in the same figure (right). The direct and the adjoint distributions for the super-critical configuration of the same problem are shown in Fig. 4.6. The behaviour of the adjoint eigenmodes shows noticeable differences with respect to what observed in spatially large systems, i.e. MOX and UOX assembly configurations [149], where the thermal component was higher and the fast component was lower as compared to Problem III. The strong impact of the fast component in our example, and the milder impact of the thermal component, can be justified by the fact that Problem III is strongly spatially heterogeneous, with a fast spectrum localized in the fissile lump and a thermal spectrum localized in the moderator. Due to normalization the amplitude of  $\varphi^\dagger$  shown in Figs. 4.5 and 4.6 is smaller in the thermal region and larger in the fast region if compared to the results obtained from MOX and UOX assembly configurations. For comparison, all curves have been normalized. Slight but significant deviations due to the kind of eigenfunction (either  $k$ - or  $\alpha$ -) and to the presence of delayed contributions are again visible, especially for the adjoint fluxes.

The corresponding ratios for the direct and adjoint eigenfunctions are displayed in Figs. 4.7 and 4.8, respectively. For the direct eigenfunctions, when delayed neutron contributions are taken into account deviations are rather small (see Fig. 4.7) for both the sub- and super-critical configurations. However, it is possible to notice the

presence of a deviation between the  $k$ - and  $\alpha$ -eigenfunctions: for the sub-critical configuration, we have  $\varphi_{\alpha_0} < \varphi_{k_0}$  for energy values larger than 0.6 MeV and  $\varphi_{\alpha_0} > \varphi_{k_0}$  for energy values larger between 10 keV and 0.6 MeV; for the super-critical configuration an opposite behaviour is noticeable in the same energy ranges. This inversion is justified by the transition from a sub-critical to a super-critical system. For a sub-critical configuration, the  $k$ -eigenvalue formulation hardens the energy spectrum by artificially increasing the amplitude of fission operator by a factor  $1/k_0$ , whereas the  $\alpha$ -eigenvalue formulation promotes the thermal spectrum by the term  $\alpha_0/v$  and at the same modifies the delayed fission operator by the factor  $\gamma = \bar{\lambda}/(\alpha_0 + \bar{\lambda})$ . Observe that we have  $\gamma > 1$  for negative  $\alpha_0$  and  $\gamma < 1$  for positive  $\alpha_0$ . The presence of delayed neutrons shifts the behaviour where  $\varphi_{\alpha_0} < \varphi_{k_0}$  towards 0.6 MeV which is around the average emission energy for delayed neutrons [29]. According to the  $\alpha$ -eigenvalue formulation, the delayed fission operator is now rescaled by a factor  $\bar{\lambda}_j/(\bar{\lambda}_j + \alpha_0)$ , with  $\bar{\lambda}_j = \beta/\sum_j(\beta_j/\lambda_j) = 0.0768 \pm 0.0006$  s<sup>-1</sup> for U<sup>235</sup> [102]. This factor is still smaller than  $1/k_0$ , hence  $\varphi_{\alpha_0}$  is still smaller than  $\varphi_{k_0}$  at fast energy range. The symmetric argument can be applied for the super-critical case.

The ratio shown for energies between 10 keV and 20 MeV for the super-critical configuration seems smaller compared to the one computed for the sub-critical configuration. This result is coherent with the former configuration being closer to the critical state (super-critical configuration) with respect to the latter (sub-critical configuration). For energy ranges smaller than 10 keV, no significant differences are visible.

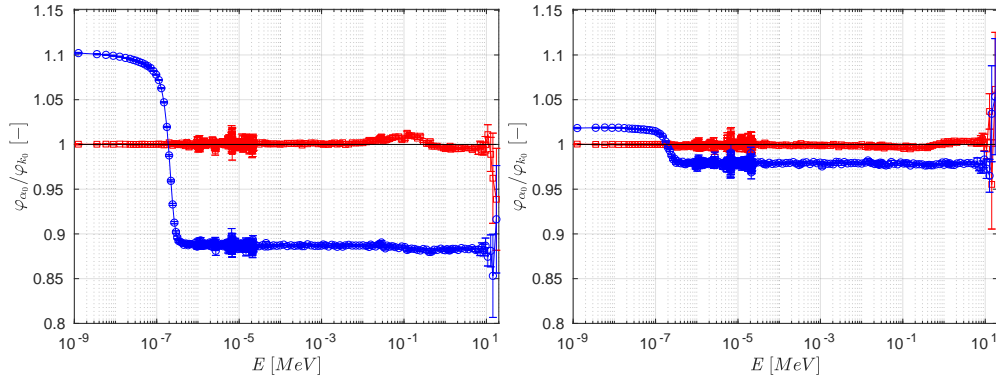


Figure 4.7: Problem III, ratios  $\varphi_{\alpha_0}/\varphi_{k_0}$  of the direct fundamental distributions, for sub-critical (left) and super-critical (right) configuration, with (red squares) and without (blue circles) delayed contributions.

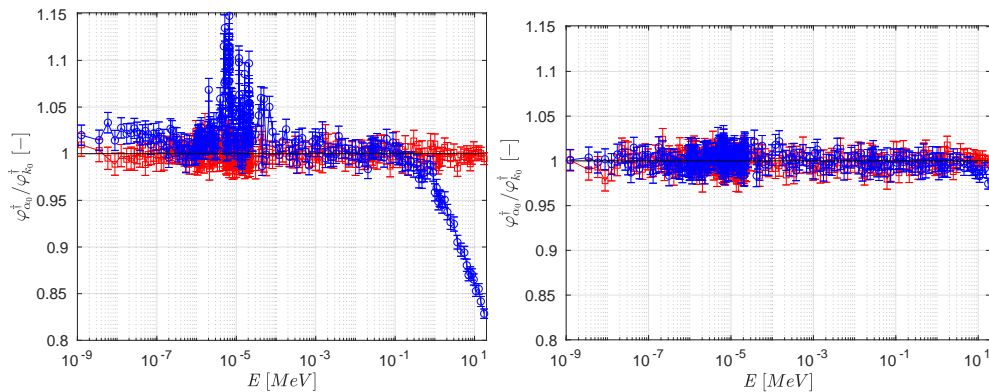


Figure 4.8: Problem III, ratios  $\varphi_{\alpha_0}^\dagger/\varphi_{k_0}^\dagger$  of the adjoint fundamental distributions, for sub-critical (left) and super-critical (right) configuration, with (red squares) and without (blue circles) delayed contributions.

On the contrary, for the simulations excluding delayed neutrons deviations become larger: in the fast and epithermal region, we have  $\varphi_{\alpha_0} < \varphi_{k_0}$ , whereas  $\varphi_{\alpha_0} > \varphi_{k_0}$  in the thermal region. Again, if only prompt neutrons are considered, the fundamental eigenmode  $\varphi_{k_0}$  is shifted towards higher energies for a sub-critical system due to the  $1/k_0$  factor which artificially increases the number of fissions. This behaviour is smoothed in the super-critical configuration (which is sub-critical, if delayed contributions are neglected) due to the system being closer to the critical state. As for the adjoint eigenfunctions, strong deviations in the fast region ( $E > 0.1$  MeV) are

observed for the sub-critical configuration, when delayed neutrons are not considered (see Fig. 4.8). In all the other configurations, no significant differences are visible.

### 4.6.3 Analysis of the effective kinetics parameters

Based on the observed discrepancies between the fundamental  $k$ - and  $\alpha$ -eigenmodes, it would be interesting to assess which is the practical impact on the reactor parameters that depend on these quantities. In this respect, a prominent example is represented by the kinetics parameters, which are indeed bilinear forms depending on both the forward and the adjoint eigenmodes. The kinetics parameters, in turn, influence the system reactivity, through the in-hour (Nordheim) formula [4, 72]. In this section we will thus examine the practical consequences of the slight differences on the fundamental eigenmodes detected in the previous sections.

The effective kinetics parameters discussed in Section 2.7.1 for both  $k$ - and  $\alpha$ - eigenvalue formulations are here recalled. The expressions of the effective mean generation time  $\Lambda_{\text{eff},(\alpha,k)}$  and the effective delayed fraction according to Eqs. (2.103) and (2.104) respectively read

$$\beta_{\text{eff},(\alpha,k)}^j = \frac{\langle \varphi_{(\alpha,k)}^\dagger, \frac{\lambda_d^j}{4\pi} \mathcal{F}_d^j \varphi_{(\alpha,k)} \rangle}{\langle \varphi_{(\alpha,k)}^\dagger, \mathcal{F} \varphi_{(\alpha,k)} \rangle}, \quad (4.44)$$

$$\Lambda_{\text{eff},(\alpha,k)} = \frac{\langle \varphi_{(\alpha,k)}^\dagger, \frac{1}{v} \varphi_{(\alpha,k)} \rangle}{\langle \varphi_{(\alpha,k)}^\dagger, \mathcal{F} \varphi_{(\alpha,k)} \rangle}. \quad (4.45)$$

In order to assess the criticality level of the system we can resort to Eqs. (2.106) and (2.109) for the "static" reactivity  $\rho_k$  and the "dynamic" reactivity  $\rho_\alpha$  [28, 147, 72, 4, 55]

$$\rho_k = \frac{k_0 - 1}{k_0}, \quad (4.46)$$

$$\rho_\alpha = \alpha_0 \Lambda_{\text{eff},\alpha} + \sum_j \frac{\alpha_0 \beta_{\text{eff},\alpha}^j}{\alpha_0 + \lambda_j}. \quad (4.47)$$

The static reactivity  $\rho_k$  depends only by the fundamental eigenvalue  $k_0$ , whereas the dynamic reactivity  $\rho_\alpha$  requires the computation of  $\Lambda_{\text{eff},\alpha}$  and  $\beta_{\text{eff},\alpha}^j$  in addition to the fundamental eigenvalue  $\alpha_0$ . As discussed in Sections 4.3 and 4.5, the IFP method and the G-IFP method allow the computation of the bilinear forms of the kind  $\langle \varphi_k^\dagger, A \varphi_k \rangle$  and  $\langle \varphi_\alpha^\dagger, A \varphi_\alpha \rangle$  respectively, given a generic operator  $A$ . Both  $k$  and  $\alpha$  weighted effective kinetics parameters have been estimated by resorting the methods implemented in the development version of TRIPOLI-4<sup>®</sup> [150].

From Eqs. (4.21) and (4.22), we explicitly express the bilinear forms required in order to estimate the  $k$ -weighted kinetics parameters as follows

$$\langle \varphi_k^\dagger, \frac{1}{v} \varphi_k \rangle = \sum_i (\pi) t_i, \quad (4.48)$$

$$\langle \varphi_k^\dagger, \mathcal{F} \varphi_k \rangle = k \sum_i (\pi) i, \quad (4.49)$$

$$\langle \varphi_k^\dagger, \mathcal{F}_d^j \varphi_k \rangle = k \sum_i (\pi_{d,j}) i, \quad (4.50)$$

where  $\pi_i$  represents the importance of the ancestor  $i$  and  $t_i$  its corresponding lifetime. A factor  $k$  is applied for the estimation of the fission operators in order to normalize the ancestor contributions during generations.

In a similar way, the  $\alpha$ -weighted kinetics parameters can be assessed by using the following estimators:

$$\langle \varphi_\alpha^\dagger, \frac{1}{v} \varphi_\alpha \rangle = \sum_i (\pi) t_i, \quad (4.51)$$

$$\langle \varphi_\alpha^\dagger, \mathcal{F} \varphi_\alpha \rangle = \sum_i (\pi)_i, \quad (4.52)$$

$$\langle \varphi_\alpha^\dagger, \mathcal{F}_d^j \varphi_\alpha \rangle = \frac{\lambda_j + \alpha}{\lambda_j} \sum_i (\pi_{d,j})_i, \quad (4.53)$$

recalling that the  $\alpha$ -copy operator is not counted for the ancestors scoring during the generations. We remark that a weight multiplier equal to  $(\lambda_j + \alpha)/\lambda_j$  is applied for the delayed fission operator.

The effective kinetics parameters estimated for Problem I are shown in Tabs. 4.9 and 4.10 for the sub-critical configuration. Values for  $\beta_{\text{eff}}$  weighted according to the  $k$ -formulation are statistically compatible to those weighted according to the  $\alpha$ -formulation. Simulation parameters for the evaluation of these parameters are the same as those shown in Tabs. 4.3, estimated by considering 20 latent generations. A slight difference is observed in the values of  $\Lambda_{\text{eff}}$ , whereas a relatively larger difference is observed between dynamic and static reactivity. The latter deviation may be justified by the fact that the dynamic reactivity  $\rho_\alpha$  depends on the eigenfunction distributions integrated for the estimation of  $\Lambda_{\text{eff},\alpha}$  and  $\beta_{\text{eff},\alpha}$  (Eq. (2.109)), whereas the static reactivity  $\rho_k$  only depends on the fundamental eigenvalue  $k_0$ . Significant differences are observed for both reactivity and effective mean generation time values when only prompt neutrons are considered. In this case, the difference on the adjoint eigenmodes from Fig. 4.4 (left) plays a significant role in weighting the kinetics parameters.

Parameters	$\langle \varphi_\alpha^\dagger, \bullet \rangle$	$\langle \varphi_k^\dagger, \bullet \rangle$
$\rho$ [pcm]	$-669 \pm 5$	$-608 \pm 6$
$\Lambda_{\text{eff}}$ [ns]	$5.773 \pm 0.003$	$5.728 \pm 0.002$
$\beta_{\text{eff}}$ [pcm]	$644 \pm 2$	$645 \pm 2$
$\beta_{\text{eff}}^1$ [pcm]	$23.5 \pm 0.1$	$23.5 \pm 0.4$
$\beta_{\text{eff}}^2$ [pcm]	$90 \pm 0.7$	$90.9 \pm 0.8$
$\beta_{\text{eff}}^3$ [pcm]	$66.8 \pm 0.6$	$66.4 \pm 0.7$
$\beta_{\text{eff}}^4$ [pcm]	$128.7 \pm 0.9$	$128 \pm 1$
$\beta_{\text{eff}}^5$ [pcm]	$198 \pm 1$	$200 \pm 1$
$\beta_{\text{eff}}^6$ [pcm]	$63.2 \pm 0.7$	$63.1 \pm 0.7$
$\beta_{\text{eff}}^7$ [pcm]	$58 \pm 0.7$	$56.2 \pm 0.6$
$\beta_{\text{eff}}^8$ [pcm]	$15.9 \pm 0.4$	$16.6 \pm 0.3$

Table 4.9: Effective kinetics parameters of Problem I, sub-critical configuration with delayed contribution.

Parameters	$\langle \varphi_\alpha^\dagger, \bullet \rangle$	$\langle \varphi_k^\dagger, \bullet \rangle$
$\rho$ [pcm]	$-6289 \pm 50$	$-1266 \pm 4$
$\Lambda_{\text{eff}}$ [ns]	$45.6 \pm 0.3$	$5.728 \pm 0.002$

Table 4.10: Effective kinetics parameters of Problem I, sub-critical configuration without delayed contribution.

The results obtained from the super-critical configuration of the same problem are shown in Tabs. 4.11 and 4.12. The system including delayed neutrons is super-critical and all kinetics parameters are statistically compatible. Conversely, a non negligible discrepancy is still noticeable between static and dynamic reactivities for the configuration without delayed contributions. Overall, the differences between direct and adjoint eigenmodes according to the  $k$ - and the  $\alpha$ -eigenvalue formulations are observed as discrepancies of similar amplitudes in the effective kinetics parameters.

#### 4.6. ANALYSIS OF GODIVA-LIKE BENCHMARK CONFIGURATIONS

Parameters	$\langle \varphi_a^\dagger, \bullet \rangle$	$\langle \varphi_k^\dagger, \bullet \rangle$
$\rho$ [pcm]	$409 \pm 9$	$388 \pm 6$
$\Lambda_{\text{eff}}$ [ns]	$5.654 \pm 0.002$	$5.675 \pm 0.002$
$\beta_{\text{eff}}$ [pcm]	$643 \pm 5$	$644 \pm 2$
$\beta_{\text{eff}}^1$ [pcm]	$20 \pm 2$	$23.8 \pm 0.4$
$\beta_{\text{eff}}^2$ [pcm]	$93 \pm 3$	$91.1 \pm 0.8$
$\beta_{\text{eff}}^3$ [pcm]	$68 \pm 2$	$65.5 \pm 0.7$
$\beta_{\text{eff}}^4$ [pcm]	$125 \pm 2$	$128.3 \pm 0.9$
$\beta_{\text{eff}}^5$ [pcm]	$201 \pm 2$	$200 \pm 1$
$\beta_{\text{eff}}^6$ [pcm]	$61.4 \pm 0.8$	$60.9 \pm 0.7$
$\beta_{\text{eff}}^7$ [pcm]	$57.6 \pm 0.7$	$57 \pm 0.6$
$\beta_{\text{eff}}^8$ [pcm]	$17.1 \pm 0.4$	$16.9 \pm 0.3$

Table 4.11: Effective kinetics parameters of Problem I, super-critical configuration with delayed contribution.

Parameters	$\langle \varphi_a^\dagger, \bullet \rangle$	$\langle \varphi_k^\dagger, \bullet \rangle$
$\rho$ [pcm]	$-247.2 \pm 0.4$	$-261 \pm 6$
$\Lambda_{\text{eff}}$ [ns]	$5.698 \pm 0.002$	$5.677 \pm 0.002$

Table 4.12: Effective kinetics parameters of Problem I, super-critical configuration without delayed contribution.

For Problem III, the effective kinetics parameters computed for the sub-critical configuration are shown in Tabs. 4.13 and 4.14. The results from the simulation including delayed contributions shows minimal discrepancies for the values of  $\Lambda_{\text{eff}}$  and  $\beta_{\text{eff}}$ , whereas a clear difference is found between  $\rho_k$  and  $\rho_\alpha$ . Conversely, the differences in the eigenmode distributions from Figs. 4.7 and 4.8 strongly influence the parameters obtained from the simulation without delayed neutrons.

Parameters	$\langle \varphi_\alpha^\dagger, \bullet \rangle$	$\langle \varphi_k^\dagger, \bullet \rangle$
$\rho$ [pcm]	$-582 \pm 10$	$-735 \pm 20$
$\Lambda_{\text{eff}}$ [ $\mu\text{s}$ ]	$12.62 \pm 0.05$	$12.71 \pm 0.05$
$\beta_{\text{eff}}$ [pcm]	$704 \pm 7$	$706 \pm 7$
$\beta_{\text{eff}}^1$ [pcm]	$25.4 \pm 0.4$	$24 \pm 1$
$\beta_{\text{eff}}^2$ [pcm]	$97 \pm 2$	$97 \pm 2$
$\beta_{\text{eff}}^3$ [pcm]	$74 \pm 3$	$72 \pm 2$
$\beta_{\text{eff}}^4$ [pcm]	$134 \pm 3$	$144 \pm 3$
$\beta_{\text{eff}}^5$ [pcm]	$223 \pm 5$	$223 \pm 4$
$\beta_{\text{eff}}^6$ [pcm]	$70 \pm 2$	$65 \pm 2$
$\beta_{\text{eff}}^7$ [pcm]	$63 \pm 2$	$63 \pm 2$
$\beta_{\text{eff}}^8$ [pcm]	$19 \pm 1$	$18 \pm 1$

Table 4.13: Effective kinetics parameters of Problem III, sub-critical configuration with delayed contribution.

Parameters	$\langle \varphi_\alpha^\dagger, \bullet \rangle$	$\langle \varphi_k^\dagger, \bullet \rangle$
$\rho$ [pcm]	$-1658 \pm 7$	$-1437 \pm 20$
$\Lambda_{\text{eff}}$ [ $\mu\text{s}$ ]	$16.88 \pm 0.06$	$12.79 \pm 0.05$

Table 4.14: Effective kinetics parameters of Problem III, sub-critical configuration without delayed contribution.

The parameters describing the super-critical configuration of Problem III are shown in Tabs. 4.15 and 4.16. The presence of delayed neutrons and the proximity to the critical state leads to statistically compatible values of the kinetics parameters. The results obtained from the simulation including only prompt neutrons show minimal differences for  $\Lambda_{\text{eff}}$  values, whereas a more significant discrepancy is found between static and dynamic reactivity.

In conclusion, we have investigated the effective kinetics parameters related to the Godiva-like benchmark problems. As expected, the differences between  $k$ - and  $\alpha$ -eigenmode distributions are mirrored in the discrepancies between the corresponding kinetics parameters. Overall, the reactivity  $\rho$  is more affected by the choice of the eigenvalue formulation than the other kinetics parameters  $\Lambda_{\text{eff}}$  and  $\beta_{\text{eff}}$ .

The kinetics parameters and the associated reactivities are crucial for the control and the safety of nuclear reactors. A comparison with existing measurements (which typically involve neutron noise detection combined with the application of a fitting procedure based on a formulation of the in-hour equation) might help in discriminating whether the  $k$  or  $\alpha$  formulations have a prominent advantage over each other for the interpretation of these parameters.

Parameters	$\langle \varphi_{\alpha}^{\dagger}, \bullet \rangle$	$\langle \varphi_k^{\dagger}, \bullet \rangle$
$\rho$ [pcm]	$478 \pm 40$	$496 \pm 20$
$\Lambda_{\text{eff}}$ [ $\mu\text{s}$ ]	$12.16 \pm 0.04$	$12.21 \pm 0.04$
$\beta_{\text{eff}}$ [pcm]	$681 \pm 20$	$711 \pm 7$
$\beta_{\text{eff}}^1$ [pcm]	$22 \pm 7$	$28 \pm 1$
$\beta_{\text{eff}}^2$ [pcm]	$92 \pm 10$	$97 \pm 2$
$\beta_{\text{eff}}^3$ [pcm]	$77 \pm 8$	$73 \pm 2$
$\beta_{\text{eff}}^4$ [pcm]	$132 \pm 6$	$138 \pm 3$
$\beta_{\text{eff}}^5$ [pcm]	$215 \pm 6$	$232 \pm 4$
$\beta_{\text{eff}}^6$ [pcm]	$65 \pm 3$	$62 \pm 2$
$\beta_{\text{eff}}^7$ [pcm]	$61 \pm 2$	$62 \pm 2$
$\beta_{\text{eff}}^8$ [pcm]	$18 \pm 1$	$20 \pm 1$

Table 4.15: Effective kinetics parameters of Problem III, super-critical configuration with delayed contribution.

Parameters	$\langle \varphi_{\alpha}^{\dagger}, \bullet \rangle$	$\langle \varphi_k^{\dagger}, \bullet \rangle$
$\rho$ [pcm]	$-252 \pm 1$	$-213 \pm 20$
$\Lambda_{\text{eff}}$ [ $\mu\text{s}$ ]	$12.93 \pm 0.05$	$12.29 \pm 0.05$

Table 4.16: Effective kinetics parameters of Problem III, super-critical configuration without delayed contribution.

## 4.7 An application to the CROCUS reactor

In order to take into account a more realistic configuration, and ascertain whether the conclusions reached in the previous section hold true for larger reactor cores, in this section we will consider two configurations of the CROCUS critical facility, operated at the Ecole Polytechnique Fédérale de Lausanne (EPFL), Switzerland. Thanks to its detailed description and careful measurements, the CROCUS core has been selected as an international benchmark for reactivity, kinetics parameters and reactor period calculations [116, 119].

CROCUS is an open-tank type zero-power reactor, characterized by two fuel regions and moderated by light water. A radial section of this reactor is shown in Fig. 4.9: the outer fuel rods (green) are composed of metallic uranium at 0.947 wt%  $^{235}\text{U}/\text{U}$  with 2.917cm pitch, whereas the inner fuel rods (orange) are composed by  $\text{UO}_2$  at 1.806 wt%  $^{235}\text{U}/\text{U}$  with 1.837cm pitch. Details on the number and positions of these fuel rods are given in reference [119]. The core can be modeled as a cylinder with a diameter of about 60 cm and a height of 100 cm. The critical state of the system is controlled by the level of light water filling the reactor from the bottom cadmium plate. The critical configuration is achieved at a water level of 91.66 cm.

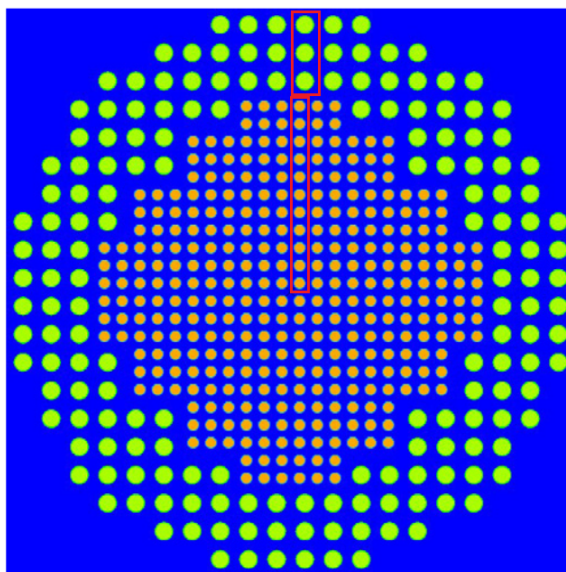


Figure 4.9: Radial section of the CROCUS reactor obtained with TRIPOLI-4<sup>®</sup>. The inner fuel rods (UO<sub>2</sub>, orange) and the outer fuel rods (metallic U, green) are moderated by light water (blue). The red regions denotes the 14 fuel rod positions defined for the flux distribution [119].

A preliminary comparison for this facility between fundamental  $\alpha$ -eigenpairs and time dependent calculations has been carried out in [112]. Moreover, the kinetics parameters of the CROCUS core for the  $k$ -eigenvalue formulation has been previously computed in [171] and the associated reactivity was examined in [172]. In the following, we will investigate the behaviour (and possible discrepancies) of the fundamental forward and adjoint modes of the  $k$  and  $\alpha$  formulations for this core, and we will then examine the impact of their respective shapes on the kinetics parameters and on the reactivity. For this purpose, we will consider two sub-critical configurations of the reactor, both obtained by lowering the water level. Configuration H1 is characterized by a water level equal to 90.8 cm, which induces a slightly sub-critical state. Configuration H2 is characterized by a water level equal to 80 cm, which corresponds to a more sub-critical condition. The fundamental eigenmodes will be computed by using TRIPOLI-4<sup>®</sup> over 111 energy meshes and along 14 fuel pin positions, from the core center to the outer region, denoted by the red rectangular regions in Fig. 4.9. The number of cycles and the particles per cycle simulated for these configurations are listed in Tab. 4.17 for the forward simulations and in Tab. 4.18 for the adjoint simulations.

configuration	active cycles	inactive cycles	particles
H1	$5 \times 10^3$	$5 \times 10^3$	$2 \times 10^4$
H2	$5 \times 10^3$	$5 \times 10^3$	$2 \times 10^4$

Table 4.17: Numerical simulation parameters for CROCUS configurations during forward simulations.

configuration	particles	latent generations
H1	$2 \times 10^7$	20
H2	$2 \times 10^7$	20

Table 4.18: Numerical simulation parameters for CROCUS configurations during adjoint simulations.

### 4.7.1 Analysis of the fundamental eigenmodes

The fundamental eigenvalues  $k_0$  and  $\alpha_0$  computed in the corresponding simulations for H1 and H2 configurations of the CROCUS reactor (with and without precursor contributions) are given in Tabs. 4.19 and 4.20, respectively.

As expected, the computed values show a slight sub-critical level for configuration H1 and a larger sub-critical state for configuration H2. According to the results obtained from the  $k$ -eigenvalue formulation, the criticality level of both configurations decreases by approximately 780 pcm when delayed neutrons are neglected. Concerning the  $\alpha$ -eigenvalue formulation, the absolute value of  $\alpha_0$  is smaller than  $1.2 \times 10^{-2} \text{ s}^{-1}$  by including delayed neutrons, whereas the absolute value of this eigenvalue is larger than  $10^2 \text{ s}^{-1}$  for the simulation without precursor contributions.

configuration	$k_0[-]$ , with delayed contributions	$k_0[-]$ , prompt fission only
H1	$0.9995 \pm 1 \times 10^{-4}$	$0.9918 \pm 1 \times 10^{-4}$
H2	$0.9919 \pm 1 \times 10^{-4}$	$0.9839 \pm 1 \times 10^{-4}$

Table 4.19: Fundamental eigenvalues  $k_0$  for H1 and H2 configurations of the CROCUS reactor.

configuration	$\alpha_0[\text{s}^{-1}]$ , including precursors	$\alpha_0[\text{s}^{-1}]$ , without precursors
H1	$-5.97 \times 10^{-3} \pm 2 \times 10^{-5}$	$-1.711 \times 10^2 \pm 2 \times 10^{-1}$
H2	$-1.1994 \times 10^{-2} \pm 3 \times 10^{-6}$	$-3.336 \times 10^2 \pm 2 \times 10^{-1}$

Table 4.20: Fundamental eigenvalues  $\alpha_0$  for H1 and H2 configurations of the CROCUS reactor.

The shapes of direct eigenmodes  $\varphi_{k_0}$  and  $\varphi_{\alpha_0}$  (with and without delayed neutron contributions) are shown as a function of energy (Fig. 4.10) and of the fuel pin position (Fig. 4.11) for H1 (left) and H2 (right) configurations. The adjoint eigenmodes are shown as a function of the fuel pin position in Fig.4.12. All curves have been normalized. No major differences can be easily spotted in these figures, so that we have computed the ratios  $\varphi_{\alpha_0}/\varphi_{k_0}$  and  $\varphi_{\alpha_0}^\dagger/\varphi_{k_0}^\dagger$  in order to investigate possible discrepancies.

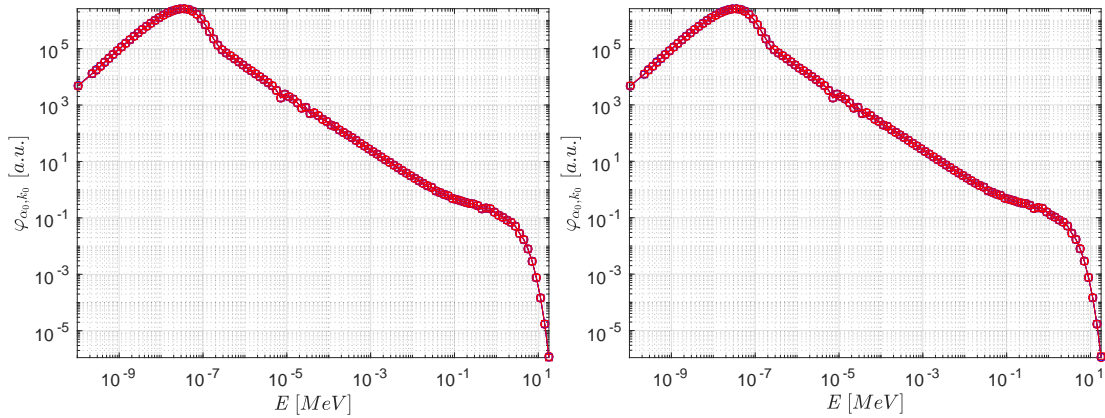


Figure 4.10: Direct fundamental eigenmodes of the CROCUS reactor as a function of the energy, H1 (left) and H2 (right) configurations according to the  $\alpha$ - (blue) and  $k$ - (red) eigenvalue formulations, with (squares) and without (circles) precursor contributions.

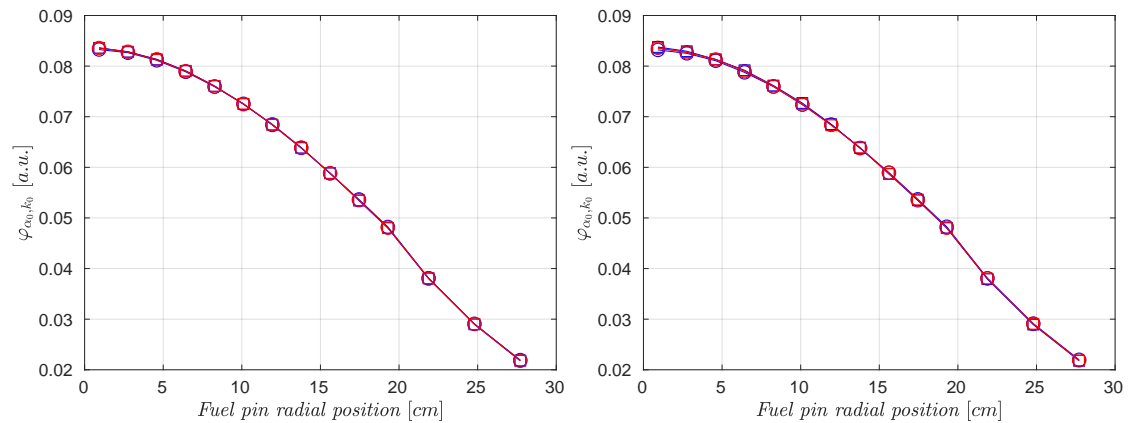


Figure 4.11: Direct fundamental eigenmodes of the CROCUS reactor as a function of the fuel pin positions, H1 (left) and H2 (right) configurations according to the  $\alpha$ - (blue) and  $k$ - (red) eigenvalue formulations, with (squares) and without (circles) precursor contributions.

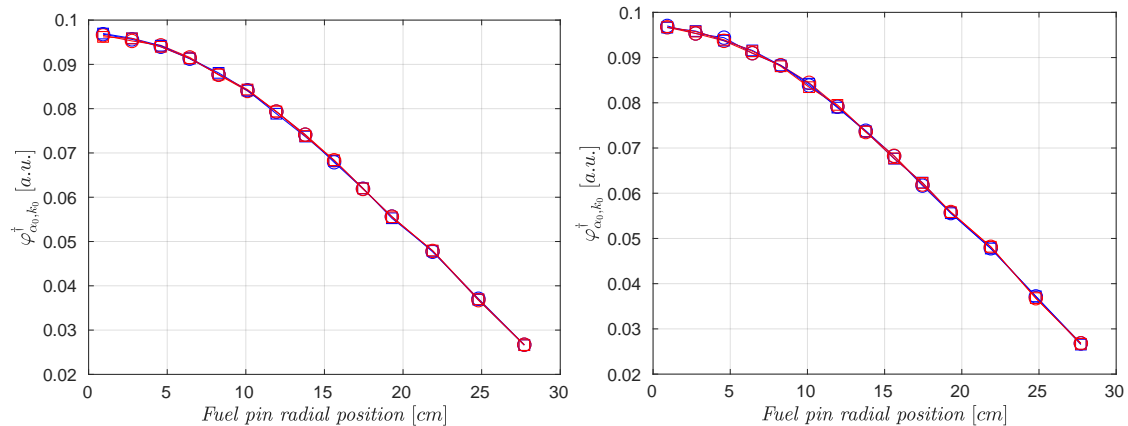


Figure 4.12: Adjoint fundamental eigenmodes of the CROCUS reactor as a function of the fuel pin positions, H1 (left) and H2 (right) configurations according to the  $\alpha$ - (blue) and  $k$ - (red) eigenvalue formulations, with (squares) and without (circles) precursor contributions.

Figure 4.13 shows the ratios of the direct fundamental eigenmodes in the energy domain. The results obtained for configuration H1 (left) are similar to those previously discussed for the Problem III of the benchmark configurations. When delayed neutrons are considered, no differences are visible between  $\varphi_{k_0}(E)$  and  $\varphi_{\alpha_0}(E)$ . This is mainly due to the system reactivity being close to critical (about -50 pcm, as shown in Tab. 4.19): the  $k$  and  $\alpha$  formulation are supposed to be very close to each other in this regime. If precursors are disregarded in the simulation, for this configuration the fundamental  $k$ -eigenmode is slightly different from the fundamental  $\alpha$ -eigenmode: a shift towards high energy values is observed. The same behaviour is found for the H2 configuration (right), characterized by a larger effect due to a larger sub-critical level with respect to the previous case (about -1600 pcm, as shown in Tab. 4.19). The effect of precursors is clearly visible for this configuration: the  $k$ -eigenmode displays significant discrepancies with respect to the  $\alpha$ -eigenmode towards high energies for this sub-critical system, but  $\varphi_{\alpha_0}(E) > \varphi_{k_0}(E)$  only for  $E > 0.6$  MeV, which is again similar to the findings of the Problem III configuration. Precursor contributions minimize the discrepancies between the two eigenvalue formulations and the delayed spectra move the threshold for  $\varphi_{\alpha_0}(E) > \varphi_{k_0}(E)$  at higher energy.

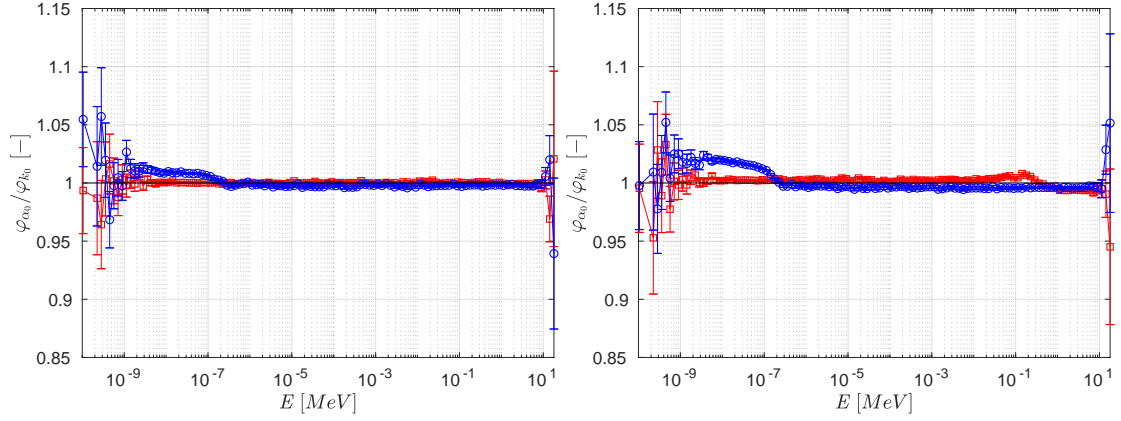


Figure 4.13: Ratios  $\varphi_{\alpha_0}/\varphi_{k_0}$  of the CROCUS reactor as a function of the energy variable, H1 (left) and H2 (right) configurations with (red squares) and without (blue circles) precursor contributions.

For the sake of completeness, we show the ratios of these eigenfunctions as a function of the fuel pin positions in Fig. 4.14 for the direct formulation and in Fig. 4.15 for the adjoint formulation. Overall, the behaviour of these two eigenmodes is similar: within uncertainty limits, no major differences can be detected with respect to the spatial coordinate.

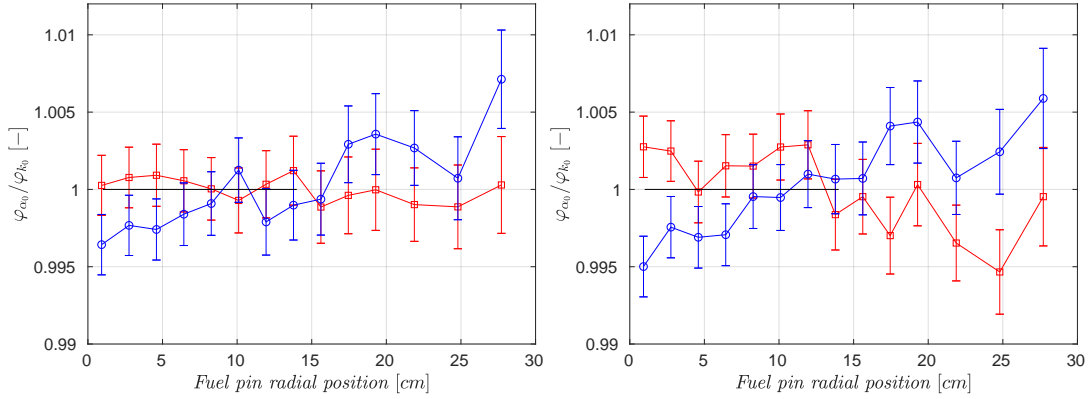


Figure 4.14: Ratios  $\varphi_{\alpha_0}/\varphi_{k_0}$  of the CROCUS reactor as a function of the fuel pin positions, H1 (left) and H2 (right) configurations with (red squares) and without (blue circles) precursor contributions.

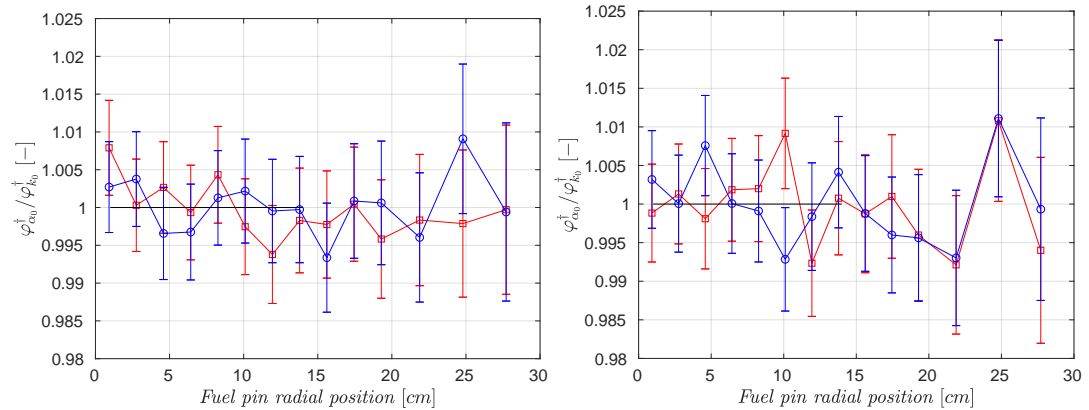


Figure 4.15: Ratios  $\varphi_{\alpha_0}^\dagger/\varphi_{k_0}^\dagger$  of the CROCUS reactor as a function of the fuel pin positions, H1 (left) and H2 (right) configurations with (red squares) and without (blue circles) precursor contributions.

## 4.7.2 Analysis of the effective kinetics parameters

The effective kinetics parameters have been computed for the two CROCUS configurations by using the newly developed IFP and G-IFP of TRIPOLI-4<sup>®</sup>. Table 4.21 shows the parameters computed for the H1 configuration with precursor contributions: the results obtained for both eigenvalue formulations are statistically compatible. As expected, the proximity to the critical level of this configuration implies very close values of the  $k$ -weighted and  $\alpha$ -weighted effective kinetics parameters. Similar results are found in Tab. 4.22 by neglecting precursor contributions.

The effective kinetics parameters of the H2 configuration with precursor contributions are shown in Tab. 4.23. A discrepancy is observed between the static and the dynamic reactivity (computed as Eqs. (2.106) and (2.109) respectively), whereas the average values of all the other kinetics parameters are within one standard deviation for the two eigenvalue formulations. Table 4.24 shows the parameters obtained when neglecting precursor contributions: no significant discrepancies are observed in the computed values.

An application related to the effective kinetics parameters is the estimation of the reactor period and the sub-criticality level of the system. Both quantities can also be measured during experiments by the pulsed neutron source method [121] and reactor noise analysis methods [108, 167, 171]. The choice of the optimal adjoint weighting function ( $\varphi_\alpha^\dagger$  or  $\varphi_k^\dagger$ ) in order to compare the results computed from numerical simulations to those obtained from measurements depend on the procedure and the techniques adopted during the experiment. Moreover, mixing  $\alpha$  and  $k$  weighted kinetics parameters can be considered for the estimation of  $\alpha$  and  $\rho$  [40].

Parameters	$\langle \varphi_\alpha^\dagger, \bullet \rangle$	$\langle \varphi_k^\dagger, \bullet \rangle$
$\rho$ [pcm]	$-73 \pm 2$	$-50 \pm 10$
$\Lambda_{\text{eff}}$ [ $\mu\text{s}$ ]	$47.69 \pm 0.03$	$47.69 \pm 0.03$
$\beta_{\text{eff}}$ [pcm]	$762 \pm 4$	$760 \pm 5$
$\beta_{\text{eff}}^1$ [pcm]	$22.3 \pm 0.6$	$23.4 \pm 0.8$
$\beta_{\text{eff}}^2$ [pcm]	$109 \pm 2$	$113 \pm 2$
$\beta_{\text{eff}}^3$ [pcm]	$66 \pm 1$	$62 \pm 1$
$\beta_{\text{eff}}^4$ [pcm]	$141 \pm 2$	$141 \pm 2$
$\beta_{\text{eff}}^5$ [pcm]	$249 \pm 3$	$245 \pm 3$
$\beta_{\text{eff}}^6$ [pcm]	$81 \pm 2$	$83 \pm 2$
$\beta_{\text{eff}}^7$ [pcm]	$68 \pm 1$	$67 \pm 1$
$\beta_{\text{eff}}^8$ [pcm]	$26.5 \pm 0.8$	$26 \pm 0.8$

Table 4.21: Effective kinetics parameters for the H1 configuration with delayed contribution.

Parameters	$\langle \varphi_\alpha^\dagger, \bullet \rangle$	$\langle \varphi_k^\dagger, \bullet \rangle$
$\rho$ [pcm]	$-824 \pm 1$	$-827 \pm 10$
$\Lambda_{\text{eff}}$ [ $\mu\text{s}$ ]	$48.15 \pm 0.03$	$48.11 \pm 0.03$

Table 4.22: Effective kinetics parameters for the H1 configuration without delayed contribution.

Parameters	$\langle \varphi_{\alpha}^{\dagger}, \bullet \rangle$	$\langle \varphi_k^{\dagger}, \bullet \rangle$
$\rho$ [pcm]	$-723 \pm 10$	$-822 \pm 10$
$\Lambda_{\text{eff}}$ [ $\mu\text{s}$ ]	$48.06 \pm 0.03$	$48.01 \pm 0.03$
$\beta_{\text{eff}}$ [pcm]	$763 \pm 5$	$766 \pm 5$
$\beta_{\text{eff}}^1$ [pcm]	$23.2 \pm 0.2$	$22.2 \pm 0.7$
$\beta_{\text{eff}}^2$ [pcm]	$113 \pm 2$	$113 \pm 2$
$\beta_{\text{eff}}^3$ [pcm]	$64 \pm 1$	$66 \pm 1$
$\beta_{\text{eff}}^4$ [pcm]	$140 \pm 2$	$143 \pm 2$
$\beta_{\text{eff}}^5$ [pcm]	$247 \pm 3$	$251 \pm 3$
$\beta_{\text{eff}}^6$ [pcm]	$82 \pm 2$	$82 \pm 2$
$\beta_{\text{eff}}^7$ [pcm]	$68 \pm 2$	$66 \pm 1$
$\beta_{\text{eff}}^8$ [pcm]	$24.8 \pm 0.9$	$24 \pm 0.8$

Table 4.23: Effective kinetics parameters for the H2 configuration with delayed contribution.

Parameters	$\langle \varphi_{\alpha}^{\dagger}, \bullet \rangle$	$\langle \varphi_k^{\dagger}, \bullet \rangle$
$\rho$ [pcm]	$-1621 \pm 2$	$-1638 \pm 10$
$\Lambda_{\text{eff}}$ [ $\mu\text{s}$ ]	$48.59 \pm 0.03$	$48.39 \pm 0.03$

Table 4.24: Effective kinetics parameters for the H2 configuration without delayed contribution.

## 4.8 Conclusions

Inspired by the analysis originally proposed by D. E. Cullen [28], we have applied Monte Carlo methods for the estimation of  $k$  and  $\alpha$  fundamental eigenmodes. We have extended the findings discussed in [28] in two directions, by addressing the evaluation of the fundamental adjoint eigenmodes and the influence of precursor contributions. Additional information regarding the discrepancies between the two eigenvalue formulations was found by assessing the effective kinetics parameters weighted by the  $k$ - or by the  $\alpha$ -eigenmodes. We have focused our attention on the analysis of two Godiva-like benchmark configurations and the CROCUS reactor. In this way, we have explored thermal and fast spectra, homogeneous and heterogeneous media, simplified and realistic systems.

Significant, albeit globally small, differences have been detected, as expected on physical grounds based on previous investigations. In particular, we have recovered the same behaviour previously analyzed [28] in the energy domain for the distribution of the direct fundamental eigenfunctions  $\varphi_{k_0}$  and  $\varphi_{\alpha_0}$ , and we have found similar discrepancies in the corresponding adjoint fundamental distributions  $\varphi_{k_0}^{\dagger}$  and  $\varphi_{\alpha_0}^{\dagger}$ . Moreover, the presence of precursors has a non-trivial influence on the eigenfunctions, and this impact has been carefully examined for each configuration. Overall, the presence of precursors reduces the discrepancies between the two eigenmodes.

As a general remark, based on the configurations investigated here, it seems that the discrepancies between the  $k$ - and  $\alpha$ -eigenfunctions are enhanced by the presence of strong spatial heterogeneities, such as those occurring in a core surrounded by a thick moderator/reflector. In this case, the system will be characterized by multiple time scales (as shown in [28]), related to the different times required by the neutrons to explore the multiplying and the diffusing region. Then, it appears that the  $\alpha$ -eigenvalue formulation is more sensitive to these different time scales than the  $k$ -eigenvalue formulation, which is coherent with  $\alpha$  being related to the time behaviour of the system and  $k$  being related to the fission generation behavior. These discrepancies on the eigenmodes are mirrored in the kinetics parameters and on the reactivity. In this respect, it is interesting to remark that the CROCUS reactor can be basically considered as a homogeneous system, with minimal discrepancies between the  $\alpha$  and  $k$  formulations.



## Chapter 5

# A new matrix-filling Monte Carlo method for $\alpha$ -spectral analysis

In the previous chapter, we have seen that Monte Carlo methods can be successfully applied to determining the forward and adjoint fundamental modes and the associated eigenvalues of both  $k$ - and  $\alpha$ -eigenvalue problems without approximations, which paves the way towards reference solutions characterizing the asymptotic behaviour of nuclear systems. In view of a full spectral analysis, the fundamental modes alone might prove insufficient so as to characterize the systems under analysis: for instance, the shape of the first excited eigenmode can provide valuable information concerning the behaviour of a perturbation introduced in the core, and the eigenvalue gap (e.g., the dominance ratio  $DR = k_1/k_0$ ) would convey the intensity of such perturbation with respect to the fundamental mode [12, 13, 14, 161, 52, 154]. A natural question therefore arises whether the Monte Carlo methods described in Chapter 4 can be extended and generalized to higher eigenmodes and eigenvalues.

For the case of  $k$ -eigenvalue problems, extensive work has been carried out in recent years in order to establish modified power-iteration algorithms capable of extracting the first excited eigenmode  $\varphi_{k_1}$  and the associated eigenvalue  $k_1$ , and possibly also higher eigenpairs, without introducing approximations [136, 137]. Basically, all these methods are built upon the key idea that the eigenvalue formulation can be made *local* in the phase-space, so that a system of coupled eigenvalue equations emerges, each defined over a portion of the phase space: by imposing suitable constraints on the available degrees of freedom offered by this system of equations, one may force the solution of the power iteration to converge to several eigenpairs, namely,  $(k_0, \varphi_{k_0})$ ,  $(k_1, \varphi_{k_1})$ , and so on.

In this respect, we recall the strategy from a seminal paper by Booth [12]. Let us recast the  $k$ -eigenvalue problem from Eq. (2.65) and the operator  $\mathcal{K}$  from Eq. (2.66) as

$$k\varphi_k = [\mathcal{M}^{-1}\mathcal{F}]\varphi_k = \mathcal{K}\varphi_k. \quad (5.1)$$

Suppose that the initial guess for the power iteration is written as  $\varphi = \sum_m w_{k_m} \varphi_{k_m}$ , where  $\varphi_{k_m}$  are the eigenfunction of order  $m$ , with  $m \geq 0$ , and  $w_{k_m}$  are the expansion coefficients. Let us assume that the eigenvalues are ordered such that  $k_0 > |k_1| \geq |k_2| \geq \dots$ . If  $w_{k_0} \neq 0$ , by successively applying the  $\mathcal{K}$  operator the power iteration yields

$$\lim_{n \rightarrow \infty} \frac{1}{k_0^n} \mathcal{K}^n \varphi = \varphi_{k_0}, \quad (5.2)$$

where  $n$  is the iteration index, and we obtain the fundamental mode. However, if we can set  $w_{k_0} = 0$ , then we will have

$$\lim_{n \rightarrow \infty} \frac{1}{k_1^n} \mathcal{K}^n \varphi = \varphi_{k_1}, \quad (5.3)$$

i.e., the power iteration will converge to the first excited mode, provided that we can remove the fundamental mode. In order to ensure this condition, the idea is to solve the power iteration separately on two regions  $R^+$  and

$R^-$  of the phase-space:

$$k_1 = \frac{\langle \mathcal{K}\varphi_{k_1} \rangle_{R^+}}{\langle \varphi_{k_1} \rangle_{R^+}} = \frac{\langle \mathcal{K}\varphi_{k_1} \rangle_{R^-}}{\langle \varphi_{k_1} \rangle_{R^-}} \quad (5.4)$$

since the eigenvalue equation (5.1) holds on every subset of the viable domain [34, 114]. The two subsets  $R^+$  and  $R^-$  are not known a priori and must be progressively refined as the calculation proceeds. We can then consider two different factors,  $k_1^+$  and  $k_1^-$ , defined as

$$k_1^+ = \frac{\langle \mathcal{K}\varphi_{k_1} \rangle_{R^+}}{\langle \varphi_{k_1} \rangle_{R^+}}, \quad (5.5)$$

and

$$k_1^- = \frac{\langle \mathcal{K}\varphi_{k_1} \rangle_{R^-}}{\langle \varphi_{k_1} \rangle_{R^-}}. \quad (5.6)$$

Now, if the power iteration were to be applied separately on each region, the two eigenvalue problems would still converge to the fundamental mode. In order to prevent this from happening, Booth proposes to postulate an expansion of the kind  $\varphi = w_{k_0}\varphi_{k_0} + w_{k_1}\varphi_{k_1}$  and to formally determine the conditions on the relative weight given to  $\varphi_{k_0}$  and  $\varphi_{k_1}$  in order to enforce the subtraction of  $\varphi_{k_0}$  to the solution that must converge to  $\varphi_{k_1}$  and conversely the subtraction of  $\varphi_{k_1}$  to the solution that must converge to  $\varphi_{k_0}$ . Since the first excited eigenmode is partially positive and partially negative on the phase-space, the use of subtraction methods necessarily demands the introduction of particles carrying statistical weights of alternating signs. Furthermore, in order for the proposed method to converge, particles having a negative/positive weight must annihilate particles having a positive/negative weight when meeting in the phase-space: this is called the *weight cancellation procedure* [14, 137].

Booth's technique is capable of determining the eigenpair  $(k_1, \varphi_{k_1})$  without any approximation, and as such represents an ingenious extension of the standard power iteration algorithm [12]. Several refinements of this pioneering approach have been later proposed, in particular concerning the use of more efficient or more robust (albeit approximated) methods for the weight cancellation [13, 14, 137]. Although these methods have shown a great potential for extracting higher-order eigenmodes in  $k$ -eigenvalue problems, their use in production Monte Carlo codes is still hindered by the complexity of their implementation and most importantly by the possible numerical instabilities that have been met in some applications, for which investigations are still ongoing [161].

## 5.1 Matrix-filling methods: the fission matrix approach

Actually, the idea of extracting higher harmonics in  $k$ -eigenvalue problems by Monte Carlo methods is not new, and several methods have been proposed in the literature. Among these approaches, a prominent role is played by the *fission matrix* method, whereupon a standard Monte Carlo power iteration is used in order to estimate the elements of a matrix that represents a discretized version of the operators appearing in the  $k$ -eigenvalue problem [22]. The obtained matrix can be then analyzed by classical numerical methods in order to extract the full spectrum and the associated eigenmodes: this approach is not exact, since the matrix has necessarily a finite size and thus discretization errors are introduced. Nonetheless, it offers a robust and reliable approach to the spectral analysis of  $k$ -eigenvalue problems for reactor physics applications: the fission matrix has a long history [105, 71, 53] and has been extensively investigated [152, 76, 35, 156]. An extension of this approach has also been studied in literature: the *Transient Fission Matrix method* [87, 86, 85]. Conversely to the original fission matrix method, the TFM approach preserves the temporal behaviour of the particles and distinguishes prompt neutrons from delayed neutrons at fission events. Further details related to this approach will be provided in Section 5.4 and in the Appendix A.

In the following we provide a short overview of the forward and adjoint forms of the standard fission matrix treatment for  $k$ -eigenvalue problems.

### 5.1.1 The forward formulation

Recall the  $k$ -eigenvalue problem formulation from Eq. (2.65)

$$\mathcal{M}\varphi_k(\mathbf{r}, \boldsymbol{\Omega}, E) = \frac{1}{k} \frac{\chi_f(E)}{4\pi} Q_f(\mathbf{r}), \quad (5.7)$$

where  $Q_f(\mathbf{r})$  is the fission neutron source defined as

$$Q_f(\mathbf{r}) = \int_{4\pi} d\Omega \int_0^\infty dE \bar{\nu}_f(E) \Sigma_f(\mathbf{r}, E) \varphi_k(\mathbf{r}, \Omega, E). \quad (5.8)$$

Let us now introduce the Green's function  $G(\mathbf{r}_0 \rightarrow \mathbf{r}, \Omega_0 \rightarrow \Omega, E_0 \rightarrow E)$  associated to the operator  $M$ , namely

$$MG(\mathbf{r}_0 \rightarrow \mathbf{r}, \Omega_0 \rightarrow \Omega, E_0 \rightarrow E) = \delta(\mathbf{r}_0 - \mathbf{r}) \delta(\Omega_0 - \Omega) \delta(E_0 - E), \quad (5.9)$$

which physically represents the response of the system to the injection of a pulse source.

Exploiting the linearity of the problem and the superposition principle, the direct eigenmode  $\varphi_k$  is obtained as

$$\varphi_k(\mathbf{r}, \Omega, E) = \frac{1}{k} \int_V d\mathbf{r}_0 \int_{4\pi} d\Omega_0 \int_0^\infty dE_0 \frac{\chi_f(E_0)}{4\pi} Q_f(\mathbf{r}_0) G(\mathbf{r}_0 \rightarrow \mathbf{r}, \Omega_0 \rightarrow \Omega, E_0 \rightarrow E). \quad (5.10)$$

Equation (5.10) for the eigenfunction  $\varphi_k$  is multiplied by  $\bar{\nu}_f \Sigma_f$  and integrated in energy and direction in order to express  $Q_f$  as

$$Q_f(\mathbf{r}) = \frac{1}{k} \int_V d\mathbf{r}_0 Q_f(\mathbf{r}_0) H(\mathbf{r}_0 \rightarrow \mathbf{r}), \quad (5.11)$$

where  $H(\mathbf{r}_0 \rightarrow \mathbf{r})$  is a kernel representing the Green's function averaged on energy and direction, here explicitly expressed as

$$H(\mathbf{r}_0 \rightarrow \mathbf{r}) = \int_{4\pi} d\Omega \int_0^\infty dE \int_{4\pi} d\Omega_0 \int_0^\infty dE_0 \bar{\nu}_f(E) \Sigma_f(\mathbf{r}, E) \frac{\chi(E_0)}{4\pi} G(\mathbf{r}_0 \rightarrow \mathbf{r}, \Omega_0 \rightarrow \Omega, E_0 \rightarrow E). \quad (5.12)$$

No approximations have been introduced so far in this procedure and the averaged quantities can be estimated during a Monte Carlo simulation: typically, one chooses to estimate the fission matrix elements during a regular power iteration. Then,  $N$  finite spatial regions are defined for the fission sites of neutrons of generation  $g$ ,  $V_j$ , and neutrons of generation  $g + 1$ ,  $V_i$ , in order to express the spatially discretized version of Eq. (5.11) as

$$Q_i = \frac{1}{k} \sum_{j=1}^N K_{i,j} Q_j, \quad (5.13)$$

where

$$K_{i,j} = \int_{\mathbf{r}_0 \in V_j} d\mathbf{r}_0 \int_{\mathbf{r} \in V_i} d\mathbf{r} \frac{Q_f(\mathbf{r}_0)}{Q_j} H(\mathbf{r}_0 \rightarrow \mathbf{r}), \quad (5.14)$$

and

$$Q_j = \int_{\mathbf{r}' \in V_j} d\mathbf{r}' Q_f(\mathbf{r}'). \quad (5.15)$$

From a physical point of view, the element located at position  $(i, j)$  of the  $N \times N$  matrix  $K_{i,j}$  represents the number of fission neutrons born in region  $i$  stemming from one fission neutron born in region  $j$ . The matrix  $K_{i,j}$  in Eq. (5.14) is defined as the *fission matrix*: the eigenvalue  $k$  associated to the  $n^{\text{th}}$  eigenvector with  $0 \leq n \leq N - 1$  can be obtained from it and the corresponding eigenfunction is a discretized version of the neutron source distribution  $Q_f(\mathbf{r})$  of order  $n$  solving the  $k$ -eigenvalue problem in the form

$$Q_f = \frac{1}{k} \mathcal{K} Q_f. \quad (5.16)$$

Fission matrix elements are associated to discrete spatial intervals mapping the geometrical domain of the system. It can be shown that the fundamental eigenvector and eigenvalue extracted from the fission matrix is exact, since the elements of  $K_{i,j}$  are by construction weighted on the fundamental mode obtained by the power iteration. On the contrary, higher-order eigenvectors and eigenvalues will have a bias due to the discretization of the phase-space, since they have been weighted by the fundamental mode instead of the corresponding higher-order eigenmode. This bias vanishes in the limit of an infinitely fine discretization [22] (i.e., when the matrix size goes to infinity). Moreover, fission matrix elements are estimated as scores during a Monte Carlo simulation and as such they are intrinsically affected by a statistical error. The uncertainty related to these estimators will be propagated into the

computation of the eigenpairs associated to the fission matrix, as shown in Section 5.3.1.

### 5.1.2 The backward formulation

The same procedure can be applied to the adjoint formulation of the  $k$ -eigenvalue problem [22], now defined as

$$\mathbf{M}^\dagger \varphi_k^\dagger(\mathbf{r}, \boldsymbol{\Omega}, E) = \frac{1}{k} \bar{\nu}_f(E) \Sigma_f(\mathbf{r}, E) Q_f^\dagger(\mathbf{r}), \quad (5.17)$$

where the adjoint fission neutron source  $Q_f^\dagger(\mathbf{r})$  is introduced as

$$Q_f^\dagger(\mathbf{r}) = \int_{4\pi} d\boldsymbol{\Omega} \int_0^\infty dE \frac{\chi_f(E)}{4\pi} \varphi_k^\dagger(\mathbf{r}, \boldsymbol{\Omega}, E). \quad (5.18)$$

The adjoint Green's function  $G^\dagger$  is defined as:

$$\mathcal{M}^\dagger G^\dagger(\mathbf{r}_0 \rightarrow \mathbf{r}, \boldsymbol{\Omega}_0 \rightarrow \boldsymbol{\Omega}, E_0 \rightarrow E) = \delta(\mathbf{r} - \mathbf{r}_0) \delta(\boldsymbol{\Omega} - \boldsymbol{\Omega}_0) \delta(E - E_0). \quad (5.19)$$

Similarly to the previous procedure, the adjoint eigenfunction  $\varphi_k^\dagger$  is obtained as

$$\varphi_k^\dagger(\mathbf{r}, \boldsymbol{\Omega}, E) = \frac{1}{k} \int_V d\mathbf{r}_0 \int_{4\pi} d\boldsymbol{\Omega}_0 \int_0^\infty dE_0 \bar{\nu}_f(E_0) \Sigma_f(\mathbf{r}_0, E_0) Q_f^\dagger(\mathbf{r}_0) G^\dagger(\mathbf{r}_0 \rightarrow \mathbf{r}, \boldsymbol{\Omega}_0 \rightarrow \boldsymbol{\Omega}, E_0 \rightarrow E). \quad (5.20)$$

Then, the fission spectrum  $\chi_f(E)$  is multiplied and the equation is integrated in energy and direction in order to express the adjoint fission source  $Q_f^\dagger$ , as

$$Q_f^\dagger(\mathbf{r}) = \frac{1}{k} \int_V d\mathbf{r}_0 Q_f^\dagger(\mathbf{r}_0) H^\dagger(\mathbf{r}_0 \rightarrow \mathbf{r}), \quad (5.21)$$

and the adjoint kernel  $H^\dagger(\mathbf{r}_0 \rightarrow \mathbf{r})$  for the adjoint Green's function averaged on energy and direction as

$$H^\dagger(\mathbf{r}_0 \rightarrow \mathbf{r}) = \int_{4\pi} d\boldsymbol{\Omega} \int_0^\infty dE \int_{4\pi} d\boldsymbol{\Omega}_0 \int_0^\infty dE_0 \frac{\chi_f(E)}{4\pi} \bar{\nu}_f(E_0) \Sigma_f(\mathbf{r}_0, E_0) G^\dagger(\mathbf{r}_0 \rightarrow \mathbf{r}, \boldsymbol{\Omega}_0 \rightarrow \boldsymbol{\Omega}, E_0 \rightarrow E). \quad (5.22)$$

The direct and the adjoint Green's function,  $G$  and  $G^\dagger$  respectively, are related by the reciprocity theorem

$$G^\dagger(\mathbf{r}_0 \rightarrow \mathbf{r}, \boldsymbol{\Omega}_0 \rightarrow \boldsymbol{\Omega}, E_0 \rightarrow E) = G(\mathbf{r} \rightarrow \mathbf{r}_0, \boldsymbol{\Omega} \rightarrow \boldsymbol{\Omega}_0, E \rightarrow E_0), \quad (5.23)$$

hence, also the direct and adjoint kernels,  $H$  and  $H^\dagger$  respectively, are related as

$$H^\dagger(\mathbf{r}_0 \rightarrow \mathbf{r}) = H(\mathbf{r} \rightarrow \mathbf{r}_0). \quad (5.24)$$

Exploiting this property, the adjoint fission source can be expressed via the direct kernel as follows

$$Q_f^\dagger(\mathbf{r}) = \frac{1}{k} \int_V d\mathbf{r}_0 Q_f^\dagger(\mathbf{r}_0) H(\mathbf{r} \rightarrow \mathbf{r}_0). \quad (5.25)$$

Finally, a spatial grid is considered in order to split  $N$  finite regions for the volumes  $V_j$  and  $V_i$ , introducing a discrete version of the problem as

$$Q_i^\dagger = \frac{1}{k} \sum_{j=1}^N K_{i,j}^\dagger Q_j^\dagger. \quad (5.26)$$

where  $K_{i,j}^\dagger$  is the *adjoint fission matrix* and it is defined as

$$K_{i,j}^\dagger = \int_{\mathbf{r}_0 \in V_j} d\mathbf{r}_0 \int_{\mathbf{r} \in V_i} d\mathbf{r} \frac{Q_f^\dagger(\mathbf{r}_0)}{Q_j^\dagger} H(\mathbf{r} \rightarrow \mathbf{r}_0), \quad (5.27)$$

where

$$Q_j^\dagger = \int_{\mathbf{r}' \in V_j} d\mathbf{r}' Q_f^\dagger(\mathbf{r}'). \quad (5.28)$$

It is possible to relate the forward and the adjoint fission matrices by considering the elements at positions  $(i, j)$  and  $(j, i)$  respectively:

$$K_{i,j} = \int_{\mathbf{r}_0 \in V_j} d\mathbf{r}_0 \int_{\mathbf{r} \in V_i} d\mathbf{r} \frac{Q_f(\mathbf{r}_0)}{Q_j} H(\mathbf{r}_0 \rightarrow \mathbf{r}), \quad (5.29)$$

$$K_{j,i}^\dagger = \int_{\mathbf{r}_0 \in V_j} d\mathbf{r}_0 \int_{\mathbf{r} \in V_i} d\mathbf{r} \frac{Q_f^\dagger(\mathbf{r})}{Q_i} H(\mathbf{r}_0 \rightarrow \mathbf{r}). \quad (5.30)$$

From inspection of these definitions, two different spatial weighting functions are applied to the forward and adjoint fission matrices:  $Q_f(\mathbf{r}_0)/Q_j$  and  $Q_f^\dagger(\mathbf{r})/Q_i$  respectively [22]. If the spatial discretization is chosen sufficiently fine, so that

$$\frac{Q_f(\mathbf{r}_0)}{Q_j} \rightarrow \frac{1}{V_j}, \quad (5.31)$$

and

$$\frac{Q_f^\dagger(\mathbf{r})}{Q_i} \rightarrow \frac{1}{V_i}, \quad (5.32)$$

the matrix element  $K_{j,i}^\dagger$  converges to the matrix element  $K_{i,j}$ , hence, the adjoint fission matrix can be obtained by transposition of the direct fission matrix.

A final remark concerns the estimation of the  $k$ -eigenmodes, which can be performed by combining the discrete linear transport operators in order to express the formulation of the  $k$ -eigenvalue problem:

$$M\varphi_k = \frac{1}{k}F\varphi_k, \quad (5.33)$$

where  $M$  and  $F$  are the matrix forms of the net disappearance operator  $\mathcal{M}$  and total fission operator  $\mathcal{F}$  from Eqs. (2.32) and (2.63), respectively. This formulation allows the computation of the eigenmodes  $\varphi_k$  as a function of the phase-space coordinates. Conversely, the fission matrix yields the emission distribution  $S_{f,k}$ , which only depends on the spatial coordinates. In principle, the implementation of matrix-form operators for the  $k$ -eigenvalue problem allows the computation of the entire  $k$ -spectrum and of high-order eigenfunctions  $\varphi_k$ .

## 5.2 A new matrix-filling method for $\alpha$ -eigenvalues

Similarly to the case of  $k$ -eigenvalues, intensive work has been carried out concerning the possibility of estimating higher-order eigenvalue and eigenfunctions for  $\alpha$ -eigenvalue problems.

Despite some successful attempts, generalized power iteration methods performed via Monte Carlo simulations for higher  $\alpha$ -eigenvalues and eigenmodes (based on previous investigations for  $k$ -eigenvalues) have received only limited attention [162]. On the contrary, matrix-filling Monte Carlo methods have recently drawn much interest [6, 7, 8, 153]. We remark in passing that an independent approach has been recently proposed for  $\alpha$ -eigenvalue problems, based on a time-discretization of the fission matrix [68]. However, it appears that such method allows only determining the eigenvalues but not the eigenvectors.

The matrix-filling approach proposed by Betzler [8] is very similar in spirit to the better-known fission matrix method for  $k$ -eigenvalues introduced in the previous section [35, 22]. Although the  $\alpha$ -eigenvalues and eigenmodes thus estimated are generally biased because of the finite size of the matrix, this method allows obtaining a fairly accurate picture of the entire spectrum and thus grasping the time evolution of the system [6, 7], even for complex three-dimensional configurations [8]. Moreover, once the  $\alpha$ -spectrum and the associated eigenvectors have been determined from the matrix, the full time-dependent evolution of the neutron and precursor populations can also be reconstructed, at least in principle, by using the direct and adjoint matrices [8]. The idea is to compute the coefficients  $w_{\alpha_m}$  by solving Eq. (2.88) derived in Section 2.6.2. These coefficients preserve the time dependence of

particles and stem from the separation between time and phase-space coordinates.

The matrix-filling Monte Carlo method of [8] is based on a transition rate method (related to the adjoint formulation of the  $\alpha$ -eigenvalue equation) and suffers from two approximations: the first is due to the fact that the exact adjoint formulation is in practice replaced by a forward formulation, in order to avoid the explicit simulation of backward random walks [8]. The second is due to the fact that the matrix elements are estimated and filled in the course of a  $k$ -eigenvalue Monte Carlo calculation, which induces a systematic bias even on the fundamental eigenvalue and eigenvector [8]. The adjoint formulation is required since the authors of [8] formally work with the propagator of the underlying random walks, which is by construction associated to the adjoint evolution operators. Although both approximation errors vanish in the limit of a sufficiently fine discretization of the phase-space, for realistic systems this might require very large matrix sizes, entailing severe memory footprint issues: contrary to the fission matrix, where only a spatial discretization is required, the matrix associated to  $\alpha$ -eigenvalue problems demands a full discretization of the phase-space, including position, direction and energy.

In this chapter we will propose a new matrix-filling Monte Carlo method for  $\alpha$ -eigenvalue problems that will improve the estimation of the matrix elements in two directions. First, we will show that it is convenient to fill the elements of the matrix by using the  $\alpha$ - $k$  modified power iteration: this approach allows natively preserving the fundamental eigenvalue and eigenvector, which will be computed exactly. Second, we will show that it is actually possible to compute the matrix elements corresponding to the adjoint  $\alpha$ -eigenvalue equations by using the Generalized Iterated Fission Probability (G-IFP): the obtained adjoint-weighted matrix will correspondingly preserve the fundamental (adjoint) eigenvalue and eigenvector, as opposed to building the adjoint operator matrix by transposing the direct operator matrix.

### 5.2.1 Monte Carlo estimators for the operators

The direct and adjoint formulations for the  $\alpha$ -eigenvalue problem introduced in Eqs. (2.76) and (2.80) are respectively recalled in the following equations

$$\mathcal{A}\Psi_\alpha = \alpha\mathcal{V}^{-1}\Psi_\alpha, \quad (5.34)$$

$$\mathcal{A}^\dagger\Psi_\alpha^\dagger = \alpha\mathcal{V}^{-1}\Psi_\alpha^\dagger, \quad (5.35)$$

where the vector  $\Psi_\alpha^\dagger = \{\varphi_\alpha^\dagger, c_{\alpha,1}^\dagger, \dots, c_{\alpha,J}^\dagger\}^T$  is composed of the neutron flux and the precursor concentrations of  $J$  families.

In order to derive a numerically tractable formulation of the systems in Eqs. (5.34) and (5.35), we would like to replace the operators by matrices whose elements can be explicitly computed [8]. For this purpose, it is convenient to discretize the phase-space over elements of the kind  $\int_{V_n} d\mathbf{r} \int_{\Omega_m} d\Omega \int_{E_g} dE$ , where  $V_n$ ,  $\Omega_m$  and  $E_g$  denote position, angle and energy intervals, respectively. The idea is then to approximate any generic operator  $\mathcal{H}$  appearing in Eqs. (5.34) and (5.35) by its average over the phase-space element  $n, m, g$ : this defines the matrix elements

$$H_{n,m,g} = \langle \mathcal{H} \rangle_{n,m,g} \simeq \frac{\langle \mathcal{H}f \rangle_{n,m,g}}{\langle f \rangle_{n,m,g}}, \quad (5.36)$$

for an arbitrary weighting function  $f$ . Consequently, the eigenvalue problem in Eq. (5.34) is replaced by the matrix formulation

$$A\Psi_\alpha = \alpha V^{-1}\Psi_\alpha \quad (5.37)$$

and the adjoint problem in Eq. (5.35) is replaced by

$$A^\dagger\Psi_\alpha^\dagger = \alpha V^{-1}\Psi_\alpha^\dagger. \quad (5.38)$$

Once the matrix elements have been estimated, the spectrum and the eigenvectors can be extracted by using standard linear algebra libraries [8], similarly to what is done for the fission matrices for  $k$ -eigenvalue problems [22]. In the limit of a sufficiently fine discretization of the position, angle and energy intervals the spectrum and the eigenvectors of the matrices converge to those of the exact formulation. The accuracy of the introduced approximation and the rate of convergence depend on the choice of the weighting function. We are thus left with two constraints: the matrix elements  $H_{n,m,g}$  must correspond to scores that can be practically estimated by Monte Carlo methods, and the weighting function must be chosen so to minimize the discretization bias.

## 5.2.2 Matrix representation of the operators

In order to fill the elements of the (direct) fission matrix corresponding to  $k$ -eigenvalue problems, the natural choice is to use the fundamental  $k$ -eigenmode, which can be estimated by the regular power iteration method in Monte Carlo criticality calculations, previously described in Section 4.2 [22]. This approach preserves the fundamental eigenvalue and eigenvector that can be computed from the resulting matrix, in the sense that they are unbiased independently of the size of the discretization intervals. This property however does not carry over to higher eigenvalues and eigenvectors of the direct fission matrix, nor to the fundamental (and higher) eigenmode of the transposed fission matrix.

By analogy, and in view of obtaining a similar unbiased estimate of the fundamental  $\alpha$ -eigenpair, it seems reasonable to choose the fundamental  $\alpha$ -eigenmode as a weighting function for the forward eigenvalue problem in Eq. (2.76). The fundamental eigen-pair  $(\alpha_0, \Psi_{\alpha_0})$  can be determined by applying the Monte Carlo implementation of the  $\alpha$ - $k$  power iteration, previously described in Section 4.4. As mentioned, a few other methods exist to estimate  $(\alpha_0, \Psi_{\alpha_0})$ , each with distinct merits and drawbacks [170, 108, 138, 69]. Here we have chosen the  $\alpha$ - $k$  method, which is relatively straightforward and can be conveniently adapted to adjoint calculations, independently of the sign of the system reactivity [147].

Once the discretized matrix  $A$  has been filled, the adjoint matrix  $A^\dagger$  can be in principle obtained by transposing  $A$  [8], similarly as done for the adjoint fission matrix in  $k$ -eigenvalue problems [22]. This approach would preserve the spectrum, since the eigenvalues associated to a transposed real matrix are identical to those computed from the original matrix. However, it would also induce a bias on the fundamental adjoint eigenvector, since the matrix elements would have been weighted by the forward fundamental eigenmode  $\varphi_{\alpha_0}$  instead of the adjoint fundamental eigenmode  $\varphi_{\alpha_0}^\dagger$  [8]. This issue is entirely analogous to what happens for the adjoint fission matrix in  $k$ -eigenvalue problems [22]. Although this bias vanishes in the limit of sufficiently large matrices, for the sake of numerical accuracy (and in view of reducing the memory footprint) it would be convenient to estimate the adjoint matrix elements directly. We will thoroughly examine these issues in Section 5.3.

As previously described in Section 4.5, a generalization of the Iterated Fission Probability (IFP) method has been proposed in order to evaluate  $\varphi_{\alpha_0}^\dagger$  (and more generally bi-linear forms requiring both  $\varphi_{\alpha_0}$  and  $\varphi_{\alpha_0}^\dagger$ ) by relating the fundamental adjoint eigenfunction to the neutron importance  $I_\alpha$  [147], similarly to what is done for the regular  $k$ -eigenvalue IFP formulation [110, 75]. The Generalized IFP method provides estimates of the neutron importance  $I_\alpha$  in  $\alpha$ -eigenvalue problems by recording the descendants after a given number of latent generations for an ancestor neutron starting with coordinates  $\mathbf{r}, \boldsymbol{\Omega}, E$ . In practice,  $I_\alpha$  is estimated by using a fixed-source calculation, where neutrons are followed over the latent generations. Since  $I_\alpha \propto \varphi_{\alpha_0}^\dagger$ , the importance of the ancestor neutron is computed at the end of the latent generations as

$$\langle \varphi_{\alpha_0}^\dagger Q \rangle \propto \sum_i \pi_i \quad (5.39)$$

where  $\pi_i$  is the corresponding statistical weight of the descendants of the ancestor  $i$  collected at the end of the G-IFP cycle for the neutrons initially sampled from a fixed source  $Q$ , the sum being extended over the ancestors. In this way, it is possible to estimate the elements of the adjoint matrix  $A^\dagger$  by using  $\varphi_{\alpha_0}^\dagger$  as weighting function. The adjoint operators estimated in this way require a proper normalization as in Section 5.2.4.

## 5.2.3 Estimating the direct matrix elements

Suppose now that we partition the phase-space into  $N$  space intervals,  $M$  angle intervals and  $G$  energy intervals. The method proposed in this chapter for the direct matrices closely follows the strategy of [8], except for the choice of  $\varphi_\alpha$  and  $c_\alpha^j$  as the weighting functions and the use of the neutron flux  $\varphi$  (instead of the neutron density  $n$ ) as the normalization of the operators applied to neutrons. The corresponding matrix elements will be thus filled by using the following Monte Carlo estimators.

Neutrons start their flights from source sites and travel through the medium according to the streaming operator  $\mathcal{L}$ . In order to estimate the corresponding matrix elements, this term is first transformed by applying the Gauss

theorem, yielding

$$\langle \mathcal{L}\varphi_\alpha \rangle = \langle \boldsymbol{\Omega} \cdot \nabla \varphi_\alpha(\mathbf{r}, \boldsymbol{\Omega}, E) \rangle_{n,m,g} = \left\langle \int_{S_n} d\mathbf{r}' \boldsymbol{\Omega} \cdot \mathbf{n} \varphi_\alpha(\mathbf{r}', \boldsymbol{\Omega}, E) \right\rangle_{m,g}, \quad (5.40)$$

where  $S_n$  is the surface enclosing the space element  $n$  and  $\mathbf{n}$  is the normal to the surface. This term can be estimated by computing the current of neutrons streaming in and out the surfaces of the space element  $n$ , projected over the flight direction  $\boldsymbol{\Omega}$  [8]. This operator acts on the spatial coordinates of the neutrons, as well as on their directions if reflection events occurred.

At collision sites, the matrix elements associated to the inverse speed operator  $\mathcal{V}^{-1}$  and the removal operator  $\mathcal{R}$  are respectively estimated as

$$\langle \mathcal{V}^{-1}\varphi_\alpha \rangle = \left\langle \frac{1}{v(E)} \varphi_\alpha(\mathbf{r}, \boldsymbol{\Omega}, E) \right\rangle_{n,m,g}, \quad (5.41)$$

$$\langle \mathcal{R}\varphi_\alpha \rangle = \langle \Sigma_t(\mathbf{r}, E) \varphi_\alpha(\mathbf{r}, \boldsymbol{\Omega}, E) \rangle_{n,m,g}. \quad (5.42)$$

Since these operators do not act on neutron positions in the phase-space, only the diagonal elements of the corresponding matrices will be filled.

For fissile materials, the prompt fission operator  $\mathcal{F}_p$  is approximated by the estimation of matrix elements according to the following relation

$$\langle \mathcal{F}_p \varphi_\alpha \rangle = \left\langle \frac{\chi_p(E)}{4\pi} \langle \bar{v}_p(E') \Sigma_f(\mathbf{r}, E') \varphi_\alpha(\mathbf{r}, \boldsymbol{\Omega}', E') \rangle_{m',g'} \right\rangle_{n,m,g}. \quad (5.43)$$

Moreover, if precursors are considered, the matrix elements representing the precursor production operator  $\mathcal{F}_d^j$  and the delayed neutron emission  $\chi_d^j$  can be expressed as

$$\langle \mathcal{F}_d^j \varphi_\alpha \rangle = \langle \langle \bar{v}_d^j(E') \Sigma_f(\mathbf{r}, E') \varphi_\alpha(\mathbf{r}, \boldsymbol{\Omega}', E') \rangle_{m',g'} \rangle_n, \quad (5.44)$$

$$\left\langle \lambda_j \frac{\chi_d^j}{4\pi} c_\alpha^j \right\rangle = \left\langle \frac{\chi_d^j(E)}{4\pi} \langle \lambda_j c_\alpha^j(\mathbf{r}) \rangle_n \right\rangle_{m,g}. \quad (5.45)$$

Finally, the scattering operator  $\mathcal{S}$  is computed from the matrix elements estimated as

$$\langle \mathcal{S}\varphi_\alpha \rangle = \langle \langle \Sigma_s(\mathbf{r}, \boldsymbol{\Omega}' \rightarrow \boldsymbol{\Omega}, E' \rightarrow E) \varphi_\alpha(\mathbf{r}, \boldsymbol{\Omega}', E') \rangle_{m',g'} \rangle_{n,m,g}. \quad (5.46)$$

All these collision operators act on the energy and the direction of neutrons according to the collision kernel laws.

The matrix elements related to operators applied to the neutron flux  $\varphi_\alpha$  are normalized by

$$\langle \varphi_\alpha \rangle_{n,m,g}, \quad (5.47)$$

with respect to the incoming coordinates of the particle. The precursor concentration of family  $j$  is applied as a normalization for delayed neutron emission and it is estimated in its discretized form as

$$\langle c_\alpha^j \rangle_n = \left\langle \frac{1}{\lambda_j + \alpha} \mathcal{F}_d^j \varphi_\alpha \right\rangle_n. \quad (5.48)$$

When including the precursor contributions, the total matrix operator size is  $(NMG + N_f J)^2$ , where  $N_f \leq N$  is the number of fissile regions for which the precursor contributions must be assigned. Mainly due to the structure of the gradient operator and of the diagonal matrix associated to the precursor decay constants [8], the matrix operator is however considerably sparse. Assuming a Cartesian grid for the space coordinates, with  $N_x$ ,  $N_y$  and  $N_z$  components along each axis ( $N = N_x \times N_y \times N_z$ ), the maximum number of non-null matrix entries is

$$\begin{aligned} & MG \left[ NMG + N_x N_y (N_z - 1) + N_y N_z (N_x - 1) + N_x N_z (N_y - 1) \right] + N_f J \\ & \ll (NMG + N_f J)^2, \end{aligned} \quad (5.49)$$

which is an important issue when considering real-world applications.

For illustration, the sparsity pattern of the maximum number of non-null elements of the matrix operator  $A$  from Eq. (5.37) is shown in Fig. 5.1.

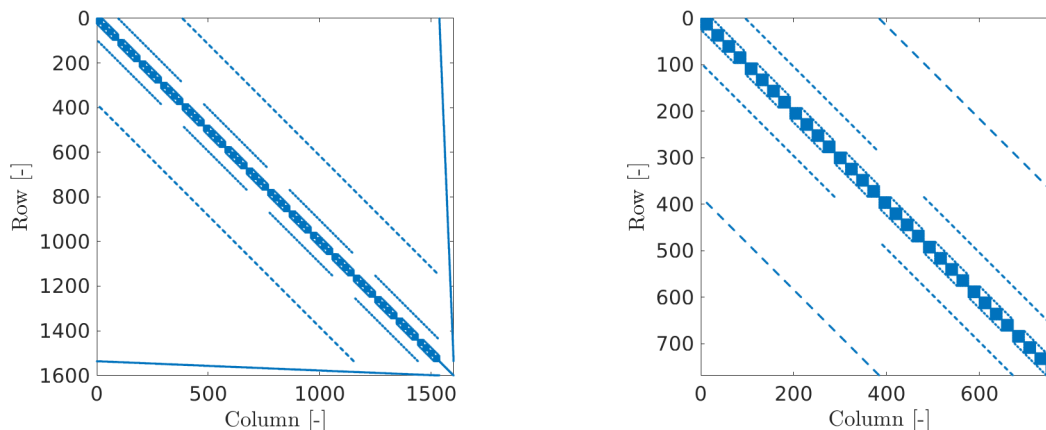


Figure 5.1: Sparsity pattern of the maximum number of non-null elements of the matrix operator  $A$  for the following phase-space discretization:  $N_x = N_y = N_z = 4$ ,  $M_x = M_y = M_z = 2$ ,  $G = 3$  and  $J = 1$ . The complete matrix sparsity pattern (left) and a zoom of the first 768 rows/columns (right) have been shown in the figure.

#### 5.2.4 Estimating the adjoint matrix elements

For the direct matrices, the  $\alpha$ - $k$  power iteration ensures that particles are sampled according to the fundamental eigenmode distribution  $\varphi_{\alpha_0}$  and matrix elements can be constructed as regular reaction rates, as detailed above. For the adjoint matrix elements, on the contrary, the idea is to carefully select a source distribution  $Q$  such that Eq. (5.39) yields the desired adjoint matrix element. Indeed, the adjoint matrix elements illustrated in the previous sections can all be written in the form of a scalar product involving a ‘source’ weighted by the fundamental adjoint mode, which can be thus estimated by computing the neutron importance function by the G-IFP method. Bearing in mind these considerations, two cases are encountered: if the source for the matrix element is a probability density function (e.g., a fission spectrum), this probability density can be straightforwardly used so as to sample the initial coordinates of the neutron whose importance must be assessed. If the source for the matrix does not lend itself to be interpreted as a probability density function (e.g., the total cross section appearing in the adjoint collision operator  $\mathcal{R}^\dagger$ ), then an artificial uniform coordinate is sampled in the selected bin corresponding to the matrix element, and the source appearing in the expression of the matrix element will be used as a final weighting factor for the obtained importance following from the sampled neutron. For the discretized operators, a uniform meshing of the phase-space is preferred, since the effect of the distribution will vanish when normalizing by the bin-integrated adjoint flux  $\langle \varphi_\alpha^\dagger \rangle_{nmg}$ .

The adjoint streaming matrix is expressed by applying again Gauss’ theorem in order to convert the volume integration into a surface integration over the boundaries of the spatial bin. This leads to

$$\langle \mathcal{L}^\dagger \varphi_\alpha^\dagger \rangle = \langle -\mathbf{\Omega} \cdot \nabla \varphi_\alpha^\dagger(\mathbf{r}, \mathbf{\Omega}, E) \rangle_{n,m,g} = - \left\langle \int_{S_n} d\mathbf{r}' \mathbf{\Omega} \cdot \mathbf{n} \varphi_\alpha^\dagger(\mathbf{r}', \mathbf{\Omega}, E) \right\rangle_{m,g}. \quad (5.50)$$

The expression in Eq. (5.50) can be given a probabilistic interpretation: the integral over the surface means that the starting points for the neutron ancestors must be taken uniformly over the boundaries of the spatial bins. The angular factor  $\mathbf{\Omega} \cdot \mathbf{n}$ , where  $\mathbf{n}$  is the normal vector of the surface  $S_n$ , implies that the starting direction for the ancestors must be sampled by respecting an isotropic incident flux on  $S_n$ . In particular, the term  $\cos \theta_0 = \mathbf{\Omega}_0 \cdot \mathbf{n}$  implies that in polar coordinates ancestors starting on the surface must enter the domain with  $\theta_0 = \arcsin(2\xi - 1)$  in two dimensions and  $\theta_0 = 1/2 \arccos(1 - 2\xi)$  in three dimensions,  $\xi$  being uniformly distributed in  $(0, 1]$  [168]. This completely defines the source for the importance calculation associated to the streaming term.

Similarly as in the direct case, the non-trivial part of the inverse speed matrix and the adjoint removal matrix is

represented by a diagonal matrix with corresponding elements

$$\langle \mathcal{V}^{-1} \varphi_\alpha^\dagger \rangle = \left\langle \frac{1}{v(E)} \varphi_\alpha^\dagger(\mathbf{r}, \boldsymbol{\Omega}, E) \right\rangle_{n,m,g}, \quad (5.51)$$

$$\langle \mathcal{R}^\dagger \varphi_\alpha^\dagger \rangle = \langle \Sigma_t(\mathbf{r}, E) \varphi_\alpha^\dagger(\mathbf{r}, \boldsymbol{\Omega}, E) \rangle_{n,m,g}. \quad (5.52)$$

The adjoint scattering and prompt fission matrix elements, respectively

$$\langle \mathcal{S}^\dagger \varphi_\alpha^\dagger \rangle = \langle \langle \Sigma_s(\mathbf{r}, \boldsymbol{\Omega} \rightarrow \boldsymbol{\Omega}', E \rightarrow E') \varphi_\alpha^\dagger(\mathbf{r}, \boldsymbol{\Omega}', E') \rangle_{m',g'} \rangle_{n,m,g}, \quad (5.53)$$

$$\langle \mathcal{F}_p^\dagger \varphi_\alpha^\dagger \rangle = \left\langle \bar{v}_p(E) \Sigma_f(\mathbf{r}, E) \left\langle \frac{\chi_p(E')}{4\pi} \varphi_\alpha^\dagger(\mathbf{r}, \boldsymbol{\Omega}', E') \right\rangle_{m',g'} \right\rangle_{n,m,g}, \quad (5.54)$$

are obtained by uniformly sampling the incident energy and direction, then sampling the scattering (respectively fission) spectrum and finally computing the adjoint flux by using the G-IFP scheme.

Finally, the adjoint operators related to the precursors are represented by the following matrix elements

$$\langle \lambda_j \mathcal{F}_{d,j}^\dagger \varphi_\alpha^\dagger \rangle = \left\langle \left\langle \frac{\chi_d^j(E')}{4\pi} \lambda_j \varphi_\alpha^\dagger(\mathbf{r}, \boldsymbol{\Omega}', E') \right\rangle_{m',g'} \right\rangle_n, \quad (5.55)$$

$$\langle \bar{v}_d^j \Sigma_f c_{\alpha,j}^\dagger \rangle = \langle \bar{v}_d^j(E) \Sigma_f(\mathbf{r}, E) \langle c_{\alpha,j}^\dagger(\mathbf{r}) \rangle_{m',g'} \rangle_n, \quad (5.56)$$

All the adjoint operators applied to the adjoint neutron flux  $\varphi^\dagger$  are normalized by

$$\langle \varphi_\alpha^\dagger \rangle_{n,m,g}, \quad (5.57)$$

with respect to the outgoing coordinates, whereas the operator applied to the precursors concentration is normalized by

$$\langle c_{\alpha,j}^\dagger \rangle_n = \left\langle \frac{\lambda_j}{\lambda_j + \alpha} \mathcal{F}_{d,j}^\dagger \varphi_\alpha^\dagger \right\rangle_n. \quad (5.58)$$

It is worth noting that Eqs. (5.51) (5.52) (5.57) can be estimated in the same calculation, since the same source function  $Q$  is applied. However, each matrix elements characterized by a different sampling law requires a separate and independent simulation.

## 5.2.5 Estimating the eigenpairs

The matrix-form of all operators described in Sections 5.2.3 and 5.2.4 are scored as a three-column vector representing the row numbers, the column numbers and the corresponding non-zeros matrix element values. This storage method for the matrix elements provides an optimization for memory occupation of the matrix elements due to the high sparsity pattern of the matrix-form operators. The same procedure has been applied for the estimation of the fission matrix elements [22].

Then, the matrix elements need to be post-processed in order to assemble the matrix-form of the sought eigenvalue problem. For this purpose, a MATLAB code has been implemented to normalize each matrix element (Eq. (5.36)) and to combine them in the final form of the eigenvalue problem [101]. For small matrix size (about  $1.6 \times 10^7$  elements), the *eig* command in MATLAB provides the full set of eigenpairs associated with the generalized eigenvalue problem of the kind:

$$Ax = \lambda Bx, \quad (5.59)$$

where  $\lambda$  and  $x$  are the eigenvalues and the eigenvectors, respectively, solving the eigenvalue problem defined by the generic dense matrices  $A$  and  $B$ . The algorithm used for the computation of the eigenpairs is the QZ algorithm [103]. For larger matrix size with high sparsity pattern, the *eigs* command uses an iterative algorithm for the computation of the first eigenpairs of the problem [145]. Nevertheless, this iterative process has hard time to converge to the correct solution if delayed contributions are considered: this is mainly due to the presence of clusters of eigenvalues on the right of the negative values of the decay constants  $-\lambda_j$  [133, 132]. The effect of the eigenvalue clustering will be detailed in Chapter 6. Similar issues for the estimating the full  $\alpha$ -spectrum (prompt

and delayed contributions) for large matrices were already encountered in the reference [8] when using an iterative eigenvalue solver [91]. In order to overcome this problem, we decided to maintain a dense structure for the matrices associated to the transport operators and to use the QZ algorithm [103] for the computation of all eigenpairs.

## 5.3 Numerical simulations

In order to assess the impact of using the  $\alpha$ - $k$  power iteration and the G-IFP method in order to fill the matrix elements of the direct and adjoint  $\alpha$ -matrices, respectively, we have selected some simplified benchmark configurations that allow more easily probing the proposed methods by comparing the obtained results to reference solutions.

### 5.3.1 The rod model

The rod model is among the simplest space- and direction-dependent transport problems: neutrons move at constant speed  $v$  along a line, where only two directions of flight are allowed, namely forward ( $\Omega = +$ ) and backward ( $\Omega = -$ ) [159]. We will furthermore assume that scattering and fission are isotropic. Defining  $\varphi_\alpha(x, \pm)$  the angular flux in the positive and negative direction, the  $\alpha$  eigenvalue equations read

$$\pm \frac{\partial}{\partial x} \varphi_\alpha(x, \pm) + \left[ \frac{\alpha}{v} + \Sigma_t \right] \varphi_\alpha(x, \pm) = \frac{\zeta_\alpha}{2} \varphi_\alpha(x), \quad (5.60)$$

where we have defined  $\varphi_\alpha(x) = \varphi_\alpha(x, +) + \varphi_\alpha(x, -)$ , and

$$\zeta_\alpha = \Sigma_s + \bar{v}_p \Sigma_f + \sum_{j=1}^J \frac{\lambda_j}{\lambda_j + \alpha} \bar{v}_d^j \Sigma_f. \quad (5.61)$$

Let us consider a segment  $[0, L]$ , with leakage boundary conditions  $\varphi_\alpha(0, +) = 0$  and  $\varphi_\alpha(L, -) = 0$ . It is possible to derive an equation for  $\varphi_\alpha(x)$  alone, namely,

$$-D_\alpha \frac{\partial^2}{\partial x^2} \varphi_\alpha(x) = \frac{\zeta_\alpha D_\alpha - 1}{D_\alpha} \varphi_\alpha(x), \quad (5.62)$$

with Robin boundary conditions  $\varphi_\alpha(0) - D_\alpha \partial \varphi_\alpha(0) / \partial x = 0$  and  $\varphi_\alpha(L) + D_\alpha \partial \varphi_\alpha(L) / \partial x = 0$ , and

$$D_\alpha = \frac{1}{\Sigma_t + \frac{\alpha}{v}}. \quad (5.63)$$

Taking into account the boundary conditions, the solution of Eq. (5.62) is expressed as

$$\varphi_\alpha(x) = \sqrt{\zeta_\alpha D_\alpha - 1} \cos\left(\frac{\sqrt{\zeta_\alpha D_\alpha - 1}}{D_\alpha} x\right) + \sin\left(\frac{\sqrt{\zeta_\alpha D_\alpha - 1}}{D_\alpha} x\right), \quad (5.64)$$

from which we can obtain the angular flux  $\varphi_\alpha(x, \pm)$  and the precursor concentration

$$c_\alpha^j = \frac{1}{\lambda_j + \alpha} \bar{v}_d^j \Sigma_f \varphi_\alpha(x) \quad (5.65)$$

by observing that the particle current  $P_\alpha(x) = \varphi_\alpha(x, +) - \varphi_\alpha(x, -)$  satisfies  $P_\alpha(x) = -D_\alpha \partial_x \varphi_\alpha(x)$ . The adjoint eigenmodes satisfy the relation  $\varphi_\alpha^\dagger(x, \pm) = \varphi_\alpha(x, \mp)$ . The  $\alpha$ -eigenvalues stem from the dispersion law [170]

$$\Lambda(\alpha) = 2 \sqrt{\zeta_\alpha D_\alpha - 1} \cos\left(\frac{\sqrt{\zeta_\alpha D_\alpha - 1}}{D_\alpha} L\right) - \zeta_\alpha D_\alpha \cos\left(\frac{\sqrt{\zeta_\alpha D_\alpha - 1}}{D_\alpha} L\right) = 0, \quad (5.66)$$

which is obtained by imposing the boundary conditions on the general solutions in Eq. (5.64). The zeros of Eq. (5.66) form the discrete spectrum of the  $\alpha$ -eigenvalues for the rod model. When the precursor contributions are neglected,  $\Lambda(\alpha)$  yields a finite number of real eigenvalues, plus a countable infinity of complex eigenvalues associated to oscillating modes [104]; when precursors are taken into account,  $J$  additional sets of denumerable real

eigenvalues are introduced by the  $J$  singularities at  $\alpha = -\lambda_j$ , accumulating at the right of each  $-\lambda_j$  (the "clusters" mentioned above).

### Analysis of the direct eigenpairs

We begin our analysis by considering the case of direct eigenvalues and eigenfunctions. The physical parameters for the rod model are given in Tab. 5.1. For this example, we have chosen a deep sub-critical configuration and we have neglected the contributions of precursors. The dominant  $\alpha$ -eigenvalue is  $\alpha_0 = -0.91112$  (with corresponding  $k$ -eigenvalue  $k_0 = 0.21945$ ). The matrix elements have been computed as described in the previous sections, based on the  $\alpha$ - $k$  power iteration. Since the transport model does not depend on energy and only two discrete directions are allowed, the only discretization left is with respect to the space coordinates, which makes easier the investigation of the convergence of the proposed methods.

$v$ [cm/s]	$\Sigma_c$ [cm $^{-1}$ ]	$\Sigma_f$ [cm $^{-1}$ ]	$\Sigma_s$ [cm $^{-1}$ ]	$\bar{v}_p$ [-]	$L$ [cm]
10	1	0.1	1	2.5	10

Table 5.1: Parameter values for the rod model.

The Monte Carlo matrix-filling calculation based on the  $\alpha$ - $k$  power iteration has been run with  $10^3$  inactive cycles,  $10^3$  active cycles used for scoring the matrix elements, and  $10^5$  particles per cycle. The results of the spectral analysis from the  $\alpha$ -weighted matrices are recalled in Tab. 5.2 for a discretization of  $N = 1024$  spatial meshes. An excellent agreement is found between the numerical values coming from the  $A$  matrix filled by the Monte Carlo calculation and the exact reference stemming from the numerical analysis of the roots of the dispersion law in Eq. (5.66). Correspondingly, the first few eigenfunctions are compared in Fig. 5.2 for the same spatial discretization: again, an excellent agreement is found between the eigenvectors of the  $A$  matrix filled by the Monte Carlo calculation and the exact solutions stemming from Eq. (5.64).

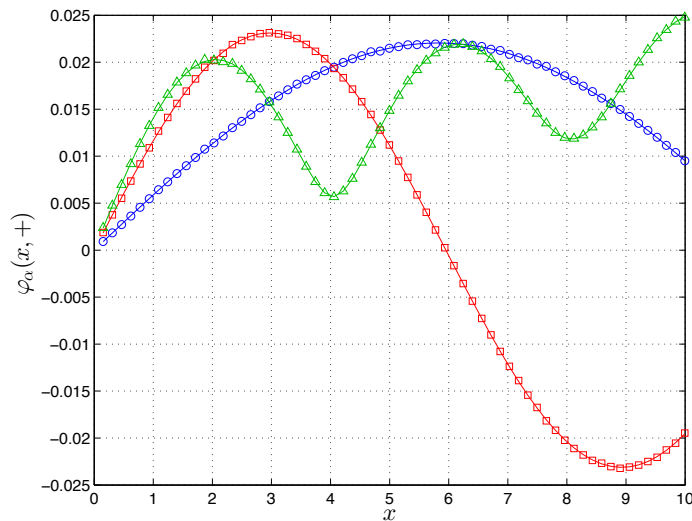


Figure 5.2: The first few (angular) eigenmodes  $\varphi_\alpha(x, +)$ : the eigenvectors of the  $A$  matrix filled by the Monte Carlo calculation (symbols) are compared to the exact solutions stemming from Eq. (5.64). Blue circles: fundamental eigenmode  $\varphi_{\alpha_0}(x, +)$ ; red squares: second eigenmode  $\varphi_{\alpha_1}(x, +)$ ; green triangles: third eigenmode  $\varphi_{\alpha_2}(x, +)$ .

weighting function	$\alpha_0$ [s <sup>-1</sup> ]	$\alpha_1$ [s <sup>-1</sup> ]	$\alpha_{2,3}$ [s <sup>-1</sup> ]
exact	-0.91112	-1.14021	-1.59033 ± 0.46007i
$\alpha$ - $k$	-0.91113	-1.14081	-1.59245 ± 0.45965i
Generalized IFP	-0.91102	-1.14101	-1.59233 ± 0.45948i
$k$	-0.91104	-1.14049	-1.59232 ± 0.45890i
fixed-source	-0.91135	-1.14078	-1.59273 ± 0.45864i

Table 5.2: Rod model. Comparison of the  $\alpha$  eigenvalues obtained from the matrices filled with the method shown in the first column, for  $N = 1024$  spatial meshes. Model parameters are shown in Tab. 5.1.

As discussed in the previous sections, an important issue concerns the convergence of the eigenvalues and eigenvectors of  $A$  with respect to the size of the matrix, i.e., the discretization of the viable phase-space. The key point is that the use of the  $\alpha$ - $k$  power iteration in order to weight the matrix elements by the fundamental eigenfunction  $\varphi_{\alpha_0}$  is expected to preserve the fundamental eigenvector of  $A$  for any choice of the matrix size. For the purpose of probing the behaviour of  $A$ , in addition to the  $\alpha$ -weighted matrix we have produced two other matrices obtained by weighting their respective elements by using the fundamental mode of the  $k$ -eigenvalue power iteration (with  $10^3$  inactive cycles,  $10^3$  active cycles used for scoring the matrix elements, and  $10^5$  particles per cycle) and by using the flux resulting from a fixed-source calculation starting from a uniformly distributed isotropic source within the domain (with  $10^8$  particles). In the limit of very large  $N$ , all these methods are expected to converge to the exact limit  $\mathcal{A}$ : for a more refined phase-space discretization, the choice of the weighting function  $f$  introduced in Eq. (5.36) becomes less important. The corresponding numerical values are recalled in Tab. 5.2 for  $N = 1024$  spatial meshes and different weighting functions.

The convergence analysis of the  $\alpha$ -eigenvalues as a function of the spatial discretization  $N$  and of the choice of the weighting function for  $A$  is shown in Fig. 5.3. As conjectured, the fundamental eigenvalue  $\alpha_0$  resulting from the  $\alpha$ -weighted matrix  $A$  is unbiased with respect to the exact reference root of the dispersion law in Eq. (5.66), independently of the discretization  $N$  (Fig. 5.3, left). On the contrary, the fundamental eigenvalues  $\alpha_0$  resulting from the matrix  $A$  with the two other weighting schemes shows a bias that is progressively reduced as  $N$  increases. Even for this very simple benchmark example, it takes roughly  $N = 128$  in order for the other schemes to converge to the true fundamental eigenvalue, which motivates the choice of the  $\alpha$ -weighting schemes. Concerning the second and third eigenvalue  $\alpha_1$  and  $\alpha_2$ , as expected the higher-order eigenfunctions are not preserved and the  $\alpha$ -weighting method does not offer any specific advantage (Fig. 5.3, right). For higher-order eigenvalues the rate of convergence of the three schemes is similar.

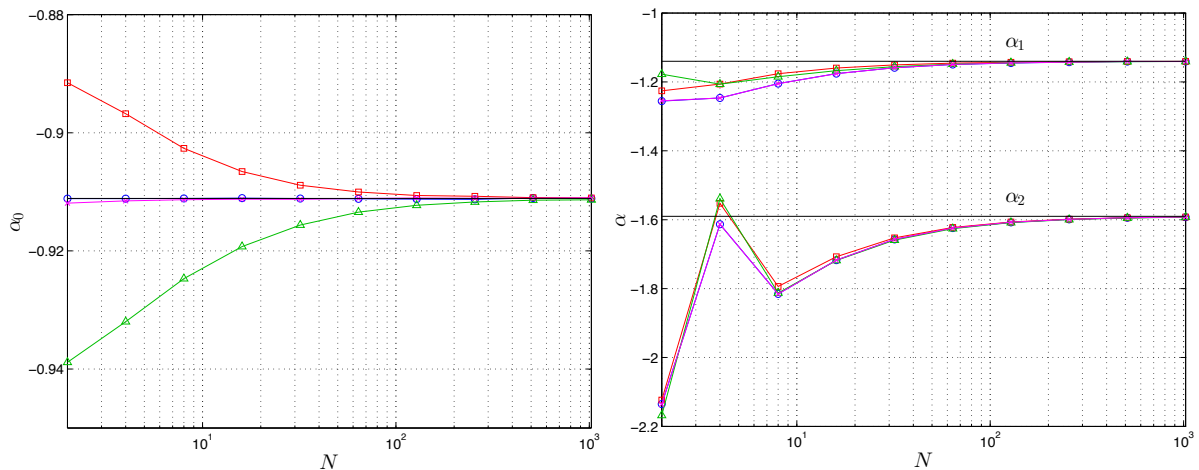


Figure 5.3: Convergence of the first few eigenvalues  $\alpha_i$  as a function of the number of spatial meshes  $N$  and of the weighting function for the matrix  $A$ . Left: the fundamental eigenvalue  $\alpha_0$ ; right:  $\alpha_1$  and  $Re[\alpha_2]$ . Black solid lines correspond to the exact reference values from the roots of the dispersion law in Eq. (5.66). Blue circles correspond to results obtained from the  $\alpha$ -weighted  $A$  matrix; red squares to the  $k$ -weighted  $A$  matrix; green triangles symbols to the matrix  $A$  weighted by a fixed-source flux. Solid lines have been added to guide the eye. In addition, we display with magenta diamonds the corresponding eigenvalues obtained from the adjoint matrix  $A^\dagger$  weighted by the adjoint  $\alpha$ -eigenfunction resulting from the Generalized IFP method.

An important issue concerns the impact of the *statistical uncertainty* intrinsically induced by the Monte Carlo method on the elements of the matrices: in particular, we are interested in assessing the effects of such fluctuations on the derived spectrum and eigenvectors. For this purpose, we have performed an ensemble of independent replicas of the  $\alpha$ - $k$  power iterations and we have computed the average and the dispersion of the obtained  $\alpha$  spectrum and eigenvectors, as a function of the number of simulated particles per cycle. Numerical findings are reported in Tab. 5.3 and show that the standard deviation of the first few eigenvalues scales roughly as  $1/\sqrt{P}$ ,  $P$  being the number of particles per cycle.

	Particles per cycle	$\alpha_0$ [ $s^{-1}$ ]	$\alpha_1$ [ $s^{-1}$ ]	$Re[\alpha_{2,3}]$ [ $s^{-1}$ ]	$Im[\alpha_{2,3}]$ [ $s^{-1}$ ]
exact		-0.911121	-1.140209	-1.590327	$\pm 0.460074$
Average	$10^3$	-0.91112	-1.14497	-1.60753	$\pm 0.45378$
	$10^4$	-0.911123	-1.14509	-1.60762	$\pm 0.45387$
	$10^5$	-0.911117	-1.145099	-1.607615	$\pm 0.453870$
Std	$10^3$	$2 \times 10^{-5}$	$5 \times 10^{-5}$	$3 \times 10^{-5}$	$7 \times 10^{-5}$
	$10^4$	$8 \times 10^{-6}$	$1 \times 10^{-5}$	$1 \times 10^{-5}$	$2 \times 10^{-5}$
	$10^5$	$2 \times 10^{-6}$	$5 \times 10^{-6}$	$3 \times 10^{-6}$	$7 \times 10^{-6}$

Table 5.3: Rod model. Comparison of the eigenvalues obtained from the matrices scored during  $10^3$  replicas of  $\alpha$ - $k$  power iterations, each using  $10^3$  inactive cycles,  $10^3$  active cycles and a variable number of particles per cycle.

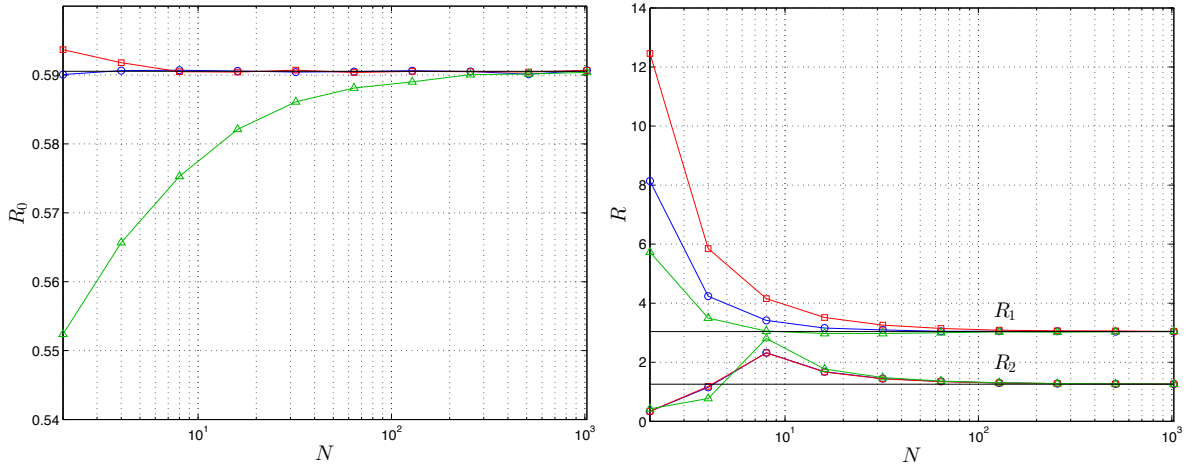


Figure 5.4: Convergence of the first few estimators  $R_i$  as a function of the number of spatial meshes  $N$  and of the weighting function for the matrix  $A$ . Black solid lines correspond to the exact reference values based on Eq. (5.64). Blue circles correspond to results obtained from the  $\alpha$ -weighted  $A$  matrix; red squares correspond to the  $k$ -weighted  $A$  matrix; green triangles correspond to the matrix  $A$  weighted by a fixed-source flux. Left: the estimator  $R_0$  associated to the fundamental eigenfunction  $\varphi_{\alpha_0}(x, +)$ ; right: the estimator  $R_1$  associated to the second eigenfunction  $\varphi_{\alpha_1}(x, +)$  and the estimator  $R_2$  associated to the second eigenfunction  $\varphi_{\alpha_2}(x, +)$ . Solid lines have been added to guide the eye.

In order to perform a similar analysis on the behaviour of the eigenmodes, we have introduced an estimator defined as the normalized integral of the eigenfunction of order  $i$  over the half-domain, namely,

$$R_i = \frac{|\int_{\frac{L}{2}}^L dx \varphi_{\alpha_i}(x, +)|}{|\int_0^L dx \varphi_{\alpha_i}(x, +)|}, \quad (5.67)$$

where  $L$  is the length of the rod. The reference value for  $R_i$  can be computed based on Eq. (5.64). The numerical values for the first few  $R_i$  are compared to the exact solutions in Tab. 5.4 for  $N = 1024$  spatial meshes and different weighting functions.

weighting function	$R_0$ [-]	$R_1$ [-]	$R_{2,3}$ [-]
exact	0.59054	3.04076	1.25702
$\alpha - k$	0.59068	3.03938	1.26403
$k$	0.59068	3.04243	1.26346
fixed-source	0.59039	3.05016	1.26317

Table 5.4: Rod model. Comparison of the first few estimators  $R_i$  obtained from the matrices filled with the method shown in the first column, for  $N = 1024$  spatial meshes.

The convergence analysis of the estimator  $R_i$  computed by the matrix  $A$  as a function of the spatial discretization  $N$  and of the choice of the weighting function for  $A$  is shown in Fig. 5.4. As conjectured, the estimator  $R_0$  associated to the fundamental eigenfunction resulting from the  $\alpha$ -weighted matrix  $A$  is unbiased with respect to the exact solution, independently of the discretization  $N$ . On the contrary, the estimator  $R_0$  resulting from the matrix  $A$  with the two other weighting schemes shows a bias that decreases with increasing  $N$ . It takes roughly only  $N = 8$  in order for the  $k$ -weighted scheme to converge to the true fundamental eigenvalue, which can be understood by observing that the deviation between  $\varphi_{k_0}(x, +)$  and  $\varphi_{\alpha_0}(x, +)$  is rather small for the parameters chosen here. For the matrix weighted on the fixed-source flux, the deviation is much larger, and convergence is achieved after  $N = 256$ . Concerning the estimators  $R_1$  and  $R_2$  associated with the second and third eigenfunction, all weighting schemes are biased, and the rate of convergence of the three schemes is similar.

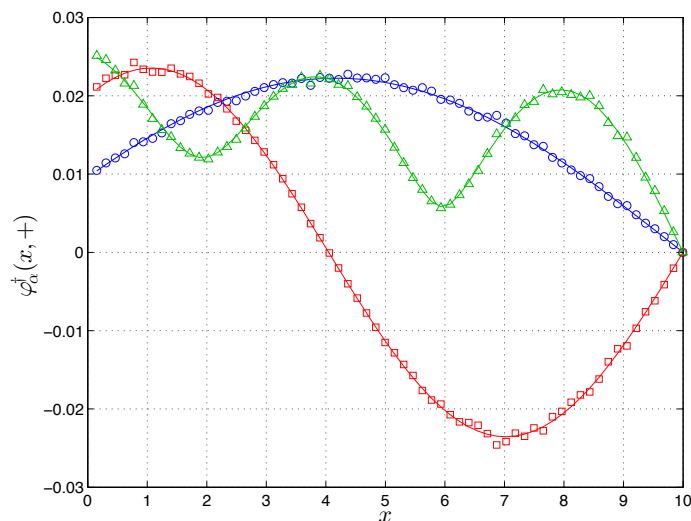


Figure 5.5: The first few (angular) adjoint eigenmodes  $\varphi_\alpha^\dagger(x, +)$ : the eigenvectors of the  $A$  matrix filled by the Monte Carlo calculation (symbols) are compared to the exact solutions stemming from the equation adjoint to Eq. (5.64) (solid lines). Blue circles: fundamental adjoint eigenmode  $\varphi_{\alpha_0}^\dagger(x, +)$ ; red squares: second adjoint eigenmode  $\varphi_{\alpha_1}^\dagger(x, +)$ ; green triangles: third adjoint eigenmode  $\varphi_{\alpha_2}^\dagger(x, +)$ .

In order to assess the impact of the statistical uncertainty induced by the Monte Carlo method on the eigenvectors, we have performed an ensemble of independent replicas of the  $\alpha$ - $k$  power iterations and we have computed the average and the dispersion of the obtained  $\alpha$ -eigenvectors, as a function of the number of simulated particles per cycle. Numerical findings are reported in Tab. 5.5 and show that the standard deviation of the first few estimators  $R_i$  scales approximately as  $1/\sqrt{P}$ ,  $P$  being the number of particles per cycle.

	Particles per cycle	$R_0$ [-]	$R_1$ [-]	$R_2$ [-]
exact		0.590542	3.0408	1.25702
average	$10^3$	0.59049	3.052	1.302
	$10^4$	0.59053	3.053	1.3021
	$10^5$	0.590534	3.0512	1.30201
Std	$10^3$	$7.7 \times 10^{-5}$	$3.3 \times 10^{-3}$	$2.2 \times 10^{-3}$
	$10^4$	$2.4 \times 10^{-5}$	$1.0 \times 10^{-3}$	$5.5 \times 10^{-4}$
	$10^5$	$7.4 \times 10^{-6}$	$3.3 \times 10^{-4}$	$6.2 \times 10^{-5}$

Table 5.5: Rod model. Comparison of the estimators  $R_i$  obtained from the matrices scored during  $10^3$  replicas of  $\alpha$ - $k$  power iterations, each using  $10^3$  inactive cycles,  $10^3$  active cycles and a variable number of particles per cycle.

### Analysis of the adjoint eigenpairs

We will now focus on the adjoint matrix  $A^\dagger$ , whose elements have been filled by using the Generalized IFP method, as detailed above. For this example, the Monte Carlo calculation has been performed with  $10^8$  particles, and 15 latent generations. The  $\alpha_0$  value needed for the Generalized IFP algorithm has been obtained from the direct calculations done in the previous section. The results of the spectral analysis from the adjoint  $\alpha$ -weighted matrix are recalled in Tab. 5.2 for a discretization of  $N = 1024$  spatial meshes. An excellent agreement is found between the numerical values coming from the  $A^\dagger$  matrix filled by the Monte Carlo calculation and the exact results stemming from the roots of the dispersion law in Eq. (5.66). This means that the relation  $\alpha^\dagger = \alpha$  on the spectrum of the  $\alpha$ -eigenvalues is correctly preserved when weighting  $A^\dagger$  by the fundamental eigenfunction  $\varphi_{\alpha_0}^\dagger$ . This property is also preserved when approximating  $A^\dagger$  by taking the transposed matrix  $A^T$  (although  $A$  is weighted by the direct fundamental eigenfunction), since by construction transposition preserves the spectrum. The first few adjoint eigenfunctions are compared in Fig. 5.5 for the same spatial discretization: again, an excellent agreement is found between the eigenvectors of the  $A^\dagger$  matrix filled by the Generalized IFP method and the exact solutions

stemming from the eigenfunctions adjoint to Eq. (5.64). Observe in particular that  $\varphi_\alpha^\dagger$  satisfies  $\varphi_\alpha^\dagger(x, \pm) = \varphi_\alpha(x, \mp)$ , as expected.

The convergence of the eigenvalues associated to the  $A^\dagger$  matrix is analyzed in Fig. 5.3: not surprisingly, the convergence of the eigenvalues with respect to the matrix discretization  $N$  follows the same pattern as in the direct case. The fundamental eigenvalue  $\alpha_0$  is similarly preserved by the matrix  $A^\dagger$ , independently of  $N$ , whereas the higher eigenvalues are not and converge to the true values in the limit of large  $N$ .

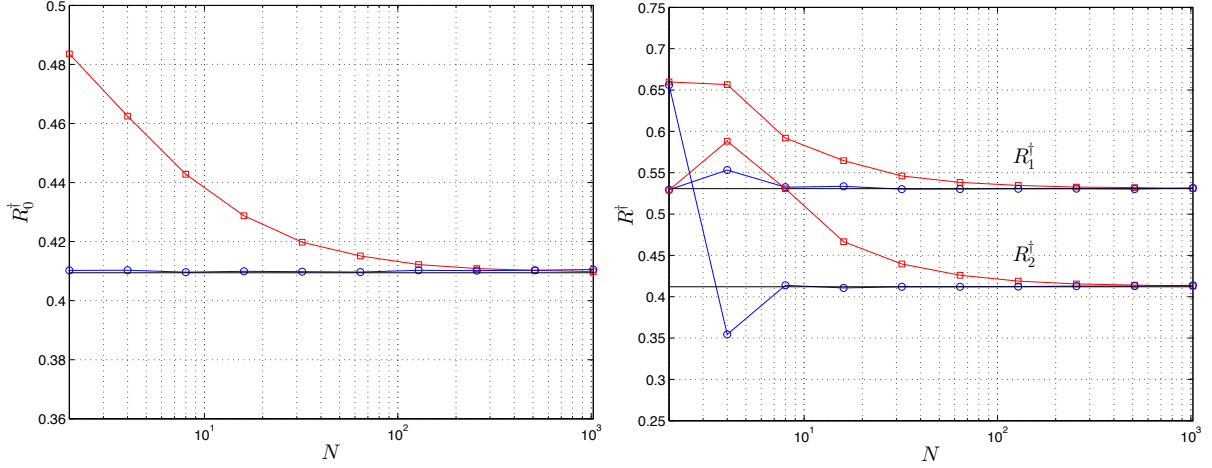


Figure 5.6: Convergence of the first few estimators  $R_i^\dagger$  as a function of the number of spatial meshes  $N$ . Black solid lines correspond to the exact reference values based on Eq. (5.64). Blue circles correspond to results obtained from the adjoint  $\alpha$ -weighted  $A^\dagger$  matrix; red squares correspond to the direct  $\alpha$ -weighted  $A^T$  matrix. Left: the estimator  $R_0^\dagger$  associated to the fundamental adjoint eigenfunction  $\varphi_{\alpha_0}^\dagger(x, +)$ ; right: the estimator  $R_1^\dagger$  associated to the second adjoint eigenfunction  $\varphi_{\alpha_1}^\dagger(x, +)$  and the estimator  $R_2^\dagger$  associated to the second adjoint eigenfunction  $\varphi_{\alpha_2}^\dagger(x, +)$ . Solid lines have been added to guide the eye.

Weighting function	$R_0^\dagger$ [-]	$R_1^\dagger$ [-]	$R_{2,3}^\dagger$ [-]
exact	0.40946	4.04076	1.65441
Generalized IFP	0.41055	4.00166	1.65293
$\alpha$ - $k$ and transposition	0.40982	4.03249	1.65836

Table 5.6: Rod model. Comparison of the adjoint estimators  $R_i^\dagger$  obtained from the matrices filled with the method shown in the first column, for  $N = 1024$  spatial meshes.

In order to analyze the behaviour of the adjoint eigenmodes, we introduce the estimator

$$R_i^\dagger = \frac{|\int_{\frac{L}{2}}^L dx \varphi_{\alpha_i}^\dagger(x, +)|}{|\int_0^L dx \varphi_{\alpha_i}^\dagger(x, +)|}. \quad (5.68)$$

The reference value for  $R_i^\dagger$  can be computed based on the adjoint eigenfunctions derived from Eq. (5.64). Numerical values corresponding to the generalized IFP method and to the transposed matrix obtained from the  $\alpha$ - $k$  method are recalled in Tab. 5.6 for  $N = 1024$  spatial meshes. The convergence analysis of the estimator  $R_i^\dagger$  estimated by the matrix  $A^\dagger$  as a function of the spatial discretization  $N$  is shown in Fig. 5.6. As conjectured, the estimator  $R_0^\dagger$  associated to the fundamental adjoint eigenfunction resulting from the adjoint  $\alpha$ -weighted matrix  $A^\dagger$  is unbiased with respect to the exact solution, independently of the discretization  $N$ . As for the estimator  $R_1^\dagger$  associated with the second eigenfunction, the adjoint  $\alpha$ -weighted matrix  $A^\dagger$  yields a biased result, which converges to the exact limit after approximately  $N = 32$ .

In the same figure we also display the estimators of the adjoint eigenfunctions obtained by taking the transposed direct  $\alpha$ -weighted matrix  $A^T$  in order to approximate  $A^\dagger$ . Figure 5.6 shows that this approach leads to a bias on  $R_i^\dagger$

for the fundamental and the first eigenfunction. Although the bias vanishes as expected in the limit of large  $N$ , this analysis suggests that it is general preferable to compute  $A^\dagger$  rather than approximating the adjoint-weighted matrix by using the transposed matrix  $A^T$ .

### 5.3.2 A continuous-energy transport model

We consider now a continuous-energy transport model in an infinite medium. The model includes scattering with an amnesia kernel [34], capture and fission with two precursor families. All cross sections  $\Sigma_r$  are assumed to have a  $1/\sqrt{E}$  behaviour, i.e.,  $\Sigma_r(E) = \Sigma_r^0/\sqrt{E}$ . The scattering kernel  $M(E)$  is a Maxwell distribution with average energy  $E_s$ . The prompt  $\chi_p(E)$  and delayed  $\chi_d^j(E)$  fission kernels are also assumed to be Maxwellian distributions with average  $E_p$  and  $E_d^j$ ,  $j = 1, 2$ , respectively. These distributions can be expressed as normalized probability density functions, given the following equation

$$M(E) = \frac{2}{\sqrt{\pi}} \frac{1}{\bar{E}^{3/2}} \sqrt{E} e^{-E/\bar{E}}, \quad (5.69)$$

where  $\bar{E}$  is the average energy of the corresponding distribution. The fission multiplicities are taken constant, for the sake of simplicity.

The resulting  $\alpha$  eigenvalue problem reads

$$\left[ \frac{\alpha}{v(E)} + \Sigma_t(E) \right] \varphi_\alpha(E) = M(E) \int_0^\infty dE' \Sigma_s(E') \varphi_\alpha(E') + \chi_p(E) \int_0^\infty dE' \bar{v}_p \Sigma_f(E') \varphi_\alpha(E') + \sum_j \frac{\lambda_j}{\lambda_j + \alpha} \chi_d^j(E) \int_0^\infty dE' \bar{v}_d^j \Sigma_f(E') \varphi_\alpha(E'), \quad (5.70)$$

where  $v(E) = \sqrt{E}$ . By virtue of the simple functional forms chosen for this configuration, the eigenvalues and eigenfunctions can be determined exactly. In particular, the eigenvalues are the roots of the dispersion law

$$\Lambda(\alpha) = \alpha + \Sigma_a^0 - \bar{v}_p \Sigma_f^0 - \sum_j \frac{\lambda_j}{\lambda_j + \alpha} \bar{v}_d^j \Sigma_f^0 = 0, \quad (5.71)$$

where  $\Sigma_a^0 = \Sigma_t^0 - \Sigma_s^0$ , and the eigenfunctions read

$$\varphi_\alpha(E) = \frac{\sqrt{E}}{\alpha + \Sigma_t^0} \left[ \Sigma_s^0 M(E) + \bar{v}_p \Sigma_f^0 \chi_p(E) + \sum_j \frac{\lambda_j}{\lambda_j + \alpha} \bar{v}_d^j \Sigma_f^0 \chi_d^j(E) \right], \quad (5.72)$$

for the values  $\alpha$  that satisfy the dispersion law. As for the adjoint eigenvalue problem, we have the equation

$$\left[ \frac{\alpha}{v(E)} + \Sigma_t(E) \right] \varphi_\alpha^\dagger(E) = \Sigma_s(E) \int_0^\infty dE' M(E') \varphi_\alpha^\dagger(E') + \bar{v}_p \Sigma_f(E) \int_0^\infty dE' \chi_p(E') \varphi_\alpha^\dagger(E') + \sum_j \frac{\lambda_j}{\lambda_j + \alpha} \bar{v}_d^j \Sigma_f(E) \int_0^\infty dE' \chi_d^j(E') \varphi_\alpha^\dagger(E'). \quad (5.73)$$

By inspection, the eigenfunctions are  $\varphi_\alpha^\dagger(E) = 1$ , independently of  $\alpha$ , with the same associated spectrum as in the direct problem.

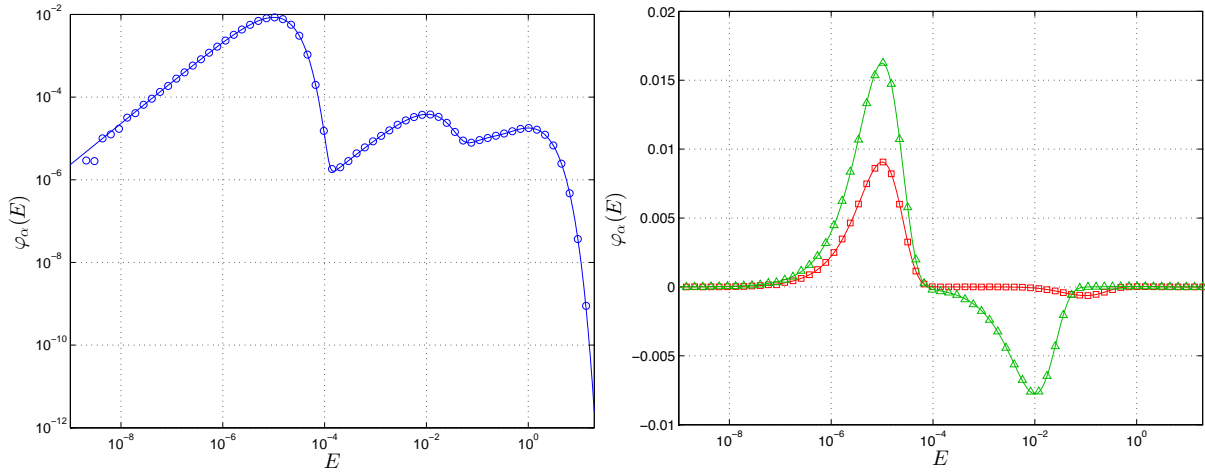


Figure 5.7: A continuous-energy transport problem. Comparison of the direct eigenfunctions resulting from the matrices filled by  $\alpha$ - $k$  power iteration (displayed as symbols) with the reference solutions given in Eq. (5.72) (displayed as solid lines). Left: blue circles denote the fundamental eigenfunction  $\varphi_{\alpha_0}(E)$ : right: red squares the second eigenfunction  $\varphi_{\alpha_1}(E)$  and green triangles the third eigenfunction  $\varphi_{\alpha_2}(E)$ .

For this example, we have chosen the following parameters:  $\Sigma_c^0 = 0.6$ ,  $\Sigma_s^0 = 0.3$ ,  $\Sigma_f^0 = 0.1$ ; for the fission multiplicities we have set  $\bar{\nu}_p = 2$  and  $\bar{\nu}_d^j = \beta_j \bar{\nu}_d$ , with  $\bar{\nu}_d = 0.5$ ,  $\beta_1 = 0.25$  and  $\beta_2 = 0.75$ ; for the scattering law we have taken  $E_s = 10^{-5}$ ; for the prompt and delayed fission kernels we have taken the averages  $E_p = 1$ ,  $E_d^1 = 0.1$  and  $E_d^2 = 0.01$ , respectively; for the precursor decay constants we have taken  $\lambda_1 = 2.5$  and  $\lambda_2 = 5$ .

weighting function	$\alpha_0$ [s <sup>-1</sup> ]	$\alpha_1$ [s <sup>-1</sup> ]	$\alpha_2$ [s <sup>-1</sup> ]
exact	-0.44365	-2.51495	-5.04140
$\alpha$ - $k$	-0.44369	-2.51490	-5.04141
Generalized IFP	-0.44367	-2.51493	-5.04132

Table 5.7: Continuous-energy model. Comparison of the first few eigenvalues obtained from the matrices scored with the method shown in the first column, with  $N = 1024$  energy groups.

The first few eigenvalues obtained from the matrices are compared to the reference solutions in Tab. 5.7 for  $N = 1024$  energy meshes. The direct eigenfunctions resulting from the matrices filled by  $\alpha$ - $k$  power iteration (with  $10^3$  inactive cycles,  $10^3$  active cycles and  $10^5$  particles per cycle) are compared to the analytical solutions in Fig. 5.7, for a discretization corresponding to  $G = 256$  energy intervals. The first few modes are in excellent agreement with the reference solutions. The numerical findings for the adjoint problem, obtained from the Generalized IFP method with  $10^8$  particles and 15 latent generations, are shown in Fig. 5.8: again, an excellent agreement is found between the eigenvectors stemming from the matrices and the exact solutions, despite the fact that the adjoint eigenfunctions for this problem are degenerate.

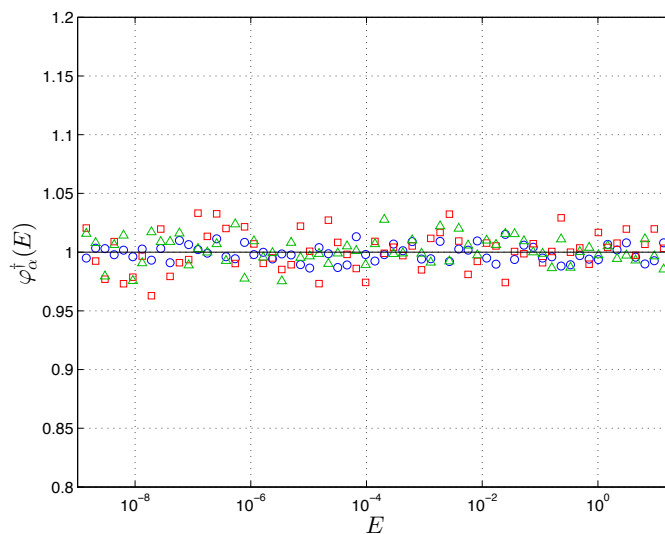


Figure 5.8: A continuous-energy transport problem. Comparison of the adjoint eigenfunctions resulting from the matrices filled by Generalized IFP method (displayed as symbols) with the reference solutions given in Eq. (5.72) (displayed as solid lines). Blue circles denote the fundamental adjoint eigenfunction  $\varphi_{\alpha_0}^\dagger(E)$ ; red squares the second adjoint eigenfunction  $\varphi_{\alpha_1}^\dagger(E)$ ; green triangles the third adjoint eigenfunction  $\varphi_{\alpha_2}^\dagger(E)$ .

## 5.4 Discussion

The examples discussed in the previous section are very simple and have been precisely chosen in order to compare the obtained numerical results against reference solutions. In view of the application of the proposed methods to real-world reactor configurations, some issues must be carefully examined and taken into account.

The first concerns the size of the matrix operators and hence the involved memory footprint. A first glance to the involved order of magnitudes might suggest that the overall size of the matrices involved in  $\alpha$ -eigenvalue problems may become too large to work with for any practical case, due to the need of separately discretizing space, direction and energy (contrary to the  $k$ -eigenvalue problem, where only a spatial discretization is typically required [35, 22]). Consider for instance a three-dimensional configuration, and assume that each variable is partitioned into  $10^2$  bins: this would lead to a total number of  $10^{10}$  bins, i.e., to a number of  $10^{20}$  matrix entries. This applies to both direct and adjoint matrices. Such huge number, supposing that each entry is represented by a double-precision floating-point number, clearly corresponds to an unaffordable memory on current machines (and on future, at least for a very long time).

In practice, however, the  $\alpha$ -eigenvalue matrices have been already applied to realistic systems, including small research reactors [8]: as discussed in Section 5.2.1, the involved matrices have a sparse nature, and the number of non-null entries is much smaller than the total size of the matrices (see in particular Eq. (5.49)). Furthermore, one can often take advantage of the existing symmetries in order to reduce the dimension of the problem. Moreover, for the energy and angle variable  $10^2$  bins are probably excessive with respect to most problems of interest. To provide an example, for a two-dimensional representation of a reactor core, by taking  $N_x = N_y = 10^2$  for the spatial mesh,  $M = 8$  for the directions,  $G = 30$  for the energy groups and  $J = 6$  for the precursor families, we would have  $\sim 6 \times 10^{13}$  bins for the full matrix, but less than  $\sim 6 \times 10^8$  non-null entries. Even in this case, however, and despite all the simplifications, the memory footprint would be challenging for current machines. Numerical tests of convergence should be also performed a posteriori in order to ensure that at least the spatial shape of the eigenvectors has been correctly captured. The benchmark configurations examined in this chapter clearly do not address these problems, since only a single dimension has been discretized and careful convergence tests were thus possible.

The second issue concerns the applicability of these matrices to the analysis of system changes. The whole  $\alpha$ -eigenvalue expansion is based on the assumption that the physical properties of the system under analysis (such as cross sections, fission spectra, multiplicities, etc.) do not evolve with time: eigenvalues and eigenvectors are

computed for a specific state. In real-world configurations, these properties naturally change, due to external actions (control rod movements), physical feedbacks (Doppler effect, etc.), or both. In principle, once the system changes the computed alpha eigenvalues and eigenvectors are no longer valid and cannot be used. This leads to two different approaches: one can either introduce (short) time steps and re-compute the required matrices at each time step, or use some clever interpolation between the initial and final configurations of the system. The former method would lead to an unreasonable memory occupation (and most probably also computation time). The latter method has been suggested [85] and successfully applied [87] for the Transient Fission Matrix method, and seems thus much more promising. In particular, the application of perturbation techniques such as correlated sampling has been shown to enhance the performances of the interpolation methods in realistic applications, including multi-physics feedbacks [86]. An overview of the Transient Fission Matrix method is provided in Appendix A.

In view of these considerations, and based on the increasing availability of direct time-dependent Monte Carlo simulations for reactor physics problems (which natively include moving geometries and physical feedbacks [141, 41]), the main interest of the  $\alpha$ -eigenvalue matrix operators seems for higher-order mode analysis rather than for reconstructing the time evolution of a system via eigenmode expansion: knowledge of the first few  $\alpha$ -eigenvalues and eigenfunctions for a given reactor state might help, e.g., in locating the most appropriate detector positions for on-line core monitoring. Nonetheless, a comparison in terms of performances and accuracy with respect to existing matrix-based methods (using time-dependent Monte Carlo methods as a reference) for the approximation of the reactor kinetics will deserve further investigation.

## 5.5 Conclusions

Knowledge of the  $\alpha$ -eigenpairs is key to several applications in reactor physics. In a series of recent works, it has been proposed to use Monte Carlo methods in order to estimate the elements of the matrices that represent the discretized formulation of the operators involved in the  $\alpha$ -eigenvalue problem. In this chapter, we have suggested some strategies to overcome two possible shortcomings of the existing algorithms. We have shown that the bias possibly appearing on the direct fundamental eigenvalue and eigenvector for smaller sizes of the discretized matrix can be removed by using the  $\alpha$ - $k$  modified power iteration method as a weighing function. This corresponds to weighting the matrix elements by the fundamental mode  $\varphi_{\alpha 0}$ , which is expected to preserve the fundamental eigenvalue and eigenvector of the matrix, similarly to what occurs for the fission matrix in  $k$ -eigenvalue problems. We have successively shown that the matrix associated to the adjoint  $\alpha$ -eigenvalue problem can be estimated by using the G-IFP method, which was recently introduced as a reference Monte Carlo method to compute the fundamental adjoint  $\alpha$ -eigenfunction. Since this approach corresponds to weighting the matrix elements by the fundamental adjoint eigenfunction, the fundamental adjoint eigenvector of the discretized matrix will be similarly preserved.

The proposed direct and adjoint methods have been verified on two benchmark problems where exact reference solutions were available for both the eigenvalue spectrum and the direct and adjoint eigenfunctions, and their convergence and accuracy have been extensively assessed. The impact of alternative weighting schemes (such as the  $k$ -eigenvalue fundamental mode or the flux resulting from solving a fixed-source problem) and the differences between the adjoint matrix and the transposed direct matrix are most probably emphasized by the choice of the benchmark problems presented in this chapter: in the remaining parts of this manuscript, we will extensively assess the performances and the robustness of the proposed method for more realistic configurations combining spatial and energy heterogeneities.

We conclude by observing that the strategy presented in order to fill the matrix elements of the adjoint matrix by the G-IFP method might be easily extended to the  $k$ -eigenvalue formulation: instead of using the transposed direct fission matrix, one could use the regular IFP method (which yields the importance function for the  $k$ -eigenvalue problems) so as to produce the adjoint fission matrix, thus avoiding the bias on the fundamental adjoint eigenvector. Moreover, since the proposed method estimate the linear and adjoint transport operators, it is in principle possible to combine the corresponding matrices in order to recast and solve eigenvalue problems different from the  $\alpha$ -formulation.



## Chapter 6

# Eigenvalue separation: a numerical investigation

### 6.1 Introduction

In the previous Chapter, we have successfully generalized the well-known fission matrix method so as to fill by Monte Carlo simulations the elements of matrix operators involved in the  $\alpha$ -eigenvalue formulation, which allows having a complete (albeit approximated) picture of the whole  $\alpha$ -spectrum. In this Chapter, these tools will be deployed together with the fission matrix method for the spectral analysis of a few relevant benchmark configurations, for the purpose of illustrating how the higher-order  $k$ - and  $\alpha$ -eigenvalues and eigenfunctions behave as a function of the physical parameters. Such investigation extends the work done in Chapter 4 concerning the fundamental eigenvalues and eigenfunctions. All the simulations presented in this Chapter have been performed by using the newly implemented test-bed Monte Carlo code described in Section 3.7.1. As mentioned in Chapter 1, the tightness (or equivalently the level of decoupling) of a reactor core is typically characterized in terms of the eigenvalue separation, which for the  $k$ -eigenvalue formulation reads

$$\text{E.S.}_n(k) = \frac{1}{k_n} - \frac{1}{k_0}, \quad (6.1)$$

with  $n \geq 1$  [37, 98, 144, 73, 120]. The case  $n = 1$  plays a peculiar role, and is frequently referred to without using the index [120], namely,

$$\text{E.S.} = \text{E.S.}_1(k) = \frac{1}{k_1} - \frac{1}{k_0}. \quad (6.2)$$

The system is said to be *tightly coupled* if the first two eigenvalues are separated, and *loosely coupled* otherwise. A closely related quantity is the dominance ratio

$$\text{DR} = \frac{k_1}{k_0}, \quad (6.3)$$

which is a bounded value smaller than one and it can be monotonically mapped onto the E.S., thus sharing the same information content.

As for the  $\alpha$ -eigenvalues, the concept of eigenvalue separation or dominance ratio does not seem to have drawn much attention, to the best of our knowledge, although in the mathematical literature the analogous notion of *spectral gap* is widely used for eigenvalue problems similar to the  $\alpha$ -eigenvalue formulation (for instance in the context of the time-dependent diffusion equation [84, 125, 26, 2, 44]). In the same spirit as for the  $k$ -eigenvalue problems, we can thus introduce the notion of eigenvalue separation for the  $\alpha$ -eigenvalues, which immediately calls for a distinction between the formulation including the precursor contributions (usually called the “delayed eigenvalues”) and the one neglecting the precursor contributions (usually called the “prompt eigenvalues”). In the following, we will denote by  $\alpha$  the eigenvalues including the delayed contributions, whereas  $\alpha_p$  will denote the

eigenvalues including only the prompt contributions. This distinction stems from the fact that, for a typical PWR reactor, the  $\alpha$ -spectrum will have a natural ordering imposed by the fact that [72, 133, 132, 70]

$$v_d^j \ll 1, \text{ and } \lambda_j \ll \Sigma_t v. \quad (6.4)$$

As a consequence, the  $\alpha$ -spectrum splits into a “prompt” component and a “delayed” component, which are easily distinguished on the complex plane [133, 132]. Numerical investigations have shown that the delayed part of the  $\alpha$  spectrum consists of  $J$  “clusters” of real eigenvalues, with the  $j$ -th cluster,  $j = 1, \dots, J$ , being a denumerable set of eigenvalues in the interval  $(-\lambda_j, -\lambda_{j-1})$ ,  $J$  being the total number of precursor families (we set  $\lambda_0$  to infinity). These eigenvalues are tightly regrouped at the right of each decay constant  $-\lambda_j$  for family  $j$  on the complex plane [70, 133, 132]. The occurrence of the clustering of delayed eigenvalues had been first suggested by [45]. These considerations have been previously introduced for the “rod model” analysis in Section 5.3.1. The prompt part of the  $\alpha$ -spectrum contains discrete eigenvalues, these latter appearing at the left of  $-\lambda_j$  [70, 133, 132, 1] and a continuum portion (if any) at the left of the Corngold limit. In view of these considerations, it seems natural to introduce the *delayed* eigenvalue separation

$$\text{E.S.}_n(\alpha_d) = \alpha_{d,n} - \alpha_0, \quad (6.5)$$

where  $\alpha_{d,n}$  is the delayed eigenvalue of order  $n$  and  $\alpha_0$  is the fundamental eigenvalue, and the *prompt* eigenvalue separation

$$\text{E.S.}_n(\alpha_p) = \alpha_{p,n} - \alpha_{p,0}, \quad (6.6)$$

where  $\alpha_{p,n}$  is the prompt eigenvalue of order  $n$  and  $\alpha_{p,0}$  is the prompt eigenvalue with the largest real part.

Experimental and numerical investigations have shown that a small  $\text{E.S.}(k)$  would increase the probability for a system to propagate instabilities, thus enhancing complex space-time patterns (as opposed to systems displaying a large  $\text{E.S.}$ , which behave as point-kinetics) [120]. This is especially relevant for loosely-coupled nuclear reactors, such as breeders having alternating regions of highly-enriched fuel and depleted blankets [120]. By virtue of its key role in understanding the system kinetics, and in particular the reactor response due to external perturbations and tilts, the  $k$ -eigenvalue separation has been extensively investigated [127, 38, 3, 54, 113, 78].

In the following, we will explore and compare the properties of  $\text{E.S.}_n(k)$ ,  $\text{E.S.}_n(\alpha_d)$  and  $\text{E.S.}_n(\alpha_p)$  for a few significant configurations, and will complement this analysis by a careful investigation of the associated fundamental and higher-order eigenmodes. In order to probe the behavior of these estimators, we have selected some simple systems, so that we can avoid unnecessary complications and yet retain the key physical ingredients. The underlying idea is to ascertain whether the  $k$  and  $\alpha$  spectral analysis can provide useful information concerning the system response when a parameter related to a decoupling effect is progressively increased. The eigenpairs associated to the eigenvalue problems discussed in this chapter have been computed with the MATLAB script mentioned in Section 5.2.5, based on the matrices estimated by the test-bed Monte Carlo code.

## 6.2 Choice of the benchmark configurations

In [120] it has been pointed out that homogeneous and heterogeneous systems behave quite differently with respect to eigenvalue separation. In homogeneous systems, small  $\text{E.S.}(k)$  can be attained only by increasing the system size. Under these circumstances, not only  $\text{E.S.}_1(k)$ , but all higher-order  $\text{E.S.}_n(k)$  will be small: the physical meaning of this behavior is that many  $k$ -eigenmodes will be excited simultaneously. Thus, subject to local perturbations, the system will generally respond with complex space-dependent patterns, where several  $k$ -eigenmodes may be present at the same time, and the fundamental eigenmode will not have a privileged role [120]. On the contrary, in heterogeneous systems it is possible to have a small  $\text{E.S.}_1(k)$ , but much larger higher-order  $\text{E.S.}_n(k)$ : these configurations are typically obtained in loosely-coupled cores where two fissile regions are separated by a sufficiently thick central moderator or absorber layer.

Based on these observations, for our numerical investigations we have selected two families of benchmark configurations, respectively homogeneous and heterogeneous, whose physical parameters will be presented in Section 6.3.

The systems will be made progressively more decoupled, in the sense defined above, by acting on the overall

system size (for the homogeneous configurations), and on the thickness of the layers (for the heterogeneous configurations): specific details will be provided in the following sections. In order to make our comparisons fair, we have decided to make each configuration critical (i.e.,  $k_0 = 1$  or equivalently  $\alpha_0 = 0$ ) by adjusting a free parameter. In practice, this is achieved by adjusting the capture cross section of the fissile material: the computed  $k_0$  must lie close to 1, within 20 pcm uncertainty. An important point is that, since we set the physical parameters so that the configurations are critical, the fundamental  $k$ -eigenmode will coincide with the fundamental  $\alpha$ -eigenmode. As a consequence, we will be allowed to use the regular  $k$  power iteration in order to weight the matrix elements required for the spectral analysis, which ensures faster convergence of the Monte Carlo methods.

For both the homogeneous and heterogeneous systems, we will investigate 6 different configurations, corresponding to an increasing degree of decoupling. Several kinds of boundary conditions will be tested, in order to ascertain their impact on the eigenvalue separation. Since the properties of the  $\alpha$  eigenvalue separation are rather unexplored, we have primarily used the  $k$ -eigenvalue separation to assess the degree of decoupling of the proposed configuration, by setting a target of at least DR = 0.95 for the most decoupled configuration of the benchmarks. For each case, we will analyze the dominance ratio from Eq. (6.3), the  $k$ -eigenvalue separation from Eq. (6.1), and the prompt and delayed  $\alpha$ -eigenvalue separation using Eqs. (6.6) and (6.5). Moreover, when significant, we will show the first few  $k$ - and  $\alpha$ -eigenmodes.

### 6.3 Simulation settings

The configurations analyzed in this chapter address multi-group particle transport in simplified 1D and 2D geometries, with reflecting and leakage boundary conditions. The energy domain is partitioned into three groups: fast, epithermal and thermal. Macroscopic cross sections, velocity, neutron yields and prompt fission emission spectra have been taken with minimal modifications from the reference [163], where homogenized materials compatible with realistic configurations had been previously proposed. In particular, we have adjusted the velocities and consequently modified the macroscopic cross sections defined for the UO<sub>2</sub> and H<sub>2</sub>O materials of reference [163] in order to preserve reaction rates.

Precursor families (which were not available in [163]) are defined by using the <sup>235</sup>U delayed data from the ENDF/B-VI nuclear library [102] recalled by Cullen in [29]. The average delayed emission energy  $\bar{E}_d^j$  is associated to a specific speed  $\bar{v}$ , which is linearly interpolated between the velocity values ( $v_1$  and  $v_2$ ) defined in reference [163]. Emission probabilities for each delayed neutron are linearly interpolated as:

$$\chi_{d1}^j = 1 - \frac{|\bar{v} - v_1|}{v_1 - v_2}, \quad (6.7)$$

$$\chi_{d2}^j = 1 - \frac{|\bar{v} - v_2|}{v_1 - v_2}, \quad (6.8)$$

for the first and the second energy group, respectively.

According to these modifications, the materials UO<sub>2</sub> and H<sub>2</sub>O will have the properties shown in Tabs. 6.1, 6.2 and 6.3, respectively.

parameters	fast group	epithermal group	thermal group
$v(g)$ [cm/s]	$1.66743 \times 10^9$	$1.73734 \times 10^7$	$3.46850 \times 10^5$
$\Sigma_c(g)$ [cm <sup>-1</sup> ]	$3.264 \times 10^{-4}$	$9.7371 \times 10^{-3}$	$2.9252 \times 10^{-2}$
$\Sigma_f(g)$ [cm <sup>-1</sup> ]	$3.0586 \times 10^{-3}$	$2.1579 \times 10^{-3}$	$5.6928 \times 10^{-2}$
$\Sigma_s(1 \rightarrow g)$ [cm <sup>-1</sup> ]	$2.21062 \times 10^{-1}$	$7.3843 \times 10^{-2}$	0
$\Sigma_s(2 \rightarrow g)$ [cm <sup>-1</sup> ]	0	$7.77642 \times 10^{-1}$	$4.3803 \times 10^{-2}$
$\Sigma_s(3 \rightarrow g)$ [cm <sup>-1</sup> ]	0	0	1.55272
$\bar{v}(g)$ [-]	2.4	2.4	2.4
$\chi_p(g)$ [-]	0.878198	0.121802	0

Table 6.1: Parameters of the fissile material for the heterogeneous configuration.

parameters	1 <sup>st</sup> family	2 <sup>nd</sup> family	3 <sup>rd</sup> family	4 <sup>th</sup> family	5 <sup>th</sup> family	6 <sup>th</sup> family
$\beta_j$ [pcm]	$2.275 \times 10^1$	$1.17455 \times 10^2$	$1.12138 \times 10^2$	$2.51407 \times 10^2$	$1.03077 \times 10^2$	$4.3173 \times 10^1$
$\lambda_j$ [ $\text{cm}^{-1}$ ]	$1.3336 \times 10^{-2}$	$3.2739 \times 10^{-2}$	$1.2078 \times 10^{-1}$	$3.0278 \times 10^{-1}$	$8.4949 \times 10^{-1}$	2.8530
$\chi_d^j(1)$ [-]	0.52296	0.56487	0.54697	0.61504	0.59265	0.60533
$\chi_d^j(2)$ [-]	0.47704	0.43513	0.45303	0.38496	0.40735	0.39467

Table 6.2: Delayed parameters of the fissile material.

parameters	fast group	epithermal group	thermal group
$v(g)$ [cm/s]	$1.66743 \times 10^9$	$1.73734 \times 10^7$	$3.46850 \times 10^5$
$\Sigma_c(g)$ [ $\text{cm}^{-1}$ ]	$3.05 \times 10^{-4}$	$3.699 \times 10^{-4}$	$1.825 \times 10^{-2}$
$\Sigma_s(1 \rightarrow g)$ [ $\text{cm}^{-1}$ ]	$2.27125 \times 10^{-1}$	$1.0464 \times 10^{-1}$	0
$\Sigma_s(2 \rightarrow g)$ [ $\text{cm}^{-1}$ ]	0	1.02817	$9.7961 \times 10^{-2}$
$\Sigma_s(3 \rightarrow g)$ [ $\text{cm}^{-1}$ ]	0	0	2.76295

Table 6.3: Parameters of the moderator material for the heterogeneous configuration.

The heterogeneous configurations described in Section 6.5 are composed of these two materials. The homogeneous configurations analyzed in Section 6.4 are characterized by a single material obtained by summing the macroscopic cross sections of the fissile and the moderator materials. Properties and parameters of this homogenized material are defined in Tab. 6.4.

parameters	fast group	epithermal group	thermal group
$v(g)$ [cm/s]	$1.66743 \times 10^9$	$1.73734 \times 10^7$	$3.46850 \times 10^5$
$\Sigma_c(g)$ [ $\text{cm}^{-1}$ ]	$6.314 \times 10^{-4}$	$1.0107 \times 10^{-2}$	$4.7502 \times 10^{-2}$
$\Sigma_f(g)$ [ $\text{cm}^{-1}$ ]	$3.0586 \times 10^{-3}$	$2.1579 \times 10^{-3}$	$5.6928 \times 10^{-2}$
$\Sigma_s(1 \rightarrow g)$ [ $\text{cm}^{-1}$ ]	$4.48187 \times 10^{-1}$	$1.78483 \times 10^{-1}$	0
$\Sigma_s(2 \rightarrow g)$ [ $\text{cm}^{-1}$ ]	0	1.805812	$1.41764 \times 10^{-1}$
$\Sigma_s(3 \rightarrow g)$ [ $\text{cm}^{-1}$ ]	0	0	$1.55272 \times 10^1$
$\bar{v}(g)$ [-]	2.4	2.4	2.4
$\chi_p(g)$ [-]	0.878198	0.121802	4.31567

Table 6.4: Parameters of the material for the homogeneous configurations.

## 6.4 Homogeneous benchmark configurations

We begin our analysis with the case of homogeneous configurations. The occurrence of decoupling effects for homogeneous configurations can emerge for a sufficiently large size of the system with respect to the neutron migration area [120]. In this section, we investigate the presence of these effects for critical 1D and 2D homogeneous configurations with reflective and leakage boundary conditions.

The critical state of the homogeneous configurations having reflective boundary conditions can be determined exactly. The critical level is attained by adjusting the macroscopic capture cross sections by a factor  $a$  as follows:

$$\Sigma'_c = a\Sigma_c. \quad (6.9)$$

The value of  $a$  corresponding to the physical parameters given in Tab. 6.4 is equal to  $a = 1.49698$  independently of the domain size. For a given parameter  $a$ , the dominance ratio will be imposed by adjusting the size of the domain [120]. Six cases have been selected for the analysis of homogeneous systems, each defined by a characteristic length  $L$  ranging from 50 cm to 100 cm. This length corresponds to the actual length of the geometry for 1D configurations and to the side of a square geometry for 2D configurations.

The parametric study performed for homogeneous systems with leakage boundary conditions requires an additional step, since the size of the domain  $L$  does influence the critical state of the configuration. In particular, we have started our analysis from the largest (the most decoupled) 1D and 2D configurations found for reflective boundary conditions. Then, we have estimated the new coefficient  $a$  in order to readjust the configuration to the critical level after replacing reflective boundary conditions with leakage boundary conditions. This change of the boundary conditions implies that the critical level depends on the size of the system. For this reason, we have adjusted a second time the capture cross section by adding a factor  $b$  as follows:

$$\Sigma'_c = a\Sigma_c + \frac{b}{v}, \quad (6.10)$$

for each size of the configuration under analysis.

The introduction of a second factor  $b/v$  allows a finer adjustment with respect to the multiplicative factor  $a$ . This additional adjustment is required in order to calibrate all cases of different sizes to the critical level. This adjustment has been performed during a power iteration calculation that iteratively seeks the value of  $b$  which makes the system critical.

### 6.4.1 Homogeneous configurations with reflective boundary conditions

#### 1D geometry

The first benchmark configuration analyzed in this section concerns 1D homogeneous systems of different lengths with reflective boundary conditions. The fundamental eigenvalues  $k_0$  computed by the  $k$  power iteration are shown in the second column of Tab. 6.5. For these calculations,  $5 \times 10^4$  particles per cycle are simulated, for a total of  $4.1 \times 10^3$  cycles ( $4 \times 10^3$  active,  $10^2$  inactive). During these simulations, we have activated the matrix-filling methods.

In order to build the matrix operators, the length of the domain has been partitioned into  $N_x = c \times L$  space intervals along the  $x$ -axis, where  $c = 10 \text{ cm}^{-1}$ , in order to keep a constant bin width. The cosine of the particle direction with respect to the  $x$ -axis is uniformly partitioned into  $M_x = 4$  intervals, whereas the energy groups and precursor families are fixed at  $G = 3$  and  $J = 6$ , respectively. The total size of the matrix defining the  $\alpha$ -eigenvalue problem ranges from  $9.0 \times 10^3$  ( $L = 50 \text{ cm}$ ) to  $1.8 \times 10^4$  ( $L = 100 \text{ cm}$ ), whereas the matrix defining the  $k$ -eigenvalue problem ranges from  $6.0 \times 10^3$  to  $1.2 \times 10^4$ . The eigenvalues computed from the matrix-form of the corresponding eigenvalue problem are shown in Tabs. 6.5 ( $k$ -eigenvalues), 6.6 ( $\alpha$ -eigenvalues) and 6.7 (prompt  $\alpha$ -eigenvalues). All fundamental eigenvalues  $k_0$  computed from the matrix of the corresponding eigenvalue problem are within  $2\sigma$  standard deviation from the Monte Carlo results obtained from the  $k$  power iteration. The absolute values of the fundamental eigenvalues  $\alpha_0$  are smaller than  $2 \times 10^{-3} \text{ s}^{-1}$ .

L [cm]	$k_0^{MC}$ [-]	$k_0$ [-]	$k_1$ [-]	$k_2$ [-]	$k_3$ [-]	$k_4$ [-]	$k_5$ [-]
50	$0.9999 \pm 1.0 \times 10^{-4}$	1.0000	0.9832	0.9356	0.8644	0.7789	0.6881
60	$0.9999 \pm 1.0 \times 10^{-4}$	1.0000	0.9882	0.9545	0.9024	0.8369	0.7639
70	$0.9999 \pm 1.0 \times 10^{-4}$	1.0000	0.9914	0.9661	0.9266	0.8757	0.8167
80	$1.0001 \pm 1.0 \times 10^{-4}$	1.0001	0.9934	0.9741	0.9431	0.9025	0.8543
90	$0.9999 \pm 1.0 \times 10^{-4}$	1.0000	0.9948	0.9793	0.9544	0.9215	0.8817
100	$0.9999 \pm 1.0 \times 10^{-4}$	0.9999	0.9956	0.9831	0.9628	0.9355	0.9023

Table 6.5: First  $k$ -eigenvalues for the 1D homogeneous configuration with reflective boundary conditions as a function of the size  $L$  of the system. The second column displays the fundamental eigenvalues  $k_0$  computed by the test-bed Monte Carlo code for the  $k$ -eigenvalue problem and the corresponding standard deviations. All other eigenvalues have been computed from the matrix-form of the  $k$ -eigenvalue problem of the corresponding case.

L [cm]	$\alpha_0$ [s <sup>-1</sup> ]	$\alpha_1$ [s <sup>-1</sup> ]	$\alpha_2$ [s <sup>-1</sup> ]	$\alpha_3$ [s <sup>-1</sup> ]	$\alpha_4$ [s <sup>-1</sup> ]	$\alpha_5$ [s <sup>-1</sup> ]
50	$4.518 \times 10^{-4}$	$-1.315 \times 10^{-2}$	$-1.329 \times 10^{-2}$	$-1.332 \times 10^{-2}$	$-1.332 \times 10^{-2}$	$-1.333 \times 10^{-2}$
60	$-4.818 \times 10^{-4}$	$-1.307 \times 10^{-2}$	$-1.327 \times 10^{-2}$	$-1.331 \times 10^{-2}$	$-1.332 \times 10^{-2}$	$-1.333 \times 10^{-2}$
70	$-1.451 \times 10^{-4}$	$-1.296 \times 10^{-2}$	$-1.325 \times 10^{-2}$	$-1.330 \times 10^{-2}$	$-1.331 \times 10^{-2}$	$-1.333 \times 10^{-2}$
80	$1.771 \times 10^{-3}$	$-1.282 \times 10^{-2}$	$-1.322 \times 10^{-2}$	$-1.329 \times 10^{-2}$	$-1.331 \times 10^{-2}$	$-1.333 \times 10^{-2}$
90	$-6.398 \times 10^{-4}$	$-1.267 \times 10^{-2}$	$-1.319 \times 10^{-2}$	$-1.327 \times 10^{-2}$	$-1.330 \times 10^{-2}$	$-1.333 \times 10^{-2}$
100	$-1.032 \times 10^{-3}$	$-1.251 \times 10^{-2}$	$-1.315 \times 10^{-2}$	$-1.326 \times 10^{-2}$	$-1.329 \times 10^{-2}$	$-1.333 \times 10^{-2}$

Table 6.6: First  $\alpha$ -eigenvalues for the 1D homogeneous configuration with reflective boundary conditions as a function of the size L of the system. These values have been computed from the matrix-form of the  $\alpha$ -eigenvalue problem of the corresponding case.

L	$\alpha_{p,0}$ [s <sup>-1</sup> ]	$\alpha_{p,1}$ [s <sup>-1</sup> ]	$\alpha_{p,2}$ [s <sup>-1</sup> ]	$\alpha_{p,3}$ [s <sup>-1</sup> ]	$\alpha_{p,4}$ [s <sup>-1</sup> ]	$\alpha_{p,5}$ [s <sup>-1</sup> ]
50	$-3.015 \times 10^2$	$-1.086 \times 10^3$	$-3.333 \times 10^3$	$-6.762 \times 10^3$	$-1.102 \times 10^4$	$-1.576 \times 10^4$
60	$-3.047 \times 10^2$	$-8.536 \times 10^2$	$-2.437 \times 10^3$	$-4.922 \times 10^3$	$-8.114 \times 10^3$	$-1.179 \times 10^4$
70	$-3.033 \times 10^2$	$-7.049 \times 10^2$	$-1.888 \times 10^3$	$-3.763 \times 10^3$	$-6.215 \times 10^3$	$-9.118 \times 10^3$
80	$-2.975 \times 10^2$	$-6.087 \times 10^2$	$-1.514 \times 10^3$	$-2.977 \times 10^3$	$-4.916 \times 10^3$	$-7.258 \times 10^3$
90	$-3.055 \times 10^2$	$-5.481 \times 10^2$	$-1.270 \times 10^3$	$-2.444 \times 10^3$	$-4.008 \times 10^3$	$-5.920 \times 10^3$
100	$-3.063 \times 10^2$	$-5.059 \times 10^2$	$-1.090 \times 10^3$	$-2.048 \times 10^3$	$-3.337 \times 10^3$	$-4.927 \times 10^3$

Table 6.7: First prompt  $\alpha$ -eigenvalues for the 1D homogeneous configuration with reflective boundary conditions as a function of the size L of the system. These values have been computed from the matrix-form of the  $\alpha$ -eigenvalue problem of the corresponding case.

For the sake of completeness, we show both the  $k$ - and the  $\alpha$ -spectra on the complex plane in Fig. 6.1. The (very small) imaginary part of the  $k$ -spectrum is merely due to the statistical uncertainties propagated from the stochastic estimation of the matrix elements on the eigenvalues. The  $\alpha$ -spectrum displays two circles due to the four direction intervals chosen for the simulations: this feature is repeated for each energy group considered in the spectrum, as already pointed out in reference [8]. Figure 6.2 shows the zoom on all delayed eigenvalue clusters (left) and on the delayed eigenvalue cluster associated to the first precursor family (right). The eigenvalues are concentrated on the right of the  $-\lambda_j$  values, as expected from reference [133, 132]. The dominant eigenvalue  $\alpha_{d,0}^j$  of the  $j$ -th delayed cluster is separated from the other eigenvalues of the same precursor family [133, 132]. The zoom of Fig. 6.2 (left) shows the gap between  $\alpha_{d,0}^j$  and  $-\lambda_j$  values for the last precursor families ( $j = 4, 5, 6$ ). The computed values of  $\alpha_{d,0}^j$  and  $\alpha_{d,1}^j$  for the last three precursor families are shown in Tab. 6.8.

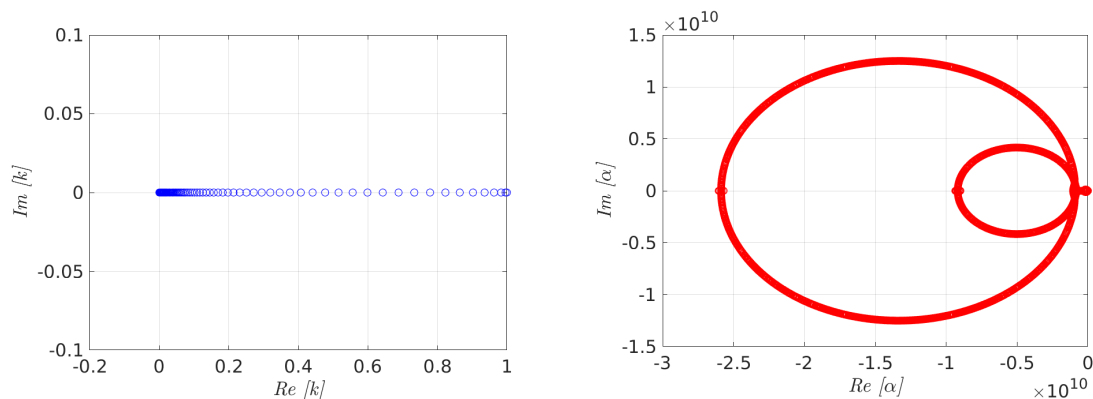


Figure 6.1: Spectra of the  $k$  (left) and the  $\alpha$  (right) eigenvalue problem for the 1D homogeneous configuration with reflective boundary conditions for the most decoupled case ( $L = 100$  cm).

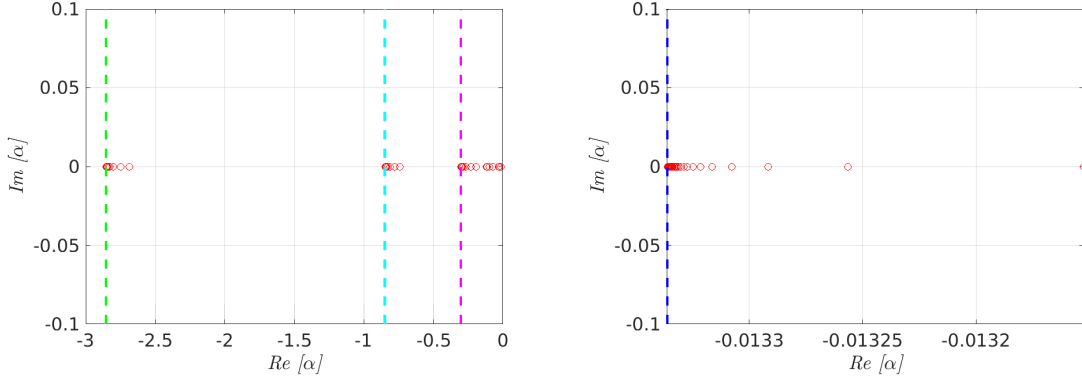


Figure 6.2: Zoom on the  $\alpha$ -spectrum on the delayed region (left) and in the first delayed cluster (right) for the 1D homogeneous configuration with reflective boundary conditions for the most decoupled case ( $L = 100$  cm). Vertical lines have been added in order to indicate the values of  $-\lambda_1$  (blue),  $-\lambda_4$  (magenta),  $-\lambda_5$  (cyan) and  $-\lambda_6$  (green).

L [cm]	$\alpha_{d,0}^4$ [s $^{-1}$ ]	$\alpha_{d,1}^4$ [s $^{-1}$ ]	$\alpha_{d,0}^5$ [s $^{-1}$ ]	$\alpha_{d,1}^5$ [s $^{-1}$ ]	$\alpha_{d,0}^6$ [s $^{-1}$ ]	$\alpha_{d,1}^6$ [s $^{-1}$ ]
50	$-1.914 \times 10^{-1}$	$-2.693 \times 10^{-1}$	$-7.383 \times 10^{-1}$	$-8.139 \times 10^{-1}$	-2.684	-2.802
60	$-1.921 \times 10^{-1}$	$-2.596 \times 10^{-1}$	$-7.393 \times 10^{-1}$	$-8.049 \times 10^{-1}$	-2.686	-2.789
70	$-1.919 \times 10^{-1}$	$-2.505 \times 10^{-1}$	$-7.390 \times 10^{-1}$	$-7.960 \times 10^{-1}$	-2.685	-2.776
80	$-1.904 \times 10^{-1}$	$-2.420 \times 10^{-1}$	$-7.371 \times 10^{-1}$	$-7.882 \times 10^{-1}$	-2.683	-2.765
90	$-1.923 \times 10^{-1}$	$-2.353 \times 10^{-1}$	$-7.392 \times 10^{-1}$	$-7.821 \times 10^{-1}$	-2.686	-2.755
100	$-1.926 \times 10^{-1}$	$-2.300 \times 10^{-1}$	$-7.400 \times 10^{-1}$	$-7.776 \times 10^{-1}$	-2.686	-2.748

Table 6.8: First  $\alpha$ -eigenvalues of the clusters associated to the last three precursor families ( $j = 4, 5, 6$ ) for the 1D homogeneous configuration with reflective boundary conditions as a function of the size  $L$  of the system. These values have been computed from the matrix-form of the  $\alpha$ -eigenvalue problem of the corresponding case.

The  $k$ -eigenvalues computed from the matrix-form of the  $k$ -eigenvalue problem are used in order to estimate the dominance ratio DR and the eigenvalue separations  $E.S._n(k)$  of the first five orders: they are shown in Tab. 6.9 and plotted in Fig. 6.3. The values of the dominance ratio increase for increasing length of the system from  $DR = 0.9832$  up to  $DR = 0.9957$ . The values of the eigenvalue separation for these homogeneous configurations decrease for increasing length of the system and an even faster decrease is observed for higher orders. This behaviour seems to support the claims previously discussed in the literature [120].

L [cm]	DR [-]	$E.S._1(k)$ [-]	$E.S._2(k)$ [-]	$E.S._3(k)$ [-]	$E.S._4(k)$ [-]	$E.S._5(k)$ [-]
50	$9.832 \times 10^{-1}$	$1.710 \times 10^{-2}$	$6.886 \times 10^{-2}$	$1.569 \times 10^{-1}$	$2.838 \times 10^{-1}$	$4.534 \times 10^{-1}$
60	$9.882 \times 10^{-1}$	$1.190 \times 10^{-2}$	$4.762 \times 10^{-2}$	$1.081 \times 10^{-1}$	$1.949 \times 10^{-1}$	$3.091 \times 10^{-1}$
70	$9.914 \times 10^{-1}$	$8.689 \times 10^{-3}$	$3.503 \times 10^{-2}$	$7.923 \times 10^{-2}$	$1.420 \times 10^{-1}$	$2.245 \times 10^{-1}$
80	$9.933 \times 10^{-1}$	$6.726 \times 10^{-3}$	$2.671 \times 10^{-2}$	$6.044 \times 10^{-2}$	$1.081 \times 10^{-1}$	$1.707 \times 10^{-1}$
90	$9.948 \times 10^{-1}$	$5.232 \times 10^{-3}$	$2.108 \times 10^{-2}$	$4.776 \times 10^{-2}$	$8.520 \times 10^{-2}$	$1.341 \times 10^{-1}$
100	$9.957 \times 10^{-1}$	$4.301 \times 10^{-3}$	$1.708 \times 10^{-2}$	$3.861 \times 10^{-2}$	$6.884 \times 10^{-2}$	$1.082 \times 10^{-1}$

Table 6.9: Dominance ratio and  $E.S._n(k)$  eigenvalue separations of the first  $k$ -eigenvalues for the 1D homogeneous configuration with reflective boundary conditions as a function of the size  $L$  of the system.

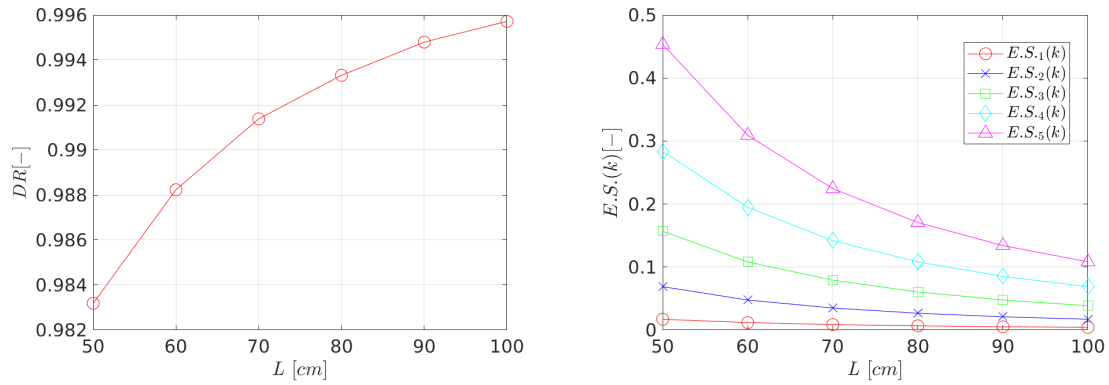


Figure 6.3: Dominance ratio (left) and  $k$ -eigenvalue separations (right) for the 1D homogeneous configuration with reflective boundary conditions as a function of the size  $L$  of the system. The first five order of eigenvalue separations are shown, in order, as:  $E.S.1(k)$  red circles,  $E.S.2(k)$  blue crosses,  $E.S.3(k)$  green squares,  $E.S.4(k)$  cyan diamonds and  $E.S.5(k)$  magenta triangles.

The  $\alpha$ -eigenvalues computed from the matrix-form of the  $\alpha$ -eigenvalue problem are used in order to estimate the delayed  $E.S.(\alpha_d)$  and the prompt  $E.S.(\alpha_p)$  eigenvalue separations of the first five orders. The delayed results are shown in Tab. 6.10, whereas the prompt results are shown in Tab. 6.11. The values of delayed eigenvalue separations (Fig. 6.4, left) are almost insensitive to the length of the system. This is mainly due to the presence of the clusters of the delayed eigenvalues. Conversely, and quite surprisingly, the behaviour of the prompt  $\alpha$ -eigenvalue separations (Fig. 6.4, right) is qualitatively similar to the  $k$ -eigenvalue separations.

$L$ [cm]	$E.S.1(\alpha_d)$ [ $s^{-1}$ ]	$E.S.2(\alpha_d)$ [ $s^{-1}$ ]	$E.S.3(\alpha_d)$ [ $s^{-1}$ ]	$E.S.4(\alpha_d)$ [ $s^{-1}$ ]	$E.S.5(\alpha_d)$ [ $s^{-1}$ ]
50	$-1.360 \times 10^{-2}$	$-1.374 \times 10^{-2}$	$-1.377 \times 10^{-2}$	$-1.378 \times 10^{-2}$	$-1.378 \times 10^{-2}$
60	$-1.259 \times 10^{-2}$	$-1.279 \times 10^{-2}$	$-1.283 \times 10^{-2}$	$-1.284 \times 10^{-2}$	$-1.284 \times 10^{-2}$
70	$-1.281 \times 10^{-2}$	$-1.310 \times 10^{-2}$	$-1.315 \times 10^{-2}$	$-1.317 \times 10^{-2}$	$-1.318 \times 10^{-2}$
80	$-1.460 \times 10^{-2}$	$-1.499 \times 10^{-2}$	$-1.506 \times 10^{-2}$	$-1.508 \times 10^{-2}$	$-1.509 \times 10^{-2}$
90	$-1.203 \times 10^{-2}$	$-1.255 \times 10^{-2}$	$-1.263 \times 10^{-2}$	$-1.266 \times 10^{-2}$	$-1.267 \times 10^{-2}$
100	$-1.148 \times 10^{-2}$	$-1.212 \times 10^{-2}$	$-1.222 \times 10^{-2}$	$-1.226 \times 10^{-2}$	$-1.228 \times 10^{-2}$

Table 6.10: Eigenvalue separations of the first delayed  $\alpha$ -eigenvalues for the 1D homogeneous configuration with reflective boundary conditions as a function of the size  $L$  of the system.

$L$ [cm]	$E.S.1(\alpha_p)$ [ $s^{-1}$ ]	$E.S.2(\alpha_p)$ [ $s^{-1}$ ]	$E.S.3(\alpha_p)$ [ $s^{-1}$ ]	$E.S.4(\alpha_p)$ [ $s^{-1}$ ]	$E.S.5(\alpha_p)$ [ $s^{-1}$ ]
50	$-7.849 \times 10^2$	$-3.032 \times 10^3$	$-6.460 \times 10^3$	$-1.072 \times 10^4$	$-1.546 \times 10^4$
60	$-5.490 \times 10^2$	$-2.133 \times 10^3$	$-4.617 \times 10^3$	$-7.810 \times 10^3$	$-1.148 \times 10^4$
70	$-4.016 \times 10^2$	$-1.585 \times 10^3$	$-3.460 \times 10^3$	$-5.911 \times 10^3$	$-8.815 \times 10^3$
80	$-3.112 \times 10^2$	$-1.217 \times 10^3$	$-2.679 \times 10^3$	$-4.618 \times 10^3$	$-6.960 \times 10^3$
90	$-2.426 \times 10^2$	$-9.647 \times 10^2$	$-2.138 \times 10^3$	$-3.703 \times 10^3$	$-5.615 \times 10^3$
100	$-1.996 \times 10^2$	$-7.840 \times 10^2$	$-1.741 \times 10^3$	$-3.030 \times 10^3$	$-4.621 \times 10^3$

Table 6.11: Eigenvalue separations of the first prompt  $\alpha$ -eigenvalues for the 1D homogeneous configuration with reflective boundary conditions as a function of the size  $L$  of the system.

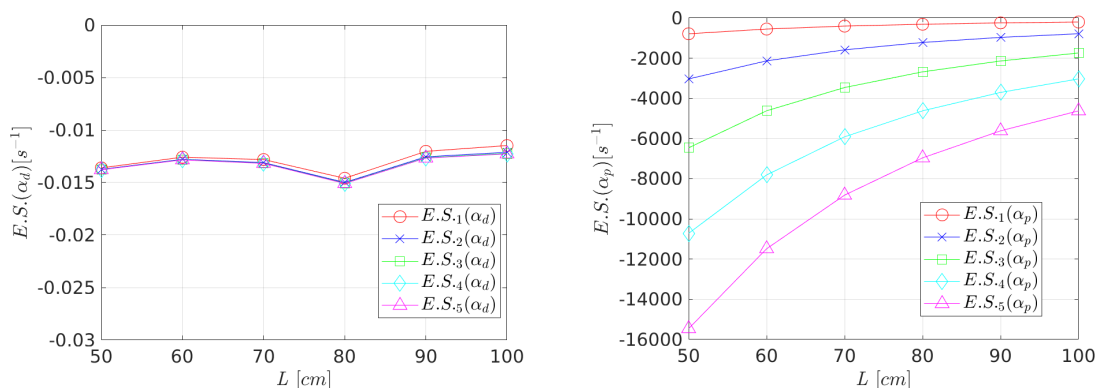


Figure 6.4: Delayed (left) and prompt (right)  $\alpha$ -eigenvalue separations for the 1D homogeneous configuration with reflective boundary conditions as a function of the size  $L$  of the system. The first five order of eigenvalue separations are shown, in order, as:  $E.S.1(\alpha)$  red circles,  $E.S.2(\alpha)$  blue crosses,  $E.S.3(\alpha)$  green squares,  $E.S.4(\alpha)$  cyan diamonds and  $E.S.5(\alpha)$  magenta triangles.

We have also examined the corresponding fundamental and first-order eigenmodes for  $k$ ,  $\alpha$  and prompt  $\alpha$  eigenvalue formulations. The reflective boundary conditions force the fundamental mode to be spatially flat, whereas the derivative of the first-order mode is null at the boundaries and displays a node (i.e. a spatial location where the eigenfunction flips sign) at the center of the system. No visible differences are observed with respect to the eigenvalue formulation and to the length of the system. The  $\alpha$ -eigenmodes associated to each dominant eigenvalue  $\alpha_{d,0}^j$  as the  $j$ -th delayed cluster have the same spatial distribution of the fundamental eigenmodes  $\varphi_{\alpha,0}$  and  $\varphi_{\alpha_p,0}$ , as expected from reference [133, 132]. Moreover, the  $\alpha$ -eigenmodes associated to the precursor concentrations of the fundamental order  $c_{\alpha,0}^j$  are positive, whereas precursor concentrations associated to the dominant eigenvalue  $\alpha_{d,0}^j$  of each delayed cluster change sign [133, 132].

## 2D geometry

The second set of benchmark configurations analyzed in this section concerns 2D homogeneous systems of different sizes with reflective boundary conditions. The geometry for these configurations is a square of side  $L$ . The fundamental eigenvalues  $k_0$  computed by the  $k$  power iteration are shown in the second column of Tab. 6.12. For these calculations,  $5 \times 10^4$  particles per cycle are simulated, for a total of  $4.1 \times 10^3$  cycles ( $4 \times 10^3$  active,  $10^2$  discarded). During these simulations, we have activated the matrix-filling methods.

For the matrix operators, the size of the domain has been partitioned into  $N_x = N_y = c \times L$  space intervals along both  $x$ - and  $y$ - axes, where  $c = 0.3 \text{ cm}^{-1}$ , in order to keep a constant bin size. The cosine of the particle direction with respect to both spatial axes is uniformly partitioned into  $M_x = M_y = 2$  intervals, whereas the energy groups and precursor families are fixed at  $G = 3$  and  $J = 6$ , respectively. The total size of the matrix defining the  $\alpha$ -eigenvalue problem ranges from  $4.050 \times 10^3$  ( $L = 50 \text{ cm}$ ) to  $1.620 \times 10^4$  ( $L = 100 \text{ cm}$ ), whereas the matrix defining the  $k$ -eigenvalue problem ranges from  $2.700 \times 10^3$  to  $1.080 \times 10^4$ . The eigenvalues computed from the matrix-form of the corresponding eigenvalue problem are shown in Tabs. 6.12 ( $k$ -eigenvalues), 6.13 ( $\alpha$ -eigenvalues) and 6.14 (prompt  $\alpha$ -eigenvalues). All fundamental eigenvalues  $k_0$  computed from the matrix of the corresponding eigenvalue problem are within  $1\sigma$  standard deviation from the Monte Carlo results obtained from the  $k$  power iteration. The absolute values of the fundamental eigenvalues  $\alpha_0$  are smaller than  $2 \times 10^{-3} \text{ s}^{-1}$ .

L [cm]	$k_0^{MC}$ [-]	$k_0$ [-]	$k_1$ [-]	$k_2$ [-]	$k_3$ [-]	$k_4$ [-]	$k_5$ [-]
50	$0.9999 \pm 1 \times 10^{-4}$	1.0000	0.9320	0.9316	0.8702	0.7664	0.7661
60	$0.9999 \pm 1 \times 10^{-4}$	0.9999	0.9522	0.9515	0.9070	0.8277	0.8274
70	$0.9999 \pm 1 \times 10^{-4}$	0.9999	0.9642	0.9641	0.9300	0.8685	0.8683
80	$1.0000 \pm 1 \times 10^{-4}$	1.0000	0.9726	0.9722	0.9462	0.8971	0.8963
90	$0.9999 \pm 1 \times 10^{-4}$	0.9999	0.9781	0.9780	0.9568	0.9168	0.9167
100	$1.0000 \pm 1 \times 10^{-4}$	1.0000	0.9824	0.9821	0.9651	0.9322	0.9316

Table 6.12: First  $k$ -eigenvalues for the 2D homogeneous configuration with reflective boundary conditions as a function of the size L of the system. The second column displays the fundamental eigenvalues  $k_0$  computed by the test-bed Monte Carlo code for the  $k$ -eigenvalue problem and the corresponding standard deviations. All other eigenvalues have been computed from the matrix-form of the  $k$ -eigenvalue problem of the corresponding case.

L [cm]	$\alpha_0$ [ $s^{-1}$ ]	$\alpha_1$ [ $s^{-1}$ ]	$\alpha_2$ [ $s^{-1}$ ]	$\alpha_3$ [ $s^{-1}$ ]	$\alpha_4$ [ $s^{-1}$ ]	$\alpha_5$ [ $s^{-1}$ ]
50	$-5.026 \times 10^{-4}$	$-1.329 \times 10^{-2}$	$-1.329 \times 10^{-2}$	$-1.332 \times 10^{-2}$	$-1.333 \times 10^{-2}$	$-1.333 \times 10^{-2}$
60	$-1.077 \times 10^{-3}$	$-1.327 \times 10^{-2}$	$-1.328 \times 10^{-2}$	$-1.331 \times 10^{-2}$	$-1.332 \times 10^{-2}$	$-1.333 \times 10^{-2}$
70	$-1.648 \times 10^{-3}$	$-1.325 \times 10^{-2}$	$-1.325 \times 10^{-2}$	$-1.330 \times 10^{-2}$	$-1.332 \times 10^{-2}$	$-1.333 \times 10^{-2}$
80	$-7.121 \times 10^{-4}$	$-1.323 \times 10^{-2}$	$-1.323 \times 10^{-2}$	$-1.328 \times 10^{-2}$	$-1.331 \times 10^{-2}$	$-1.333 \times 10^{-2}$
90	$-1.350 \times 10^{-3}$	$-1.320 \times 10^{-2}$	$-1.320 \times 10^{-2}$	$-1.327 \times 10^{-2}$	$-1.330 \times 10^{-2}$	$-1.333 \times 10^{-2}$
100	$4.074 \times 10^{-4}$	$-1.316 \times 10^{-2}$	$-1.316 \times 10^{-2}$	$-1.325 \times 10^{-2}$	$-1.329 \times 10^{-2}$	$-1.333 \times 10^{-2}$

Table 6.13: First  $\alpha$ -eigenvalues for the 2D homogeneous configuration with reflective boundary conditions as a function of the size L of the system. These values have been computed from the matrix-form of the  $\alpha$ -eigenvalue problem of the corresponding case.

L [cm]	$\alpha_{p,0}$ [ $s^{-1}$ ]	$\alpha_{p,1}$ [ $s^{-1}$ ]	$\alpha_{p,2}$ [ $s^{-1}$ ]	$\alpha_{p,3}$ [ $s^{-1}$ ]	$\alpha_{p,4}$ [ $s^{-1}$ ]	$\alpha_{p,5}$ [ $s^{-1}$ ]
50	$-3.046 \times 10^2$	$-3.556 \times 10^3$	$-3.576 \times 10^3$	$-6.672 \times 10^3$	$-1.232 \times 10^4$	$-1.232 \times 10^4$
60	$-3.068 \times 10^2$	$-2.574 \times 10^3$	$-2.604 \times 10^3$	$-4.800 \times 10^3$	$-8.917 \times 10^3$	$-8.933 \times 10^3$
70	$-3.087 \times 10^2$	$-1.997 \times 10^3$	$-2.002 \times 10^3$	$-3.653 \times 10^3$	$-6.760 \times 10^3$	$-6.773 \times 10^3$
80	$-3.058 \times 10^2$	$-1.594 \times 10^3$	$-1.612 \times 10^3$	$-2.865 \times 10^3$	$-5.296 \times 10^3$	$-5.337 \times 10^3$
90	$-3.074 \times 10^2$	$-1.334 \times 10^3$	$-1.335 \times 10^3$	$-2.349 \times 10^3$	$-4.305 \times 10^3$	$-4.311 \times 10^3$
100	$-3.017 \times 10^2$	$-1.127 \times 10^3$	$-1.145 \times 10^3$	$-1.954 \times 10^3$	$-3.546 \times 10^3$	$-3.574 \times 10^3$

Table 6.14: First prompt  $\alpha$ -eigenvalues for the 2D homogeneous configuration with reflective boundary conditions as a function of the size L of the system. These values have been computed from the matrix-form of the  $\alpha$ -eigenvalue problem of the corresponding case.

The  $k$ - and the  $\alpha$ -eigenvalue distributions are shown on the complex plane in Fig. 6.5. For the 2D geometry, the prompt  $\alpha$  eigenvalues fill one circle by leaving two circular regions empty along the imaginary axis. This behaviour is repeated for the three energy groups. Figure 6.6 shows the zoom on all delayed eigenvalue clusters (left) and on the delayed eigenvalue cluster associated to the first precursor family (right). Same comments as those presented for the 1D configuration can be applied to the distribution of the delayed  $\alpha$ -eigenvalues on the complex plane. The zoom of Fig. 6.6 (left) shows the gap between  $\alpha_{d,0}^j$  and  $-\lambda_j$  values for the last precursor families. The computed values of  $\alpha_{d,0}^j$  and  $\alpha_{d,1}^j$  for the last three precursor families ( $j = 4, 5, 6$ ) are shown in Tab. 6.15.

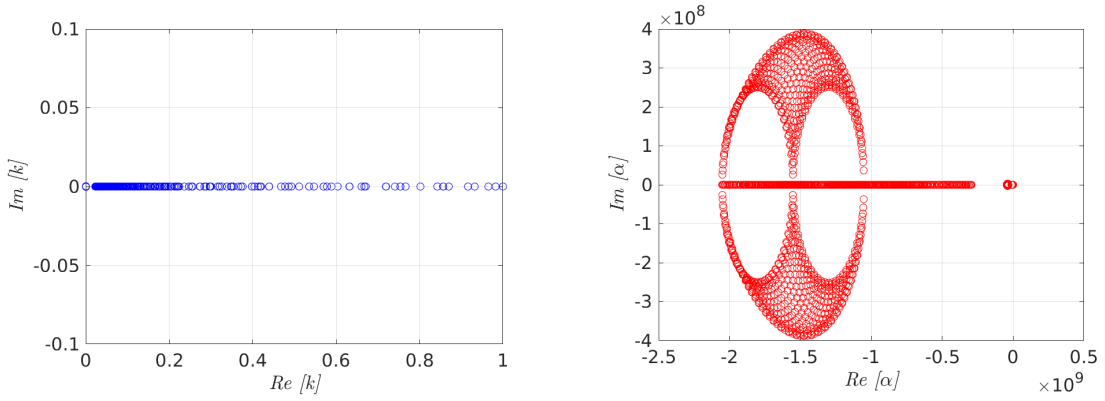


Figure 6.5: Spectra of the  $k$  (left) and the  $\alpha$  (right) eigenvalue problem for the 2D homogeneous configuration with reflective boundary conditions for the most decoupled case ( $L = 100$  cm).

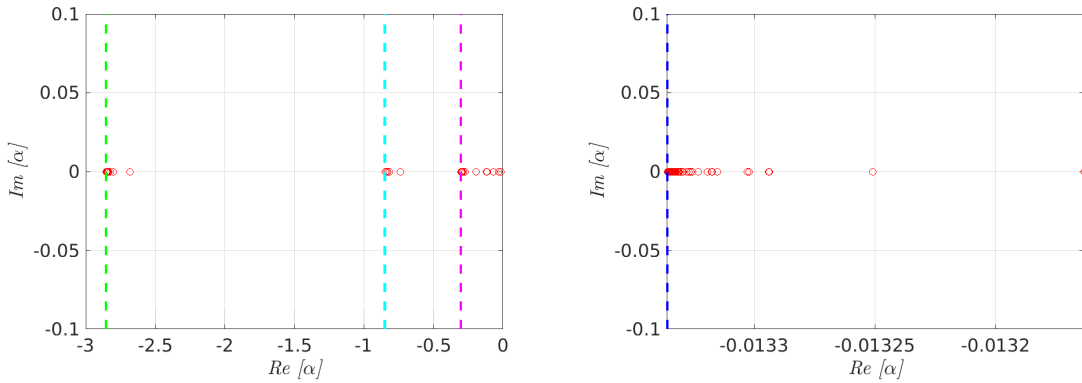


Figure 6.6: Zoom on the  $\alpha$ -spectrum in the delayed region (left) and on the first delayed cluster (right) for the 2D homogeneous configuration with reflective boundary conditions for the most decoupled case ( $L = 100$  cm). Vertical lines have been added in order to indicate the values of  $-\lambda_1$  (blue),  $-\lambda_4$  (magenta),  $-\lambda_5$  (cyan) and  $-\lambda_6$  (green).

$L$ [cm]	$\alpha_{d,0}^4$ [ $s^{-1}$ ]	$\alpha_{d,1}^4$ [ $s^{-1}$ ]	$\alpha_{d,0}^5$ [ $s^{-1}$ ]	$\alpha_{d,1}^5$ [ $s^{-1}$ ]	$\alpha_{d,0}^6$ [ $s^{-1}$ ]	$\alpha_{d,1}^6$ [ $s^{-1}$ ]
50	$-1.923 \times 10^{-1}$	$-2.931 \times 10^{-1}$	$-7.393 \times 10^{-1}$	$-8.386 \times 10^{-1}$	-2.684	-2.838
60	$-1.929 \times 10^{-1}$	$-2.892 \times 10^{-1}$	$-7.401 \times 10^{-1}$	$-8.344 \times 10^{-1}$	-2.686	-2.832
70	$-1.931 \times 10^{-1}$	$-2.849 \times 10^{-1}$	$-7.405 \times 10^{-1}$	$-8.299 \times 10^{-1}$	-2.687	-2.825
80	$-1.924 \times 10^{-1}$	$-2.802 \times 10^{-1}$	$-7.399 \times 10^{-1}$	$-8.251 \times 10^{-1}$	-2.685	-2.818
90	$-1.930 \times 10^{-1}$	$-2.757 \times 10^{-1}$	$-7.402 \times 10^{-1}$	$-8.204 \times 10^{-1}$	-2.687	-2.812
100	$-1.915 \times 10^{-1}$	$-2.704 \times 10^{-1}$	$-7.388 \times 10^{-1}$	$-8.152 \times 10^{-1}$	-2.684	-2.804

Table 6.15: First  $\alpha$ -eigenvalues of the clusters associated to the last three precursor families ( $j = 4, 5, 6$ ) for the 2D homogeneous configuration with reflective boundary conditions as a function of the size  $L$  of the system. These values have been computed from the matrix-form of the  $\alpha$ -eigenvalue problem of the corresponding case.

The  $k$ -eigenvalues computed from the matrix-form of the  $k$ -eigenvalue problem are used in order to estimate the dominance ratio DR and the eigenvalue separations  $E.S._n(k)$  of the first five orders: they are shown in Tab. 6.16 and plotted in Fig. 6.7. The values of the dominance ratio increase for increasing size of the system from  $DR = 0.9321$  up to  $DR = 0.9824$ . The values of the eigenvalue separation for this homogeneous configurations decrease for increasing size of the system and an even faster decrease is observed for higher-orders. Contrary to the case of the 1D configuration, the first and second, fourth and fifth orders of eigenvalue separations are extremely close for the 2D configuration: this feature is related to the symmetry properties of this system, which induces a degeneracy in the eigenvalues.

L [cm]	DR [-]	E.S. <sub>1</sub> (k) [-]	E.S. <sub>2</sub> (k) [-]	E.S. <sub>3</sub> (k) [-]	E.S. <sub>4</sub> (k) [-]	E.S. <sub>5</sub> (k) [-]
50	$9.321 \times 10^{-1}$	$7.290 \times 10^{-2}$	$7.337 \times 10^{-2}$	$1.491 \times 10^{-1}$	$3.047 \times 10^{-1}$	$3.053 \times 10^{-1}$
60	$9.522 \times 10^{-1}$	$5.015 \times 10^{-2}$	$5.085 \times 10^{-2}$	$1.025 \times 10^{-1}$	$2.081 \times 10^{-1}$	$2.086 \times 10^{-1}$
70	$9.643 \times 10^{-1}$	$3.706 \times 10^{-2}$	$3.717 \times 10^{-2}$	$7.509 \times 10^{-2}$	$1.513 \times 10^{-1}$	$1.516 \times 10^{-1}$
80	$9.726 \times 10^{-1}$	$2.814 \times 10^{-2}$	$2.851 \times 10^{-2}$	$5.685 \times 10^{-2}$	$1.146 \times 10^{-1}$	$1.157 \times 10^{-1}$
90	$9.781 \times 10^{-1}$	$2.234 \times 10^{-2}$	$2.237 \times 10^{-2}$	$4.503 \times 10^{-2}$	$9.060 \times 10^{-2}$	$9.073 \times 10^{-2}$
100	$9.824 \times 10^{-1}$	$1.790 \times 10^{-2}$	$1.830 \times 10^{-2}$	$3.624 \times 10^{-2}$	$7.272 \times 10^{-2}$	$7.340 \times 10^{-2}$

Table 6.16: Dominance ratio and E.S.<sub>n</sub>(k) eigenvalue separations of the first k-eigenvalues for the 2D homogeneous configuration with reflective boundary conditions as a function of the size L of the system.

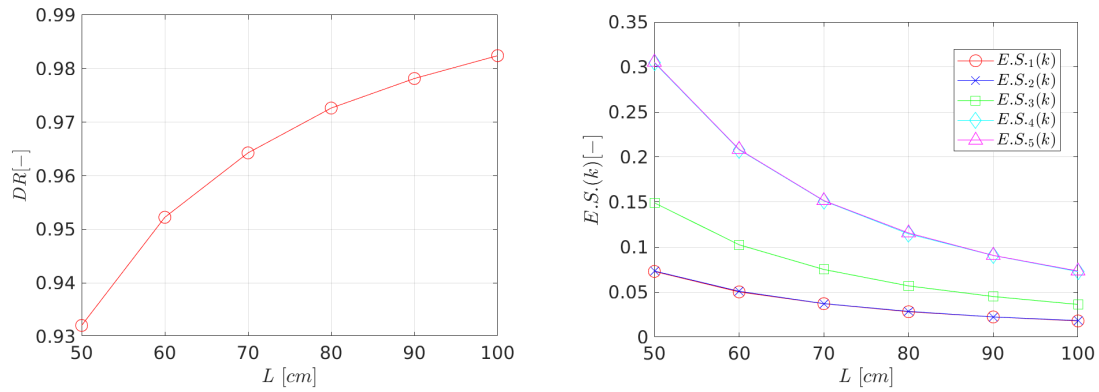


Figure 6.7: Dominance ratio (left) and k-eigenvalue separations (right) for the 2D homogeneous configuration with reflective boundary conditions as a function of the size L of the system. The first five order of eigenvalue separations are shown, in order, as: E.S.<sub>1</sub>(k) red circles, E.S.<sub>2</sub>(k) blue crosses, E.S.<sub>3</sub>(k) green squares, E.S.<sub>4</sub>(k) cyan diamonds and E.S.<sub>5</sub>(k) magenta triangles.

The  $\alpha$ -eigenvalues computed from the matrix-form of the  $\alpha$ -eigenvalue problem are used in order to estimate the delayed E.S.<sub>( $\alpha_d$ ) and the prompt E.S.<sub>( $\alpha_p$ ) eigenvalue separations of the first five orders. The delayed results are shown in Tab. 6.17, whereas the prompt results are shown in Tab. 6.18. The values of delayed eigenvalue separations (Fig. 6.8, left) are almost constant as a function of the length of the system, similarly as previously discussed for the 1D configuration. Moreover, also for this 2D configurations the behaviour of the prompt  $\alpha$ -eigenvalue separations (Fig. 6.4, right) is qualitatively similar to the k-eigenvalue separations. It appears that the information content of the E.S.(k) concerning the system decoupling is also conveyed by the E.S.<sub>( $\alpha_p$ )</sub>, whereas the E.S.<sub>( $\alpha_d$ )</sub> are less affected, if affected at all. Furthermore, the degeneracy observed for the E.S.(k) affects also the E.S.<sub>( $\alpha_p$ )</sub>, hinting once again to the symmetry properties of these 2D configurations.</sub></sub>

L [cm]	E.S. <sub>1</sub> ( $\alpha_d$ ) [s <sup>-1</sup> ]	E.S. <sub>2</sub> ( $\alpha_d$ ) [s <sup>-1</sup> ]	E.S. <sub>3</sub> ( $\alpha_d$ ) [s <sup>-1</sup> ]	E.S. <sub>4</sub> ( $\alpha_d$ ) [s <sup>-1</sup> ]	E.S. <sub>5</sub> ( $\alpha_d$ ) [s <sup>-1</sup> ]
50	$-1.279 \times 10^{-2}$	$-1.279 \times 10^{-2}$	$-1.281 \times 10^{-2}$	$-1.282 \times 10^{-2}$	$-1.282 \times 10^{-2}$
60	$-1.220 \times 10^{-2}$	$-1.220 \times 10^{-2}$	$-1.223 \times 10^{-2}$	$-1.224 \times 10^{-2}$	$-1.224 \times 10^{-2}$
70	$-1.160 \times 10^{-2}$	$-1.161 \times 10^{-2}$	$-1.165 \times 10^{-2}$	$-1.167 \times 10^{-2}$	$-1.167 \times 10^{-2}$
80	$-1.251 \times 10^{-2}$	$-1.252 \times 10^{-2}$	$-1.257 \times 10^{-2}$	$-1.260 \times 10^{-2}$	$-1.260 \times 10^{-2}$
90	$-1.185 \times 10^{-2}$	$-1.185 \times 10^{-2}$	$-1.192 \times 10^{-2}$	$-1.195 \times 10^{-2}$	$-1.195 \times 10^{-2}$
100	$-1.357 \times 10^{-2}$	$-1.357 \times 10^{-2}$	$-1.366 \times 10^{-2}$	$-1.370 \times 10^{-2}$	$-1.370 \times 10^{-2}$

Table 6.17: Eigenvalue separations of the first delayed  $\alpha$ -eigenvalues for the 2D homogeneous configuration with reflective boundary conditions as a function of the size L of the system.

L [cm]	E.S. <sub>1</sub> ( $\alpha_p$ ) [ $s^{-1}$ ]	E.S. <sub>2</sub> ( $\alpha_p$ ) [ $s^{-1}$ ]	E.S. <sub>3</sub> ( $\alpha_p$ ) [ $s^{-1}$ ]	E.S. <sub>4</sub> ( $\alpha_p$ ) [ $s^{-1}$ ]	E.S. <sub>5</sub> ( $\alpha_p$ ) [ $s^{-1}$ ]
50	$-3.251 \times 10^3$	$-3.556 \times 10^3$	$-6.368 \times 10^3$	$-1.201 \times 10^4$	$-1.203 \times 10^4$
60	$-2.267 \times 10^3$	$-2.574 \times 10^3$	$-4.493 \times 10^3$	$-8.610 \times 10^3$	$-8.626 \times 10^3$
70	$-1.689 \times 10^3$	$-1.997 \times 10^3$	$-3.344 \times 10^3$	$-6.452 \times 10^3$	$-6.465 \times 10^3$
80	$-1.289 \times 10^3$	$-1.594 \times 10^3$	$-2.559 \times 10^3$	$-4.990 \times 10^3$	$-5.031 \times 10^3$
90	$-1.027 \times 10^3$	$-1.334 \times 10^3$	$-2.041 \times 10^3$	$-3.998 \times 10^3$	$-4.004 \times 10^3$
100	$-8.257 \times 10^2$	$-1.127 \times 10^2$	$-1.653 \times 10^3$	$-3.244 \times 10^3$	$-3.273 \times 10^3$

Table 6.18: Eigenvalue separations of the first prompt  $\alpha$ -eigenvalues for the 2D homogeneous configuration with reflective boundary conditions as a function of the size L of the system.

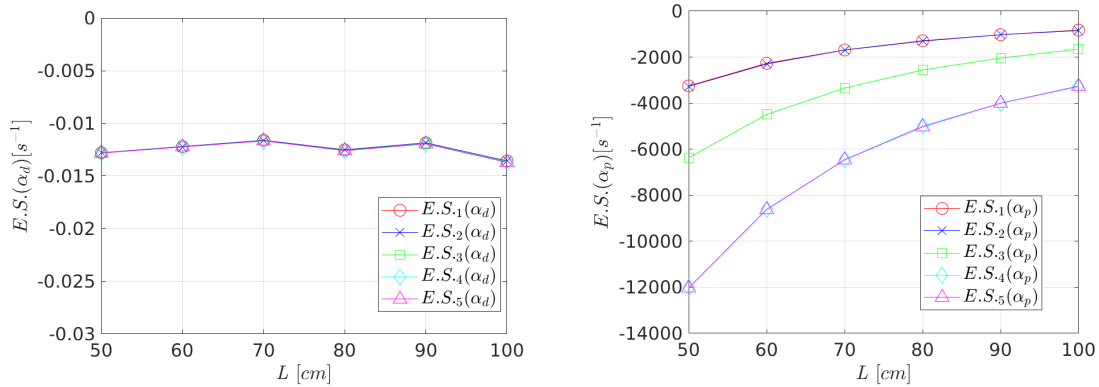


Figure 6.8: Delayed (left) and prompt (right)  $\alpha$ -eigenvalue separations for the 2D homogeneous configuration with reflective boundary conditions as a function of the size L of the system. The first five order of eigenvalue separations are shown, in order, as: E.S.<sub>1</sub>( $\alpha$ ) red circles, E.S.<sub>2</sub>( $\alpha$ ) blue crosses, E.S.<sub>3</sub>( $\alpha$ ) green squares, E.S.<sub>4</sub>( $\alpha$ ) cyan diamonds and E.S.<sub>5</sub>( $\alpha$ ) magenta triangles.

The corresponding fundamental and first-order eigenmodes have been examined for  $k$ ,  $\alpha$  and prompt  $\alpha$  eigenvalue formulations for the most decoupled case ( $L = 100$  cm). The conclusions related to the eigenmodes described for the 1D configuration apply also to this 2D system.

## 6.4.2 Homogeneous configurations with leakage boundary conditions

### Critical configuration search

We examine now 1D homogeneous systems of different lengths with leakage boundary conditions. For these systems the factor  $a$  has been computed for the most decoupled case ( $L = 100$  cm) from a parametric research around the value computed for the reflected configurations of the previous sections. A value  $a = 1.4875$  applied to the macroscopic capture cross section leads to  $k_0 = 0.9999 \pm 10^{-4}$  from a  $k$  power iteration performed with  $2 \times 10^4$  particles per cycle and a total of  $6 \times 10^3$  cycles ( $5 \times 10^3$  active,  $10^3$  inactive). Then, we have considered the same lengths defined for Section 6.4.1 and we have estimated the coefficient  $b$  from Eq. (6.10) in order to readjust each case to the critical level. The values  $b$  have been iteratively computed by simulating  $5 \times 10^4$  particles per cycle and a total of  $5 \times 10^3$  cycles.

Furthermore, for 2D homogeneous systems of different sizes with leakage boundary conditions, a factor  $a = 1.4775$  has been applied to the macroscopic capture cross section. The  $k$  power iteration converges to the fundamental eigenvalue  $k_0 = 1.0001 \pm 10^{-4}$ . For this simulation we have set  $2 \times 10^4$  particles per cycle and a total of  $6 \times 10^3$  cycles ( $5 \times 10^3$  active,  $10^3$  inactive). The values  $b$  (from Eq. (6.10)) have been iteratively computed by simulating  $5 \times 10^4$  particles per cycle and a total of  $5 \times 10^3$  cycles.

In the following, we will show the results computed for the 1D configurations (Section 6.4.2) and for the 2D configurations (Section 6.4.2).

### 1D geometry

The fundamental eigenvalues  $k_0$  computed by the  $k$  power iteration are shown in the second column of Tab. 6.19. For these calculations,  $10^5$  particles per cycle are simulated, for a total of  $1.2 \times 10^3$  cycles ( $10^3$  active,  $2 \times 10^2$  inactive).

In order to compute the matrix operators, the length of the domain has been partitioned into  $N_x = c \times L$  space intervals along the  $x$ -axis, where  $c = 10 \text{ cm}^{-1}$ , in order to keep a constant bin width. The cosine of the particle direction with respect to the  $x$ -axis is uniformly partitioned into  $M = 4$  intervals, whereas the energy groups and precursor families are fixed at  $G = 3$  and  $J = 6$ , respectively. The total size of the matrix defining the  $\alpha$ -eigenvalue problem ranges from  $9.0 \times 10^3$  ( $L = 50 \text{ cm}$ ) to  $1.8 \times 10^4$  ( $L = 100 \text{ cm}$ ), whereas the matrix defining the  $k$ -eigenvalue problem ranges from  $6.0 \times 10^3$  to  $1.2 \times 10^4$ . The eigenvalues computed from the matrix-form of the corresponding eigenvalue problem are shown in Tabs. 6.19 ( $k$ -eigenvalues), 6.20 ( $\alpha$ -eigenvalues) and 6.21 (prompt  $\alpha$ -eigenvalues). All fundamental eigenvalues  $k_0$  computed from the matrix of the corresponding eigenvalue problem are within  $2\sigma$  standard deviation from the Monte Carlo results obtained from the  $k$  power iteration. The absolute values of the fundamental eigenvalues  $\alpha_0$  are smaller than  $2 \times 10^{-3} \text{ s}^{-1}$ . The dominant eigenvalue  $\alpha_{d,0}^j$  of the  $j$ -th delayed cluster is separated from the other eigenvalues of the same precursor family [133, 132]. The computed values of  $\alpha_{d,0}^j$  and  $\alpha_{d,1}^j$  for the last three precursor families ( $j = 4, 5, 6$ ) are shown in Tab. 6.22.

L [cm]	$k_0^{MC}$ [-]	$k_0$ [-]	$k_1$ [-]	$k_2$ [-]	$k_3$ [-]	$k_4$ [-]	$k_5$ [-]
50	$1.0000 \pm 1 \times 10^{-4}$	1.0001	0.9546	0.8856	0.8019	0.7117	0.6221
60	$1.0003 \pm 1 \times 10^{-4}$	1.0002	0.9680	0.9176	0.8539	0.7820	0.7066
70	$1.0002 \pm 1 \times 10^{-4}$	1.0002	0.9760	0.9379	0.8881	0.8304	0.7676
80	$1.0000 \pm 1 \times 10^{-4}$	1.0001	0.9814	0.9514	0.9118	0.8647	0.8123
90	$1.0002 \pm 1 \times 10^{-4}$	1.0002	0.9851	0.9611	0.9289	0.8900	0.8460
100	$0.9999 \pm 1 \times 10^{-4}$	0.9999	0.9878	0.9680	0.9414	0.9090	0.8718

Table 6.19: First  $k$ -eigenvalues for the 1D homogeneous configuration with leakage boundary conditions as a function of the size  $L$  of the system. The second column displays the fundamental eigenvalues  $k_0$  computed by the test-bed Monte Carlo code for the  $k$ -eigenvalue problem and the corresponding standard deviations. All other eigenvalues have been computed from the matrix-form of the  $k$ -eigenvalue problem of the corresponding case.

L [cm]	$\alpha_0$ [ $\text{s}^{-1}$ ]	$\alpha_1$ [ $\text{s}^{-1}$ ]	$\alpha_2$ [ $\text{s}^{-1}$ ]	$\alpha_3$ [ $\text{s}^{-1}$ ]	$\alpha_4$ [ $\text{s}^{-1}$ ]	$\alpha_5$ [ $\text{s}^{-1}$ ]
50	$8.262 \times 10^{-4}$	$-1.327 \times 10^{-2}$	$-1.331 \times 10^{-2}$	$-1.332 \times 10^{-2}$	$-1.333 \times 10^{-2}$	$-1.333 \times 10^{-2}$
60	$2.611 \times 10^{-3}$	$-1.324 \times 10^{-2}$	$-1.330 \times 10^{-2}$	$-1.332 \times 10^{-2}$	$-1.332 \times 10^{-2}$	$-1.333 \times 10^{-2}$
70	$3.631 \times 10^{-3}$	$-1.321 \times 10^{-2}$	$-1.329 \times 10^{-2}$	$-1.331 \times 10^{-2}$	$-1.332 \times 10^{-2}$	$-1.333 \times 10^{-2}$
80	$7.799 \times 10^{-4}$	$-1.317 \times 10^{-2}$	$-1.328 \times 10^{-2}$	$-1.330 \times 10^{-2}$	$-1.332 \times 10^{-2}$	$-1.333 \times 10^{-2}$
90	$2.426 \times 10^{-3}$	$-1.313 \times 10^{-2}$	$-1.326 \times 10^{-2}$	$-1.330 \times 10^{-2}$	$-1.331 \times 10^{-2}$	$-1.333 \times 10^{-2}$
100	$-1.496 \times 10^{-3}$	$-1.308 \times 10^{-2}$	$-1.324 \times 10^{-2}$	$-1.329 \times 10^{-2}$	$-1.331 \times 10^{-2}$	$-1.333 \times 10^{-2}$

Table 6.20: First  $\alpha$ -eigenvalues for the 1D homogeneous configuration with leakage boundary conditions as a function of the size  $L$  of the system. These values have been computed from the matrix-form of the  $\alpha$ -eigenvalue problem of the corresponding case.

## 6.4. HOMOGENEOUS BENCHMARK CONFIGURATIONS

L [cm]	$\alpha_{p,0}$ [s <sup>-1</sup> ]	$\alpha_{p,1}$ [s <sup>-1</sup> ]	$\alpha_{p,2}$ [s <sup>-1</sup> ]	$\alpha_{p,3}$ [s <sup>-1</sup> ]	$\alpha_{p,4}$ [s <sup>-1</sup> ]	$\alpha_{p,5}$ [s <sup>-1</sup> ]
50	$-2.972 \times 10^2$	$-2.399 \times 10^3$	$-5.658 \times 10^3$	$-9.739 \times 10^3$	$-1.434 \times 10^4$	$-1.921 \times 10^4$
60	$-2.926 \times 10^2$	$-1.783 \times 10^3$	$-4.157 \times 10^3$	$-7.217 \times 10^3$	$-1.078 \times 10^4$	$-1.466 \times 10^4$
70	$-2.907 \times 10^2$	$-1.416 \times 10^3$	$-3.206 \times 10^3$	$-5.573 \times 10^3$	$-8.386 \times 10^3$	$-1.153 \times 10^4$
80	$-2.995 \times 10^2$	$-1.167 \times 10^3$	$-2.574 \times 10^3$	$-4.449 \times 10^3$	$-6.717 \times 10^3$	$-9.295 \times 10^3$
90	$-2.949 \times 10^2$	$-9.951 \times 10^2$	$-2.119 \times 10^3$	$-3.640 \times 10^3$	$-5.499 \times 10^3$	$-7.638 \times 10^3$
100	$-3.081 \times 10^2$	$-8.681 \times 10^2$	$-1.796 \times 10^3$	$-3.049 \times 10^3$	$-4.592 \times 10^3$	$-6.383 \times 10^3$

Table 6.21: First prompt  $\alpha$ -eigenvalues for the 1D homogeneous configuration with leakage boundary conditions as a function of the size L of the system. These values have been computed from the matrix-form of the  $\alpha$ -eigenvalue problem of the corresponding case.

L [cm]	$\alpha_{d,0}^4$ [s <sup>-1</sup> ]	$\alpha_{d,1}^4$ [s <sup>-1</sup> ]	$\alpha_{d,0}^5$ [s <sup>-1</sup> ]	$\alpha_{d,1}^5$ [s <sup>-1</sup> ]	$\alpha_{d,0}^6$ [s <sup>-1</sup> ]	$\alpha_{d,1}^6$ [s <sup>-1</sup> ]
50	$-1.910 \times 10^{-1}$	$-2.883 \times 10^{-1}$	$-7.378 \times 10^{-1}$	$-8.334 \times 10^{-1}$	-2.683	-2.831
60	$-1.900 \times 10^{-1}$	$-2.830 \times 10^{-1}$	$-7.370 \times 10^{-1}$	$-8.281 \times 10^{-1}$	-2.681	-2.823
70	$-1.893 \times 10^{-1}$	$-2.775 \times 10^{-1}$	$-7.356 \times 10^{-1}$	$-8.223 \times 10^{-1}$	-2.680	-2.814
80	$-1.912 \times 10^{-1}$	$-2.717 \times 10^{-1}$	$-7.383 \times 10^{-1}$	$-8.166 \times 10^{-1}$	-2.683	-2.806
90	$-1.902 \times 10^{-1}$	$-2.661 \times 10^{-1}$	$-7.367 \times 10^{-1}$	$-8.110 \times 10^{-1}$	-2.680	-2.798
100	$-1.931 \times 10^{-1}$	$-2.605 \times 10^{-1}$	$-7.404 \times 10^{-1}$	$-8.055 \times 10^{-1}$	-2.687	-2.791

Table 6.22: First  $\alpha$ -eigenvalues of the clusters associated to the last three precursor families ( $j = 4, 5, 6$ ) for the 1D homogeneous configuration with leakage boundary conditions as a function of the size L of the system. These values have been computed from the matrix-form of the  $\alpha$ -eigenvalue problem of the corresponding case.

The  $k$ -eigenvalues computed from the matrix-form of the  $k$ -eigenvalue problem are used in order to estimate the dominance ratio DR and the eigenvalue separations  $E.S._n(k)$  of the first five orders: they are shown in Tab. 6.23 and plotted in Fig. 6.9. The values of the dominance ratio increase for increasing length of the system from DR = 0.9546 up to DR = 0.9879. No major differences are observed with respect to the behaviour previously analyzed for the reflected system from Fig. 6.3.

L [cm]	DR [-]	$E.S._1(k)$ [-]	$E.S._2(k)$ [-]	$E.S._3(k)$ [-]	$E.S._4(k)$ [-]	$E.S._5(k)$ [-]
50	$9.546 \times 10^{-1}$	$4.758 \times 10^{-2}$	$1.292 \times 10^{-1}$	$2.471 \times 10^{-1}$	$4.051 \times 10^{-1}$	$6.076 \times 10^{-1}$
60	$9.679 \times 10^{-1}$	$3.321 \times 10^{-2}$	$9.003 \times 10^{-2}$	$1.713 \times 10^{-1}$	$2.790 \times 10^{-1}$	$4.154 \times 10^{-1}$
70	$9.758 \times 10^{-1}$	$2.481 \times 10^{-2}$	$6.650 \times 10^{-2}$	$1.262 \times 10^{-1}$	$2.045 \times 10^{-1}$	$3.030 \times 10^{-1}$
80	$9.813 \times 10^{-1}$	$1.903 \times 10^{-2}$	$5.119 \times 10^{-2}$	$9.681 \times 10^{-2}$	$1.565 \times 10^{-1}$	$2.311 \times 10^{-1}$
90	$9.849 \times 10^{-1}$	$1.528 \times 10^{-2}$	$4.067 \times 10^{-2}$	$7.675 \times 10^{-2}$	$1.238 \times 10^{-1}$	$1.822 \times 10^{-1}$
100	$9.879 \times 10^{-1}$	$1.220 \times 10^{-2}$	$3.294 \times 10^{-2}$	$6.212 \times 10^{-2}$	$1.000 \times 10^{-1}$	$1.469 \times 10^{-1}$

Table 6.23: Dominance ratio and  $E.S._n(k)$  eigenvalue separations of the first  $k$ -eigenvalues for the 1D homogeneous configuration with leakage boundary conditions as a function of the size L of the system.

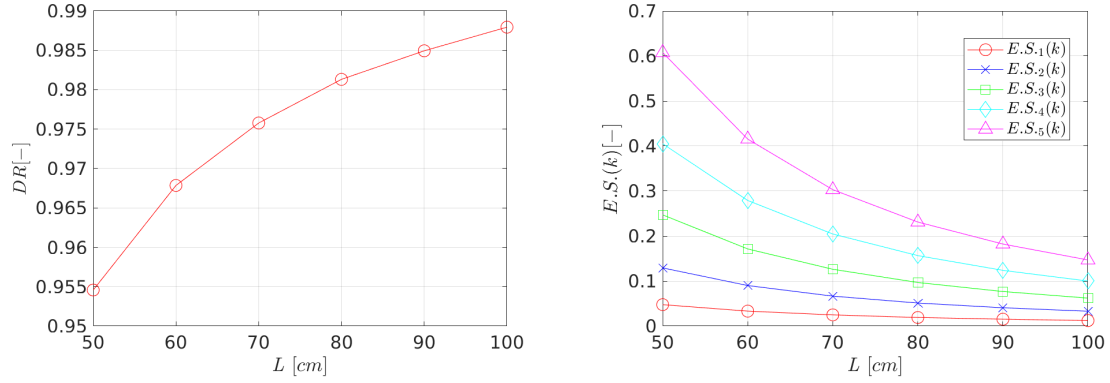


Figure 6.9: Dominance ratio (left) and  $k$ -eigenvalue separations (right) for the 1D homogeneous configuration with leakage boundary conditions as a function of the size  $L$  of the system. The first five order of eigenvalue separations are shown, in order, as:  $E.S._1(k)$  red circles,  $E.S._2(k)$  blue crosses,  $E.S._3(k)$  green squares,  $E.S._4(k)$  cyan diamonds and  $E.S._5(k)$  magenta triangles.

The  $\alpha$ -eigenvalues computed from the matrix-form of the  $\alpha$ -eigenvalue problem are used in order to estimate the delayed  $E.S.(\alpha_d)$  and the prompt  $E.S.(\alpha_p)$  eigenvalue separations of the first five orders. The delayed results are shown in Tab. 6.24, whereas the prompt results are shown in Tab. 6.25. The eigenvalue separations  $E.S.(\alpha_d)$  and the eigenvalue separations  $E.S.(\alpha_p)$  are shown in Fig. 6.10. The conclusions drawn from these results are similar to those drawn from the corresponding reflective case previously discussed in Section 6.4.1.

$L$ [cm]	$E.S._1(\alpha_d)$ [ $s^{-1}$ ]	$E.S._2(\alpha_d)$ [ $s^{-1}$ ]	$E.S._3(\alpha_d)$ [ $s^{-1}$ ]	$E.S._4(\alpha_d)$ [ $s^{-1}$ ]	$E.S._5(\alpha_d)$ [ $s^{-1}$ ]
50	$-1.410 \times 10^{-2}$	$-1.414 \times 10^{-2}$	$-1.415 \times 10^{-2}$	$-1.415 \times 10^{-2}$	$-1.416 \times 10^{-2}$
60	$-1.585 \times 10^{-2}$	$-1.591 \times 10^{-2}$	$-1.593 \times 10^{-2}$	$-1.594 \times 10^{-2}$	$-1.594 \times 10^{-2}$
70	$-1.684 \times 10^{-2}$	$-1.692 \times 10^{-2}$	$-1.694 \times 10^{-2}$	$-1.695 \times 10^{-2}$	$-1.696 \times 10^{-2}$
80	$-1.395 \times 10^{-2}$	$-1.406 \times 10^{-2}$	$-1.408 \times 10^{-2}$	$-1.410 \times 10^{-2}$	$-1.410 \times 10^{-2}$
90	$-1.555 \times 10^{-2}$	$-1.569 \times 10^{-2}$	$-1.572 \times 10^{-2}$	$-1.574 \times 10^{-2}$	$-1.575 \times 10^{-2}$
100	$-1.158 \times 10^{-2}$	$-1.175 \times 10^{-2}$	$-1.179 \times 10^{-2}$	$-1.181 \times 10^{-2}$	$-1.182 \times 10^{-2}$

Table 6.24: Eigenvalue separations of the first delayed  $\alpha$ -eigenvalues for the 1D homogeneous configuration with leakage boundary conditions as a function of the size  $L$  of the system.

$L$ [cm]	$E.S._1(\alpha_p)$ [ $s^{-1}$ ]	$E.S._2(\alpha_p)$ [ $s^{-1}$ ]	$E.S._3(\alpha_p)$ [ $s^{-1}$ ]	$E.S._4(\alpha_p)$ [ $s^{-1}$ ]	$E.S._5(\alpha_p)$ [ $s^{-1}$ ]
50	$-2.102 \times 10^3$	$-5.361 \times 10^3$	$-9.441 \times 10^3$	$-1.404 \times 10^4$	$-1.891 \times 10^4$
60	$-1.491 \times 10^3$	$-3.864 \times 10^3$	$-6.924 \times 10^3$	$-1.049 \times 10^4$	$-1.437 \times 10^4$
70	$-1.125 \times 10^3$	$-2.915 \times 10^3$	$-5.283 \times 10^3$	$-8.096 \times 10^3$	$-1.124 \times 10^4$
80	$-8.677 \times 10^2$	$-2.274 \times 10^3$	$-4.150 \times 10^3$	$-6.417 \times 10^3$	$-8.995 \times 10^3$
90	$-7.002 \times 10^2$	$-1.824 \times 10^3$	$-3.345 \times 10^3$	$-5.204 \times 10^3$	$-7.344 \times 10^3$
100	$-5.599 \times 10^2$	$-1.488 \times 10^3$	$-2.741 \times 10^3$	$-4.284 \times 10^3$	$-6.075 \times 10^3$

Table 6.25: Eigenvalue separations of the first prompt  $\alpha$ -eigenvalues for the 1D homogeneous configuration with leakage boundary conditions as a function of the size  $L$  of the system.

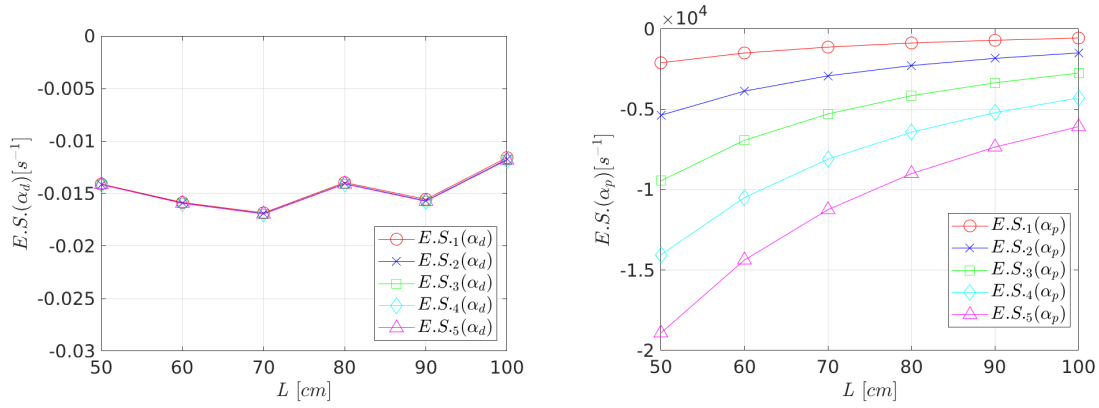


Figure 6.10: Delayed (left) and prompt (right)  $\alpha$ -eigenvalue separations for the 1D homogeneous configuration with leakage boundary conditions as a function of the size  $L$  of the system. The first five order of eigenvalue separations are shown, in order, as:  $E.S._1(\alpha)$  red circles,  $E.S._2(\alpha)$  blue crosses,  $E.S._3(\alpha)$  green squares,  $E.S._4(\alpha)$  cyan diamonds and  $E.S._5(\alpha)$  magenta triangles.

The similar behaviour observed between the 1D homogeneous configurations with reflective and leakage boundary conditions was expected, since the length of each case has been chosen in order to enhance the decoupling effects. The selected geometries are very large with respect to the neutron migration area, hence only a small percentage of the simulated particles will be affected by the boundaries.

Nevertheless, the effect of the leakage boundary conditions is clearly visible for the spatial shape of the fundamental and first-order eigenmodes of  $k$ ,  $\alpha$  and prompt  $\alpha$  eigenvalue formulations. The usual cosine distributions are found for the fundamental eigenfunction and a node is observed in the center of the system for the first-order eigenfunction. No visible differences are observed with respect to the eigenvalue formulation and to the length of the system. Same comments as those given for the 1D configuration with reflective boundary conditions apply to the analysis of the delayed  $\alpha$ -eigenmodes.

## 2D geometry

The fundamental eigenvalues  $k_0$  computed by the  $k$  power iteration are shown in the second column of Tab. 6.26. For these calculations,  $10^5$  particles per cycle are simulated, for a total of  $1.2 \times 10^3$  cycles ( $10^3$  active,  $2 \times 10^2$  inactive).

In order to compute the matrix operators, the size of the domain has been partitioned into  $N_x = N_y = c \times L$  space intervals along both  $x$ - and  $y$ - axes, where  $c = 0.3 \text{ cm}^{-1}$ , in order to keep a constant bin size. The cosine of the particle direction with respect to both spatial axes is uniformly partitioned into  $M_x = M_y = 2$  intervals, whereas the energy groups and precursor families are fixed at  $G = 3$  and  $J = 6$ , respectively. The total size of the matrix defining the  $\alpha$ -eigenvalue problem ranges from  $4.050 \times 10^3$  ( $L = 50 \text{ cm}$ ) to  $1.620 \times 10^4$  ( $L = 100 \text{ cm}$ ), whereas the matrix defining the  $k$ -eigenvalue problem ranges from  $2.700 \times 10^3$  to  $1.080 \times 10^4$ . The eigenvalues computed from the matrix-form of the corresponding eigenvalue problem are shown in Tabs. 6.26 ( $k$ -eigenvalues), 6.27 ( $\alpha$ -eigenvalues) and 6.28 (prompt  $\alpha$ -eigenvalues). All fundamental eigenvalues  $k_0$  computed from the matrix of the corresponding eigenvalue problem are within  $2\sigma$  standard deviation from the Monte Carlo results obtained from the  $k$  power iteration. The absolute values of the fundamental eigenvalues  $\alpha_0$  are smaller than  $2.5 \times 10^{-3} \text{ s}^{-1}$ . The dominant eigenvalue  $\alpha_{d,0}^j$  of the  $j$ -th delayed cluster is separated from the other eigenvalues of the same precursor family. The computed values of  $\alpha_{d,0}^j$  and  $\alpha_{d,1}^j$  for the last three precursor families ( $j = 4, 5, 6$ ) are shown in Tab. 6.29.

L [cm]	$k_0^{MC}$ [-]	$k_0$ [-]	$k_1$ [-]	$k_2$ [-]	$k_3$ [-]	$k_4$ [-]	$k_5$ [-]
50	$0.9999 \pm 1 \times 10^{-4}$	1.0001	0.8649	0.8645	0.7540	0.6749	0.6744
60	$0.9999 \pm 1 \times 10^{-4}$	1.0000	0.9024	0.9019	0.8174	0.7527	0.7525
70	$1.0002 \pm 1 \times 10^{-4}$	1.0003	0.9265	0.9256	0.8597	0.8075	0.8067
80	$0.9999 \pm 1 \times 10^{-4}$	1.0000	0.9424	0.9419	0.8894	0.8464	0.8455
90	$1.0003 \pm 1 \times 10^{-4}$	1.0001	0.9542	0.9535	0.9107	0.8749	0.8743
100	$0.9999 \pm 1 \times 10^{-4}$	1.0000	0.9622	0.9618	0.9263	0.8964	0.8959

Table 6.26: First  $k$ -eigenvalues for the 2D homogeneous configuration with leakage boundary conditions as a function of the size L of the system. The second column displays mean value and standard deviation of the fundamental eigenvalues  $k_0$  computed at the end of a power iteration with the test-bed Monte Carlo code for the  $k$ -eigenvalue problem. All other eigenvalues have been computed from the matrix-form of linear transport operator combined for the definition of the  $k$ -eigenvalue problem.

L [cm]	$\alpha_0$ [ $s^{-1}$ ]	$\alpha_1$ [ $s^{-1}$ ]	$\alpha_2$ [ $s^{-1}$ ]	$\alpha_3$ [ $s^{-1}$ ]	$\alpha_4$ [ $s^{-1}$ ]	$\alpha_5$ [ $s^{-1}$ ]
50	$1.376 \times 10^{-3}$	$-1.332 \times 10^{-2}$	$-1.332 \times 10^{-2}$	$-1.333 \times 10^{-2}$	$-1.333 \times 10^{-2}$	$-1.333 \times 10^{-2}$
60	$-1.466 \times 10^{-4}$	$-1.331 \times 10^{-2}$	$-1.331 \times 10^{-2}$	$-1.332 \times 10^{-2}$	$-1.333 \times 10^{-2}$	$-1.333 \times 10^{-2}$
70	$4.043 \times 10^{-3}$	$-1.330 \times 10^{-2}$	$-1.330 \times 10^{-2}$	$-1.332 \times 10^{-2}$	$-1.332 \times 10^{-2}$	$-1.333 \times 10^{-2}$
80	$5.862 \times 10^{-4}$	$-1.329 \times 10^{-2}$	$-1.329 \times 10^{-2}$	$-1.331 \times 10^{-2}$	$-1.332 \times 10^{-2}$	$-1.333 \times 10^{-2}$
90	$2.012 \times 10^{-3}$	$-1.327 \times 10^{-2}$	$-1.327 \times 10^{-2}$	$-1.330 \times 10^{-2}$	$-1.331 \times 10^{-2}$	$-1.333 \times 10^{-2}$
100	$-5.929 \times 10^{-4}$	$-1.326 \times 10^{-2}$	$-1.326 \times 10^{-2}$	$-1.330 \times 10^{-2}$	$-1.331 \times 10^{-2}$	$-1.333 \times 10^{-2}$

Table 6.27: First  $\alpha$ -eigenvalues for the 2D homogeneous configuration with leakage boundary conditions as a function of the size L of the system. These values have been computed from the matrix-form of linear transport operator combined for the definition of the  $\alpha$ -eigenvalue problem.

L [cm]	$\alpha_{p,0}$ [ $s^{-1}$ ]	$\alpha_{p,1}$ [ $s^{-1}$ ]	$\alpha_{p,2}$ [ $s^{-1}$ ]	$\alpha_{p,3}$ [ $s^{-1}$ ]	$\alpha_{p,4}$ [ $s^{-1}$ ]	$\alpha_{p,5}$ [ $s^{-1}$ ]
50	$-2.922 \times 10^2$	$-6.768 \times 10^3$	$-6.788 \times 10^3$	$-1.269 \times 10^4$	$-1.739 \times 10^4$	$-1.742 \times 10^4$
60	$-2.991 \times 10^2$	$-4.936 \times 10^3$	$-4.962 \times 10^3$	$-9.293 \times 10^3$	$-1.287 \times 10^4$	$-1.288 \times 10^4$
70	$-2.888 \times 10^2$	$-3.778 \times 10^3$	$-3.823 \times 10^3$	$-7.115 \times 10^3$	$-9.880 \times 10^3$	$-9.917 \times 10^3$
80	$-2.983 \times 10^2$	$-3.016 \times 10^3$	$-3.039 \times 10^3$	$-5.626 \times 10^3$	$-7.836 \times 10^3$	$-7.879 \times 10^3$
90	$-2.950 \times 10^2$	$-2.455 \times 10^3$	$-2.490 \times 10^3$	$-4.575 \times 10^3$	$-6.376 \times 10^3$	$-6.406 \times 10^3$
100	$-3.033 \times 10^2$	$-2.079 \times 10^3$	$-2.095 \times 10^3$	$-3.812 \times 10^3$	$-5.297 \times 10^3$	$-5.323 \times 10^3$

Table 6.28: First prompt  $\alpha$ -eigenvalues for the 2D homogeneous configuration with leakage boundary conditions as a function of the size L of the system. These values have been computed from the matrix-form of the  $\alpha$ -eigenvalue problem of the corresponding case.

L [cm]	$\alpha_{d,0}^4$ [s <sup>-1</sup> ]	$\alpha_{d,1}^4$ [s <sup>-1</sup> ]	$\alpha_{d,0}^5$ [s <sup>-1</sup> ]	$\alpha_{d,1}^5$ [s <sup>-1</sup> ]	$\alpha_{d,0}^6$ [s <sup>-1</sup> ]	$\alpha_{d,1}^6$ [s <sup>-1</sup> ]
50	$-1.909 \times 10^{-1}$	$-2.980 \times 10^{-1}$	$-7.379 \times 10^{-1}$	$-8.441 \times 10^{-1}$	-2.683	-2.845
60	$-1.919 \times 10^{-1}$	$-2.960 \times 10^{-1}$	$-7.389 \times 10^{-1}$	$-8.418 \times 10^{-1}$	-2.685	-2.842
70	$-1.889 \times 10^{-1}$	$-2.937 \times 10^{-1}$	$-7.358 \times 10^{-1}$	$-8.394 \times 10^{-1}$	-2.679	-2.839
80	$-1.914 \times 10^{-1}$	$-2.913 \times 10^{-1}$	$-7.381 \times 10^{-1}$	$-8.367 \times 10^{-1}$	-2.682	-2.835
90	$-1.905 \times 10^{-1}$	$-2.885 \times 10^{-1}$	$-7.371 \times 10^{-1}$	$-8.336 \times 10^{-1}$	-2.682	-2.831
100	$-1.924 \times 10^{-1}$	$-2.858 \times 10^{-1}$	$-7.393 \times 10^{-1}$	$-8.308 \times 10^{-1}$	-2.686	-2.826

Table 6.29: First  $\alpha$ -eigenvalues of the clusters associated to the last three precursor families ( $j = 4, 5, 6$ ) for the 2D homogeneous configuration with leakage boundary conditions as a function of the size L of the system. These values have been computed from the matrix-form of the  $\alpha$ -eigenvalue problem of the corresponding case.

The  $k$ -eigenvalues computed from the matrix-form of the  $k$ -eigenvalue problem are used in order to estimate the dominance ratio DR and the eigenvalue separations  $E.S._n(k)$  of the first five orders: they are shown in Tab. 6.30 and plotted in Fig. 6.11. The values of the dominance ratio increase for increasing length of the system from DR = 0.8648 up to DR = 0.9622. No major differences are observed with respect to the behaviour previously analyzed for the reflected system from Fig. 6.3. In particular, we observe that also for these 2D configurations the first and second, fourth and fifth orders of eigenvalue separations are extremely close. This degeneracy observed in the eigenvalues is related to the symmetry properties of the analyzed configurations.

L [cm]	DR [-]	$E.S._1(k)$ [-]	$E.S._2(k)$ [-]	$E.S._3(k)$ [-]	$E.S._4(k)$ [-]	$E.S._5(k)$ [-]
50	$8.648 \times 10^{-1}$	$1.563 \times 10^{-1}$	$1.568 \times 10^{-1}$	$3.264 \times 10^{-1}$	$4.817 \times 10^{-1}$	$4.829 \times 10^{-1}$
60	$9.024 \times 10^{-1}$	$1.081 \times 10^{-1}$	$1.088 \times 10^{-1}$	$2.235 \times 10^{-1}$	$3.286 \times 10^{-1}$	$3.289 \times 10^{-1}$
70	$9.262 \times 10^{-1}$	$7.963 \times 10^{-2}$	$8.069 \times 10^{-2}$	$1.634 \times 10^{-1}$	$2.387 \times 10^{-1}$	$2.398 \times 10^{-1}$
80	$9.424 \times 10^{-1}$	$6.113 \times 10^{-2}$	$6.169 \times 10^{-2}$	$1.244 \times 10^{-1}$	$1.816 \times 10^{-1}$	$1.827 \times 10^{-1}$
90	$9.541 \times 10^{-1}$	$4.809 \times 10^{-2}$	$4.892 \times 10^{-2}$	$9.822 \times 10^{-2}$	$1.431 \times 10^{-1}$	$1.439 \times 10^{-1}$
100	$9.622 \times 10^{-1}$	$3.929 \times 10^{-2}$	$3.963 \times 10^{-2}$	$7.952 \times 10^{-2}$	$1.155 \times 10^{-1}$	$1.162 \times 10^{-1}$

Table 6.30: Dominance ratio and  $E.S._n(k)$  eigenvalue separations of the first  $k$ -eigenvalues for the 2D homogeneous configuration with leakage boundary conditions as a function of the size L of the system.

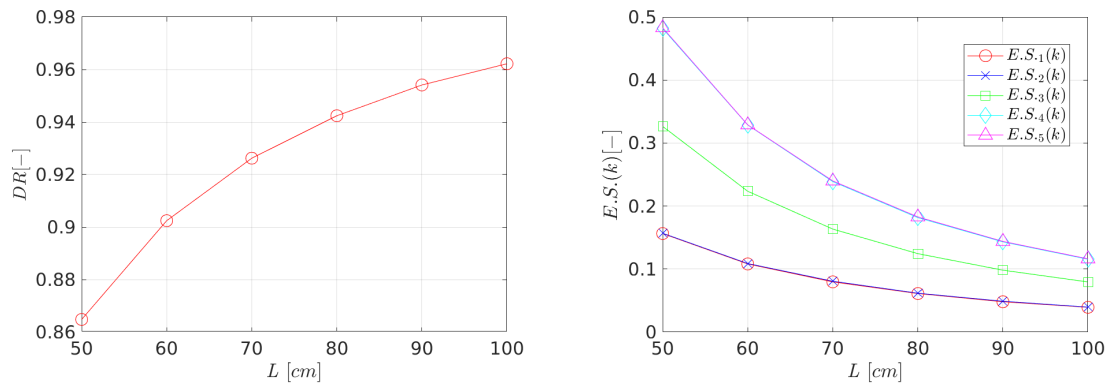


Figure 6.11: Dominance ratio (left) and  $k$ -eigenvalue separations (right) for the 2D homogeneous configuration with leakage boundary conditions as a function of the size L of the system. The first five order of eigenvalue separations are shown, in order, as:  $E.S._1(k)$  red circles,  $E.S._2(k)$  blue crosses,  $E.S._3(k)$  green squares,  $E.S._4(k)$  cyan diamonds and  $E.S._5(k)$  magenta triangles.

The  $\alpha$ -eigenvalues computed from the matrix-form of the  $\alpha$ -eigenvalue problem are used in order to estimate the delayed  $E.S.(\alpha_d)$  and the prompt  $E.S.(\alpha_p)$  eigenvalue separations of the first five orders. The delayed results are shown in Tab. 6.31, whereas the prompt results are shown in Tab. 6.32. The eigenvalue separations  $E.S.(\alpha_d)$

and the eigenvalue separations  $E.S.(\alpha_p)$  are shown in Fig. 6.12. The conclusions drawn from these results are equivalent to those found for the corresponding reflective case previously discussed in Section 6.4.1.

L [cm]	$E.S.1(\alpha_d)$ [ $s^{-1}$ ]	$E.S.2(\alpha_d)$ [ $s^{-1}$ ]	$E.S.3(\alpha_d)$ [ $s^{-1}$ ]	$E.S.4(\alpha_d)$ [ $s^{-1}$ ]	$E.S.5(\alpha_d)$ [ $s^{-1}$ ]
50	$-1.469 \times 10^{-2}$	$-1.469 \times 10^{-2}$	$-1.470 \times 10^{-2}$	$-1.471 \times 10^{-2}$	$-1.471 \times 10^{-2}$
60	$-1.316 \times 10^{-2}$	$-1.316 \times 10^{-2}$	$-1.318 \times 10^{-2}$	$-1.318 \times 10^{-2}$	$-1.318 \times 10^{-2}$
70	$-1.734 \times 10^{-2}$	$-1.734 \times 10^{-2}$	$-1.736 \times 10^{-2}$	$-1.737 \times 10^{-2}$	$-1.737 \times 10^{-2}$
80	$-1.387 \times 10^{-2}$	$-1.387 \times 10^{-2}$	$-1.390 \times 10^{-2}$	$-1.391 \times 10^{-2}$	$-1.391 \times 10^{-2}$
90	$-1.528 \times 10^{-2}$	$-1.528 \times 10^{-2}$	$-1.532 \times 10^{-2}$	$-1.533 \times 10^{-2}$	$-1.533 \times 10^{-2}$
100	$-1.267 \times 10^{-2}$	$-1.267 \times 10^{-2}$	$-1.271 \times 10^{-2}$	$-1.272 \times 10^{-2}$	$-1.272 \times 10^{-2}$

Table 6.31: Eigenvalue separations of the first prompt  $\alpha$ -eigenvalues for the 2D homogeneous configuration with reflective boundary conditions as a function of the size L of the system.

L [cm]	$E.S.1(\alpha_p)$ [ $s^{-1}$ ]	$E.S.2(\alpha_p)$ [ $s^{-1}$ ]	$E.S.3(\alpha_p)$ [ $s^{-1}$ ]	$E.S.4(\alpha_p)$ [ $s^{-1}$ ]	$E.S.5(\alpha_p)$ [ $s^{-1}$ ]
50	$-6.476 \times 10^3$	$-6.496 \times 10^3$	$-1.240 \times 10^4$	$-1.710 \times 10^4$	$-1.713 \times 10^4$
60	$-4.637 \times 10^3$	$-4.663 \times 10^3$	$-8.994 \times 10^3$	$-1.257 \times 10^4$	$-1.258 \times 10^4$
70	$-3.490 \times 10^3$	$-3.534 \times 10^3$	$-6.827 \times 10^3$	$-9.591 \times 10^3$	$-9.628 \times 10^3$
80	$-2.717 \times 10^3$	$-2.741 \times 10^3$	$-5.328 \times 10^3$	$-7.537 \times 10^3$	$-7.581 \times 10^3$
90	$-2.160 \times 10^3$	$-2.195 \times 10^3$	$-4.280 \times 10^3$	$-6.081 \times 10^3$	$-6.111 \times 10^3$
100	$-1.776 \times 10^3$	$-1.791 \times 10^3$	$-3.509 \times 10^3$	$-4.994 \times 10^3$	$-5.020 \times 10^3$

Table 6.32: Eigenvalue separations of the first prompt  $\alpha$ -eigenvalues for the 2D homogeneous configuration with leakage boundary conditions as a function of the size L of the system.

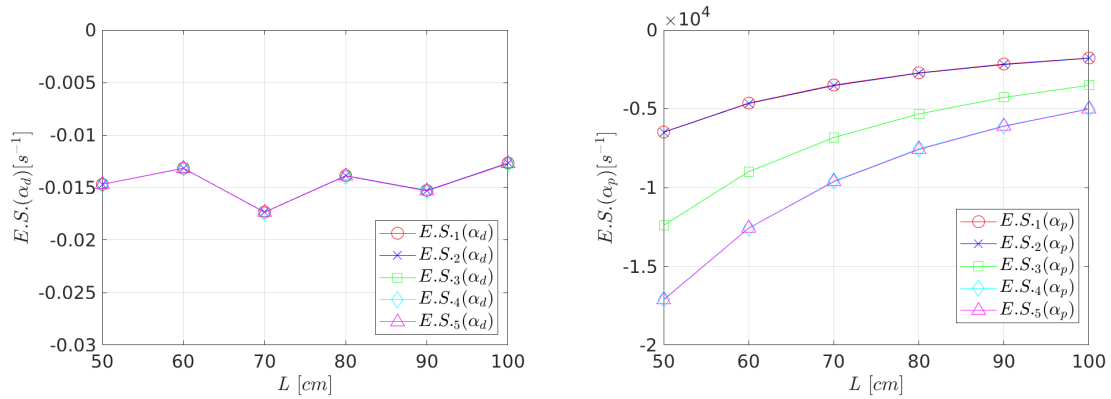


Figure 6.12: Delayed (left) and prompt (right)  $\alpha$ -eigenvalue separations for the 2D homogeneous configuration with leakage boundary conditions as a function of the size L of the system. The first five order of eigenvalue separations are shown, in order, as:  $E.S.1(\alpha)$  red circles,  $E.S.2(\alpha)$  blue crosses,  $E.S.3(\alpha)$  green squares,  $E.S.4(\alpha)$  cyan diamonds and  $E.S.5(\alpha)$  magenta triangles.

The similar behaviour observed between the 2D homogeneous configurations with reflective and leakage boundary conditions was expected, since the size of each case has been chosen in order to enhance the decoupling effects. The selected geometries are very large with respect to the neutron migration area, hence only a small percentage of the simulated particles will be affected by the boundaries.

Nevertheless, the effect of leakage boundary conditions is clearly visible for the spatial shape of the fundamental (Fig. 6.13), first-order (Fig. 6.14) and second-order (Fig. 6.15) eigenmodes of  $k$ ,  $\alpha$  and prompt  $\alpha$  eigenvalue formulations. The usual Bessel-like distributions are found for the fundamental eigenfunction and the presence of a node is observed for the first-order eigenfunction. The second-order distributions are similar to the first-order distributions rotated by  $90^\circ$ : such behaviour confirms the presence of a degeneracy for higher-order eigenpairs due

to the symmetries of the configuration. Same comments as those presented for the 2D configuration with reflective boundary conditions apply to the analysis of the delayed  $\alpha$ -eigenmodes.

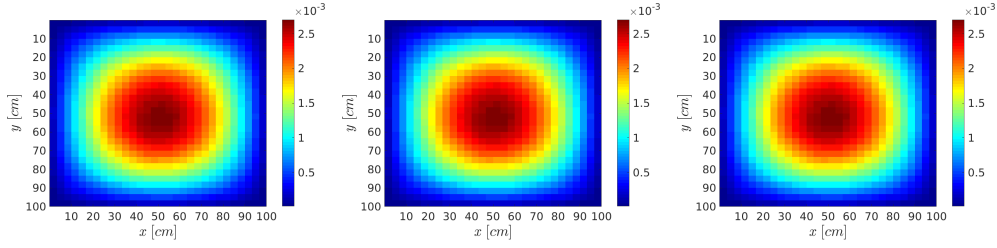


Figure 6.13: Spatial distribution of the  $k$  (left),  $\alpha$  (center) and prompt  $\alpha$  (right) fundamental eigenmodes for the 2D homogeneous configuration with leakage boundary conditions for the most decoupled case ( $L = 100$  cm).

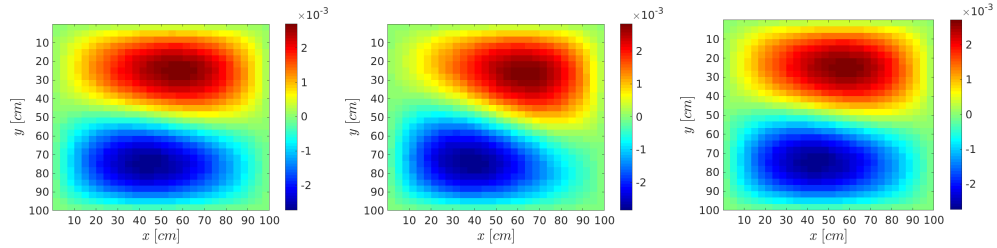


Figure 6.14: Spatial distribution of the  $k$  (left),  $\alpha$  (center) and prompt  $\alpha$  (right) first-order eigenmodes for the 2D homogeneous configuration with leakage boundary conditions for the most decoupled case ( $L = 100$  cm).

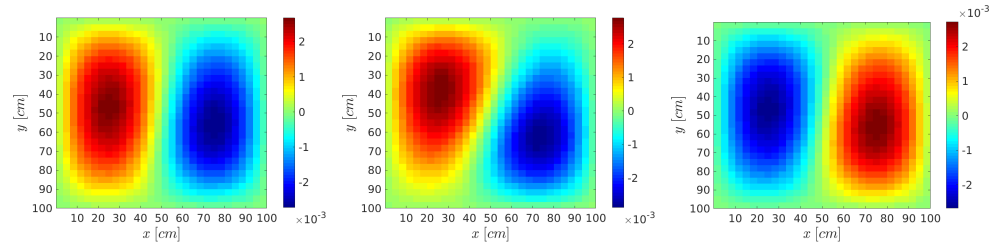


Figure 6.15: Spatial distribution of the  $k$  (left),  $\alpha$  (center) and prompt  $\alpha$  (right) second-order eigenmodes for the 2D homogeneous configuration with leakage boundary conditions for the most decoupled case ( $L = 100$  cm).

## 6.5 Heterogeneous benchmark configurations

The occurrence of decoupling effects for heterogeneous configurations can be observed when neutrons are localized into distinct regions of the system, due to the presence of strong spatial heterogeneities [120]. A perturbation induced in a specific spatial location of the system has to overcome such heterogeneity in order to reach the other decoupled regions. In this section, we investigate the spectral properties induced by the presence of these effects for a critical 1D heterogeneous configuration with leakage boundary conditions.

In particular, we have considered a three-region slab geometry in which two fissile regions (of length  $L_{\text{fissile}} = 20$  cm, respectively) are separated by a progressively larger moderator region (defined by the length  $L_{\text{moderator}}$ ). Six cases have been selected for our analysis, with the total length of the geometry  $L = 2L_{\text{fissile}} + L_{\text{moderator}}$ . The choice of this configuration was inspired by the three-region slab geometry benchmark problem analyzed in reference [165]. The parameters describing these regions have been shown in Tabs. 6.1 and 6.2 for the fissile material and in Tab. 6.3 for the moderator material. The first step of our analysis consists in the search of a critical configuration by  $k$  power iteration.

The adjustment to the critical level for this first step of the parametric study has been performed by modifying the macroscopic capture cross section in the fissile material by a parameter  $a$  following Eq. (6.9). Then, we

analyzed five additional cases by decreasing the length of the moderator region in order to increase the coupling between the fissile regions. All cases have been readjusted to the critical level by an iteratively search of a coefficient  $b$  applied to the macroscopic capture cross section of the fissile material according to Eq. 6.10.

### 6.5.1 1D heterogeneous configurations

In order to investigate the three-region slab geometries considered in this section, we have started by considering a configuration characterized by regions having equal width. The emergence of decoupling effect was observed for a 20 cm long slab region in reference [165], hence the length of the system will be set to 60 cm. A value  $a = 1.167$  applied to the macroscopic capture cross section of the fissile regions leads to  $k_0 = 1.0002 \pm 4 \times 10^{-4}$  from a  $k$  power iteration performed with  $2 \times 10^4$  particles per cycle and a total of  $6 \times 10^2$  cycles ( $5 \times 10^2$  active,  $10^2$  inactive). Five smaller lengths of the moderator region have been also considered: 15 cm, 10 cm, 7 cm, 5 cm and 2 cm, respectively. The coefficient  $b$  from Eq. (6.10) has been iteratively computed by simulating  $5 \times 10^4$  particles per cycle and a total of  $2 \times 10^3$  cycles. The fundamental eigenvalues  $k_0$  computed by the  $k$  power iteration are shown in the second column of Tab. 6.33. For these calculations,  $10^5$  particles per cycle are simulated, for a total of  $1.2 \times 10^3$  cycles ( $10^3$  active,  $2 \times 10^2$  inactive).

In order to compute the matrix operators, the length of the domain has been partitioned into  $N_x = c \times L$  space intervals along the x-axis, where  $c = 20 \text{ cm}^{-1}$ , in order to keep a constant bin width. The cosine of the particle direction with respect to the x-axis is uniformly partitioned into  $M_x = 4$  intervals, whereas the energy groups and precursor families are fixed at  $G = 3$  and  $J = 6$ , respectively. The total size of the matrix defining the  $\alpha$ -eigenvalue problem ranges from  $1.512 \times 10^4$  ( $L = 42 \text{ cm}$ ) to  $2.160 \times 10^4$  ( $L = 60 \text{ cm}$ ), whereas the matrix defining the  $k$ -eigenvalue problem ranges from  $1.008 \times 10^4$  to  $1.440 \times 10^4$ . The eigenvalues computed from the matrix-form of the corresponding eigenvalue problem are shown in Tabs. 6.33 ( $k$ -eigenvalues), 6.34 ( $\alpha$ -eigenvalues) and 6.35 (prompt  $\alpha$ -eigenvalues). All fundamental eigenvalues  $k_0$  computed from the matrix of the corresponding eigenvalue problem are within  $2\sigma$  standard deviation from the Monte Carlo results obtained from the  $k$  power iteration. The absolute values of the fundamental eigenvalues  $\alpha_0$  are smaller than  $2.5 \times 10^{-3} \text{ s}^{-1}$ . The dominant eigenvalue  $\alpha_{d,0}^j$  of the  $j$ -th delayed cluster is separated from the other eigenvalues of the same precursor family [133, 132]. The computed values of  $\alpha_{d,0}^j$  and  $\alpha_{d,1}^j$  for the last three precursor families ( $j = 4, 5, 6$ ) are shown in Tab. 6.36.

L [cm]	$k_0^{MC}$ [-]	$k_0$ [-]	$k_1$ [-]	$k_2$ [-]	$k_3$ [-]	$k_4$ [-]	$k_5$ [-]
42	$0.9997 \pm 2 \times 10^{-4}$	0.9999	0.7907	0.5538	0.3909	0.2600	0.1904
45	$1.0003 \pm 2 \times 10^{-4}$	1.0001	0.8669	0.5699	0.4539	0.2726	0.2252
47	$1.0000 \pm 2 \times 10^{-4}$	1.0001	0.9122	0.5700	0.4891	0.2750	0.2422
50	$1.0002 \pm 2 \times 10^{-4}$	1.0001	0.9571	0.5650	0.5234	0.2747	0.2577
55	$0.9996 \pm 2 \times 10^{-4}$	0.9998	0.9882	0.5585	0.5469	0.2725	0.2676
60	$0.9999 \pm 2 \times 10^{-4}$	0.9998	0.9969	0.5563	0.5533	0.2716	0.2703

Table 6.33: First  $k$ -eigenvalues for the 1D heterogeneous configuration as a function of the size  $L$  of the system. The second column displays mean value and standard deviation of the fundamental eigenvalues  $k_0$  computed at the end of a power iteration with the test-bed Monte Carlo code for the  $k$ -eigenvalue problem. All other eigenvalues have been computed from the matrix-form of linear transport operator combined for the definition of the  $k$ -eigenvalue problem.

## 6.5. HETEROGENEOUS BENCHMARK CONFIGURATIONS

L [cm]	$\alpha_0$ [s <sup>-1</sup> ]	$\alpha_1$ [s <sup>-1</sup> ]	$\alpha_2$ [s <sup>-1</sup> ]	$\alpha_3$ [s <sup>-1</sup> ]	$\alpha_4$ [s <sup>-1</sup> ]	$\alpha_5$ [s <sup>-1</sup> ]
42	$-1.973 \times 10^{-3}$	$-1.332 \times 10^{-2}$	$-1.333 \times 10^{-2}$	$-1.333 \times 10^{-2}$	$-1.333 \times 10^{-2}$	$-1.333 \times 10^{-2}$
45	$1.522 \times 10^{-3}$	$-1.332 \times 10^{-2}$	$-1.333 \times 10^{-2}$	$-1.333 \times 10^{-2}$	$-1.333 \times 10^{-2}$	$-1.333 \times 10^{-2}$
47	$6.714 \times 10^{-4}$	$-1.330 \times 10^{-2}$	$-1.333 \times 10^{-2}$	$-1.333 \times 10^{-2}$	$-1.333 \times 10^{-2}$	$-1.333 \times 10^{-2}$
50	$1.209 \times 10^{-3}$	$-1.326 \times 10^{-2}$	$-1.333 \times 10^{-2}$	$-1.333 \times 10^{-2}$	$-1.333 \times 10^{-2}$	$-1.333 \times 10^{-2}$
55	$-2.429 \times 10^{-3}$	$-1.305 \times 10^{-2}$	$-1.333 \times 10^{-2}$	$-1.333 \times 10^{-2}$	$-1.333 \times 10^{-2}$	$-1.333 \times 10^{-2}$
60	$-2.466 \times 10^{-3}$	$-1.205 \times 10^{-2}$	$-1.333 \times 10^{-2}$	$-1.333 \times 10^{-2}$	$-1.333 \times 10^{-2}$	$-1.333 \times 10^{-2}$

Table 6.34: First  $\alpha$ -eigenvalues for the 1D heterogeneous configuration as a function of the size L of the system. These values have been computed from the matrix-form of linear transport operator combined for the definition of the  $\alpha$ -eigenvalue problem.

L [cm]	$\alpha_{p,0}$ [s <sup>-1</sup> ]	$\alpha_{p,1}$ [s <sup>-1</sup> ]	$\alpha_{p,2}$ [s <sup>-1</sup> ]	$\alpha_{p,3}$ [s <sup>-1</sup> ]	$\alpha_{p,4}$ [s <sup>-1</sup> ]	$\alpha_{p,5}$ [s <sup>-1</sup> ]
42	$-2.419 \times 10^2$	$-9.153 \times 10^3$	$-1.716 \times 10^4$	$-2.791 \times 10^4$	$-3.332 \times 10^4$	$-4.229 \times 10^4$
45	$-1.900 \times 10^2$	$-5.471 \times 10^3$	$-1.211 \times 10^4$	$-2.164 \times 10^4$	$-2.708 \times 10^4$	$-3.382 \times 10^4$
47	$-1.874 \times 10^2$	$-3.470 \times 10^3$	$-1.025 \times 10^4$	$-1.757 \times 10^4$	$-2.403 \times 10^4$	$-2.927 \times 10^4$
50	$-1.908 \times 10^2$	$-1.686 \times 10^3$	$-8.744 \times 10^3$	$-1.359 \times 10^4$	$-2.017 \times 10^4$	$-2.509 \times 10^4$
55	$-2.076 \times 10^2$	$-5.880 \times 10^2$	$-7.671 \times 10^3$	$-1.051 \times 10^4$	$-1.514 \times 10^4$	$-2.035 \times 10^4$
60	$-2.115 \times 10^2$	$-3.062 \times 10^2$	$-7.196 \times 10^3$	$-9.122 \times 10^3$	$-1.218 \times 10^4$	$-1.635 \times 10^4$

Table 6.35: First prompt  $\alpha$ -eigenvalues for the 1D heterogeneous configuration as a function of the size L of the system. These values have been computed from the matrix-form of linear transport operator combined for the definition of the  $\alpha$ -eigenvalue problem.

L [cm]	$\alpha_{d,0}^4$ [s <sup>-1</sup> ]	$\alpha_{d,1}^4$ [s <sup>-1</sup> ]	$\alpha_{d,0}^5$ [s <sup>-1</sup> ]	$\alpha_{d,1}^5$ [s <sup>-1</sup> ]	$\alpha_{d,0}^6$ [s <sup>-1</sup> ]	$\alpha_{d,1}^6$ [s <sup>-1</sup> ]
42	$-1.936 \times 10^{-1}$	$-2.998 \times 10^{-1}$	$-7.407 \times 10^{-1}$	$-8.461 \times 10^{-1}$	-2.687	-2.848
45	$-1.908 \times 10^{-1}$	$-2.978 \times 10^{-1}$	$-7.376 \times 10^{-1}$	$-8.438 \times 10^{-1}$	-2.681	-2.845
47	$-1.915 \times 10^{-1}$	$-2.950 \times 10^{-1}$	$-7.384 \times 10^{-1}$	$-8.407 \times 10^{-1}$	-2.680	-2.841
50	$-1.913 \times 10^{-1}$	$-2.872 \times 10^{-1}$	$-7.374 \times 10^{-1}$	$-8.322 \times 10^{-1}$	-2.681	-2.829
55	$-1.943 \times 10^{-1}$	$-2.588 \times 10^{-1}$	$-7.415 \times 10^{-1}$	$-8.039 \times 10^{-1}$	-2.687	-2.787
60	$-1.942 \times 10^{-1}$	$-2.208 \times 10^{-1}$	$-7.408 \times 10^{-1}$	$-7.683 \times 10^{-1}$	-2.688	-2.733

Table 6.36: First  $\alpha$ -eigenvalues of the clusters associated to the last three precursor families ( $j = 4, 5, 6$ ) for the 1D heterogeneous configuration as a function of the size L of the system. These values have been computed from the matrix-form of the  $\alpha$ -eigenvalue problem of the corresponding case.

The  $k$ -eigenvalues computed from the matrix-form of the  $k$ -eigenvalue problem are used in order to estimate the dominance ratio DR and the eigenvalue separations  $E.S._n(k)$  of the first five orders: they are shown in Tab. 6.37 and plotted in Fig. 6.9. The values of the dominance ratio increase for increasing length of the system from DR = 0.7908 up to DR = 0.9971. The eigenvalue separation  $E.S._1(k)$  for this heterogeneous configuration decreases for increasing length of the system. Contrary to the results observed for the homogeneous configurations (Figs. 6.3 and 6.9), the higher-order eigenvalue separations  $E.S._n(k)$ ,  $n > 1$ , are much larger than the first-order  $E.S._1(k)$ ; moreover,  $E.S._{2n+1}(k)$  converges to  $E.S._{2n}(k)$  for stronger decoupling between the fissile regions (Fig. 6.9). This convergence behaviour may be related to the symmetry of the system, induced by the two fissile region being of equal length.

L [cm]	DR [-]	E.S. <sub>1</sub> (k) [-]	E.S. <sub>2</sub> (k) [-]	E.S. <sub>3</sub> (k) [-]	E.S. <sub>4</sub> (k) [-]	E.S. <sub>5</sub> (k) [-]
42	$7.908 \times 10^{-1}$	$2.646 \times 10^{-1}$	$8.056 \times 10^{-1}$	$1.558 \times 10^0$	$2.846 \times 10^0$	$4.253 \times 10^0$
45	$8.668 \times 10^{-1}$	$1.537 \times 10^{-1}$	$7.549 \times 10^{-1}$	$1.203 \times 10^0$	$2.669 \times 10^0$	$3.440 \times 10^0$
47	$9.122 \times 10^{-1}$	$9.628 \times 10^{-2}$	$7.545 \times 10^{-1}$	$1.045 \times 10^0$	$2.637 \times 10^0$	$3.129 \times 10^0$
50	$9.570 \times 10^{-1}$	$4.488 \times 10^{-2}$	$7.700 \times 10^{-1}$	$9.108 \times 10^{-1}$	$2.640 \times 10^0$	$2.881 \times 10^0$
55	$9.884 \times 10^{-1}$	$1.173 \times 10^{-2}$	$7.903 \times 10^{-1}$	$8.285 \times 10^{-1}$	$2.669 \times 10^0$	$2.736 \times 10^0$
60	$9.971 \times 10^{-1}$	$2.947 \times 10^{-3}$	$7.975 \times 10^{-1}$	$8.072 \times 10^{-1}$	$2.682 \times 10^0$	$2.699 \times 10^0$

Table 6.37: Dominance ratio and E.S.<sub>n</sub>(k) eigenvalue separations of the first k-eigenvalues for the 1D heterogeneous configuration.

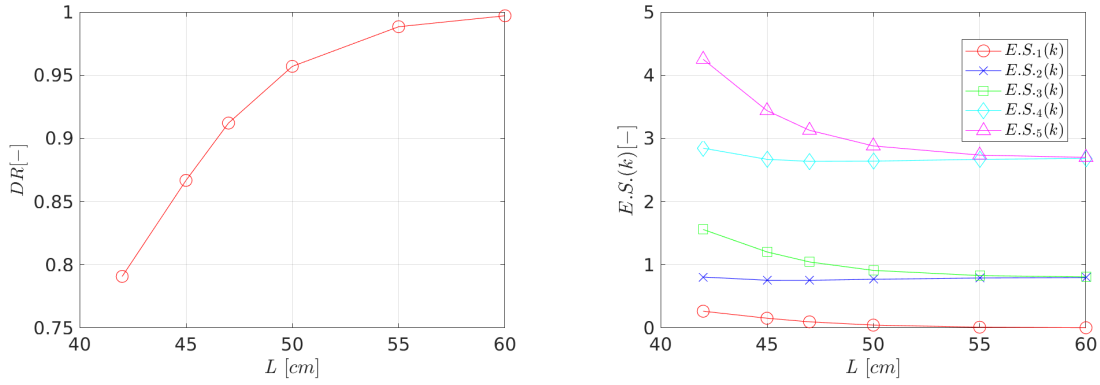


Figure 6.16: Dominance ratio (left) and k-eigenvalue separations (right) for the 1D heterogeneous configuration as a function of the size L of the system. The first five order of eigenvalue separations are shown, in order, as: E.S.<sub>1</sub>(k) red circles, E.S.<sub>2</sub>(k) blue crosses, E.S.<sub>3</sub>(k) green squares, E.S.<sub>4</sub>(k) cyan diamonds and E.S.<sub>5</sub>(k) magenta triangles.

The  $\alpha$ -eigenvalues computed from the matrix-form of the  $\alpha$ -eigenvalue problem are used in order to estimate the delayed E.S.<sub>( $\alpha_d$ ) and the prompt E.S.<sub>( $\alpha_p$ ) eigenvalue separations of the first five orders. The delayed results are shown in Tab. 6.38, whereas the prompt results are shown in Tab. 6.39. The delayed eigenvalue separations (Fig. 6.17, left) are almost insensitive to the length of the system. The prompt  $\alpha$ -eigenvalue separations (Fig. 6.17, right) have a distinct behaviour as opposed to the k-eigenvalue separations. Moreover, also E.S.<sub>( $\alpha_p$ )<sub>2n+1</sub> seems to converge to E.S.<sub>( $\alpha_p$ )<sub>2n</sub>, but a larger gap is observed between these two orders of eigenvalue separations with respect to the k-eigenvalue separations of the corresponding orders. These results are specific to the presence of a non-fissile region for this heterogeneous configuration. Contrary to the k-eigenvalue formulation, the  $\alpha$ -eigenvalue formulation is sensible to the time scales of the system: the moderator region subtly modifies the impact of the fissile regions of the former eigenvalue formulation with respect to the latter.</sub></sub></sub></sub>

L [cm]	E.S. <sub>1</sub> ( $\alpha_d$ ) [s <sup>-1</sup> ]	E.S. <sub>2</sub> ( $\alpha_d$ ) [s <sup>-1</sup> ]	E.S. <sub>3</sub> ( $\alpha_d$ ) [s <sup>-1</sup> ]	E.S. <sub>4</sub> ( $\alpha_d$ ) [s <sup>-1</sup> ]	E.S. <sub>5</sub> ( $\alpha_d$ ) [s <sup>-1</sup> ]
42	$-1.135 \times 10^{-2}$	$-1.136 \times 10^{-2}$	$-1.136 \times 10^{-2}$	$-1.136 \times 10^{-2}$	$-1.136 \times 10^{-2}$
45	$-1.484 \times 10^{-2}$	$-1.485 \times 10^{-2}$	$-1.486 \times 10^{-2}$	$-1.486 \times 10^{-2}$	$-1.486 \times 10^{-2}$
47	$-1.397 \times 10^{-2}$	$-1.400 \times 10^{-2}$	$-1.400 \times 10^{-2}$	$-1.401 \times 10^{-2}$	$-1.401 \times 10^{-2}$
50	$-1.447 \times 10^{-2}$	$-1.454 \times 10^{-2}$	$-1.454 \times 10^{-2}$	$-1.454 \times 10^{-2}$	$-1.454 \times 10^{-2}$
55	$-1.062 \times 10^{-2}$	$-1.090 \times 10^{-2}$	$-1.090 \times 10^{-2}$	$-1.091 \times 10^{-2}$	$-1.091 \times 10^{-2}$
60	$-9.583 \times 10^{-3}$	$-1.087 \times 10^{-2}$	$-1.087 \times 10^{-2}$	$-1.087 \times 10^{-2}$	$-1.087 \times 10^{-2}$

Table 6.38: Eigenvalue separations of the first delayed  $\alpha$ -eigenvalues for the 1D homogeneous configuration with reflective boundary conditions as a function of the size L of the system.

L [cm]	E.S. <sub>1</sub> ( $\alpha_p$ ) [s <sup>-1</sup> ]	E.S. <sub>2</sub> ( $\alpha_p$ ) [s <sup>-1</sup> ]	E.S. <sub>3</sub> ( $\alpha_p$ ) [s <sup>-1</sup> ]	E.S. <sub>4</sub> ( $\alpha_p$ ) [s <sup>-1</sup> ]	E.S. <sub>5</sub> ( $\alpha_p$ ) [s <sup>-1</sup> ]
42	$-8.911 \times 10^3$	$-1.692 \times 10^4$	$-2.766 \times 10^4$	$-3.308 \times 10^4$	$-4.205 \times 10^4$
45	$-5.281 \times 10^3$	$-1.192 \times 10^4$	$-2.145 \times 10^4$	$-2.689 \times 10^4$	$-3.363 \times 10^4$
47	$-3.283 \times 10^3$	$-1.006 \times 10^4$	$-1.738 \times 10^4$	$-2.385 \times 10^4$	$-2.908 \times 10^4$
50	$-1.495 \times 10^3$	$-8.553 \times 10^3$	$-1.340 \times 10^4$	$-1.998 \times 10^4$	$-2.480 \times 10^4$
55	$-3.804 \times 10^2$	$-7.464 \times 10^3$	$-1.031 \times 10^4$	$-1.493 \times 10^4$	$-2.014 \times 10^4$
60	$-9.470 \times 10^1$	$-6.984 \times 10^3$	$-8.911 \times 10^3$	$-1.197 \times 10^4$	$-1.614 \times 10^4$

Table 6.39: Eigenvalue separations of the first prompt  $\alpha$ -eigenvalues for the 1D homogeneous configuration with reflective boundary conditions.

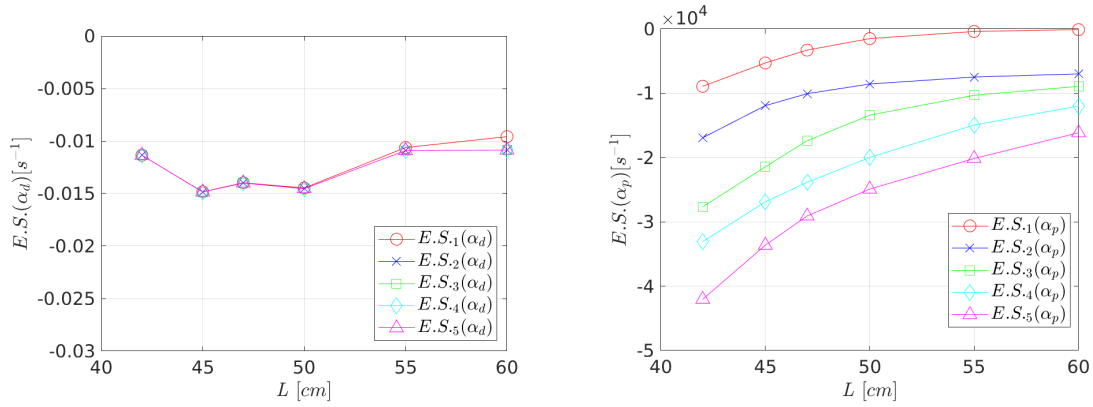


Figure 6.17: Delayed (left) and prompt (right)  $\alpha$ -eigenvalue separations for the 1D heterogeneous configuration as a function of the size  $L$  of the system. The first five order of eigenvalue separations are shown, in order, as: E.S.<sub>1</sub> red circles, E.S.<sub>2</sub> blue crosses, E.S.<sub>3</sub> green squares, E.S.<sub>4</sub> cyan diamonds and E.S.<sub>5</sub> magenta triangles.

The corresponding fundamental (Fig. 6.18) and first-order (Fig. 6.19) eigenmodes are examined for  $k$ ,  $\alpha$  and prompt  $\alpha$  eigenvalue formulations. By inspection of the fundamental eigenfunction, the central region of the system over-moderates for small length of the moderator region (from  $L = 42$  cm, up to  $L = 47$  cm). For larger sizes of the central region, the over-moderation effects are progressively less visible, only at the frontiers with the fissile material. The spatial shape drops in the central region by decoupling the system behaviour into two distinct spatial regions (from  $L = 50$  cm, up to  $L = 60$  cm). No visible differences are observed with respect to the eigenvalue formulation and to the length of the system. Same comments as those presented for the 1D homogeneous configuration can be applied for the analysis of the delayed  $\alpha$ -eigenmodes.

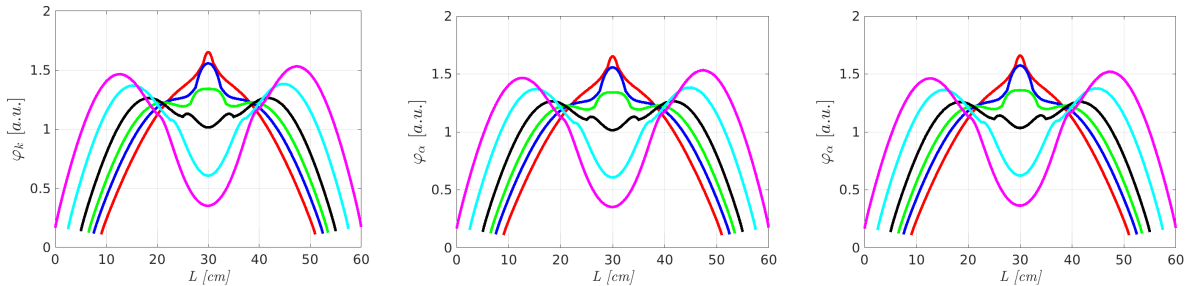


Figure 6.18: Spatial distribution of the  $k$  (left),  $\alpha$  (center) and prompt  $\alpha$  fundamental eigenmodes for the 1D heterogeneous as a function of the size  $L$  of the system. Color legend according to the ascending order of the size  $L$  of the system is:  $L = 42$  cm red,  $L = 45$  cm blue,  $L = 47$  cm green,  $L = 50$  cm black,  $L = 55$  cm cyan and  $L = 60$  cm magenta.

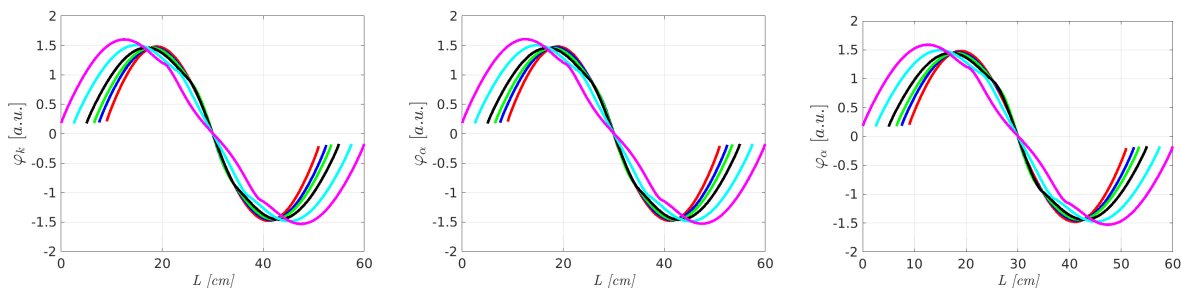


Figure 6.19: Spatial distribution of the  $k$  (left),  $\alpha$  (center) and prompt  $\alpha$  first-order eigenmodes for the 1D heterogeneous as a function of the size  $L$  of the system. Color legend according to the ascending order of the size  $L$  of the system is:  $L = 42$  cm red,  $L = 45$  cm blue,  $L = 47$  cm green,  $L = 50$  cm black,  $L = 55$  cm cyan and  $L = 60$  cm magenta.

## 6.6 Conclusions

Eigenvalue separation is a convenient estimator to provide information on the degree of decoupling of a reactor core in a concise manner. In this Chapter, we have shown that the novel matrix-filling Monte Carlo methods developed in Chapter 5 can be usefully used to assess these quantities. In order to better grasp the physical meaning of the eigenvalue separation, which is traditionally formulated for the  $k$ -eigenvalue problems, we have extended this analysis to the case of  $\alpha$ -eigenvalues, both with and without precursor contributions. For this purpose, we have selected a series of benchmark configurations covering homogeneous and heterogeneous systems.

Our main findings are the following: homogeneous and heterogeneous system behave differently with respect to the decoupling parameter, in particular concerning higher-order eigenvalue separations, which is consistent with previous claims appeared in the literature for the case of  $k$ -eigenvalue separations [120]. The delayed  $\alpha$ -eigenvalue are rather insensitive to the decoupling effects, and can hardly be used as a reliable estimator to detect such effects. On the contrary, prompt eigenvalues respond to the decoupling parameter in a way that is qualitatively similar to the  $k$ -eigenvalue for the homogeneous configurations, and might be thus usefully used as a complement to the classical  $k$ -eigenvalue separations for reactor diagnostic. Distinct behaviours were found between the prompt  $\alpha$ -eigenvalue separation and the  $k$ -eigenvalue separation for the heterogeneous configurations, which suggests to a difference in the response of the systems to a perturbation. In order to better apprehend the impact of these results on the way a system reacts to an external impulsion, reference kinetics simulations would be needed. This would allow discriminating which between the  $\alpha$  eigenvalue separation of the  $k$  eigenvalue separation is the more pertinent approach to the quantification of perturbations affecting the time behaviour of the neutron flux.

Our analysis has been carried out on benchmark configurations in multi-group transport, so that the validity of the obtained results should be taken with care, as it might not be easily transposable to more realistic systems. This issue will be partially dealt with in the following Chapter, where we will deploy these Monte Carlo methods to continuous-energy transport for the investigation of the EOLE critical facility.

Despite their apparent simplicity, it should be noted that the simulations of the configurations discussed in this chapter were time and memory consuming, due to the very nature of the matrix-filling methods. To provide a rough estimate of the CPU and RAM burden involved in these calculations, in Tab. 6.40 we provide a few significant examples for some representative configurations.

configuration	1D homogeneous	2D homogeneous
$\alpha$ -matrix size [-]	$1.8 \times 10^3$	$1.62 \times 10^3$
$k$ -matrix size [-]	$1.2 \times 10^3$	$1.08 \times 10^3$
$t_{MC}$ [s]	$6 \times 10^4$	$3.6 \times 10^4$
$t_{MC}^+$ [s]	$1.12 \times 10^5$	$6.7 \times 10^4$
$\alpha$ -matrix storage [MB]	$7.6 \times 10^0$	$7.0 \times 10^0$
$k$ -matrix storage [MB]	$7.6 \times 10^0$	$7.0 \times 10^0$
$t_{eig}$ $\alpha$ -matrix [s]	$4.3 \times 10^3$	$3.3 \times 10^3$
$t_{eig}$ $k$ -matrix [s]	$1.26 \times 10^4$	$1.04 \times 10^4$

Table 6.40: Computational time and memory occupation of the homogeneous configurations with leakage boundary conditions for the most decoupled case ( $L = 100$  cm). The simulation times associated to the Monte Carlo simulations performed with the test-bed code including and without matrix elements estimation are expressed as  $t_{MC}^+$  and  $t_{MC}$ , respectively.

In particular, we recall that the difference between the  $\alpha$ - and the  $k$ -matrix size is related to the delayed contribution, which is collapsed for the  $k$ -formulation expressed by Eq. (2.65). However, the storage associated to the operators in their matrix-form is exactly the same: these operators are assembled only in the post-processing MATLAB code, previously described in Section 5.2.5. Despite the smaller size of the  $k$ -matrix with respect to the  $\alpha$ -matrix, an additional operation is required in order to compute the  $k$ -eigenpairs: the discretized form of the net leakage operator  $M$  (Eq. (2.32)) has to be inverted.



## Chapter 7

# Spectral analysis of the EOLE reactor: the EPILOGUE experimental program

### 7.1 Introduction

In the previous chapter, we have seen that the numerical tools developed in this thesis can be successfully applied to the analysis of multiplying systems. In particular, we have been able to perform the spectral analysis and to detect decoupling effects in simplified benchmark configurations, based on the test-bed Monte Carlo code developed from scratch for this purpose.

In order to extend this analysis to more realistic systems, we have successively developed the necessary routines and algorithms in TRIPOLI-4<sup>®</sup>, so that we can carry out spectral analysis in continuous-energy Monte Carlo transport with complex geometries.

In this respect, we have chosen to revisit the EPILOGUE experimental campaign, which was the last one to be performed in the EOLE critical facility at CEA Cadarache [50, 51, 49]. The EPILOGUE campaign was especially conceived in order to ascertain whether heterogeneities and decoupling effects might occur in small reactor cores, in view of the investigation of similar effects in large cores of Generation III+ reactors [9].

We will focus on two experimental configurations of the EPILOGUE program: the "low fuel bubble" experiment, and the "water blade" experiment. In the former, a portion of the borated water around the fuel pins was replaced, which was supposed to mimic the effects of a clear water "bubble" passing through the core; in the latter, a row and a column of fuel pins were replaced by moderator (the "blade"), in order to induce a supposedly strong heterogeneity in the core. In both cases, the final goal was to determine to what extent these perturbations affected the neutron population by creating spatial effects (detectors located at different regions responding in different manners), as opposed to the expected point-kinetics behaviour of the EOLE facility.

Our contribution to the analysis of such experiments was twofold. On one hand, we have taken part in the post-processing of raw data of the "low fuel bubble" experiment (which have been finalized during a visit to the Cadarache center during the first year of the thesis), and the analysis of the such findings by comparison to Monte Carlo simulations. On the other hand, we have applied the newly developed spectral analysis tools of TRIPOLI-4<sup>®</sup> to the "water blade" configuration, as an effective complement to the measurements.

This chapter is organized in three main sections. First, we describe the EOLE configurations and provide the main features of each system. Then, we present the experiments and the results obtained during rod-drop measurements in order to investigate the effect of perturbations and the occurrence of spatial kinetics effects induced by reactivity insertions. Finally, we perform a spectral analysis (on both the  $k$ - and the  $\alpha$ -modal basis) of different configurations of the EOLE facility, in order to assess the decoupling effects introduced by a strong heterogeneity. The eigenpairs associated to the eigenvalue problems discussed in this chapter have been computed with the

MATLAB code described in Section 5.2.5, based on the matrices filled with TRIPOLI-4®.

## 7.2 The EPILOGUE program and the EOLE configurations

The EPILOGUE program consists of a set of experiments performed on the EOLE zero-power facility operated at CEA/Cadarache in 2017. One of the principal goals of this program was to qualify local perturbations induced by in-core instrumentation in nuclear reactor cores of generation III+ [49]. The EOLE core has been assembled according to different configurations in order to cover a broad spectrum of situations so as to improve the knowledge of generation III+ nuclear reactors.

For the purpose of this work, we have analyzed three of the seven different configurations examined during the EPILOGUE program:

- the *reference configuration* in the absence of strong spatial heterogeneities of the core,
- the *low bubble fuel configuration* for the analysis of reactivity variations and spatial kinetics effects resulting from measurements with in-core detectors,
- the *water blade configuration* in the presence of strong spatial heterogeneities in the core.

The reference configuration was mainly used for the calibration of the instrumentation and for the first estimations of reactivity insertions induced by local perturbations. During the latest days of the program, the low fuel bubble configuration was examined in order to investigate the presence of spatial kinetics effects by analyzing efficiency variations of the in-core fission chambers. For this purpose, rod-drop experiments were performed and various detectors were placed in different positions of the core region. Three methods were used in order to convert detector counting in reactivity values. Discrepancies between such values obtained at different locations of the core may suggest the presence of spatial kinetics effects.

The main aim of the water blade configuration is to induce a local over-moderation effect in the core region. In principle, the water layer substituting a section of fuel pins would separate the radial neutron flux distribution into two distinct regions. This decoupling effect will be analyzed via spectral analysis by resorting to the matrix-filling method discussed in Chapter 5 and recently implemented in TRIPOLI-4®. Moreover, additional configurations of the core are simulated in order to extract additional information on the impact of the moderator region. In particular, we will numerically explore the effects of adding two additional water blade configurations (obtained by replacing more fuel elements with light borated water) with the aim of enhancing the decoupling of the core region.

In the following section we describe in details the core configurations of the EPILOGUE program considered in this work. The corresponding experimental and numerical results will be analyzed in Sections 7.3 and 7.4, respectively.

### 7.2.1 The reference configuration

The critical core configuration is obtained with 720 fuel pins in the central region, a total of 985 UO<sub>2</sub> fuel pins and a Boron concentration of 302.6 ppm. A schematic representation of the radial section of this configuration is shown in Fig. 7.1. The parameters measured during the first core divergence are shown in the first two parts of Tab. 7.1. The pilot rod is made of natural B<sub>4</sub>C. The moderator is borated light water, its temperature is  $\theta = 20.0 \pm 0.1$  °C. In addition to the fission chambers monitors (positions 16-09 and 26-33), three fission chambers were placed in the core and in the reflector region: a Ø4 mm chamber in 26-26, a Ø8 mm chamber in 01-21 and a long Ø8 mm chamber with so-called "reduced-gap" (i.e. reduced distance between electrodes) in 36-36. The computed reactivity variations and effective kinetic parameters are shown in the last part of Tab. 7.1. The reactivity measurements have been computed with TRIPOLI-4® by using JEFF-3.1.1 nuclear data libraries [134] (JEFF-3.2 for the temperature coefficient of fuel and moderator,  $\theta = 20.0 \pm 0.1$  °C). The kinetics parameters have been computed by applying the Nauchi method [109].

The Boron concentration ( $C_{\text{Boron}}$  of Tab. 7.1) has been determined based on the analyses performed by the SA3C/LARC (the analysis laboratory of CEA/Cadarache) and the online tracking performed by the SPEX/L2EM

(the EOLE/MINERVE operation laboratory of CEA/Cadarache) from volumetric monitoring of the moderator in the storage tanks. The concentration is adjusted according to the value obtained by LARC, once these analyses have been performed.

parameter	value
$C_{\text{Boron}}$ [ppm]	$303 \pm 8$
$\tau_2$ [s]	$37.7 \pm 0.3$
$\rho$ [pcm]	$115 \pm 6$
$H_{\text{pilot rod}}$ [mm]	$290 \pm 5$
$\Delta\rho_{\text{pilot rod}}$ [pcm]	$160 \pm 8$
$\Delta\rho_4$ control rods [pcm]	$7052 \pm 360$
$\Delta\rho_1$ control rod [pcm]	$1494 \pm 84$
$\Delta\rho/\Delta C_{\text{Boron}}$ [pcm/ppm]	$-14.0 \pm 0.2$
$\Delta\rho/\Delta\theta$ [pcm/°C]	$-9.1 \pm 0.1$
$\beta_{\text{eff}}$ [pcm]	$782 \pm 20$
$\Lambda_{\text{eff}}$ [ $\mu\text{s}$ ]	$30.5 \pm 0.8$

Table 7.1: Neutronics parameters computed for the reference configuration. Values reported in this table have been extracted from reference [50, 51].

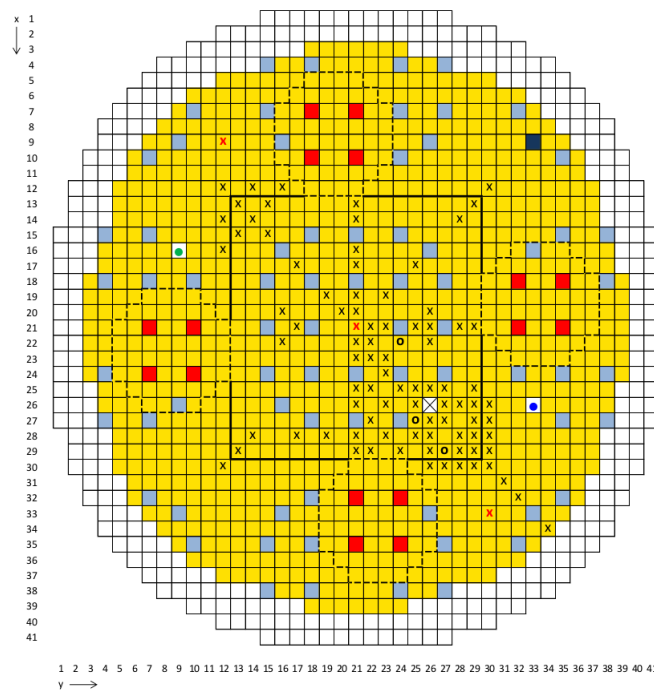


Figure 7.1: Schematic radial section of the EOLE reactor in the reference configuration. Fuel elements of enriched  $\text{UO}_2$  at 3.7% are colored in yellow and are distinguished in monitored fuel elements (black cross, black circle and red cross). Locations for control rods (red), pilot rod (dark blue) and guide tube (white, black cross) are shown. Two fission chambers are shown: CF2268 (white, green circle) and CF2269 (white, blue circle). All the remaining elements are filled with borated light water (light grey).

### 7.2.2 Low fuel bubble configuration

The critical core configuration is obtained with 720 fuel pins in the central region, a total of 993  $\text{UO}_2$  fuel pins (the 8 central guide tubes of the experimental area being replaced by fuel pins) and a Boron concentration of 275.6 ppm. The 25 central pins (block of 5 by 5 pins) are held in position by a block of high density polyethylene

(HDPE) simulating a bubble of light water spreading along the pins. The height of this bubble region is 20 cm, and the bottom of this region is located at the bottom of the fuel active height (dimension 135 mm). A schematic representation of the radial section of this configuration is shown in Fig. 7.2. The parameters measured during the first core divergence are shown in the first two parts of Tab. 7.2. The pilot rod is made of natural  $B_4C$ . The moderator is borated light water, its temperature is  $\theta = 20.0 \pm 0.1^\circ\text{C}$ . In addition to the fission chambers monitors (positions 16-09 and 26-33), three fission chambers were placed in the core and in the reflector region: a  $\varnothing 4$  mm chamber in 01-21, a  $\varnothing 8$  mm chamber in 36-06 and a long  $\varnothing 8$  mm chamber with so-called "reduced gap" in 36-36. The computed reactivity variations and effective kinetic parameters are shown in the last part of Tab. 7.2. The reactivity measurements have been computed with TRIPOLI-4<sup>®</sup> by using JEFF-3.1.1 nuclear data libraries [134] (JEFF-3.2 for the temperature coefficient of fuel and moderator,  $\theta = 20.0 \pm 0.1^\circ\text{C}$ ). The kinetics parameters have been computed by applying the Nauchi method [109].

The Boron concentration ( $C_{\text{Boron}}$  of Tab. 7.2) has been determined based on the analyses performed by the SA3C/LARC (the analysis laboratory of CEA/Cadarache) and the online tracking performed by the SPEX/L2EM (the EOLE/MINERVE operation laboratory of CEA/Cadarache) from volumetric monitoring of the moderator in the storage tanks. The concentration is adjusted according to the value obtained by LARC, once these analyses have been performed.

parameter	value
$C_{\text{Boron}}$ [ppm]	$276 \pm 7$
$\tau_2$ [s]	$38.7 \pm 0.6$
$\rho$ [pcm]	$114 \pm 6$
$H_{\text{pilot rod}}$ [mm]	$391 \pm 5$
$\Delta\rho_{\text{pilot rod}}$ [pcm]	$209 \pm 11$
$\Delta\rho_4$ control rods [pcm]	$7380 \pm 381$
$\Delta\rho_1$ control rod [pcm]	$1568 \pm 78$
$\Delta\rho/\Delta C_{\text{Boron}}$ [pcm/ppm]	$-14.7 \pm 0.2$
$\Delta\rho/\Delta\theta$ [pcm/ $^\circ\text{C}$ ]	$-9.2 \pm 0.2$
$\beta_{\text{eff}}$ [pcm]	$784 \pm 20$
$\Lambda_{\text{eff}}$ [ $\mu\text{s}$ ]	$30.6 \pm 0.8$

Table 7.2: Neutronics parameters measured and computed for the low fuel bubble configuration. Values reported in this table have been extracted from reference [50, 51].

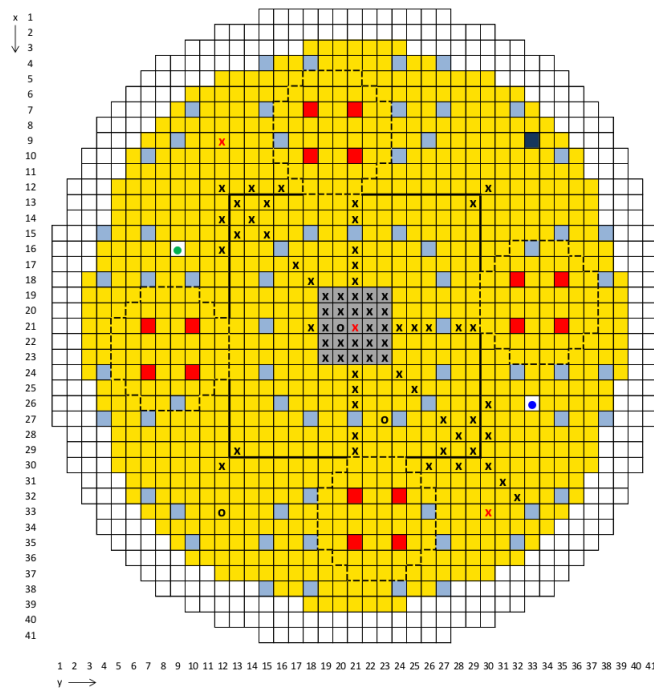


Figure 7.2: Schematic radial section of the EOLE reactor in the low fuel bubble configuration. Fuel elements of enriched  $\text{UO}_2$  at 3.7% are colored in yellow and are distinguished in monitored fuel elements (black cross, black circle and red cross). Locations for control rods (red), pilot rod (dark blue) and bubble region (dark grey) are shown. Two fission chambers are shown: CF2268 (white, green circle) and CF2269 (white, blue circle). All the remaining elements are filled with borated light water (light grey).

### 7.2.3 Water blade configuration

The critical core configuration is obtained with 720 fuel pins in the central region, a total of 952  $\text{UO}_2$  fuel pins and a Boron concentration of 302.6 ppm. A row and a column of fuel pins have been removed from the central region of the core. Moreover, 2 pins made of  $B_4C$  have been placed on opposite locations with respect to the water blade in order to compensate the induced change in reactivity. A schematic representation of the radial section of this configuration is shown in Fig. 7.3. The parameters measured during the first core divergence are shown in the first two parts of Tab. 7.3. The pilot rod is made of natural  $B_4C$ . The moderator is borated light water, its temperature is  $\theta = 20.0 \pm 0.1^\circ\text{C}$ . In addition to the fission chambers monitors (positions 16-09 and 26-33), three fission chambers were placed in the core and in the reflector region: a  $\varnothing 4$  mm chamber in 00-21, a  $\varnothing 8$  mm chamber in 36-06 and a long  $\varnothing 8$  mm chamber with so-called "reduced gap" in 36-36. The computed reactivity variations and effective kinetic parameters are shown in the last part of Tab. 7.3. The reactivity measurements have been computed with TRIPOLI-4<sup>®</sup> by using JEFF-3.1.1 nuclear data libraries [134] (JEFF-3.2 for the temperature coefficient of fuel and moderator,  $\theta = 20.0 \pm 0.1^\circ\text{C}$ ). The kinetics parameters have been computed by applying the Nauchi method [109].

The Boron concentration ( $C_{\text{Boron}}$  of Tab. 7.3) has been determined based on the analyses performed by the SA3C/LARC (the analysis laboratory of CEA/Cadarache) and the online tracking performed by the SPEX/L2EM (the EOLE/MINERVE operation laboratory of CEA/Cadarache) from volumetric monitoring of the moderator in the storage tanks. The concentration is adjusted according to the value obtained by LARC, once these analyses have been performed.

parameter	value
$C_{\text{Boron}}$ [ppm]	$251 \pm 6$
$\tau_2$ [s]	$37.8 \pm 0.5$
$\rho$ [pcm]	$116 \pm 6$
$H_{\text{pilot rod}}$ [mm]	$420 \pm 5$
$\Delta\rho_{\text{pilot rod}}$ [pcm]	$246 \pm 13$
$\Delta\rho_4$ control rods [pcm]	$7336 \pm 373$
$\Delta\rho_1$ control rod [pcm]	$1341 \pm 67$
$\Delta\rho/\Delta C_{\text{Boron}}$ [pcm/ppm]	$-16.7 \pm 0.2$
$\Delta\rho/\Delta\theta$ [pcm/°C]	$-7.3 \pm 0.1$
$\beta_{\text{eff}}$ [pcm]	$778 \pm 20$
$\Lambda_{\text{eff}}$ [ $\mu\text{s}$ ]	$32.7 \pm 0.8$

Table 7.3: Neutronics parameters measured and computed for the water blade configuration. Values reported in this table have been extracted from reference [50, 51].

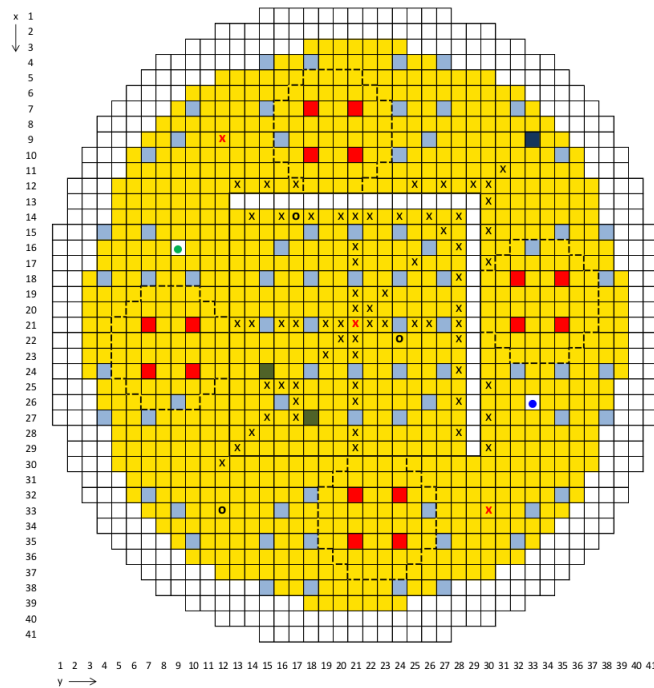


Figure 7.3: Schematic radial section of the EOLE reactor in the water blade configuration. This configuration is arranged by removing a row and a column of fuel pins from the core region. Fuel elements of enriched  $\text{UO}_2$  at 3.7% are colored in yellow and are distinguished in monitored fuel elements (black cross, black circle and red cross). Locations for control rods (red), pilot rod (dark blue) and  $B_4C$  rods (olive green) are shown. Two fission chambers are shown: CF2268 (white, green circle) and CF2269 (white, blue circle). All the remaining elements are filled with borated light water (light grey).

### 7.3 Analysis of multi-instrumented rod-drop measurements: investigation of spatial kinetics effects

The impact of spatial effects, i.e. effects that go beyond the hypothesis of the point kinetics, during power transients is becoming increasingly important in view of the possible presence of decoupling phenomena in large cores of PWR [36, 31, 135, 128, 38, 113]. The presence and detection of such effects in small cores (such as the EOLE critical facility) might foster the development of a methodology for mapping the various perturbations inherent to

the large PWR cores and for the optimization of in-core detector positions in order to cover the entire core volume.

The aim of this section is to describe the raw experimental results obtained from counting measurements from "rod-drop" experiments, performed in the course of the last sets of measurements of the EPILOGUE program [9] for the "low fuel bubble" configuration [49], in order to highlight possible spatial kinetics effects. Different tests have been performed by using fission chambers having different sensibilities and placed in different locations both inside and outside the core region. These tests concern the investigation of a possible effect related to these locations on the perturbation amplitude due to an insertion of negative reactivity caused by the pilot rod ( $\Delta\rho < \beta_{\text{eff}}/2$ , for a fast drop) or by the control rod ( $\Delta\rho \gg \beta_{\text{eff}}$ ).

### 7.3.1 Measurement results

Fission chamber measurements were performed in the "low fuel bubble" configuration. The core is at a temperature of 20°C. A schematic representation of this configuration is shown in Fig. 7.4. All fission chambers are inserted in sealed aluminium sheaths and located at the core mid-plane by using aluminium shims of the appropriate length, depending on the type of chamber. Two Ø4 mm fission chambers are positioned in the core:

- CF <sup>235</sup>U Ø4 mm (2268), located at 16-09,
- CF <sup>239</sup>Pu Ø4 mm (2266), located at 26-33.

These two monitor detectors are connected to the MCS (Multi-Channel Scaler) measurement chain (ADS 7820 and Ni-DAQ card, two channels of measurement). Five additional fission chambers are positioned in the core:

- CF <sup>235</sup>U Ø8mm with reduced gap (2284), located at 01-21,
- CF <sup>235</sup>U Ø8mm with long reduced gap (2296), located at 26-26,
- CF <sup>235</sup>U Ø8mm with long reduced gap (2295), located at 07-35,
- CF <sup>235</sup>U Ø4mm (2299), located at 21-41,
- CF <sup>235</sup>U Ø8mm (2272), located at 36-06.

The first three chambers (2284, 2295 and 2296) are connected to fast ADS amplifiers and to the measuring system XMODE. The last two (2272 and 2299) are connected to the traditional MP2 system (pre-amplifier + charge amplifier). The XMODE system is capable of recording neutronic measurements as logical (32 synchronized channels) and analogical (8 synchronized channels) data. For the acquisition of logical signals, XMODE uses a time stamping which enables to record all detector information. This operating mode is necessary for the realisation of neutron noise experiments.

The CFUL fission chambers are traditionally used for neutron noise measurements. They are characterized by a large usable volume and a large <sup>235</sup>U deposit (1 g). Such large mass of fissile isotope denotes a higher sensitivity of the fission chambers and a larger number of counting will be detected. This large counting rate is necessary in order to record signals in current mode, since the neutronic measuring system processes signal inputs obtained in current mode. The measuring sleeves for the introduction of the CFUL chambers (670 and 669) are located between the core and the vessel. The signal transmission cables (high immunity) are connected to the SPECTRON measuring system [64, 65]. This system is devoted to the analysis of neutron noise measurements and it has been developed at CEA/Cadarache. The high immunity of these cables allows to reduce the parasite capture contributions during signal acquisition in order to obtain a "smoother" signal (lower influence of the background noise in terms of electromagnetic perturbations).

A summary of the measuring devices and their associated electronics is given in the table below:

CF	location	measuring system
2268	16-09	ADS-Ni-DAQ
2269	26-33	ADS-Ni-DAQ
CFUL	670 NO	SPECTRON
CFUL	669 SE	SPECTRON
2284	01-21	ADS-XMODE
2296	26-26	ADS-XMODE
2295	07-35	ADS-XMODE
2299	21-41	MP2-channel 3
2272	36-06	MP2-channel 1

Table 7.4: Detector locations and measuring systems for the rod-drop experiments.

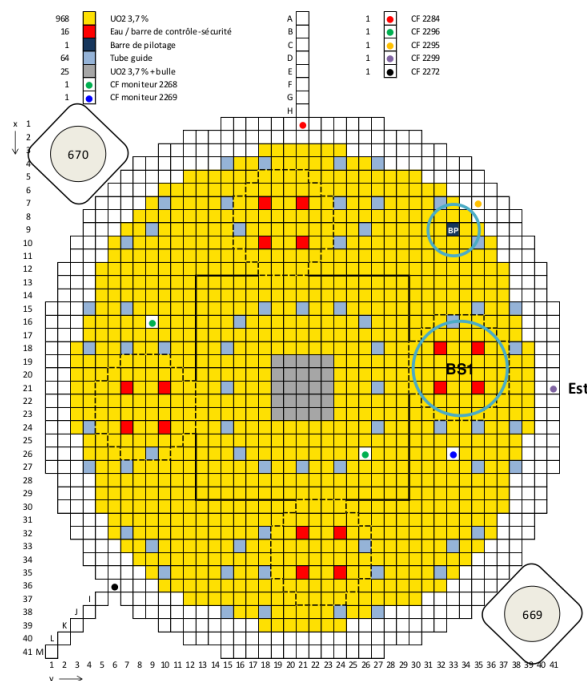


Figure 7.4: Schematic radial section of the EOLE reactor in the low fuel bubble configuration during rod-drop experiments. Fuel elements of enriched  $UO_2$  at 3.7% are located in the "bubble" region (dark grey) and around it (yellow). Locations for control rods (red) and pilot rod (dark blue) are shown. The locations of fission chambers (colored circles) are shown are detailed in Tab. 7.4. All the remaining elements are filled with borated light water (white and light grey).

### 7.3.2 Rod-drop measurements

Two types of measurements were carried out: a rod-drop measurement of control rod (BS1 Fig. 7.4) and a rapid descent of the pilot rod (BP Fig. 7.4), from a power level at 5 W or 10 W. The measurement protocol is the following:

- reach the reactor divergence and stabilize at the target power,
- after a few minutes, required in order to ensure stabilization, start the rapid descent of the pilot rod (BP),
- when the counting rate reaches about 10 counts per second (MCS) in the chamber with the larger counting rate, start a new divergence,
- stabilize the power at 5 W,

- After a few minutes for the second stabilization, start the control rod-drop (BS1).

Preliminary measurements of the settings of the various measuring systems and tests of the duplication of the signal of chambers 2299 and 2272 with the XMODE system (December 20<sup>th</sup> 2017) have been realized before the experiment at a power of 5 W. The last divergence (December 21<sup>th</sup> 2017) was followed by the drop (the last of the reactor) of all four control rods and the pilot rod. The results obtained in terms of reactivity variation are given in Tabs. 7.5 and 7.6 as an indication.

The results associated to the counts are given in pcm. The corresponding uncertainties do not consider the errors on nuclear data (4% for  $1\sigma$  standard deviation). Divergence measurements are analysed on ADS and MP2 channels only. Drop measurements of the pilot rod (BP) and the control rods (BS) are solved using three methods: inversion of the kinetics equation (method 1), non-linear fitting (method 2) and Modified Carpenter method (method 3). The first method is based on the following formula for the reactivity estimation:

$$\rho(t) = 1 + \frac{\Lambda}{n(t)\beta} \left[ \frac{dn(t)}{dt} - Q(t) - \sum_j \lambda_j c_j(t) \right], \quad (7.1)$$

where the neutron density  $n(t)$  is proportional to the counting rate registered by the detectors, and  $Q(t)$  is an external source of neutrons. The other methods are based on non-linear adjustments of the point kinetics equations, assuming known the temporal behaviours of  $\rho(t)$  and  $Q(t)$ . The Method 3 is tested on ADS only (higher count rates). Further details on these methods can be found in [17].

These methods are implemented in the TMN software [17] (Neutronic Measurement Toolbox), which is used for reactivity estimation obtained from neutronic measurements and for the manipulation of these measurements. This tool allows the analysis of power transient and neutron flux divergence. The former provides reactivity estimation for a stabilized sub-critical configuration, obtained by perturbing the initial state of the system. The latter allows the computation of both doubling time and reactivity for slightly super-critical systems.

Due to some difficulties in processing current values in TMN, measurements obtained by using SPECTRON are not reported. Methods 2 and 3 are not suitable for the reactivity variation measurements for a rod "descent", since it cannot verify the hypothesis of an instantaneous drop.

The following tables show the values of reactivity variation due to reactor divergence and to rod-drop. The blank cells show unexplained inconsistencies.

	detector	divergence	rod-drop (method 1)	rod-drop (method 2)	rod-drop (method 3)	rod-drop (average)
20 Dec	CF2295	90	$-139 \pm 1.1\%$	$-132 \pm 1.2\%$	$-125 \pm 1.2\%$	$-132 \pm 5.3\%$
20 Dec	CF2284	90	$-127 \pm 1.3\%$	$-125 \pm 1.2\%$	$-126 \pm 1.3\%$	$-126 \pm 1.1\%$
20 Dec	CF2296	90	$-127 \pm 1.2\%$	$-123 \pm 1.1\%$	$-125 \pm 1.2\%$	$-125 \pm 1.7\%$

Table 7.5: Reactivity variations: pilot rod-drop (BP), analyzed with XMODE. The uncertainties shown in the last column have been computed as root mean square of the uncertainties obtained from the implementation of the corresponding methods.

	detector	rod-drop (method 1)	rod-drop (method 2)	rod-drop (method 3)	rod-drop (average)
20 Dec	CF2295	$-1624 \pm 1.7\%$	$-1771 \pm 1.5\%$	$-1628 \pm 7.5\%$	$-1674 \pm 5.0\%$
20 Dec	CF2284	$-1397 \pm 2.2\%$	$-1616 \pm 1.5\%$	$-1613 \pm 7.7\%$	$-1542 \pm 8.1\%$
20 Dec	CF2296	$-1488 \pm 1.6\%$	$-1646 \pm 1.5\%$	$-1622 \pm 7.5\%$	$-1585 \pm 5.4\%$
21 Dec	CF2295	$-1776 \pm 1.0\%$	$-1849 \pm 1.9\%$	$-2061 \pm 7.0\%$	$-1895 \pm 7.8\%$
21 Dec	CF2296	$-1566 \pm 1.0\%$	$-1621 \pm 1.9\%$	$-1623 \pm 8.8\%$	$-1603 \pm 2.0\%$

Table 7.6: Reactivity variations: pilot rod-drop (BS1), analyzed with XMODE. The uncertainties shown in the last column have been computed as root mean square of the uncertainties obtained from the implementation of the corresponding methods.

Small discrepancies are observed in the reactivity variations for the pilot rod-drop BP (Tab. 7.5), whereas larger differences are observed in the reactivity variations for the control rod-drop BS1 (Tab. 7.6). In principle, such behaviour seems to suggest the possible presence of spatial effects.

The results obtained from the analysis of signal counting from MP2 channels are shown in Tab. 7.7. The corresponding average values (neglecting uncertainty) and the relative standard deviations of the channel measurements are shown in Tab. 7.8.

	detector	rod-drop	divergence	rod-drop (method 1)	rod-drop (method 2)	rod-drop (method 3)	rod-drop (average)
20 Dec	CF2272	5 W-BP	96	$-118 \pm 2.0\%$	$-121 \pm 1.2\%$	$-126 \pm 1.5\%$	$-122 \pm 3.1\%$
	CF2299	5 W-BP	95	$-121 \pm 4.6\%$	$-121 \pm 1.2\%$	$-123 \pm 1.3\%$	$-122 \pm 1.3\%$
	CF2272	10 W-BS	95	$-1420 \pm 1.8\%$	$-1509 \pm 1.4\%$	-	$-1464 \pm 4.3\%$
	CF2299	10 W-BS	94	$-1217 \pm 2.8\%$	$-1422 \pm 1.3\%$	-	$-1329 \pm 12.0\%$
21 Dec	CF2272	BP rod-drop	90	$-124 \pm 1.4\%$	$-125 \pm 1.2\%$	$-130 \pm 1.5\%$	$-127 \pm 2.7\%$
	CF2299	BP rod-drop	87	$-119 \pm 1.4\%$	$-120 \pm 1.2\%$	$-124 \pm 1.4\%$	$-121 \pm 2.3\%$
	CF2272	BS rod-drop	88	$-1244 \pm 3.0\%$	$-1501 \pm 1.4\%$	-	$-1373 \pm 13.2\%$
	CF2299	BS rod-drop	86	$-1872 \pm 1.3\%$	$-1882 \pm 2.3\%$	-	$-1877 \pm 0.4\%$
	CF2272	4BS rods drop	88	$-6812 \pm 1.7\%$	$-7786 \pm 1.4\%$	-	$-7299 \pm 9.4\%$
	CF2299	4BS rods drop	87	$-7581 \pm 1.8\%$	$-8053 \pm 3.4\%$	-	$-7817 \pm 4.3\%$

Table 7.7: Reactivity variations: analyzed on MP2 channels. The uncertainties shown in the last column have been computed as root mean square of the uncertainties obtained from the implementation of the corresponding methods.

detector	BP rod-drop	BS1 rod-drop
CF2272	$-124 \pm 3.4\%$	$-1418 \pm 8.7\%$
CF2299	$-121 \pm 1.7\%$	$-1603 \pm 20.5\%$

Table 7.8: Average reactivity variations: analyzed on MP2 channels. The uncertainties shown in the last column have been computed as root mean square of the uncertainties obtained from the implementation of the corresponding methods.

The values computed for the pilot rod-drop BP do not show any significant discrepancy. Larger reactivity deviations are found for the control rod-drop BS1 experiment. The standard deviation corresponding to the counting of fission chamber CF2299 is rather large, which suggests a low counting rate of the detector. This behaviour can be justified by the location of the fission chambers with respect to the position of rod BS1. The efficiency of the fission chamber CF2299 decreases after the insertion of negative reactivity, due to its proximity to the control rod. Conversely, the efficiency of fission chamber CF2272, located far from the control rod, increases, although this effect is less visible.

Table 7.9 shows the results obtained from ADS monitor channels. The results obtained at a power level of 5 W are inconsistent and are not considered in the calculation of the corresponding average value. Conversely, small standard deviations are obtained for all the other results. The accuracy of these results is probably justified by the excellent performance of the ADS systems. The average values computed from these results (neglecting uncertainty) and the corresponding standard deviations are shown in Tab. 7.10.

### 7.3. ANALYSIS OF MULTI-INSTRUMENTED ROD-DROP MEASUREMENTS: INVESTIGATION OF SPATIAL KINETICS EFFECTS

	detector	rod-drop	divergence	rod-drop (method 1)	rod-drop (method 2)	rod-drop (method 3)	rod-drop (average)
20 Dec	CF2268	5 W-BP	92	$-71 \pm 9.4\%$	$-114 \pm 18.9\%$	-	$-93 \pm 32.2\%*$
	CF2269	5 W-BP	93	$-95 \pm 5.6\%$	$-118 \pm 9.5\%$	-	$-107 \pm 15.2\%*$
	CF2268	10 W-BS	93	$-1521 \pm 4.9\%$	$-1358 \pm 3.3\%$	-	$-1439 \pm 8.0\%$
	CF2269	10 W-BS	94	$-1785 \pm 3.6\%$	$-1674 \pm 3.8\%$	-	$-1730 \pm 4.5\%$
21 Dec	CF2268	BP rod-drop	88	$-126 \pm 3.5\%$	$-125 \pm 1.7\%$	-	$-125 \pm 0.4\%$
	CF2269	BP rod-drop	89	$-123 \pm 2.8\%$	$-124 \pm 4.7\%$	-	$-123 \pm 0.2\%$
	CF2268	BS rod-drop	87	$-1454 \pm 4.5\%$	$-1402 \pm 3.4\%$	-	$-1428 \pm 2.6\%$
	CF2269	BS rod-drop	88	$-1694 \pm 4.0\%$	$-1687 \pm 4.1\%$	-	$-1690 \pm 0.3\%$
	CF2268	4BS rods drop	87	$-7309 \pm 3.4\%$	$-7204 \pm 4.0\%$	-	$-7257 \pm 1.0\%$
	CF2269	4BS rods drop	87	$-7671 \pm 3.1\%$	$-7587 \pm 3.3\%$	-	$-7629 \pm 0.8\%$

Table 7.9: Reactivity variations: analyzed on ADS monitor channels (\*incoherent values, not accounted in the average results).

detector	BP rod-drop	BS1 rod-drop
CF2268	$-125 \pm 1.5\%$	$-1434 \pm 4.9\%$
CF2269	$-123 \pm 2.4\%$	$-1710 \pm 3.0\%$

Table 7.10: Average reactivity variations: analyzed on ADS monitor channels.

The two monitor chambers show a significant deviation of the reactivity variation related to the control rod experiment. The corresponding mean value is  $-1572 \pm 195$  pcm and the original values do not overlap by considering  $2\sigma$  standard deviations. The CF2269 fission chamber is closer to the perturbation with respect to the CF2268 fission chamber and is located inside the neutron flux depression caused by the control rod-drop. Its position is responsible for a larger measured reactivity variation.

Fission rate distributions have been calculated with TRIPOLI-4<sup>®</sup> for both pilot rod-drop and control rods drop in order to determine the signal variation in the detector positions. Figure 7.5 shows the variations of these fission rates for each rod-drop experiment with respect to the unperturbed configuration.

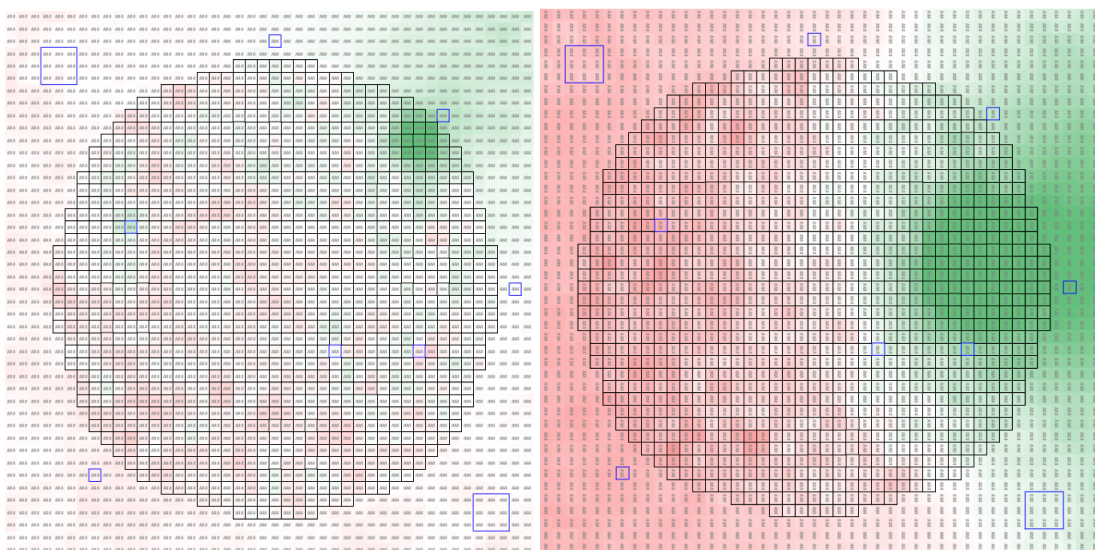


Figure 7.5: Fission rates perturbation due to pilot rod-drop (BP, left) and control rods drop (BS1, right). Perturbations with respect to the unperturbed configuration ranges from  $-41\%$  up to  $+6\%$  due to the pilot rod-drop and from  $-61\%$  up to  $+13\%$  due to control rods drop.

The variations in fission rates at detector locations are strongly influenced by the introduced perturbation. The corresponding minimum and maximum values are shown in Tab. 7.11 for the corresponding fission chamber. As expected, the largest variations are observed for detector located closer to the perturbation: CF2295 for the pilot rod-drop (the value for CF2268 is questionable, since this fission chamber is relatively far from the perturbation in order to observe such large variation), CF2299 and CF2269 for control rods drop. Values associated to the remaining detectors show smaller variations, except for the control rods drop experiment, where the reactivity insertion implies a larger deformation of the neutron flux along the radial coordinate.

detector	pilot rod-drop	control rods drop
CFUL670	0.6%	7.8%
CFUL669	0.8%	-3.2%
CF2284	-0.7%	3.1%
CF2295	-9.3%	-8.0%
CF2296	-0.8%	-3.1%
CF2272	2.0%	9.9%
CF2299	-0.7%	-21%
CF2268	-7.2%	-10.3%
CF2269	2.7%	12.4%

Table 7.11: Fission rates variations on the detector locations.

### 7.3.3 Summary of the experimental results

We have illustrated the preliminary results of the rod-drop measurements carried out at the end of the experimental campaign in the "low fuel bubble" configuration of the program EPILOGUE in EOLE. In addition to the fission chambers CF2268 and CF2269, five fission chambers of different types, connected to different measuring electronics, have been inserted in various core and reflector positions. The location of these detectors was intended to identify possible spatial kinetics effects in the raw signals. The results were processed using the TMN tool, according to three methods (inversion of kinetics, flow adjustment, Carpenter's method). The variations of the detector efficiency as a function of the respective location suggest the presence of spatial kinetic effects in the core.

The deviations counted without detector efficiency correction are consistent with the expected deviations on the variation in fission rates at the measurement sites. The mean values and the corresponding standard deviations of these measurements could be refined by a more complete calculation of the MSM (Modified Source Multiplication) factors using the new options implemented in TRIPOLI-4<sup>®</sup> for the adjoint calculations, which have been successfully tested on the control rod-drop measurements of CABRI [97].

## 7.4 Spectral analysis of the water blade configurations

The analysis of the experimental results presented in the previous section is devoted to a preliminary investigation of spatial kinetics effects during the last experiments of the EOLE reactor. In order to gain further knowledge on such effects, we have then analyzed the water blade configuration of the EPILOGUE program, which is characterized by a strong spatial heterogeneity described in Section 7.2.3. Unfortunately, it was not possible to draw solid conclusions from the data collected during the experiments performed on this configuration.

Nevertheless, the effect caused by the over-moderation of the water blade has been examined by resorting to the spectral analysis tools described in Chapter 5. In this respect, the Monte Carlo simulation has been used as a "numerical experiment", enabling the analysis of quantities that were not easily accessible by the measurements. Monte Carlo calculations were performed with TRIPOLI-4<sup>®</sup> in order to deploy the matrix-filling method and the fission matrix described in Chapter 5. These numerical simulations allow estimating:

- the fundamental and higher-order eigenpairs according to the  $\alpha$ -eigenvalue formulation,
- the fundamental and higher-order eigenpairs according to the  $k$ -eigenvalue formulation,

- the effective kinetics parameters.

The  $k$ - and the  $\alpha$ - eigenpairs yield an estimation of the critical level of the system (fundamental eigenvalues and eigenmodes) and of the behaviour of particle distribution after a perturbation (higher-order eigenvalues and eigenmodes). As discussed in the previous chapter, we can exploit the dominance ratio (Eq. (6.3)) and the eigenvalue separation (Eqs. (6.1) and (6.6)) in order to assess the degree of decoupling of the system. The spatial distributions of the eigenmodes related to both eigenvalue formulations provide an additional tool for the investigation of the decoupling effect caused by the water blade. Finally, the effective kinetic parameters computed for this configuration can be usefully compared to those obtained during the experiments (Tab. 7.3).

For the purpose of enhancing the effects induced by the water blade, we have conceived additional configurations where the original blade has been thickened by adding extra water layers (by removing fuel pins). For our analysis, we will consider the configuration without water blades (described in Section 7.2.1) as the reference. Then, we will remove additional fuel pins from the water blade configurations in order to artificially increase the thickness of the water in the core region. Figure 7.6 shows the radial section of the two new configurations that will be called for shortness "2 water blades" configuration (left) and "3 water blades" configuration (right). In the following, by analogy we will define the (single) water blade configuration as the "1 water blade" configuration.

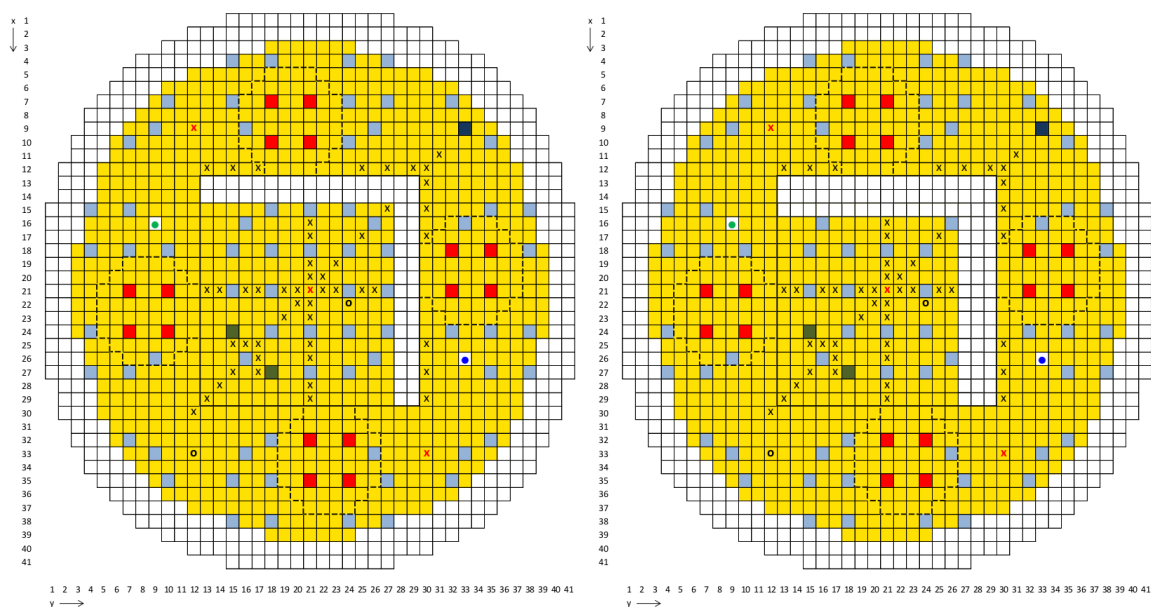


Figure 7.6: Schematic radial section of the EOLE reactor in water blade configurations. The "2 water blades" configuration (left) and the "3 water blades" configuration (right) are arranged by removing four and six lines of fuel pins from the core region. Fuel elements of enriched  $\text{UO}_2$  at 3.7% are colored in yellow and are distinguished in monitored fuel elements (black cross, black circle and red cross). Locations for control rods (red), pilot rod (dark blue) and  $B_4C$  rods (olive green) are shown. Two fission chambers are shown: CF2268 (white, green circle) and CF2269 (white, blue circle). All the remaining elements are filled with borated light water (light grey).

### 7.4.1 Simulation settings

All the configurations defined in the previous section have been simulated by using TRIPOLI-4<sup>®</sup>. Before detailing the simulation parameters of such calculations, a preliminary step is required for the calibration allowing each simulated system to be critical (similarly to the procedure adopted in Chapter 6). In order to achieve this condition, we modified the Boron concentration in the moderator of each configuration. This procedure can be performed in TRIPOLI-4<sup>®</sup> by a recently developed critical Boron concentration research routine, which iteratively seeks a multiplier coefficient for the Boron concentration  $C_{\text{Boron}}$ . For these calculations,  $10^5$  particles are simulated for a total of  $1.5 \times 10^3$  cycles ( $10^3$  active,  $5 \times 10^2$  discarded). Water composition and Boron concentration of the moderator for each configuration are shown in Tab. 7.12.

water blades [-]	H <sub>1</sub> [atoms/cm <sup>3</sup> ]	H <sub>1,H<sub>2</sub>O</sub> [atoms/cm <sup>3</sup> ]	O <sub>16</sub> [atoms/cm <sup>3</sup> ]	B <sub>10</sub> [atoms/cm <sup>3</sup> ]	B <sub>11</sub> [atoms/cm <sup>3</sup> ]	C <sub>Boron</sub> [ppm]
0	$4.675 \times 10^{-5}$	$6.669 \times 10^{-2}$	$3.339 \times 10^{-2}$	$3.286 \times 10^{-6}$	$1.323 \times 10^{-5}$	296.7
1	$3.923 \times 10^{-5}$	$6.670 \times 10^{-2}$	$3.339 \times 10^{-2}$	$2.708 \times 10^{-6}$	$1.090 \times 10^{-5}$	244.5
2	$3.923 \times 10^{-5}$	$6.670 \times 10^{-2}$	$3.339 \times 10^{-2}$	$1.878 \times 10^{-6}$	$7.561 \times 10^{-6}$	169.6
3	$3.923 \times 10^{-5}$	$6.670 \times 10^{-2}$	$3.339 \times 10^{-2}$	$7.339 \times 10^{-7}$	$2.954 \times 10^{-6}$	66.3

Table 7.12: Water composition and Boron concentration (ppm) of the moderator in water blade configurations.

As already discussed in Chapter 6, setting all these configurations to the critical level leads to two main advantages. The former is that the comparison of the dominance ratio and the eigenvalue separation is made easier by fixing the fundamental eigenvalues to the critical level. The latter stems from an algorithmic reason related to the equivalence between the  $k$ - and the  $\alpha$ -eigenvalue formulations for a critical state: this property allows us to freely choose between the  $k$  or  $\alpha$ - $k$  power iteration methods as a weighting function for the matrix-filling methods. The  $k$ -power iteration is preferred with respect to the  $\alpha$ - $k$  power iteration method, thanks to its faster convergence. Moreover, the estimation of the elements of the matrices associated to the linear transport operators is computed by using the same weighting function. Since the systems are at a critical level,  $\varphi_{k_0} \simeq \varphi_{\alpha_0}$ , the choice of the weighting function becomes arbitrary.

The discretization of the phase-space variables for the EOLE configurations implies a large dimension of the matrices corresponding to the eigenvalue formulations. The trade-off required to compute the eigenpairs in a reasonable time and be able to detect the effect of the moderator heterogeneity consists in primarily refining the spatial coordinates in the radial section of the reactor. By fixing the origin of the spatial reference system in the center of the reactor, an uniform Cartesian grid is applied on the plane that divides the two coordinates in  $N_x = N_y = 48$  spatial bins from  $-52.8$  cm to  $52.8$  cm. The axial coordinate is integrated over the whole height of the system ( $N_z = 1$ ). The angle discretization is kept at  $M_x = M_y = 2$  and  $M_z = 1$ . The energy domain is divided into  $G = 3$  groups: a fast region in the interval  $[20 \text{ MeV}, 94.66 \text{ keV}]$ , an epithermal region  $[94.66 \text{ keV}, 0.625 \text{ eV}]$  and a thermal region  $[0.625 \text{ eV}, 10^{-5} \text{ eV}]$ . According to the JEFF nuclear data library [134], a total of  $J = 8$  precursors families are considered for the fissile nuclei. The total number of elements of the matrix for the  $\alpha$ -eigenvalue problem is about  $2 \times 10^9$ .

As for the  $k$ -eigenvalue problem, we used the estimation of the fission matrix in order to perform the spectral analysis on the  $k$ -modal basis. According to this procedure, only the space coordinate needs to be discretized. The eigenmodes computed from the fission matrix represent fission rates and as so there is no interest in a fine discretization of the non-fissile regions of the reactor. Moreover, the linearity of this problem with respect to the eigenvalue allows combining the contributions of prompt and delayed fission operators. All these considerations imply a significant reduction of the matrix size for the  $k$ -eigenvalue formulation. In particular, we impose a cartesian grid on the radial section of the core region, specifically  $N_x = N_y = 74$  from  $-23.31$  cm to  $23.31$  cm along both axes. In this way, the spatial bins perfectly overlap on the square fuel pins section ( $1.26 \times 1.26 \text{ cm}^2$ ). The total number of elements of the fission matrix is about  $3 \times 10^7$ .

## 7.4.2 Eigenvalue analysis

The Boron concentrations shown in Tab. 7.12 are used for the criticality simulations in order to adjust each configuration to the critical level. All the results presented in the following paragraphs have been obtained during a standard power iteration that was used to estimate the elements of the matrices needed for the  $\alpha$ - and  $k$ - spectral analysis. In particular,  $10^5$  particles per cycles are simulated for a total of  $2.5 \times 10^3$  cycles ( $2 \times 10^3$  active,  $5 \times 10^2$  discarded).

#### 7.4. SPECTRAL ANALYSIS OF THE WATER BLADE CONFIGURATIONS

water blades [-]	$k_0^{MC}$ [-]	$k_0$ [-]	$k_1$ [-]	$k_2$ [-]	$k_3$ [-]	$k_4$ [-]	$k_5$ [-]
0	$0.99988 \pm 7$ pcm	0.99988	0.70793	0.70552	0.48323	0.48112	0.42774
1	$1.00012 \pm 7$ pcm	1.00012	0.72320	0.71284	0.49605	0.49100	0.43236
2	$1.00019 \pm 7$ pcm	1.00019	0.73302	0.72089	0.50609	0.50061	0.44342
3	$0.99997 \pm 7$ pcm	0.99997	0.74483	0.73167	0.51801	0.51488	0.45587

Table 7.13: First  $k$ -eigenvalues for EOLE water blades configurations configurations. The second column displays the fundamental eigenvalues  $k_0$  computed by TRIPOLI-4<sup>®</sup> power iteration for the  $k$ -eigenvalue problem and the corresponding standard deviations. All other eigenvalues have been computed from the fission matrix of the corresponding configuration.

The fundamental eigenvalues obtained with these calculations are shown in the second column of Tab. 7.13. These values are less than 20 pcm from the critical state, with a standard deviation of 7 pcm for the chosen number of particles and cycles. The other values presented in Tab. 7.13 have been computed from the fission matrices associated to each configuration. An excellent agreement is found between the fundamental eigenvalues  $k_0^{MC}$  (obtained by using the power iteration) and  $k_0$  (computed from the post-processed fission matrices).

During the same calculations, the discretized version of linear transport operators have been estimated and post-processed in order to obtain the matrices of the  $\alpha$ -eigenvalue problems. The real parts of the corresponding eigenvalues have been arranged in descending order in order to discriminate the fundamental eigenvalue, the clusters of delayed eigenvalues and the prompt eigenvalues. The fundamental eigenvalues  $\alpha_0$  and the first five delayed eigenvalues are shown in Tab. 7.14. The sign and the magnitude of the fundamental  $\alpha$ -eigenvalues are consistent with the  $k_0$  eigenvalues from the previous table. The absolute value of the first delayed eigenvalues collapses on the minimum decay constant equal to  $\min(\lambda) = 1.247 \times 10^{-2} \text{ s}^{-1}$ . Conversely, the first five prompt  $\alpha$ -eigenvalues shown in Tab. 7.15 exhibit significant variations as a function of the configuration and of the mode order.

water blades [-]	$\alpha_0$ [ $\text{s}^{-1}$ ]	$\alpha_1$ [ $\text{s}^{-1}$ ]	$\alpha_2$ [ $\text{s}^{-1}$ ]	$\alpha_3$ [ $\text{s}^{-1}$ ]	$\alpha_4$ [ $\text{s}^{-1}$ ]	$\alpha_5$ [ $\text{s}^{-1}$ ]
0	$-1.122 \times 10^{-3}$	$-1.246 \times 10^{-2}$	$-1.246 \times 10^{-2}$	$-1.246 \times 10^{-2}$	$-1.246 \times 10^{-2}$	$-1.247 \times 10^{-2}$
1	$1.084 \times 10^{-3}$	$-1.246 \times 10^{-2}$	$-1.246 \times 10^{-2}$	$-1.246 \times 10^{-2}$	$-1.246 \times 10^{-2}$	$-1.247 \times 10^{-2}$
2	$2.473 \times 10^{-3}$	$-1.246 \times 10^{-2}$				
3	$-5.273 \times 10^{-4}$	$-1.246 \times 10^{-2}$				

Table 7.14: First  $\alpha$ -eigenvalues for EOLE water blades configurations. These values have been computed from the matrix-form of linear transport operator combined for the definition of the  $\alpha$ -eigenvalue problem.

water blades [-]	$\alpha_{p,0}$ [ $\text{s}^{-1}$ ]	$\alpha_{p,1}$ [ $\text{s}^{-1}$ ]	$\alpha_{p,2}$ [ $\text{s}^{-1}$ ]	$\alpha_{p,3}$ [ $\text{s}^{-1}$ ]	$\alpha_{p,4}$ [ $\text{s}^{-1}$ ]	$\alpha_{p,5}$ [ $\text{s}^{-1}$ ]
0	$-2.233 \times 10^2$	$-4.277 \times 10^3$	$-4.883 \times 10^3$	$-5.167 \times 10^3$	$-6.051 \times 10^3$	$-6.068 \times 10^3$
1	$-2.010 \times 10^2$	$-5.591 \times 10^3$	$-5.662 \times 10^3$	$-7.667 \times 10^3$	$-7.688 \times 10^3$	$-8.158 \times 10^3$
2	$-1.715 \times 10^2$	$-5.000 \times 10^3$	$-5.088 \times 10^3$	$-6.252 \times 10^3$	$-7.000 \times 10^3$	$-7.022 \times 10^3$
3	$-1.508 \times 10^2$	$-4.234 \times 10^3$	$-4.328 \times 10^3$	$-6.081 \times 10^3$	$-6.103 \times 10^3$	$-6.793 \times 10^3$

Table 7.15: First prompt  $\alpha$ -eigenvalues for EOLE water blades configurations. These values have been computed from the matrix-form of linear transport operator combined for the definition of the  $\alpha$ -eigenvalue problem.

For the sake of completeness, we show both the  $k$ - and the  $\alpha$ -spectra on the complex plane in Fig. 7.7. The (small) imaginary part of the  $k$ -spectrum is merely due to the statistical uncertainties propagated from the stochastic estimation of the matrix elements on the eigenvalues. Figure 7.8 shows the zoom on all delayed eigenvalue clusters (left) and on the delayed eigenvalue cluster associated to the first precursor family (right). The eigenvalues are concentrated on the right of the  $-\lambda_j$  values. The dominant eigenvalue  $\alpha_{d,0}^j$  of the  $j$ -th delayed cluster is separated from the other eigenvalues of the same precursor family. The zoom of Fig. 7.8 (left) shows the gap between  $\alpha_{d,0}^j$  and  $-\lambda_j$  values for the last precursor families. The computed values of  $\alpha_{d,0}^j$  and  $\alpha_{d,1}^j$  for the last three precursor families ( $j = 6, 7, 8$ ) are shown in Tab. 7.16. Values for the  $-\lambda_j$  shown in Fig. are:  $-\lambda_1 = -1.2467 \times 10^{-2} \text{ s}^{-1}$ ,

$-\lambda_6 = -6.6649 \times 10^{-1} \text{ s}^{-1}$ ,  $-\lambda_7 = -1.6348 \text{ s}^{-1}$  and  $-\lambda_8 = -3.5546 \text{ s}^{-1}$ .

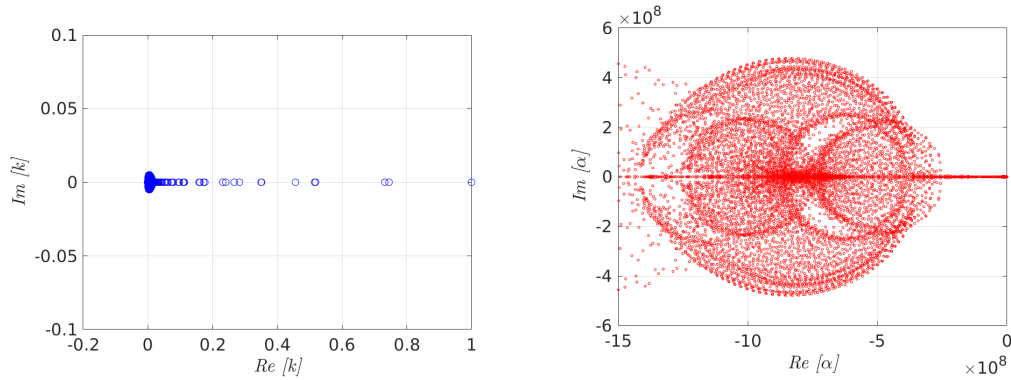


Figure 7.7: Spectra of the  $k$  (left) and the  $\alpha$  (right) eigenvalue problem for the "3 water blades" configuration.

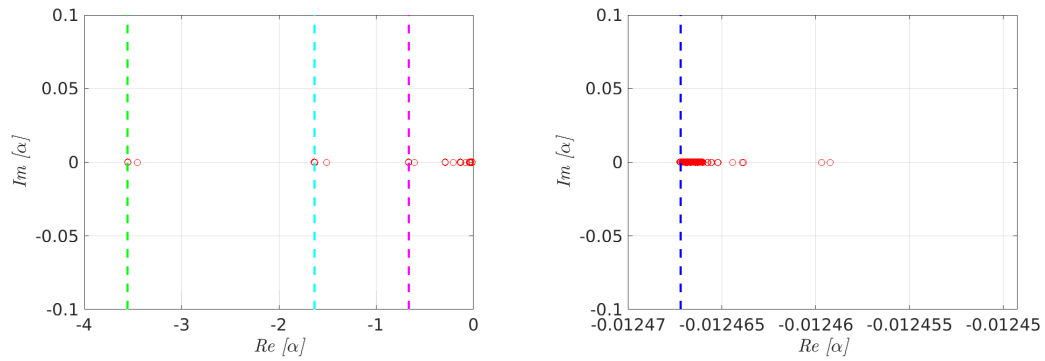


Figure 7.8: Zoom on the  $\alpha$ -spectrum on the delayed region (left) and in the first delayed cluster (right) for the "3 water blades" configuration. Vertical lines have been added in order to indicate the values of  $-\lambda_1$  (blue),  $-\lambda_6$  (magenta),  $-\lambda_7$  (cyan) and  $-\lambda_8$  (green).

water blades [-]	$\alpha_{d,0}^6 [\text{s}^{-1}]$	$\alpha_{d,1}^6 [\text{s}^{-1}]$	$\alpha_{d,0}^7 [\text{s}^{-1}]$	$\alpha_{d,1}^7 [\text{s}^{-1}]$	$\alpha_{d,0}^8 [\text{s}^{-1}]$	$\alpha_{d,1}^8 [\text{s}^{-1}]$
0	$-6.079 \times 10^{-1}$	$-6.653 \times 10^{-1}$	-1.506	-1.632	-3.453	-3.553
1	$-6.074 \times 10^{-1}$	$-6.653 \times 10^{-1}$	-1.505	-1.632	-3.453	-3.553
2	$-6.069 \times 10^{-1}$	$-6.652 \times 10^{-1}$	-1.503	-1.632	-3.452	-3.553
3	$-6.087 \times 10^{-1}$	$-6.652 \times 10^{-1}$	-1.507	-1.632	-3.455	-3.552

Table 7.16: First  $\alpha$ -eigenvalues of the clusters associated to the last three precursor families ( $j = 6, 7, 8$ ) for the EOLE water blades configurations. These values have been computed from the matrix-form of linear transport operator combined for the definition of the  $\alpha$ -eigenvalue problem.

The eigenvalues computed for these configurations are combined in order to obtain the dominance ratio and the eigenvalue separation according to the  $k$ - and the  $\alpha$ -formulations. These values are collected in Tabs. 7.17 and 7.19 and are shown in Figs. 7.9 and 7.10.

The values of dominance ratio increase for a larger thickness of the water blade from  $\text{DR} = 0.7080$  up to  $\text{DR} = 0.7449$ . The eigenvalue separations according to the  $k$ -formulation follow a similar behaviour as the one observed in the analysis of 2D systems in Chapter 6 (Figs. 6.7 and 6.11): the first and second, the third and fourth order of the eigenvalue separations show close values. This feature might be related to the symmetry properties of this system, which would in turn induce a degeneracy in the eigenvalues. Conversely, all these values do not change significantly with respect to the chosen configuration (i.e., to the number of water blades).

water blades [-]	DR [-]	E.S. <sub>1</sub> ( <i>k</i> ) [-]	E.S. <sub>2</sub> ( <i>k</i> ) [-]	E.S. <sub>3</sub> ( <i>k</i> ) [-]	E.S. <sub>4</sub> ( <i>k</i> ) [-]	E.S. <sub>5</sub> ( <i>k</i> ) [-]
0	$7.080 \times 10^{-1}$	$4.125 \times 10^{-1}$	$4.173 \times 10^{-1}$	$1.069 \times 10^0$	$1.078 \times 10^0$	$1.338 \times 10^0$
1	$7.231 \times 10^{-1}$	$3.829 \times 10^{-1}$	$4.030 \times 10^{-1}$	$1.016 \times 10^0$	$1.037 \times 10^0$	$1.313 \times 10^0$
2	$7.329 \times 10^{-1}$	$3.644 \times 10^{-1}$	$3.874 \times 10^{-1}$	$9.761 \times 10^{-1}$	$9.977 \times 10^{-1}$	$1.255 \times 10^0$
3	$7.449 \times 10^{-1}$	$3.426 \times 10^{-1}$	$3.667 \times 10^{-1}$	$9.304 \times 10^{-1}$	$9.422 \times 10^{-1}$	$1.194 \times 10^0$

Table 7.17: Dominance ratio and E.S.<sub>*n*</sub>(*k*) eigenvalue separations of the first *k*-eigenvalues for water blade configurations.

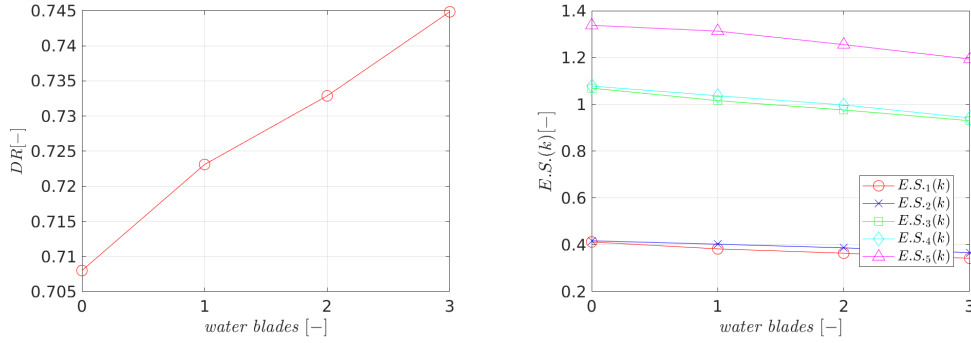


Figure 7.9: Dominance ratio (left) and *k*-eigenvalue separations (right) for EOLE water blade configurations. The first five order of eigenvalue separations are shown, in order, as: E.S.<sub>1</sub>(*k*) red circles, E.S.<sub>2</sub>(*k*) blue crosses, E.S.<sub>3</sub>(*k*) green squares, E.S.<sub>4</sub>(*k*) cyan diamonds and E.S.<sub>5</sub>(*k*) magenta triangles.

The  $\alpha$ -eigenvalues computed from the matrix-form of the  $\alpha$ -eigenvalue problem are used in order to estimate the delayed E.S.( $\alpha_d$ ) and the prompt E.S.( $\alpha_p$ ) eigenvalue separations of the first five orders. The delayed results are shown in Tab. 7.18, whereas the prompt results are shown in Tab. 7.19. The values of delayed eigenvalue separations (Fig. 6.8, left) are almost constant as a function of the water blade configuration. The prompt  $\alpha$ -eigenvalue separations (Fig. 6.4, right) have a different behaviour with respect to the *k*-eigenvalue separations. In particular, the eigenvalue separations associated to the "0 water blade" configuration appear to have a different trend with respect to the results obtained from the other configurations. This stems from this configuration not having any strong heterogeneity along the spatial coordinates. For the configurations containing the water blades, on the contrary, we notice a similar behaviour with respect to what examined for the 2D configurations of Sections 6.4.1 and 6.4.2. The proximity of the first and second, third and fourth order of the eigenvalue separations suggest again a degeneracy effect related to the symmetry of the system.

Moreover, the values of dominance ratio hint the absence of strong decoupling effects in all these configurations. For this reasons, no solid conclusions can be drawn relating spatial kinetics effects to the eigenvalue separations of the considered configurations. Therefore, in the next section we complement this analysis by considering the eigenmodes.

water blades [-]	E.S. <sub>1</sub> ( $\alpha_d$ ) [ $s^{-1}$ ]	E.S. <sub>2</sub> ( $\alpha_d$ ) [ $s^{-1}$ ]	E.S. <sub>3</sub> ( $\alpha_d$ ) [ $s^{-1}$ ]	E.S. <sub>4</sub> ( $\alpha_d$ ) [ $s^{-1}$ ]	E.S. <sub>5</sub> ( $\alpha_d$ ) [ $s^{-1}$ ]
0	$-1.134 \times 10^{-2}$				
1	$-1.354 \times 10^{-2}$	$-1.354 \times 10^{-2}$	$-1.355 \times 10^{-2}$	$-1.355 \times 10^{-2}$	$-1.355 \times 10^{-2}$
2	$-1.493 \times 10^{-2}$	$-1.493 \times 10^{-2}$	$-1.494 \times 10^{-2}$	$-1.494 \times 10^{-2}$	$-1.494 \times 10^{-2}$
3	$-1.193 \times 10^{-2}$	$-1.193 \times 10^{-2}$	$-1.194 \times 10^{-2}$	$-1.194 \times 10^{-2}$	$-1.194 \times 10^{-2}$

Table 7.18: Eigenvalue separations of the first delayed  $\alpha$ -eigenvalues for water blade configurations.

water blades [-]	$E.S.1(\alpha_p)$ [ $s^{-1}$ ]	$E.S.2(\alpha_p)$ [ $s^{-1}$ ]	$E.S.3(\alpha_p)$ [ $s^{-1}$ ]	$E.S.4(\alpha_p)$ [ $s^{-1}$ ]	$E.S.5(\alpha_p)$ [ $s^{-1}$ ]
0	$-4.054 \times 10^3$	$-4.660 \times 10^3$	$-4.943 \times 10^3$	$-5.827 \times 10^3$	$-5.844 \times 10^3$
1	$-5.390 \times 10^3$	$-5.461 \times 10^3$	$-7.466 \times 10^3$	$-7.487 \times 10^3$	$-7.957 \times 10^3$
2	$-4.828 \times 10^3$	$-4.916 \times 10^3$	$-6.080 \times 10^3$	$-6.828 \times 10^3$	$-6.851 \times 10^3$
3	$-4.083 \times 10^3$	$-4.177 \times 10^3$	$-5.930 \times 10^3$	$-5.953 \times 10^3$	$-6.642 \times 10^3$

Table 7.19: Eigenvalue separations of the first prompt  $\alpha$ -eigenvalues for water blade configurations.

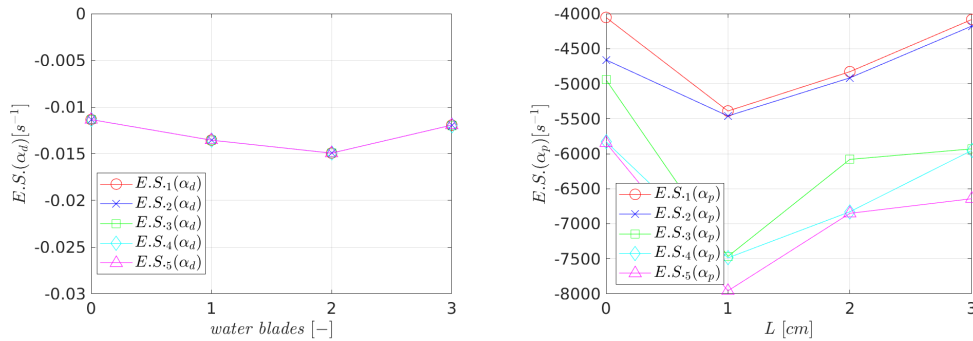


Figure 7.10: Delayed (left) and prompt (right)  $\alpha$ -eigenvalue separations for EOLE water blade configurations. The first five order of eigenvalue separations are shown, in order, as:  $E.S.1(\alpha)$  red circles,  $E.S.2(\alpha)$  blue crosses,  $E.S.3(\alpha)$  green squares,  $E.S.4(\alpha)$  cyan diamonds and  $E.S.5(\alpha)$  magenta triangles.

### 7.4.3 Eigenmode analysis

We will now examine the eigenvectors corresponding to the  $k$ - and the  $\alpha$ -eigenvalue formulation as a function of the spatial coordinates in the cross-section plane of the EOLE reactor. The distributions computed from fission matrices are fission rates  $Q_{f,k}(x,y)$  depending only on the spatial coordinates. For this reason, we applied a finer discretization in the fissile regions. Conversely,  $\alpha$ -eigenfunctions are related to particle population (neutrons and precursors), thus requiring the discretization of the whole phase-space, yielding distributions of the kind  $\varphi_\alpha(x,y,\mu_x,\mu_y,E)$  for neutrons and  $c_{j,\alpha}(x,y,E)$  for precursors.

Figures 7.11 and 7.12 show the spatial distribution of the fundamental and the first-order eigenmodes according to the  $k$ -formulation, respectively. As expected, since the fission rates are located only in the fissile fuel pins of the core, the effect of the moderator region is clearly visible. Concerning the fundamental eigenmode, the distribution corresponding to the reference configuration (top left) shows large values of the fission rates in the central region of the core and in its the peripheral region. The moderation caused by the borated water increases the fission rates in proximity of the non fissile regions with respect to the usual Bessel-like distribution expected for an homogeneous core. The replacement of fuel pins in the water layer region of the "1 water blade" configuration (top right) completely modifies the fission rates distribution in the core. Fuel pin regions over-moderated by this replacement are characterized by larger values of fission rates, whereas all the regions far from this perturbation display smaller values with respect to the distribution of the reference configuration. Increasing the thickness of the water layer in 2 (bottom left) and 3 (bottom right) water blades configurations enhance the localized behaviour of this perturbation by amplifying the fission rates of fuel pins closer to the over-moderated regions. Moreover, the absorption caused by the  $B_4C$  rods placed on the other side with respect to the water layer is clearly visible, since it reduces the fission rates in their proximity.

The adjoint distributions of the  $k$ -eigenvalue problem analyzed by transposition of the fission matrix are shown in Figs. 7.13 and 7.14 for the fundamental and the first-order eigenmodes, respectively. The presence of the strong moderator heterogeneity appears to slightly shift the peak of the adjoint eigenfunction towards the center of the water blade. Overall, a Bessel-like shape is observed for the four configurations.

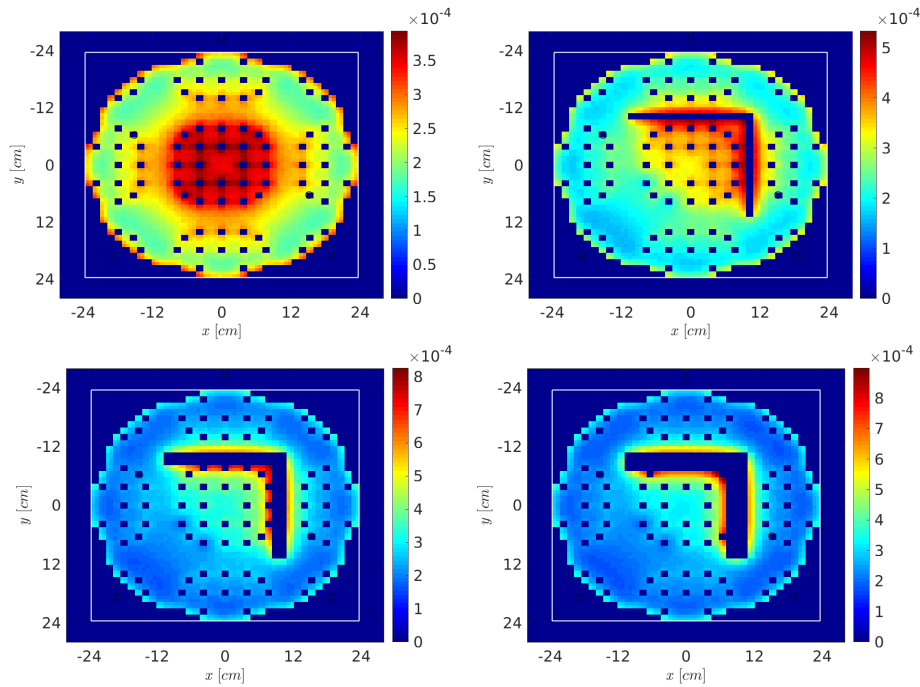


Figure 7.11: Spatial behaviour of the forward fundamental eigenmodes  $Q_{f,k_0}(x,y)$  on the EOLE cross section. Configurations with 0 (top left), 1 (top right), 2 (bottom left) and 3 (bottom right) water blades are shown. The white frame indicates the boundaries of the core region. All the eigenfunctions have been normalized. Detector positions of the water blade configuration (Section 7.2.3) are shown as black circles.

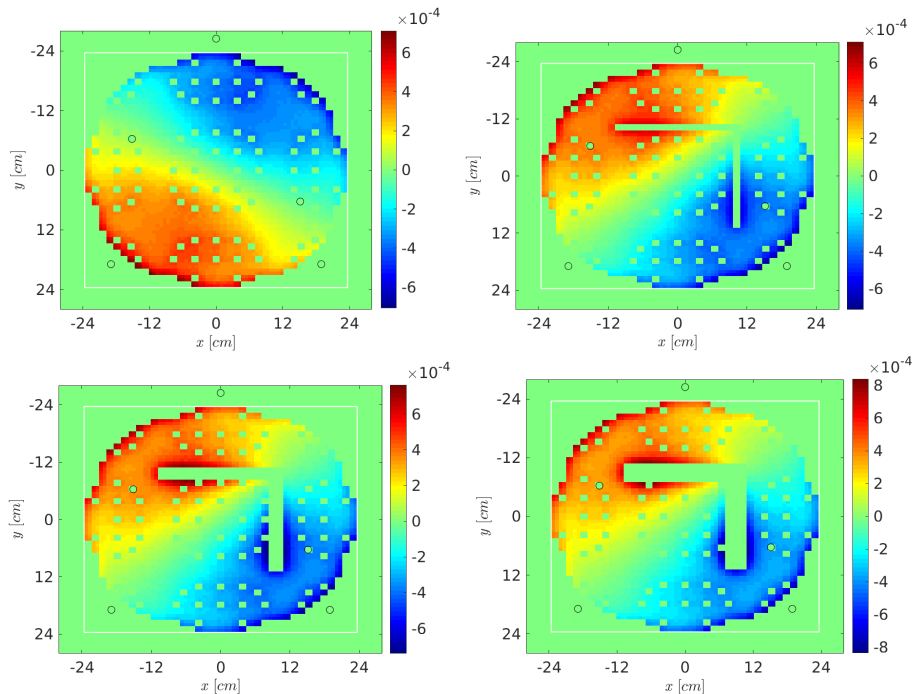


Figure 7.12: Spatial behaviour of the forward first-order eigenmodes  $Q_{f,k_1}(x,y)$  on the EOLE cross section. Configurations with 0 (top left), 1 (top right), 2 (bottom left) and 3 (bottom right) water blades are shown. The white frame indicates the boundaries of the core region. All the eigenfunctions have been normalized. Detector positions of the water blade configuration (Section 7.2.3) are shown as black circles.

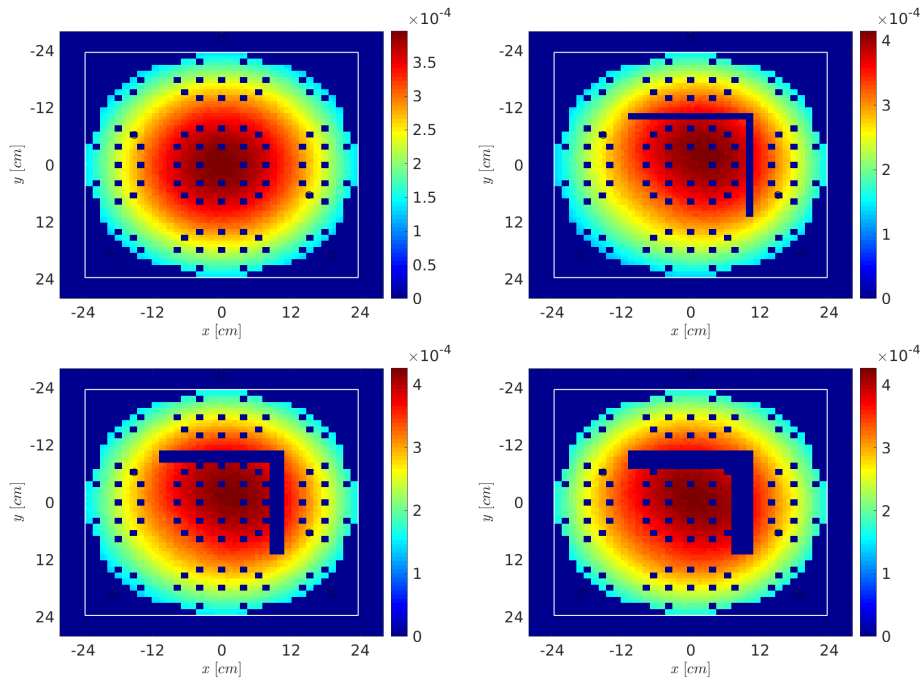


Figure 7.13: Spatial behaviour of the adjoint fundamental eigenmodes  $Q_{f,k_0}^\dagger(x,y)$  on the EOLE cross section. Configurations with 0 (top left), 1 (top right), 2 (bottom left) and 3 (bottom right) water blades are shown. The white frame indicates the boundaries of the core region. All the eigenfunctions have been normalized. Detector positions of the water blade configuration (Section 7.2.3) are shown as black circles.

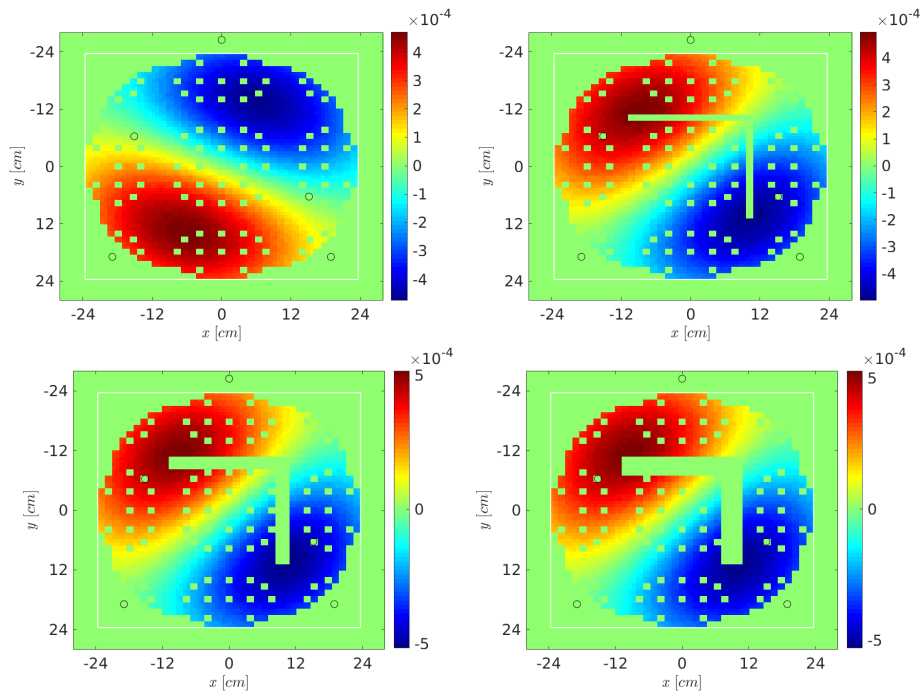


Figure 7.14: Spatial behaviour of the adjoint first-order eigenmodes  $Q_{f,k_1}^\dagger(x,y)$  on the EOLE cross section. Configurations with 0 (top left), 1 (top right), 2 (bottom left) and 3 (bottom right) water blades are shown. The white frame indicates the boundaries of the core region. All the eigenfunctions have been normalized. Detector positions of the water blade configuration (Section 7.2.3) are shown as black circles.

Concerning the  $\alpha$ -eigenmodes, we resort to the discretization of the operators in energy groups by showing

spatial distributions integrated over different energy ranges. In the Figs. 7.15 and 7.16 we display the results obtained for the four configurations (columns) in thermal, epithermal, fast and whole energy ranges (rows).

Figure 7.15 shows the fundamental eigenmodes  $\varphi_{\alpha_0}(x,y,g)$  for each configuration and energy range. The distribution for the reference configuration in the thermal energy range shows large values on the peripheral zone just outside the core and in its center. Results obtained in epithermal and fast energy range display the Bessel-like shape of the neutron flux. Such shape is recovered by integrating over the whole energy range. The effect of the water blade(s) is clearly visible in the other figures. In the thermal energy range, the flux distribution located inside the water blade region assumes larger values for increasing thickness of the water layer. This effect can be justified by the stronger over-moderation caused by gradually larger number of replaced fuel pins. In the epithermal energy range the absorption caused by the  $B_4C$  rods is visible and the neutron population migrates towards the center of the core for increasing thickness of the water layer. In the fast region, the moderator progressively reduces neutron flux moving from the "1 water blade" configuration up to "3 water blades" configuration. All these effects are present and progressively more visible in the results integrated over the whole energy range. In particular, for the "3 water blade" configuration we notice a more localized peak in the center of the core, larger values caused by the over-moderation of the water layer and smaller values due to the absorption of the  $B_4C$  rods. The behaviours discussed for the fundamental mode is observed also for the higher order modes. Nevertheless, the presence of an increasing number of nodes for higher order eigenfunctions smoothens the perturbations caused by the heterogeneity of each configuration. As previously discussed in Chapter 6 for the 2D benchmark configuration, the first-order spatial distributions (Fig. 7.16) are similar to the second-order spatial distributions (Fig. 7.17) rotated by  $90^\circ$ . This behaviour suggests the presence of a degeneracy of the analyzed configurations due the symmetries of the system. For the sake of completeness we show the fundamental and first-order prompt eigenmodes in Figs. 7.18 and 7.19, respectively.

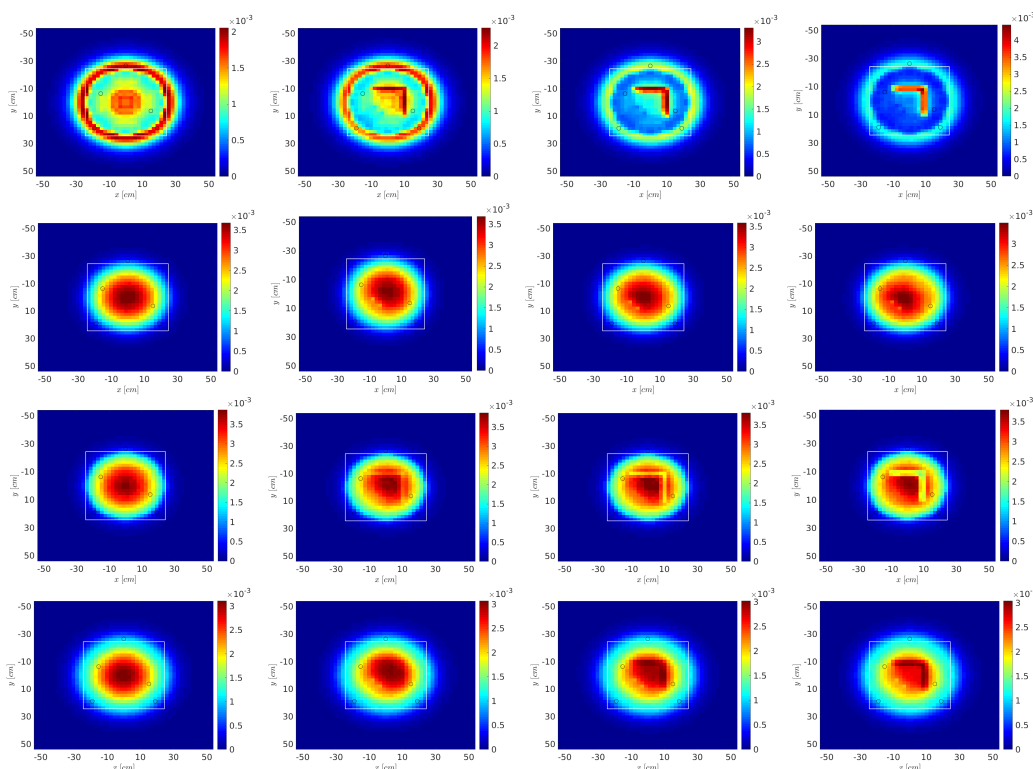


Figure 7.15: Spatial behaviour of the forward fundamental eigenmodes  $\varphi_{\alpha_0}(x,y,g)$  on the EOLE cross section. Configurations with 0 (first column), 1 (second column), 2 (third column) and 3 (fourth column) water blades are shown. The spatial eigenfunctions have been integrated in thermal (first row), epithermal (second row), fast (third row) and whole (fourth row) energy region. The white frame indicates the boundaries of the core region. All the eigenfunctions have been normalized. Detector positions of the water blade configuration (Section 7.2.3) are shown as black circles.

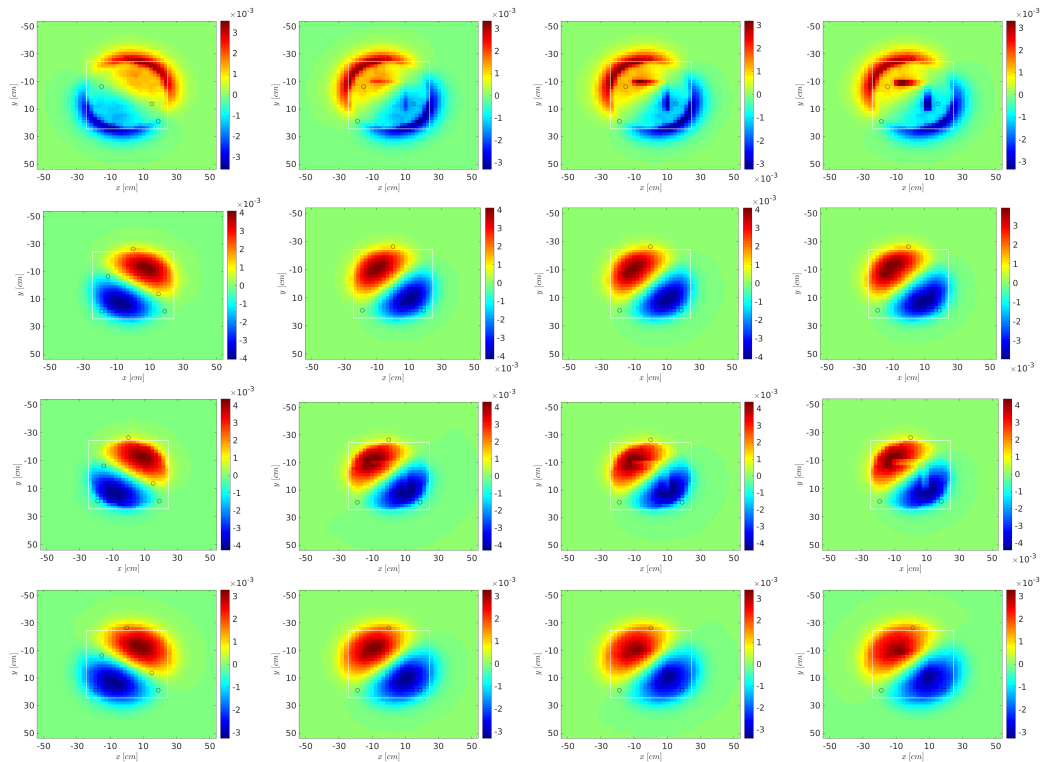


Figure 7.16: Spatial behaviour of the forward first-order eigenmodes  $\varphi_{\alpha_1}(x, y, g)$  on the EOLE cross section. Configurations with 0 (first column), 1 (second column), 2 (third column) and 3 (fourth column) water blades are shown. The spatial eigenfunctions have been integrated in thermal (first row), epithermal (second row), fast (third row) and whole (fourth row) energy region. The white frame indicates the boundaries of the core region. All the eigenfunctions have been normalized. Detector positions of the water blade configuration (Section 7.2.3) are shown as black circles.

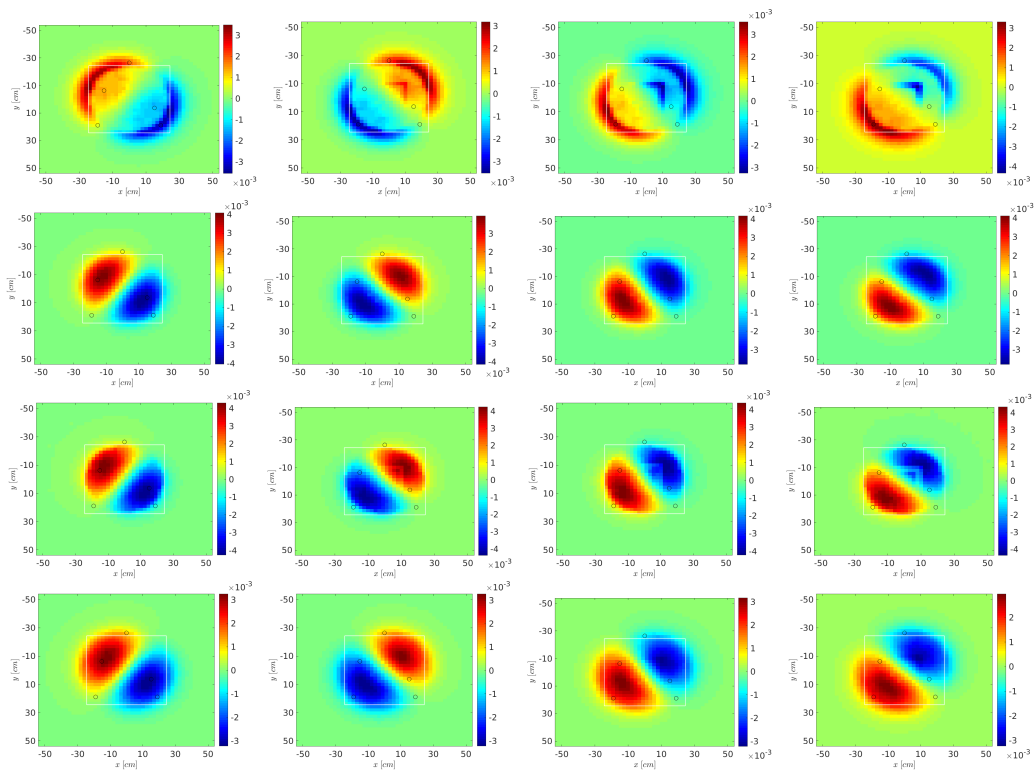


Figure 7.17: Spatial behaviour of the forward second-order eigenmodes  $\varphi_{\alpha_2}(x,y,g)$  on the EOLE cross section. Configurations with 0 (first column), 1 (second column), 2 (third column) and 3 (fourth column) water blades are shown. The spatial eigenfunctions have been integrated in thermal (first row), epithermal (second row), fast (third row) and whole (fourth row) energy region. The white frame indicates the boundaries of the core region. All the eigenfunctions have been normalized. Detector positions of the water blade configuration (Section 7.2.3) are shown as black circles.

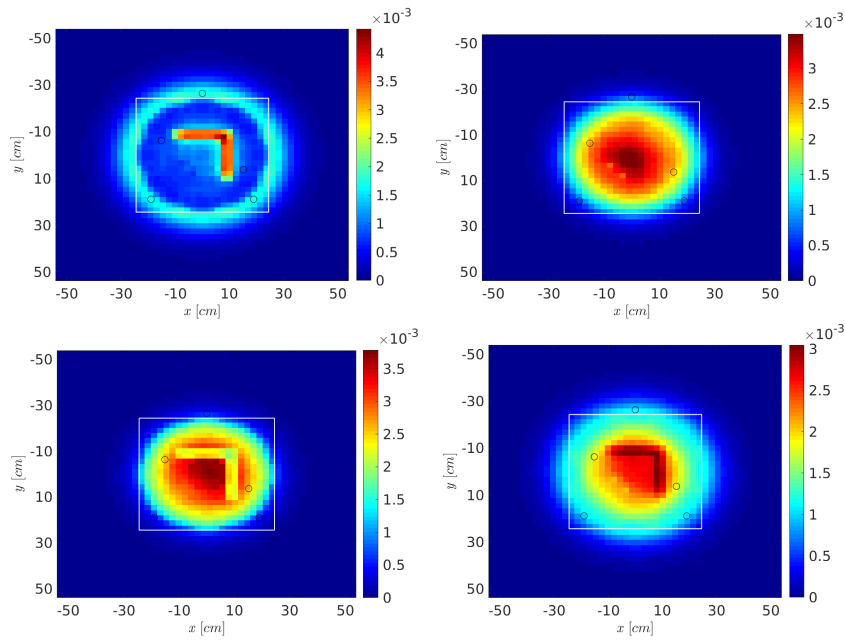


Figure 7.18: Spatial behaviour of the forward fundamental prompt eigenmodes  $\varphi_{\alpha_{p,0}}(x,y,g)$  for the "3 blades" configuration on the EOLE cross section. The spatial eigenfunctions have been integrated in thermal (top left), epithermal (top right), fast (bottom left) and whole (bottom right) energy region. The white frame indicates the boundaries of the core region. All the eigenfunctions have been normalized. Detector positions of the water blade configuration (Section 7.2.3) are shown as black circles.

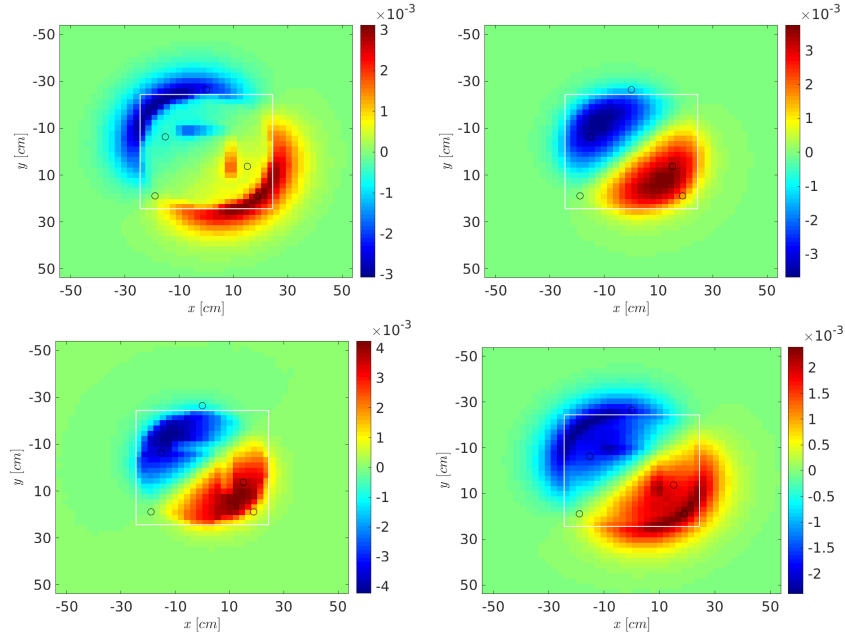


Figure 7.19: Spatial behaviour of the forward first-order prompt eigenmodes  $\varphi_{\alpha_{p,1}}(x,y,g)$  for the "3 blades" configuration on the EOLE cross section. The spatial eigenfunctions have been integrated in thermal (top left), epithermal (top right), fast (bottom left) and whole (bottom right) energy region. The white frame indicates the boundaries of the core region. All the eigenfunctions have been normalized. Detector positions of the water blade configuration (Section 7.2.3) are shown as black circles.

The adjoint distributions of the  $\alpha$ -eigenvalue problem analyzed by transposition of the  $\alpha$ -matrix are shown in Figs. 7.20 and 7.21 for the fundamental and the first-order eigenmodes, respectively. Similarly to the results analyzed for the  $k$ -formulation, the fundamental adjoint distribution presents a Bessel-like shape. Conversely, the influence of the water blade region and of the control rod absorption is clearly visible in thermal and epithermal region, respectively, for increasing thickness of the water layer.

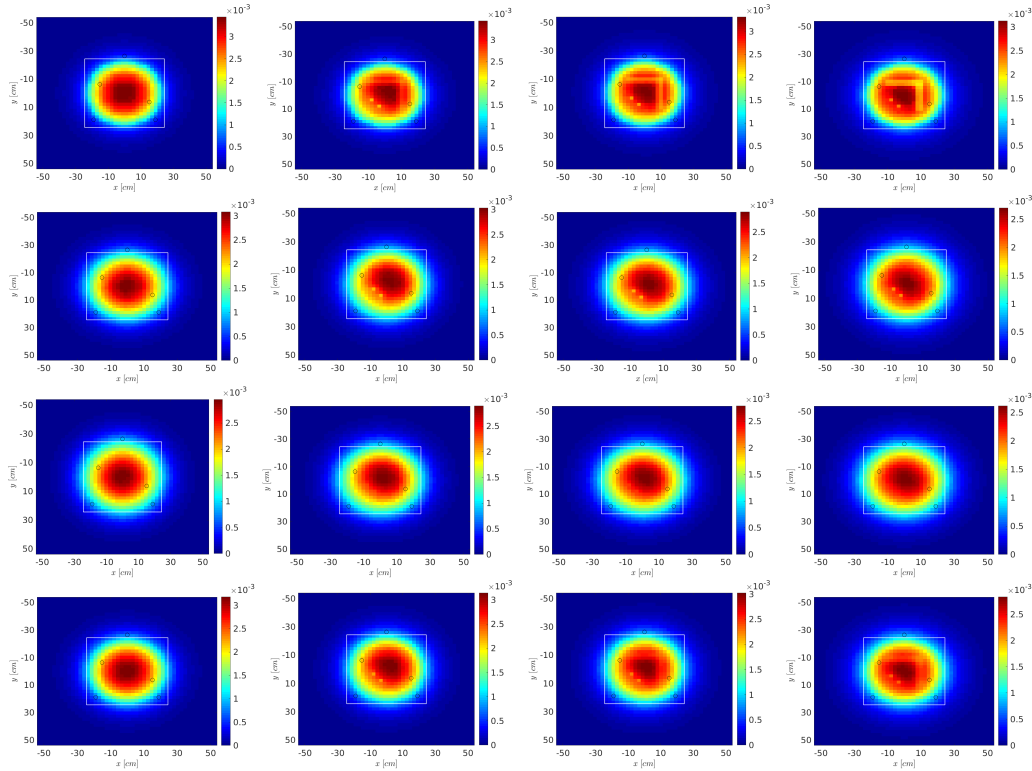


Figure 7.20: Spatial behaviour of the adjoint fundamental eigenmodes  $\varphi_{\alpha_0}^\dagger(x, y, g)$  on the EOLE cross section. Configurations with 0 (first column), 1 (second column), 2 (third column) and 3 (fourth column) water blades are shown. The spatial eigenfunctions have been integrated in thermal (first row), epithermal (second row), fast (third row) and whole (fourth row) energy region. The white frame indicates the boundaries of the core region. All the eigenfunctions have been normalized. Detector positions of the water blade configuration (Section 7.2.3) are shown as black circles.

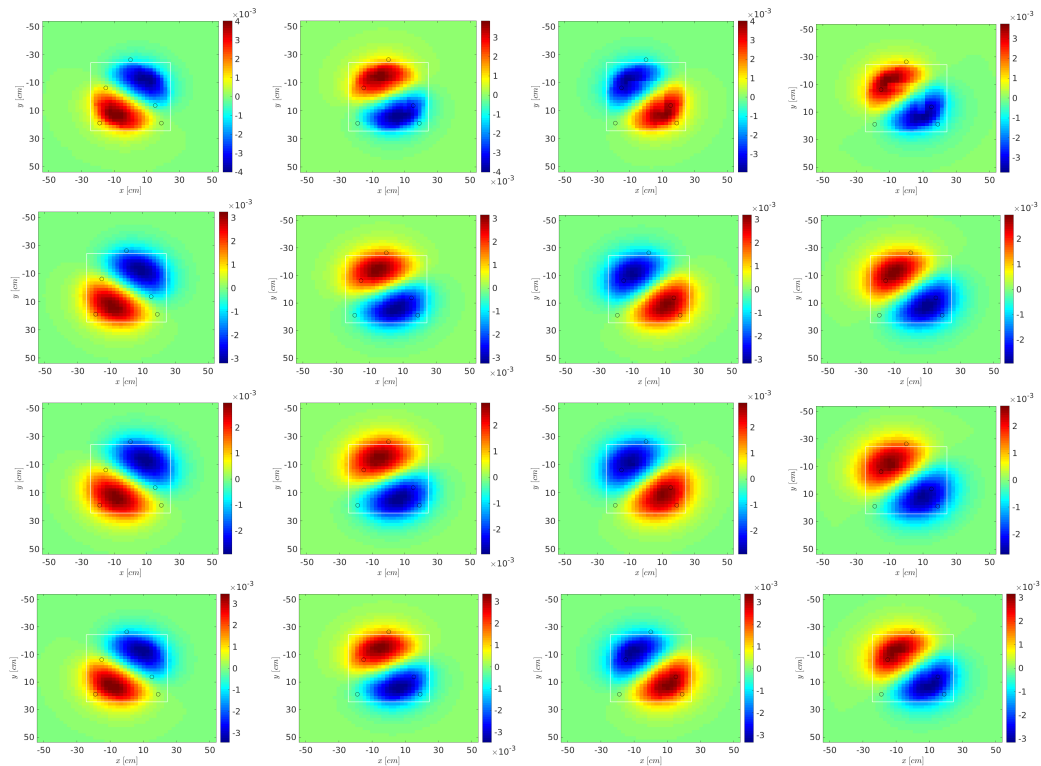


Figure 7.21: Spatial behaviour of the adjoint first-order eigenmodes  $\varphi_{\alpha_1}^\dagger(x, y, g)$  on the EOLE cross section. Configurations with 0 (first column), 1 (second column), 2 (third column) and 3 (fourth column) water blades are shown. The spatial eigenfunctions have been integrated in thermal (first row), epithermal (second row), fast (third row) and whole (fourth row) energy region. The white frame indicates the boundaries of the core region. All the eigenfunctions have been normalized. Detector positions of the water blade configuration (Section 7.2.3) are shown as black circles.

#### 7.4.4 Analysis of kinetics parameters

During the simulations described above, the effective kinetic parameters have also been computed. Criticality  $k$ -calculations were performed, so the weighting functions applied to the bilinear forms are  $\varphi_{k_0}$  and  $\varphi_{k_0}^\dagger$ . Since all these systems have been adjusted to the critical level, the  $\alpha$ - and  $k$ - fundamental eigenmodes are expected to be almost identical. The computed values for  $\rho$  have been obtained as static reactivities according to Eq. (2.106).

The computed kinetics parameters and the corresponding reactivities parameters are shown in Tab. 7.20. Reactivity mean values and standard deviations are intimately related to the fundamental eigenvalues  $k_0$  estimated for each configuration and shown in Tab. 7.13. The mean generation time  $\Lambda_{\text{eff}}$  estimated for the "1 water blade" configuration is smaller than the value given in Tab. 7.3 ( $32.7 \pm 0.8 \mu\text{s}$ ), probably due to the higher Boron content in the moderator. Due to nuclear data, the reactivity corresponding to the "1 water blade" configuration was not zero at the Boron concentration used in the experiment. In order to adjust the reactivity, we have artificially modified the Boron content of the moderator, which in turn has slightly modified the value of the mean generation time. By inspection of the values computed for the remaining configurations, we notice that increasing the water blade thickness leads to an increase of the mean generation time. This behaviour is expected since increasing the water layer implies an increase in the overall moderation of the lattice. Values concerning the effective delayed fraction  $\beta_{\text{eff}}$  from Tab. 7.3 ( $778 \pm 20 \text{ pcm}$ ) and all four simulated configurations overlap within one standard deviation.

parameters	reference	1 water blade	2 water blade	3 water blade
$\rho$ [pcm]	$-12 \pm 7$	$12 \pm 7$	$19 \pm 7$	$-3 \pm 7$
$\Lambda_{\text{eff}}$ [ $\mu\text{s}$ ]	$26.91 \pm 0.01$	$29.24 \pm 0.01$	$33.94 \pm 0.02$	$39.63 \pm 0.02$
$\beta_{\text{eff}}$ [pcm]	$791 \pm 3$	$786 \pm 3$	$775 \pm 3$	$779 \pm 3$
$\beta_{\text{eff}}^1$ [pcm]	$24.7 \pm 0.6$	$23.4 \pm 0.6$	$23.4 \pm 0.6$	$23.8 \pm 0.6$
$\beta_{\text{eff}}^2$ [pcm]	$112 \pm 1$	$117 \pm 1$	$113 \pm 1$	$113 \pm 1$
$\beta_{\text{eff}}^3$ [pcm]	$68.2 \pm 0.9$	$69 \pm 1$	$68.5 \pm 0.9$	$70 \pm 1$
$\beta_{\text{eff}}^4$ [pcm]	$151 \pm 1$	$149 \pm 1$	$144 \pm 1$	$148 \pm 1$
$\beta_{\text{eff}}^5$ [pcm]	$255 \pm 2$	$252 \pm 2$	$253 \pm 2$	$251 \pm 2$
$\beta_{\text{eff}}^6$ [pcm]	$83 \pm 1$	$82 \pm 1$	$79 \pm 1$	$82 \pm 1$
$\beta_{\text{eff}}^7$ [pcm]	$71 \pm 1$	$68.1 \pm 0.9$	$69 \pm 0.9$	$66.8 \pm 0.9$
$\beta_{\text{eff}}^8$ [pcm]	$25.8 \pm 0.6$	$25.5 \pm 0.6$	$25.2 \pm 0.6$	$25 \pm 0.6$

Table 7.20: Effective kinetics parameters for water blade configurations, weighted by the adjoint fundamental mode  $\varphi_{k_0}^\dagger$ .

## 7.5 Conclusions

In order to highlight the role of the spectral analysis in the characterization of real-world nuclear systems, we have considered different configurations of the EOLE facility. The investigation of decoupling and spatial kinetics effects analyzed by means of Monte Carlo simulation provides a useful complement of the experimental results obtained during the EPILOGUE program.

During the EPILOGUE program, rod-drop experiments have been performed in the "low fuel bubble" configuration. The measurements collected from fission chambers located at different positions with respect to the perturbation have been post-processed in order to compute a first estimation of reactivity variations. The discrepancies found in the detector efficiency and reactivity variation with respect to the fission chambers position suggests the presence of (weak) spatial kinetics effects.

We have then chosen to consider the "water blade" configuration in order to examine the influence of a strong heterogeneity introduced in the system. In order to investigate such effect, we have used the capabilities of the matrix-filling Monte Carlo methods for the spectral analysis according to both  $k$ - and  $\alpha$ -eigenvalue formulation. For the study of realistic systems the procedure proposed in Chapter 5 for the estimation of high order  $\alpha$ -eigenpairs has been implemented in the TRIPOLI-4<sup>®</sup> code. In addition to examining the reference configuration and the one containing a single water blade (which were tested in the experiment), we have used our simulation tools to consider configurations containing 2 and 3 water blades. In this respect, we have used Monte Carlo simulation

as a numerical experiment, allowing us to explore configurations that were not accessible by experiments. We have thus increased our understanding of the effects induced by the water blade on the behaviour of the eigenpairs of the  $k$ - and  $\alpha$ -eigenvalue formulation. The idea behind the "water blade" experiment in EPILOGUE was to search for decoupling effects in an heterogeneous core. Unfortunately, no decoupling effects were detected from the experimental results. For this reason, we complemented our simulations of the "single blade" configuration by adding further moderator layers.

The over-moderation caused by the presence of the water layer does have an impact on the higher order eigenvalues  $k$  and  $\alpha$ . Despite relatively small variations from the reference configuration, the dominance ratio and the eigenvalue separation calculated from these eigenvalues suggest the presence of a weak decoupling effect. This statement is also supported by the analysis of the spatial shape of both  $k$ - and  $\alpha$ -eigenmodes. Overall, the effects induced by the heterogeneity of the system are clearly detected by the spectral analysis. Nonetheless, our numerical findings seem to point out that the decoupling effects are rather mild and do not separate the system into two loosely-coupled cores, not even in the rather extreme case of 3 water blades.

Effective kinetics parameters were estimated during  $k$  power iteration proving consistent values with respect to the results obtained during the experiments and shown in Tab. 7.3. This finding is an additional evidence of the reliability of the computation of these key parameters weighted by the fundamental adjoint eigenmode. In this respect, the fundamental and the first order adjoint eigenmode distributions were shown according to both  $k$ - and  $\alpha$ -eigenvalue formulation. The importance of neutrons for the analyzed configurations shows a radially decreasing behaviour with respect to the center of the core. This result provides a useful information for the in-core detector locations that would be most sensitive to the flux behaviour within the core. In this respect, our results suggest that the analysis of the adjoint eigenmodes would have probably helped in the phase of preparation of the measurement campaign in EOLE.

The eigenvalue spectrum analysis described in this Chapter has been performed with the goal of complementing the interpretation with more traditional techniques. The experiment carried out in the EPILOGUE program was prepared independently from the PhD, but an additional work was done afterwards in order to see whether the spectral analysis would bring valuable information on the core behaviour. Our results do bring information on core coupling/decoupling effects. Although the EOLE facility has been closed, the know-how stemming from the spectral analysis methodology will be key for the future experimental programs in Zero-Power Reactors (ZPR [10]), especially in view of using forward and adjoint spectra and spatial shapes to optimize detector positions and thus enhance the detection of perturbations. This work will also profit from the PhD thesis of K. Routsonis at CEA/Cadarache (2017-2020), aimed at the optimization of detector signal response to a given perturbation (for example a rod drop). The potential outcomes of these combined approaches are numerous, covering among others space-time dynamic responses for both critical and subcritical (i.e., fuel loading or ADS) systems and detector optimization in large Gen-III cores.

To conclude, we provide in Tab. 7.21 an estimation of the computational time and the memory occupation required by TRIPOLI-4<sup>®</sup> simulations and by MATLAB *eig* routine for the computation of the eigenpairs. Despite the finer spatial discretization used for the fission matrix estimation ( $N_x = N_y = 76$ ) with respect to the  $\alpha$ -matrix ( $N_x = N_y = 48$ ), the total size of the fission matrix is smaller with respect to the matrix-form of the  $\alpha$ -eigenvalue problem, implying a large reduction in the computational time  $t_{eig}$  required by the MATLAB function *eig* for the computation of the corresponding eigenpairs. Nevertheless, the memory occupation required for the storage of the fission matrix is much larger than the one used for the  $\alpha$ -matrix. This is mainly due to the high sparsity pattern of the  $\alpha$ -matrix, defined over the whole phase-space, whereas the discretization of the fission matrix has been chosen in order to refine only the fissile region of the system.

configuration	0 water blade	3 water blade
$\alpha$ -matrix size [-]	$4.608 \times 10^4$	$4.608 \times 10^4$
fission matrix size [-]	$5.776 \times 10^3$	$5.776 \times 10^3$
$t_{MC}$ [s]	$3.37 \times 10^5$	$4.04 \times 10^5$
$t_{MC}^+$ [s]	$4.29 \times 10^5$	$5.05 \times 10^5$
$\alpha$ -matrix storage [MB]	$9.6 \times 10^0$	$9.5 \times 10^0$
fission matrix storage [MB]	$2.35 \times 10^2$	$1.91 \times 10^2$
$t_{eig}$ $\alpha$ -matrix [s]	$2.0 \times 10^4$	$2.1 \times 10^4$
$t_{eig}$ fission matrix [s]	$1.0 \times 10^2$	$9.3 \times 10^1$

Table 7.21: Computational time and memory occupation of the EOLE water blade configurations. The simulation times associated to the Monte Carlo simulations performed with TRIPOLI-4<sup>®</sup> including and without matrix elements estimation are expressed as  $t_{MC}^+$  and  $t_{MC}$ , respectively.



## Chapter 8

# Conclusions

In this thesis, we have addressed some aspects of eigenvalue problems emerging in reactor physics, and shown how Monte Carlo methods can be successfully applied to the characterization of the spectral properties of nuclear systems. After a general overview of time-dependent transport, the associated eigenvalue formulations (in particular  $k$  and  $\alpha$ ) and an introduction to Monte Carlo methods for reactor physics, the heart of the manuscript has been devoted to two main axes. The first axis concerns the application of Monte Carlo simulation to spectral analysis, with focus on the behavior of the fundamental modes, which provide information about the asymptotic behavior of the neutron and precursor population. The second axis concerns the development of new Monte Carlo methods for the estimation of higher-order eigenpairs of the  $\alpha$ -eigenvalue problem and the application of these novel algorithms to the analysis of benchmark problems and realistic reactor configurations. The newly developed methods and the simulation results obtained in this work might provide a valuable help in the analysis of reactor cores and the design of original reactor concepts. In the following, we briefly survey the contents and the major findings of this thesis.

- In Chapter 2 we have described the general framework of neutron transport problems in the context of reactor physics, by introducing in particular the time-dependent transport formulation, which is central in the assessment of operational and accidental transient regimes. The peculiar role of delayed neutron precursors has been mentioned. After introducing the integro-differential and integral formulations of the neutron transport equations, we have recalled that two major families of eigenvalue equations ( $k$  and  $\alpha$ ) can be established: the former is related to the neutron evolution as a function of the fission generations; the latter is related to the neutron evolution as a function of time (and for this reason it represents the “natural” eigenvalue formulation for time-dependent problems). We have shown that useful information can be extracted from such eigenvalue equations: the fundamental eigenpairs describe the asymptotic (in generations or in time) behavior of the reactor core, whereas higher-order quantities such as the eigenvalue separation or the first and second eigenfunctions convey the details concerning the system response to an external perturbation and thus a departure from the fundamental mode. As such, the eigenvalue formulation (either  $k$  or  $\alpha$ ) can usefully complement the full description stemming from the time-dependent transport equations, which is particularly important since the kinetics equations are often extremely demanding in terms of computer resources (time and memory).
- The basic principles of Monte Carlo simulation as applied to reactor physics have been briefly recalled in Chapter 3. In particular, we have stressed the peculiar role of Monte Carlo simulation as a numerical tool capable of producing reference (i.e., unbiased) solutions for nuclear systems: almost no approximations are introduced, since the energy, angle and space do not need to be discretized, which comes at the expense of a “slow” convergence. Monte Carlo methods have been recently extended to the case of time-dependent simulations, including delayed neutron precursors: the computer time involved in this class of simulations, despite clever variance-reduction algorithms that have been proposed in order to make such calculations feasible, is still prohibitively large for industrial applications. New strategies for the kinetic Monte Carlo simulation have been suggested, including time-dependent CADIS methods [100]. However, in the next future it seems probable that kinetic Monte Carlo simulations will be complemented, whenever possible,

by computational tools requiring more parsimonious amounts of computer resources, at the expense of sacrificing the target accuracy. In this respect, we have shown that the Monte Carlo methods devoted to eigenvalue problems might represent a good compromise between efficiency and unbiasedness.

- After setting the theoretical basis and describing the computational tools, in Chapter 4 we have illustrated our *first original contribution*, concerning the analysis of the fundamental modes of the eigenvalue formulations. We have started by recalling the algorithms implemented in the Monte Carlo code TRIPOLI-4<sup>®</sup> that allow the fundamental forward and adjoint modes to be estimated without approximations, for both  $k$ - and  $\alpha$ -eigenvalue problems. In particular, we have focused on the Iterated Fission Probability and the Generalized Iterated Fission Probability methods, which have paved the way to the calculation of the adjoint eigenmodes (until quite recently, adjoint eigenvalue calculations were not accessible by Monte Carlo methods, because of numerical instabilities). Our main finding is a thorough characterization of the discrepancies between the  $k$ - and  $\alpha$ -eigenbases close to the critical point: for an exactly critical systems, the  $k$ - and  $\alpha$ -eigenmodes coincide; on the contrary, small departures from criticality induce small, yet significant deviations in the shapes of the forward and adjoint eigenfunctions. Such discrepancies are mirrored in the key reactor parameters, which are often expressed as ratios of bilinear forms involving the forward and adjoint fundamental modes: a prominent example is represented by the kinetics parameters. Contrary to previous works, in our analysis we have explicitly taken into account the presence of the delayed neutron contributions and we have also focused on the behavior of adjoint eigenmodes. Our investigation has been carried out on two sets of configurations: some simplified benchmark systems (Godiva-like spheres) proposed by D. E. Cullen in his seminal paper, and the CROCUS zero-power facility operated at the EPFL, Switzerland. In both cases, we have shown that the effective kinetics parameters (and thus the computed reactivity, via the in-hour equation) might be affected by the choice of the eigenbasis. These slight differences have been shown to be exacerbated by the presence of heterogeneities in the core, such as a reflector region: for homogeneous cores, a point-kinetics behavior is observed, without spatial effects, and the impact of the eigenbasis becomes less relevant.
- The *second original contribution* has been presented in Chapter 5, where we have considered Monte Carlo methods for the calculation of higher-order  $k$ - and  $\alpha$ -eigenmodes and eigenvalues. We have first revisited the fission matrix approach, a matrix-filling Monte Carlo method that can be used in order to estimate the elements of a finite-size matrix whose eigenvectors and eigenvalues converge to those of the  $k$ -eigenvalue problem in the limit of infinite size. Inspired by this approach, we have proposed and developed a novel method capable of estimating the elements of a matrix whose eigenvectors and eigenvalues converge to those of the  $\alpha$ -eigenvalue problem. This new computational strategy has paved the way towards a viable strategy for  $\alpha$ -spectral analysis by Monte Carlo methods. Contrary to previous attempts proposed in the literature, our method has been shown to have two major advantages: it yields an unbiased estimate of the fundamental eigenvector (this minimizing the overall bias on the higher-order eigenvectors as well), and it can natively take into account the adjoint eigenvalue problem without introducing an additional bias due to matrix transposition. The developed method has been successfully tested and verified on benchmark problems where reference analytical solutions were available.
- In Chapter 6 we have illustrated the *third original contribution*, concerning the spectral analysis of benchmark configurations where a physical parameter allows for an incremental decoupling effect. For this purpose, we have selected a few relevant configurations involving multi-group transport with simplified physics, in order to better apprehend the key features of these configurations without being hindered by complex considerations related to nuclear data and/or detailed geometries. The methods developed in Chapter 5 have been applied to the determination of  $k$  and  $\alpha$ -eigenmodes and eigenvalues, in view of ascertaining whether the two modal expansions may convey different information content concerning the behavior of the systems under analysis. In particular, we have examined how the fundamental and higher-order eigenmodes and eigenvalues behave in the presence of decoupling factors. Two classes of systems have been considered: homogeneous cores, where the decoupling effect is introduced by increasing the system size, and heterogeneous cores, where the decoupling effect is introduced by increasing the size of a central layer separating two fissile regions. These systems have been shown to behave differently:  $k$ - and  $\alpha$ -eigenbases present distinct features; furthermore, the eigenvalue separation (i.e., the estimator related to the spectral gap between contiguous eigenvalues) and the shape of the eigenfunctions also present discrepancies. The spectral analysis as performed by Monte Carlo matrix-filling methods has turned out to be a useful and practical numerical tool to characterize such systems.

- 
- Finally, the *fourth original contribution* has been discussed in Chapter 7, where we have considered an application to a realistic system: two sets of experiments carried out during the EPILOGUE program at the EOLE critical facility of CEA Cadarache. The EPILOGUE experiment was aimed at exploring – among others – the effects of the presence of a polyethylene region (mimicking a clear water bubble in the moderator) and of a water blade (with fuel rows and columns being replaced by moderator) with respect to the reactor response. The case of the polyethylene region has been examined by comparing the experimental measurements obtained at several locations in the core (whose post-processing has been finalized during a visit to the Cadarache center during the first year of the thesis) to the fission rates computed by TRIPOLI-4<sup>®</sup> based on the fundamental  $k$ -eigenmode. This analysis suggests that (mild) spatial effects might emerge in the EOLE core, despite its small size. By building on the knowledge and numerical tools developed in the previous chapters, we have then simulated the water blade configuration, in search of possibly stronger heterogeneities and decoupling effects induced by the presence of the moderator. Instead of just interpreting the case of single water blade, which was experimentally measured, we have used Monte Carlo simulation as a “thought experiment”: we have explored the spectral effects induced by adding several other water blades into the core. The obtained results might suggest a better way of arranging the detector positions within the core, so as to emphasize their response, and might help in conceiving a future experimental campaign in a dedicated research reactor, in view of assessing the effects of heterogeneities with respect to the system behavior.

The spectral analysis performed by the implementation of matrix-filling Monte Carlo methods provides a useful tool for the investigation of kinetics and decoupling effects. In particular, we have highlighted the discrepancies in the fundamental eigenmode distributions and the effective kinetics parameters computed according to the  $k$ - and the  $\alpha$ -eigenvalue formulations. It could be interesting to extend this investigation to configurations characterized by stronger heterogeneities and different critical levels. Moreover, the fundamental distributions obtained from these eigenvalue formulations ( $\varphi_{k,0}$  and  $\varphi_{\alpha,0}$ ) should be compared to the asymptotic distribution of the system computed from a kinetic Monte Carlo simulation.

The access to high-order  $\alpha$ -eigenpairs (forward and adjoint) allows the computation of the temporal behaviour of the system via modal expansion reconstruction. The choice of the weighting function applied for the estimation of the matrix elements for the forward formulation ( $\varphi_{\alpha,0}$ , by  $\alpha$ - $k$  power iteration method) and the adjoint formulation ( $\varphi_{\alpha,0}^\dagger$ , by G-IFP method) has removed the bias on the fundamental eigenpairs. For this reason, a more precise signal reconstruction is expected and a comparison to kinetic Monte Carlo results could be envisaged.



## Appendix A

# The transient fission matrix method

The following method is based on the same principle applied on the fission matrix: the aim is to define a discrete operator representative of the  $k$ -eigenvalue problem. The generic element of this matrix is defined as the number of fission neutrons generated in the volume  $I$  from one average fission neutron born in region  $J$ . Two additional properties have been considered: the distinction between prompt and delayed neutrons and the temporal behaviour of particles.

The source fission neutrons, as well as the fission neutrons produced from it, are distinguished into prompt and delayed particles. The probability for one neutron to generate other neutrons is then split into four possibilities, hence four different matrices have been considered. Moreover, a time grid has been applied to the system in order to take into account the time associated to each particle. For each time bin considered, a different set of the four matrices needs to be accounted.

Since scoring a series of these matrices requires a large amount of storage memory, an approximation of the temporal behaviour has been introduced. In particular, a fifth matrix is considered in order to retrieve the average time response related to prompt neutrons generating prompt neutrons and it is defined as

$$T_{\chi_p \nu_p}(\mathbf{r}', \mathbf{r}) = \frac{\int_{t'' > 0} G_{\chi_p \nu_p}(t'', \mathbf{r}', \mathbf{r}) t'' dt''}{\int_{t'' > 0} G_{\chi_p \nu_p}(t'', \mathbf{r}', \mathbf{r}) dt''}, \quad (\text{A.1})$$

where  $G_{\chi_p \nu_p}(t'', \mathbf{r}', \mathbf{r})$  is a continuous operator representing the probability that a prompt neutron born at coordinates  $(\mathbf{r}', t')$  induces a prompt neutron by fission in  $(\mathbf{r}, t)$ , with  $t'' = t' - t$ .

Each sub-matrices  $G_{\chi_p \nu_p}(t'', \mathbf{r}', \mathbf{r})$  is then integrated over time in order to get four discrete operators of the same size of the fission matrix

$$\tilde{G}_{\chi_p \nu_p, d}(\mathbf{r}', \mathbf{r}) = \int_{-\infty}^t dt' G_{\chi_p \nu_p, d}(t - t', \mathbf{r}', \mathbf{r}). \quad (\text{A.2})$$

Finally, the effective lifetime  $l_{\text{eff}}$  is computed as

$$l_{\text{eff}} = \frac{\iint \tilde{N}^\dagger(\mathbf{r}) [T_{\chi_p \nu_p}(\mathbf{r}', \mathbf{r}) \tilde{G}_{\chi_p \nu_p}(\mathbf{r}', \mathbf{r})] \tilde{N}(\mathbf{r}') d\mathbf{r}' d\mathbf{r}}{\iint \tilde{N}^\dagger(\mathbf{r}) \tilde{G}_{\chi_p \nu_p}(\mathbf{r}', \mathbf{r}) \tilde{N}(\mathbf{r}') d\mathbf{r}' d\mathbf{r}}, \quad (\text{A.3})$$

where  $\tilde{N}$  and  $\tilde{N}^\dagger$  are the direct and adjoint eigenvectors associated to prompt neutron distributions, respectively. With similar reasoning, transient fission matrix has been used for the estimation of the others kinetic parameters [85].

From balance equations in terms of neutron production, variation and disappearance, a new set of equations

are retrieved in order to describe the spatial distribution of particles as a function of time

$$\begin{aligned}\frac{dN}{dt} &= \frac{1}{l_{\text{eff}}}\tilde{G}_{\chi_p\nu_p}N + \tilde{G}_{\chi_d\nu_p}\sum_j\lambda_jP_j - \frac{1}{l_{\text{eff}}}N, \\ \frac{dP_j}{dt} &= \frac{\beta_{\text{eff}}^j}{\beta_{\text{eff}}}\left[\frac{1}{l_{\text{eff}}}\tilde{G}_{\chi_p\nu_d}N + \tilde{G}_{\chi_d\nu_p}\sum_j\lambda_jP_j\right] - \lambda_jP_j,\end{aligned}\tag{A.4}$$

where  $N$  and  $P_j$  are spatial and temporal distribution related to the neutron and precursor population respectively.

This method offers an hybrid approach between the fission matrix and the  $k$  point kinetics equations. For this reason, it can be also used in order to study the evolution of the spatial distribution of particles for configurations close to a critical state.

## Appendix B

# Derivation of the point kinetics equations

The flux factorization from Eq. (2.90) can be applied to the Boltzmann Eq. (2.41), which yields

$$\begin{aligned} \frac{1}{v(E)} \frac{\partial}{\partial t} (A(t)\phi(P)) + \mathcal{M}(A(t)\phi(P)) &= \mathcal{F}_p(A(t)\phi(P)) + \sum_j \frac{\chi_d^j(E)}{4\pi} \lambda_j c_j(\mathbf{r}, t) + Q(P) \\ \frac{\partial c_j(\mathbf{r}, t)}{\partial t} &= \mathcal{F}_d^j(A(t)\phi(P)) - \lambda_j c_j(\mathbf{r}, t). \end{aligned} \quad (\text{B.1})$$

The prompt fission term is replaced by the difference between the total fission operator and the delayed fission contribution according to Eq. (2.63). Then, the derivative rule is applied to the product  $A\phi$  and the net disappearance operator  $\mathcal{M}$  is moved to the right hand side of the neutron equation. Finally, neutron equation is divided by the amplitude function  $A$  and the precursor equation is multiplied by the delayed neutron spectrum of the corresponding family, so that

$$\begin{aligned} \frac{1}{v(E)} \left[ \frac{\phi(P)}{A(t)} \frac{\partial A(t)}{\partial t} + \frac{\partial \phi(P)}{\partial t} \right] &= [\mathcal{F} - \mathcal{M}] \phi(P) + \sum_j \left[ \frac{\chi_d^j(E)}{4\pi} \mathcal{F}_d^j \phi(P) + \frac{1}{A(t)} \frac{\chi_d^j(E)}{4\pi} \lambda_j c_j(\mathbf{r}, t) \right] + \frac{1}{A(t)} Q(P) \\ \frac{\chi_d^j(E)}{4\pi} \frac{\partial c_j(\mathbf{r}, t)}{\partial t} &= \frac{\chi_d^j(E)}{4\pi} \mathcal{F}_d^j A(t)\phi(P) - \frac{\chi_d^j(E)}{4\pi} \lambda_j c_j(\mathbf{r}, t). \end{aligned} \quad (\text{B.2})$$

This set of equation is now multiplied by the adjoint fundamental mode  $\varphi_0^\dagger$  and integrated over the whole phase space:

$$\begin{aligned} \frac{1}{A(t)} \frac{\partial A(t)}{\partial t} \left\langle \varphi_0^\dagger(\mathbf{r}, \mathbf{\Omega}, E), \frac{1}{v(E)} \phi(P) \right\rangle + \frac{\partial}{\partial t} \left\langle \varphi_0^\dagger(\mathbf{r}, \mathbf{\Omega}, E), \frac{1}{v(E)} \phi(P) \right\rangle &= \langle \varphi_0^\dagger(\mathbf{r}, \mathbf{\Omega}, E), [\mathcal{F} - \mathcal{M}] \phi(P) \rangle \\ + \sum_j \left[ \left\langle \varphi_0^\dagger(\mathbf{r}, \mathbf{\Omega}, E), \frac{\chi_d^j(E)}{4\pi} \mathcal{F}_d^j \phi(P) \right\rangle + \frac{1}{A(t)} \lambda_j \left\langle \varphi_0^\dagger(\mathbf{r}, \mathbf{\Omega}, E), \frac{\chi_d^j(E)}{4\pi} c_j(\mathbf{r}, t) \right\rangle \right] &+ \frac{1}{A(t)} \langle \varphi_0^\dagger(\mathbf{r}, \mathbf{\Omega}, E), Q(P) \rangle \\ \frac{\partial}{\partial t} \left\langle \varphi_0^\dagger(\mathbf{r}, \mathbf{\Omega}, E), \frac{\chi_d^j(E)}{4\pi} c_j(\mathbf{r}, t) \right\rangle &= A(t) \left\langle \varphi_0^\dagger(\mathbf{r}, \mathbf{\Omega}, E), \frac{\chi_d^j(E)}{4\pi} \mathcal{F}_d^j \phi(P) \right\rangle - \lambda_j \left\langle \varphi_0^\dagger(\mathbf{r}, \mathbf{\Omega}, E), \frac{\chi_d^j(E)}{4\pi} c_j(\mathbf{r}, t) \right\rangle. \end{aligned} \quad (\text{B.3})$$

The assumption from Eq. (2.91) can be recalled in order to neglect the specific derivative. Moreover, we introduce a normalization function  $F$  as

$$F(t) = \left\langle \varphi_0^\dagger(\mathbf{r}, \mathbf{\Omega}, E), \mathcal{F} \phi(P) \right\rangle, \quad (\text{B.4})$$

and we divide all terms of the previous equation by this quantity. Finally, rearranging this system yields the final expression for the *exact point kinetics equations*:

$$\begin{aligned}\frac{dA(t)}{dt} &= \frac{\rho(t) - \beta(t)}{\Lambda(t)} A(t) + \sum_j \lambda_j \tilde{c}_j(t) + q(t) \\ \frac{d\tilde{c}_j(t)}{dt} &= \frac{\beta(t)}{\Lambda(t)} A(t) - \lambda_j \tilde{c}_j(t).\end{aligned}\tag{B.5}$$

## Appendix C

# Résumé en français

Dans le cadre de la sûreté des installations nucléaires, le développement des outils pour la simulation multi-physique prédictive, fiable et rapide des cœurs de réacteurs nucléaires (y compris les rétroactions thermo-hydrauliques, en conditions stationnaires et transitoires) fait l'objet d'un programme de recherche très vaste. La conception de nouvelles configurations de réacteurs, éventuellement très hétérogènes et/ou découplés, demande également une caractérisation numérique, qui pourrait compléter ou même remplacer le besoin d'installations expérimentales, notamment en vue de la caractérisation du comportement de la population de neutrons pendant les opérations et les transitoires accidentels. Ces efforts ont été capitalisés sous la forme d'agendas d'innovation SNETP, NUGENIA et H2020. Plusieurs projets européens ont été développés, tels que NURESIM (2005-2008), NURISP (2009-2012), NURES SAFE (2013-2015), HPMC (2011-2014), McSAFE (2017-2020) et son successeur McSAFER (2020). Également, des stratégies ont été proposées aux États-Unis (par exemple, le projet CESAR ou le consortium CASL) et en Chine. L'objectif final de ces efforts est d'ouvrir la voie à un *réacteur numérique*, permettant la simulation même des conditions extrêmes (c'est-à-dire inaccessibles aux expériences) et la quantification des incertitudes associées.

L'étude de la cinétique des neutrons, c'est-à-dire le comportement du transport des neutrons en fonction du temps, est principalement fondée sur des méthodes déterministes, allant d'extrêmement simplifiées (cinétique ponctuelle) à sophistiquées (théorie du transport). Pour les problèmes non stationnaires, l'état de l'art de la génération actuelle de codes de simulation numérique utilisant des méthodes déterministes repose généralement sur une approche en *deux étapes* : un calcul fin de la distribution des neutrons au niveau du réseau dans des conditions stationnaires et en deux dimensions, suivi par un calcul de l'évolution dans le temps du flux de neutrons sur la base des sections efficaces déterminées lors de la première étape et l'introduction de modèles simplifiés pour le transport (par exemple la diffusion ou le  $SP_N$ ) avec une discrétisation de l'énergie ayant un petit nombre de groupes. Ces approximations étant spécifiques à chaque type de réacteur, la validité des résultats obtenus, ainsi que la quantification des incertitudes associées aux quantités physiques d'intérêt, dépend donc de la configuration analysée. Afin de surmonter ces problèmes et de pouvoir valider les codes déterministes dans un régime non stationnaire, il est essentiel de développer des outils de calcul de référence capables de compenser le manque de données expérimentales en aux régime transitoire.

La simulation Monte Carlo est fondée sur la réalisation d'un très grand nombre de trajectoires aléatoires, dont les lois de probabilité sont déterminées en accord avec les lois physiques : la probabilité de l'interaction neutrons-matière, l'angle de la particule après une collision et les distributions d'énergie, etc. Contrairement aux méthodes déterministes, aucune approximation n'est introduite pour la variable énergie, qui est explicitement traitée lors des vols de particules et les collisions ; en outre, un traitement exact de la géométrie du réacteur est en principe possible, sans recourir à la discrétisation. Par conséquent, la simulation Monte Carlo a toujours été considérée comme la méthode de référence pour le transport de neutrons. Jusqu'à très récemment, la simulation Monte Carlo était presque exclusivement consacrée à la solution des problèmes de transport stationnaire, principalement en raison du coût de calcul élevé (exprimé en termes de CPU et charge de mémoire) nécessaires à la réalisation des trajectoires des particules. C'est également le cas du code TRIPOLI-4<sup>®</sup>, développé au CEA/Saclay.

Grâce aux performances croissantes des clusters de calcul, la disponibilité de superordinateurs pour la recherche scientifique de la dernière décennie et le parallélisme intrinsèque de la simulation Monte Carlo, cette méthode stochastique a commencé à être appliquée à l'examen des problèmes non stationnaires. À cette fin, deux obstacles formidables ont été identifiés. Le premier concerne la présence simultanée de deux temps très différents, ceux des neutrons et ceux des précurseurs de neutrons retardés, qui sont séparées par un facteur de  $10^4$  pour les réacteurs à eau légère et pourraient donc induire de sérieux problèmes de sous-échantillonnage. Le deuxième concerne la nécessité de prendre en compte les effets des rétroactions physiques pendant la période transitoire, puisque l'énergie libérée par les fissions génère des changements de température et de densité, qui modifient à leur tour les sections efficaces et donc la probabilité de collisions de neutrons. Il faut donc coupler les codes Monte Carlo avec des outils externes tels que des solveurs thermo-hydrauliques et/ou thermo-mécaniques. Ces défis demandent d'abord des techniques spécifiques de réduction de la variance pour la variable temporelle, puis des schémas de couplage entre la simulation Monte Carlo et les solveurs à rétroaction externe, en tenant compte de la stabilité et des problèmes de convergence dus à la nature stochastique de la simulation Monte Carlo. Bien qu'elles aient fait l'objet d'un important travail de recherche ces dernières années, ces méthodes Monte Carlo n'en sont qu'à leurs débuts et nécessitent des ressources informatiques si importantes que leur utilisation quotidienne pour la conception de réacteurs est encore hors de portée. Des travaux intensifs seront encore nécessaires dans un avenir proche afin de faire de ces méthodes un outil pratique pour les physiciens des réacteurs, comme en témoigne par exemple le projet McSAFER.

Une approche quelque peu complémentaire de la cinétique des réacteurs consiste à transformer le modèle initial sous une forme stationnaire, en introduisant un ensemble d'équations aux valeurs propres associées à l'équation de transport des neutrons. À cette fin, deux bases principales ont été historiquement proposées dans la littérature : les valeurs propres  $k$ , qui correspondent physiquement à la décomposition de l'évolution du système par rapport aux générations de fission successives, et les valeurs propres  $\alpha$ , qui correspondent physiquement à la décomposition de l'évolution du système par rapport au temps. Pour cette raison, la base  $\alpha$  est particulièrement adaptée à l'évolution du système étudié en fonction du temps. Une fois déterminées, les valeurs propres et les fonctions propres associées à chaque base peuvent être utilisées pour effectuer l'analyse spectrale de l'opérateur de Boltzmann et reconstruire le comportement transitoire en convoluant la base avec la source.

L'analyse des valeurs propres et des fonctions propres de l'opérateur (c'est-à-dire l'*analyse spectrale*) peut fournir la forme du mode fondamental, qui représente le comportement asymptotique de la densité neutronique par rapport au temps ou aux générations de fission, selon que l'on adopte la base  $k$  ou la base  $\alpha$ . En outre, l'analyse spectrale peut être utilisée pour évaluer la séparation des valeurs propres et en particulier le rapport de dominance entre la valeur propre fondamentale et la valeur propre suivante, qui est une mesure du degré de "découplage" d'un cœur et donc de la réponse aux perturbations externes : on dit que le système est étroitement couplé si les deux premières valeurs propres sont séparées. Enfin, l'analyse spectrale peut estimer le comportement spatial et énergétique des harmoniques d'ordres supérieurs, ce qui permettra de comprendre comment les perturbations se propagent dans le cœur du réacteur.

À cet égard, un observable fondamental est fourni par la séparation des valeurs propres  $E.S.$ , qui pour les problèmes à valeurs propres  $k$  est définie comme suit :

$$E.S._n(k) = \frac{1}{k_n} - \frac{1}{k_0} \geq 0, \quad (C.1)$$

pour  $n > 0$ . Ici  $k_n$  sont les valeurs propres  $k$  d'ordre  $n$ ,  $k_0$  étant la valeur propre fondamentale (c'est-à-dire le facteur de multiplication). Le cas  $n = 1$  joue un rôle particulier et est souvent mentionné sans utiliser l'indice, notamment,

$$E.S.(k) = E.S._1(k) = \frac{1}{k_1} - \frac{1}{k_0} \geq 0. \quad (C.2)$$

Une quantité étroitement liée est le *rapport de dominance*

$$DR = \frac{k_1}{k_0} \leq 1, \quad (C.3)$$

qui peut être tracé de façon monotone par rapport au  $E.S.$ , partageant ainsi le même contenu d'information. Bien que dans la littérature mathématique, la notion analogue d'écart spectral soit largement utilisée pour les problèmes

---

aux valeurs propres, avec une certaine similitude avec la formulation de la valeur propre  $\alpha$  (par exemple dans le contexte de l'équation de diffusion dépendant du temps), le concept de séparation de valeurs propres ou de rapport de dominance ne semble pas avoir reçu beaucoup d'attention pour les problèmes aux valeurs propres  $\alpha$ , à notre connaissance.

Des études expérimentales et numériques ont montré qu'une petite valeur de  $E.S.$  augmenterait la probabilité qu'un système propage des instabilités, amenant ainsi vers des évolutions spatio-temporels complexes (par opposition aux systèmes affichant un grand  $E.S.$ , qui se comportent comme selon la cinétique point). Ceci est particulièrement pertinent pour les cœurs faiblement couplés. En raison de son rôle clé dans la compréhension de la cinétique du système, et en particulier de la réponse du réacteur à des actions externes telles que les perturbations et les tilts, la séparation des valeurs propres a fait l'objet d'études approfondies.

Pour la formulation de la valeur propre  $k$ , les méthodes Monte Carlo peuvent déterminer (sans approximations) le mode fondamental (direct) et la valeur propre par la méthode de l'itération de puissance, qui donnera le flux de neutrons asymptotiques dans le cœur. La version stochastique de l'itération de puissance a une longue histoire, et a été utilisée presque depuis le début des méthodes Monte Carlo. Le calcul du mode adjoint fondamental, au contraire, a été hors de portée pendant de nombreuses années et a été récemment rendu possible par une avancée majeure : la redécouverte que le mode adjoint fondamental est proportionnel à la fonction d'importance des neutrons (qui peut être estimée en enregistrant la généalogie de chaque neutron ancêtre) a été la clé du développement de la *méthode de la probabilité de fission itérative* (IFP). En recourant à l'IFP, la plupart des codes Monte Carlo de production modernes (y compris TRIPOLI-4<sup>®</sup>) peuvent désormais fournir une estimation non biaisée des modes fondamentaux adjoints.

Les problèmes aux valeurs propres  $\alpha$ , bien que leur formulation soit aussi ancienne que celle des problèmes de la valeur propre  $k$ , ont donné lieu à un algorithme stochastique adapté aux méthodes Monte Carlo à une époque ultérieure. La méthode originale était inadaptée aux configurations sous-critiques (la recherche des valeurs propres a conduit à des instabilités numériques et à des terminaisons anormales) et n'incluait pas les contributions des précurseurs des neutrons retardés. Depuis lors, plusieurs améliorations (notamment en ce qui concerne la stabilité des systèmes sous-critiques) et généralisations ont été proposées et testées avec succès dans les codes Monte Carlo. L'algorithme le plus largement utilisé pour le mode propre fondamental (direct)  $\alpha$  est fondé sur une extension de l'itération de puissance traditionnelle, où la valeur propre dominante  $\alpha$  est traitée comme un paramètre et progressivement ajustée jusqu'à ce qu'une valeur propre fictive converge vers un. La caractérisation du mode fondamental adjoint pour le problème de la valeur propre  $\alpha$  a été réalisée assez récemment, sur la base d'une légère modification de la méthode IFP.

Une fois que les modes fondamentaux direct et adjoint ont été calculés par Monte Carlo, les paramètres cinétiques effectifs (c'est-à-dire pondérés par l'adjoint) du cœur peuvent être facilement déterminés : l'évolution temporelle du réacteur peut alors s'exprimer en résolvant les équations approximatives de la cinétique ponctuelle, dont les coefficients sont précisément les paramètres cinétiques. Les équations de la cinétique ponctuelle, dont la dérivation est intrinsèquement fondée sur l'intégration de la totalité de l'espace de phase de l'équation de Boltzmann en quelques paramètres effectifs (représentant l'ensemble du réacteur comme un "point", à condition que la population entière de neutrons obéisse au mode propre fondamental en ce qui concerne l'espace, l'angle et la variable énergétique), sont largement utilisées dans la communauté de la physique des réacteurs comme un outil fiable et rapide pour l'analyse de la cinétique du cœur. Cependant, leur utilisation n'est jugée appropriée que lorsque *i*) le cœur est suffisamment homogène (pour que l'approximation à un point donné soit une approximation réaliste), et lorsque *ii*) le mode fondamental de la population de neutrons est séparé de manière adéquate des harmoniques supérieures (pour que la réduction au mode fondamental soit significative). Si ces conditions ne peuvent être garanties, l'analyse des valeurs propres et des fonctions propres d'ordre supérieur devient obligatoire.

Les méthodes Monte Carlo ont également été appliquées à l'estimation des valeurs propres d'ordre supérieur et des fonctions propres, pour les problèmes aux valeurs propres  $k$  et  $\alpha$ . Contrairement au mode fondamental, qui peut être évalué en simulant des particules portant des poids statistiques positifs, la détermination exacte des modes propres supérieurs en principe nécessite des poids avec des signes alternés, ce qui est une tâche ardue pour les méthodes Monte Carlo : pour les problèmes aux valeurs propres  $k$ , certaines stratégies ingénieuses ont été proposées ces dernières années, mais la plupart sont entravées par des questions de convergence et aucune n'a conduit jusqu'à présent à une mise en œuvre pratique qui peut être transposée aux codes industriels. Pour les problèmes aux valeurs propres  $\alpha$ , le nombre de tentatives est encore plus faible.

Néanmoins, une stratégie viable pour les valeurs propres d'ordre supérieur et les fonctions propres a été développée : l'idée est de discrétiser les opérateurs apparaissant dans les équations de valeurs propres et d'obtenir des matrices de taille finie, dont les éléments peuvent être remplis au cours d'une itération régulière de puissance avec la méthode Monte Carlo [22]. Il est important de souligner que les valeurs propres résultantes et les vecteurs propres sont des approximations, pour deux raisons simultanées : la matrice a une taille finie, et la distribution des neutrons utilisée pour remplir les éléments de la matrice peut tout au plus préserver le mode fondamental et la valeur propre fondamentale. En augmentant la taille de la matrice, les valeurs propres et les vecteurs propres sont censés converger vers ceux de l'équation originale. La méthode dite de la *matrice de fission* appartient à cette catégorie d'approches et est utilisée depuis longtemps, bien qu'elle n'ait été rendue populaire que ces dernières années, lorsque la puissance des ordinateurs a augmenté et grâce à l'utilisation de techniques de stockage à matrice creuses. Sur la base d'une stratégie similaire, une approche de remplissage de matrice a également été proposée pour les problèmes aux valeurs propres  $\alpha$ , ce qui pose des défis spécifiques.

En s'appuyant sur ces considérations, l'objectif de cette thèse est double : d'une part, nous comparerons les méthodes Monte Carlo pour les problèmes aux valeurs propres et proposerons de nouvelles stratégies de calcul pour les valeurs propres  $\alpha$  ; d'autre part, nous appliquerons ces méthodes à l'étude de quelques configurations de réacteur pertinentes, afin de montrer comment des informations peuvent être extraites et utilisées afin de mieux saisir les caractéristiques des systèmes nucléaires.

Sur le plan méthodologique, dans la première partie de ce manuscrit, nous commencerons par aborder le cas des modes propres fondamentaux direct et adjoint, et nous montrerons que des divergences peuvent survenir entre la base  $k$  et  $\alpha$  loin du point critique (c'est-à-dire  $k = 1$  and  $\alpha = 0$ ). Au point critique, les deux modes fondamentaux coïncident par définition, alors que pour un écart croissant par rapport à la criticité des écarts devraient apparaître, qui sont renforcés par la présence d'effets de découplage et/ou d'hétérogénéités dans les cœurs. Ces différences spatiales et spectrales dans les modes fondamentaux se reflètent dans les paramètres cinétiques (qui sont exprimés sous forme de formes bilinéaires impliquant à la fois les modes direct et adjoint), et donc également sur la réactivité du système. Il est donc de la plus haute importance de déterminer si et dans quelle mesure l'estimation des paramètres cinétiques est affectée par les hétérogénéités du système, qui sont transmises dans les formes des modes propres. Une attention particulière sera accordée à la contribution des précurseurs de neutrons retardés, qui a été négligée jusqu'à présent dans les études précédentes.

En ce qui concerne les modes et les valeurs propres d'ordre supérieur, nous nous concentrerons sur le cas des méthodes de remplissage de matrices pour les problèmes aux valeurs propres  $\alpha$ , compte tenu de leur pertinence pour la réponse temporelle des systèmes nucléaires, et nous fournirons une nouvelle stratégie de Monte Carlo qui peut surmonter certaines des limites des approches existantes. Ces méthodes, conçues et testées dans un code Monte Carlo construit à partir de zéro dans le but d'explorer de nouveaux algorithmes, seront mises en œuvre dans TRIPOLI-4® pour être déployées pour l'analyse de configurations de réacteurs réalistes.

Dans la deuxième partie de ce manuscrit, nous étudierons l'impact de la géométrie des systèmes et de la composition des matériaux sur la cinétique du réacteur, via une décomposition en modes propres calculée par les méthodes Monte Carlo, en vue d'interpréter les données expérimentales provenant des expériences EPILOGUE menées dans l'installation critique EOLE (anciennement exploitée par le CEA à Cadarache). Nous examinerons d'abord quelques configurations de référence simplifiées, qui nous permettront de comprendre comment les mécanismes des hétérogénéités (et autres effets de découplage, comme la taille du système) se manifestent dans les valeurs propres et les vecteurs propres  $k$  et  $\alpha$ . Ensuite, nous examinerons les expériences EPILOGUE, où des configurations spéciales de réacteurs avec un fractionnement accru du modérateur à certains endroits (sous la forme d'une *lame d'eau*) ont été testées. Malheureusement, les expériences pour une seule lame d'eau n'ont pas été concluantes, peut-être en raison d'un mauvais choix des emplacements des détecteurs dans le cœur. Des simulations numériques, réalisées à l'aide du modèle TRIPOLI-4® de la configuration EOLE et des capacités de la nouvelle méthode pour l'estimation de la matrice  $\alpha$ , permettront d'explorer des détails qui étaient inaccessibles lors de la campagne expérimentale. En particulier, nous envisagerons également une configuration modifiée où des lames d'eau supplémentaires seront ajoutées : nous étudierons ainsi les effets de l'augmentation de la présence d'une région modératrice localisée sur la forme des modes propres et sur les valeurs propres, ce qui pourrait éclairer la réponse du système aux perturbations telles que les barres de contrôle ou les sources externes. À cet égard, l'approche proposée joue le rôle d'une "expérience entièrement numérique" et pourrait aider à concevoir de nouvelles campagnes expérimentales dans les réacteurs de recherche.

---

## Structure du manuscrit

Dans cette thèse, nous avons abordé certains aspects des problèmes aux valeurs propres qui apparaissent dans la physique des réacteurs, et montré comment les méthodes Monte Carlo peuvent être appliquées avec succès à la caractérisation des propriétés spectrales des systèmes nucléaires. Après une introduction général du transport en fonction du temps, des formulations aux valeurs propres associées (en particulier  $k$  et  $\alpha$ ) et une introduction aux méthodes de Monte Carlo pour la physique des réacteurs, le cœur du manuscrit a été divisé en deux axes principaux. Le premier axe concerne l'application de la simulation Monte Carlo à l'analyse spectrale, en mettant l'accent sur le comportement des modes fondamentaux, qui fournissent des informations sur le comportement asymptotique de la population de neutrons et de précurseurs. Le second axe concerne le développement de nouvelles méthodes Monte Carlo pour l'estimation d'harmoniques d'ordre supérieur du problème aux valeurs propres  $\alpha$  et l'application de ces nouveaux algorithmes à l'analyse de problèmes de référence et de configurations réalistes de réacteurs. Les méthodes nouvellement développées et les résultats de simulation obtenus dans le cadre de ce travail pourraient apporter une aide précieuse dans l'analyse des cœurs de réacteur et la conception de concepts de réacteur originaux. Dans ce qui suit, nous passons brièvement en revue le contenu et les principales conclusions de cette thèse.

- Dans le Chapitre 2, nous avons décrit le cadre général des problèmes de transport des neutrons dans le contexte de la physique des réacteurs, en introduisant notamment la formulation du transport en fonction du temps, qui est essentielle pour l'évaluation des régimes transitoires opérationnels et accidentels. Le rôle particulier des précurseurs de neutrons retardés a été mentionné. Après avoir introduit les formulations integro-différentielle et intégrale des équations de transport des neutrons, nous avons rappelé que deux grandes familles d'équations aux valeurs propres ( $k$  et  $\alpha$ ) peuvent être établies : la première est liée à l'évolution des neutrons en fonction des générations de fission ; la seconde est liée à l'évolution des neutrons en fonction du temps (et représente donc la formulation "naturelle" des valeurs propres pour les problèmes dépendant du temps). Nous avons montré que des informations utiles peuvent être extraites de telles équations aux valeurs propres : les harmoniques fondamentales décrivent le comportement asymptotique (en générations ou en temps) du cœur du réacteur, tandis que les harmoniques d'ordre supérieur, ainsi que la séparation des valeurs propres, donnent des détails sur la réponse du système à une perturbation externe, et donc sur un écart par rapport au mode fondamental. En tant que telle, la formulation aux valeurs propres ( $k$  ou  $\alpha$ ) peut utilement compléter la description complète découlant des équations de transport dépendantes du temps, ce qui est particulièrement important puisque les équations de cinétique sont souvent extrêmement exigeantes en termes de ressources informatiques (temps et mémoire).
- Les principes de base de la simulation Monte Carlo appliqués à la physique des réacteurs ont été brièvement rappelés dans le Chapitre 3. En particulier, nous avons souligné le rôle particulier de la simulation Monte Carlo en tant qu'outil numérique capable de produire des solutions de référence (c'est-à-dire non biaisées) pour les systèmes nucléaires : presque aucune approximation n'est introduite, puisque l'énergie, l'angle et l'espace n'ont pas besoin d'être discrétisés, ce qui se fait au détriment d'une convergence "lente". Les méthodes Monte Carlo ont récemment été étendues au cas des simulations dépendantes du temps, incluant les précurseurs de neutrons retardés : le temps de calcul nécessaire à cette classe de simulations, malgré les algorithmes de réduction de la variance qui ont été proposés pour rendre ces calculs réalisables, reste prohibitif pour les applications industrielles. De nouvelles stratégies pour la simulation cinétique Monte Carlo ont été proposées, y compris des méthodes CADIS dépendantes du temps. Toutefois, dans l'avenir proche, il semble probable que les simulations cinétiques Monte Carlo seront complétées, chaque fois que possible par des outils de calcul nécessitant des quantités plus parcimonieuses de ressources informatiques, au détriment de la précision de la cible. A cet égard, nous avons montré que les méthodes Monte Carlo consacrées aux problèmes aux valeurs propres pourraient représenter un bon compromis entre efficacité et absence des biais.
- Après avoir posé les bases théoriques et décrit les outils de calcul, nous avons illustré dans le Chapitre 4 *notre première contribution originale*, concernant l'analyse des modes fondamentaux des formulations aux valeurs propres. Nous avons commencé par rappeler les algorithmes implémentés dans le code Monte Carlo TRIPOLI-4<sup>®</sup> qui permettent l'estimation des modes fondamentaux directs et adjoints sans approximation, pour les problèmes aux valeurs propres  $k$  et  $\alpha$ . Nous avons notamment mis l'accent sur les méthodes IFP et GIFP. Ces méthodes ont ouvert la voie au calcul des modes propres adjoints. Notre principale conclusion est une caractérisation approfondie des écarts entre les formulations aux valeurs propres  $k$  et  $\alpha$  au tour de

la criticité : pour un système exactement critique, les modes propres  $k$  et  $\alpha$  coïncident; au contraire, de petits écarts par rapport à la criticité induisent des déviations faibles mais significatives dans les formes des fonctions propres directes et adjointes. Ces divergences se reflètent dans les paramètres clés du réacteur, qui sont souvent exprimés sous forme de rapports de formes bilinéaires impliquant les modes fondamentaux directs et adjoints : un exemple important est représenté par les paramètres cinétiques. Contrairement aux travaux précédents, dans notre analyse nous avons explicitement pris en compte la présence des contributions neutroniques retardées et nous avons également considéré le comportement des modes propres adjoints. Notre recherche a été menée sur deux séries de configurations : certains systèmes de référence simplifiés (sphères de type Godiva) proposés par D. E. Cullen, et l'installation à puissance nulle CROCUS exploitée à l'EPFL, en Suisse. Dans les deux cas, nous avons montré que les paramètres cinétiques effectifs pourraient être affectés par la choix de la base modale utilisée. Il a été démontré que ces légères différences sont exacerbées par la présence d'hétérogénéités dans le cœur : pour les cœurs homogènes, un comportement de cinétique ponctuelle est observé, sans effets spatiaux, et l'impact de la base modale choisie devient moins important.

- La *deuxième contribution originale* a été présentée dans le Chapitre 5, où nous avons examiné la méthode Monte Carlo pour le calcul des modes propres et des valeurs propres d'ordre supérieur  $k$  et  $\alpha$ . Nous avons d'abord réexaminé l'approche de la matrice de fission, une méthode Monte Carlo de remplissage de matrice qui peut être utilisée pour estimer les éléments d'une matrice de taille finie dont les vecteurs et les valeurs propres convergent vers ceux de la valeur propre  $k$  dans la limite d'une taille infinie. Inspirés par cette approche, nous avons proposé et développé une nouvelle méthode capable d'estimer les éléments d'une matrice dont les vecteurs propres et les valeurs propres convergent vers celles du problème de la valeur propre  $\alpha$ . Cette nouvelle stratégie de calcul a ouvert la voie à une stratégie d'analyse spectrale par les méthodes Monte Carlo. Contrairement aux tentatives précédentes proposées dans la littérature il a été démontré que notre méthode présente deux avantages majeurs : elle donne une estimation non biaisée du vecteur propre fondamental (ce qui minimise également le biais global sur les vecteurs propres d'ordre supérieur), et il peut prendre en compte nativement le problème de la valeur propre adjointe sans introduire un biais supplémentaire dû à la transposition matricielle. La méthode mise au point a été testée et vérifiée avec succès par rapport à des problèmes pour lesquels des solutions analytiques de référence étaient disponibles.
- Dans le Chapitre 6, nous avons illustré la *troisième contribution originale*, concernant l'analyse spectrale des configurations de référence où un paramètre physique permet un découplage du cœur. A cette fin, nous avons sélectionné quelques configurations pertinentes impliquant un transport multigroupe avec une physique simplifiée, afin de mieux appréhender les caractéristiques essentielles de ces configurations sans être gêné par des considérations liées aux données nucléaires et/ou aux géométries détaillées. Les méthodes développées dans le Chapitre 5 ont été appliquées à la détermination des modes et valeurs propres  $k$  et  $\alpha$ , afin de vérifier si les deux expansions modales peuvent véhiculer des informations différentes sur le comportement des systèmes en cours d'analyse. En particulier, nous avons examiné comment les modes propres fondamentaux et les valeurs propres d'ordre supérieur se comportent en présence de facteurs de découplage. Deux classes de systèmes ont été envisagées : les cœurs homogènes, où l'effet de découplage est introduit en augmentant la taille du système, et les cœurs hétérogènes, où l'effet de découplage est introduit en augmentant la taille d'une couche centrale séparant deux régions fissiles. Il a été démontré que ces systèmes se comportent de manière différente : les bases  $k$  et  $\alpha$  présentent des différences; de plus, la séparation des valeurs propres (c'est-à-dire l'estimateur lié à l'écart spectral entre les valeurs propres) et la forme des fonctions propres présentent également des divergences. L'analyse spectrale réalisée par les méthodes de remplissage de matrice Monte Carlo s'est révélée être un outil numérique utile et pratique pour caractériser ces systèmes.
- Enfin, la *quatrième contribution originale* a été discutée dans le Chapitre 7, où nous avons examiné une application à un système réaliste : deux séries d'expériences menées dans le cadre du programme EPILOGUE à l'installation critique EOLE du CEA Cadarache. L'expérience EPILOGUE visait à explorer - parmi d'autres - les effets de la présence d'une région de polyéthylène (imitant une bulle d'eau claire dans le modérateur) et d'une lame d'eau (les lignes et les colonnes de combustible étant remplacées par le modérateur) par rapport à la réponse du réacteur. Le cas de la région de polyéthylène a été examiné en comparant les mesures obtenues à plusieurs endroits du cœur (dont le post-traitement a été finalisé lors d'une visite du centre de Cadarache pendant la première année de la thèse) aux taux de fission calculés par TRIPOLI-4<sup>®</sup> basée sur le mode propre fondamental  $k$ . Cette analyse suggère que des effets spatiaux (légers) pourraient apparaître dans le

---

cœur EOLE, malgré sa petite taille. En s'appuyant sur les connaissances et les outils numériques développés dans les chapitres précédents, nous avons ensuite simulé la configuration des lames d'eau, à la recherche d'hétérogénéités éventuellement plus fortes et des effets de découplage induits par la présence du modérateur. Au lieu de se contenter d'interpréter les cas d'une lame d'eau unique, qui a été mesurée expérimentalement, nous avons utilisé la simulation Monte Carlo comme "expérience numérique" : nous avons exploré les effets spectraux induits par l'ajout de plusieurs autres lames d'eau dans le cœur. Les résultats obtenus pourraient suggérer une meilleure façon d'organiser les positions des détecteurs dans le cœur afin de mettre l'accent sur leur impact, et pourrait aider à concevoir une future campagne expérimentale dans un réacteur de recherche dédié, en vue d'évaluer les effets des hétérogénéités par rapport au comportement du système.



# Bibliography

- [1] Y. Asahi. Theory of Omega-d, Modes. *Journal of Science and Technology*, 12:92–106, 1975.
- [2] D. Bakry and Z. Qian. Some New Results on Eigenvectors via Dimension, Diameter, and Ricci Curvature. *Advances in Mathematics*, 155:98–153, 2000.
- [3] W. D. Beckner and R. A. Rydin. Higher-order relationship between static power tilts and eigenvalue separation in nuclear-reactors. *Nuclear Science and Engineering*, 56:131–141, 1975.
- [4] G. Bell and S. Glasstone. *Nuclear Reactor Theory*. Van Nordstrand Reinhold Company, 1970.
- [5] B. R. Betzler. Calculating  $\alpha$  Eigenvalues in a Continuous-Energy Infinite Medium with Monte Carlo. Technical Report LA-UR-12-24472, Los Alamos National Laboratory, 2012.
- [6] B. R. Betzler, W. R. Martin, B. C. Kiedrowski, and F. B. Brown. Calculating Alpha Eigenvalues of One-Dimensional Media with Monte Carlo. *Journal of Computational and Theoretical Transport*, 43:38–49, 2014.
- [7] B. R. Betzler, B. C. Kiedrowski, F. B. Brown, and W. R. Martin. Calculating Infinite-medium Alpha-eigenvalue Spectra with Monte Carlo using a Transition Rate Matrix Method. *Nuclear Engineering and Design*, 295:639–644, 2015.
- [8] B. R. Betzler, B. C. Kiedrowski, W. R. Martin, and F. B. Brown. Calculating Alpha Eigenvalues and Eigenfunctions with a Markov Transition Rate Matrix Monte Carlo Method. *Nuclear Science and Engineering*, 192:115–152, 2018.
- [9] P. Blaise and A. Santamarina. Definition of an Experimental Program in support to the APOLLO2.8/CEA2005v4 Validation for GEN-III+, EGERIE: Experimental program on Gamma Heating and Response of incore Instrumentation in Eole. Technical Report NT SPRC/LEPh/10-212 ind. 0, CEA Cadarache, 2005.
- [10] P. Blaise, B. Minot-Taioglou, P. Fougeras, K. Routsonis, C. de Saint-Jean, and D. Rochwerger. Scientific needs for a new generation critical facility at CEA: the ZEPHYR (Zero power Experimental PHYSics Reactor) ZPR. In *IGORR 19<sup>th</sup> - 19<sup>th</sup> Meeting of the International Group on Research Reactors, RRFM (European Research Reactor Conference)*, Amman, Jordan, March 2019.
- [11] T. E. Booth. A weight (charge) conserving importance-weighted comb for Monte Carlo. In *Proceedings of Radiation Protection and Shielding Division Topical Meeting conference*, Falmouth, USA, 1996.
- [12] T. E. Booth. Computing the Higher k-Eigenfunctions by Monte Carlo Power Iteration: A conjecture. *Nuclear Science and Engineering*, 143:291–300, 2003.
- [13] T. E. Booth. Power Iteration Methods for Several Largest Eigenvalue and Eigenfunctions. *Nuclear Science and Engineering*, 154:48–62, 2006.
- [14] T. E. Booth and J. E. Gubernatis. Exact Regional Monte Carlo Weight Cancellation for Second Eigenfunction Calculations. *Nuclear Science and Engineering*, 163:283–291, 2010.
- [15] J. P. Both and Y. Pénéliou. The Monte Carlo code TRIPOLI-4<sup>®</sup> and its First Benchmark Interpretations. In *Proceedings of Physor96: International Conference on the Physics of Reactors*, Mito, Ibaraki, Japan, 1996.
- [16] J. P. Both, H. Derriennic, B. Morillon, and J. C. Nimal. A survey of TRIPOLI-4<sup>®</sup>. In *Proceedings of the 8th International Conference on Radiation Shielding*, pages 373–380, Arlington, Texas, USA, 1994.

- [17] C. Bouvier. Manuel de référence de l’outil TMN. Technical Report rapport RMS N°09-0901, ind. B, CEA Cadarache, 2009.
- [18] D. Brockway, P. Soran, and P. Whalen. Monte Carlo alpha calculations. Technical Report LA-UR-85-1224, Los Alamos National Laboratory, 1985.
- [19] F. B. Brown. Fundamentals of Monte Carlo Particle Transport. Technical Report LA-UR-05-4983, Los Alamos National Laboratory, 2005.
- [20] E. Brun, F. Damian, C. M. Diop, E. Dumonteil, F. X. Hugot, C. Jouanne, Y. K. Lee, F. Malvagi, A. Mazzolo, O. Petit, J. C. Trama, T. Visonneau, and A. Zoia. TRIPOLI-4<sup>®</sup>, CEA, EDF and AREVA reference Monte Carlo code. *Annals of Nuclear Energy*, 82:151–160, 2015. Joint International Conference on Supercomputing in Nuclear Applications and Monte Carlo 2013, SNA + MC 2013. Pluri- and Trans-disciplinarity, Towards New Modeling and Numerical Simulation Paradigms.
- [21] Y. Cao and J. C. Lee. Spatial Corrections for Pulsed-Neutron Reactivity Measurements. *Nuclear Science and Engineering*, 165(3):270–282, 2010.
- [22] S. Carney, F. Brown, B. Kiedrowski, and W. Martin. Theory and applications of the fission matrix method for continuous-energy Monte Carlo. *Annals of Nuclear Energy*, 73:423–431, 2014.
- [23] K. M. Case and P. Zweifel. *Linear transport theory*. Addison-Wesley, Reading, 1967.
- [24] C. Cercignani. *The Boltzmann equation and its applications*. Springer, 1988.
- [25] E. R. Cohen, D. L. Hetrick, and W. A. Horning. A survey on nuclear reactor kinetics. In *Proceedings of the 2nd UN conference of the peaceful uses of atomic energy 2013*, Geneva, Switzerland, 1958.
- [26] R. Coifman, I. Kevrekidis, S. Lafon, M. Maggioni, and A. Nadler. Diffusion Maps, Reduction Coordinates, and Low Dimensional Representation of Stochastic Systems. *SIAM Journal on Multiscale Modeling and Simulation*, 7:621, 2008.
- [27] N. Corngold. Some Transient Phenomena in Thermalization I. Theory. *Nuclear Science and Engineering*, 19:80–90, 1964.
- [28] D. E. Cullen. Static and dynamic criticality: are they different? Technical Report UCRL-TR-201506, University of California Radiation Laboratory, 2003.
- [29] D. E. Cullen. A Simple Model of Delayed Neutron Emission. Technical Report UCRL-TR-204743, University of California, Lawrence Livermore National Laboratory, 2004.
- [30] M. Daeubler, A. Ivanov, B. L. Sjenutzer, V. Sanchez, R. Stieglitz, and R. Macian-Juan. High-fidelity coupled Monte Carlo neutron transport and thermal-hydraulic simulations using Serpent 2/SUBCHANFLOW. *Annals of Nuclear Energy*, 83:352–375, 2015.
- [31] F. D’Auria, A. Salah, G. Galassi, J. Vedovi, F. Reventos, A. Cuadra, J. L. Gago, A. Sjöberg, M. Yitbarek, O. Sandervåg, N. Garis, C. Anher, J. M. Aragonés, G. Verdú, R. Mirò, D. Ginestar, A. M. Sanchez-Hernandez, F. Maggini, J. Hadek, and D. Panayotov. Neutronics and thermal-hydraulic coupling in LWR technology. *OECD/NEA report*, 2004.
- [32] T. Downar, D. Barber, R. Miller, C. H. Lee, T. Kozlowski, D. Lee, Y. Xu, J. Gan, H. Joo, J. Jin, Y. Cho, K. Lee, and A. Ulses. PARCS: Purdue advanced reactor core simulator. In *Proceedings of PHYSOR 2002*, Seoul, Korea, 2002.
- [33] J. J. Duderstadt and L. Hamilton. *Nuclear Reactor Analysis*. J. Wiley and sons, New York, 1976.
- [34] J. J. Duderstadt and W. R. Martin. *Transport theory*. J. Wiley and sons, New York, 1979.
- [35] J. Dufek and W. Gudowski. Fission matrix based Monte Carlo criticality calculations. *Annals of Nuclear Energy*, 36:1270–1275, 2009.
- [36] S. Dulla, E. H. Mund, and P. Ravetto. The quasi-static method revisited. *Progress in Nuclear Energy*, 50: 908, 2008.
- [37] E. Dumonteil and T. Courau. Dominance ratio assessment and Monte Carlo criticality simulations. *Nuclear Technology*, 172:120–131, 2010.
- [38] D. D. Ebert, J. Clemence, and W. M. S. Jr. Interpretation of coherence function measurements in zero-power

- coupled-core reactors. *Nuclear Science and Engineering*, 55:380–386, 1974.
- [39] T. Endo and A. Yamamoto. Sensitivity analysis of prompt neutron decay constant using perturbation theory. *Journal of Nuclear Science and Technology*, 0:1–10, 2018.
- [40] T. Endo and A. Yamamoto. Conversion from prompt neutron decay constant to subcriticality using point kinetics parameters based on  $\alpha$ - and  $k_{\text{eff}}$ -eigenfunctions. In *Proceedings of ICNC 2019*, Paris, France, 2019.
- [41] M. Faucher, D. Mancusi, and A. Zoia. New kinetic simulation capabilities for TRIPOLI-4®: methods and applications. *Annals of Nuclear Energy*, 120:74–88, 2018.
- [42] S. Feghhi, M. Shahriari, and H. Afarideh. Calculation of neutron importance function in fissionable assemblies using Monte Carlo method. *Annals of Nuclear Energy*, 34:514–520, 2007.
- [43] S. Feghhi, M. Shahriari, and H. Afarideh. Calculation of the importance-weighted neutron generation time using MCNIC method. *Annals of Nuclear Energy*, 35:1397–1402, 2008.
- [44] D. Ferré, L. Hervé, and J. Ledoux. Limit theorems for stationary Markov processes with L2-spectral gap. *Annales de l'Institut Henri Poincaré, Probabilités et Statistiques*, 48:396–423, 2012.
- [45] L. R. Foulke and E. P. Gyftopoulos. Application of the Natural Mode Approximation to Space-Time Reactor Problems. *Nuclear Science and Engineering*, 30:419–435, 1967.
- [46] A. Gandini. On the standard Perturbation Theory. *Nuclear Science and Engineering*, 79:426–432, 1981.
- [47] W. Goad and R. Johnston. A Monte Carlo Method for Criticality Problems. *Nuclear Science and Engineering*, 5:371–375, 1959.
- [48] A. M. Gomez-Torres, V. H. Sanchez-Espinoza, K. Ivanov, and R. Macian-Juan. DYN SUB: A high fidelity coupled code system for the evaluation of local safety parameters - Part I: Development, implementation and verification. *Annals of Nuclear Energy*, 48:108–122, 2012.
- [49] A. Gruel. Programme EPILOGUE Rapport d'expérience. Technical Report NT SPESI/LP2E/2018-16/A, CEA Cadarache, 2018.
- [50] A. Gruel and P. Blaise. Programme EPILOGUE : conception neutronique et détermination des paramètres de sûreté – Configurations "24Gd instrumentée" et "Grappe grise". Technical Report NT SPEX/LPE/16-035 ind. B, CEA Cadarache, 2016.
- [51] A. Gruel and P. Blaise. Programme EPILOGUE : conception neutronique et détermination des paramètres de sûreté – Configurations "Référence instrumentée", "Bulle d'eau claire" et "Lame d'eau". Technical Report NT SPEX/LPE/16-031 ind. D, CEA Cadarache, 2016.
- [52] A. Gupta and R. S. Modak. Monte Carlo Solution of  $k$ -Eigenvalue Problem Using Subspace Iteration Method. *Nuclear Science and Engineering*, 194:87–103, 2019.
- [53] J. M. Hammersely and D. C. Handscomb. *Monte Carlo Method*. Methuen & Co., Chapter 8, 1964.
- [54] K. Hashimoto, T. Ohsawa, R. Miki, and T. Shibata. A practical formula for inferring eigenvalue separation from flux tilt measurements in nuclear-reactors. *Annals of Nuclear Energy*, 18(3):131–140, 1991.
- [55] A. F. Henry. The Application of Inhour Modes to the Description of Non-Separable Reactor Transients. *Nuclear Science and Engineering*, 20:338–351, 1964.
- [56] A. F. Henry. *Nuclear Reactor Analysis*. The MIT Press, 1975.
- [57] T. R. Hill. Efficient methods for time absorption (alpha) eigenvalue calculations. Technical Report LA-9602-MS (UC-32), Los Alamos National Laboratory, 1983.
- [58] J. E. Hoogenboom. *Adjoint Monte Carlo methods in neutron transport calculations*. PhD thesis, Delft, 1977.
- [59] J. E. Hoogenboom. Numerical calculation of the delayed-alpha eigenvalue using a standard criticality code. In *Physor 2002*, Seoul, Korea, 2002.
- [60] ICSBEP. *International Handbook of Evaluated Criticality Safety Benchmark Experiments*. NEA/NSC/DOC(95)/03, OECD NEA, Paris, France, 2018.
- [61] U. Imke and V. Sanchez. Validation of the subchannel code SUBCHANFLOW using the NUPEC PWR

- tests (PSBT). Technical report, Science and Technology of Nuclear Installations, 2012.
- [62] D. C. Irving. The adjoint Boltzmann equation and its simulation by Monte Carlo. *Nuclear Engineering and Design*, 15:273–293, 1971.
- [63] A. Ivanov, V. Sanchez, and U. Imke. Development of a coupling scheme between MCNP5 and SUBCHANFLOW for the pin- and fuel assembly-wise simulation of LWR and innovative reactors. In *Proceedings of M&C2011 conference*, Rio de Janeiro, Brazil, 2011.
- [64] G. D. Izarra and C. Jammes. Qualification du système de mesure du bruit neutronique SPECTRON. Technical Report NT SPEX/LDCI/2014-053 ind. A, CEA Cadarache, 2014.
- [65] C. Jammes. Système de mesure neutronique pour l’estimation du bêta effectif en mode fluctuation. Technical Report DQ SPEX/LDCI/09-29, CEA Cadarache, 2009.
- [66] A. Jinaphanh and A. Zoia. Perturbation and sensitivity calculations for time eigenvalues using the Generalized Iterated Fission Probability. *Annals of Nuclear Energy*, 133:678–687, 2019.
- [67] K. Jörgens. An Asymptotic Expansion in the Theory of Neutron Transport. *Communications on Pure and Applied Mathematics*, 11:219–242, 1958.
- [68] C. Josey and F. Brown. Computing alpha eigenvalues using the fission matrix. In *M&C 2019*, Portland, Oregon, USA, 2019.
- [69] C. J. Josey. General Improvements to the MCNP Alpha-Eigenvalue Solver. Technical Report LA-UR-18-22738, Los Alamos National Laboratory, 2018.
- [70] H. G. Kaper. The initial-value transport problem for monoenergetic neutrons in an infinite slab with delayed neutron production. *Journal of Mathematical Analysis and Applications*, 19:207–230, 1967.
- [71] E. L. Kaplan. Monte Carlo Methods for Equilibrium Solutions in Neutron Multiplication. *Lawrence Radiation Laboratory*, pages UCRL–5275–T, 1958.
- [72] G. R. Keepin. *Physics of Nuclear Kinetics*. Addison-Wesley, Reading, UK, 1965.
- [73] G. Kepisty and J. Cetnar. Dominance ratio evolution in large thermal reactors. *Annals of Nuclear Energy*, 102:85–90, 2017.
- [74] B. C. Kiedrowski and F. B. Brown. Adjoint-Based k-Eigenvalue Sensitivity Coefficients to Nuclear Data Using Continuous-Energy Monte Carlo. *Nuclear Science and Engineering*, 174(3):227–244, 2013.
- [75] B. C. Kiedrowski, F. B. Brown, and P. P. H. Wilson. Adjoint-Weighted Tallies for k-Eigenvalue Calculations with Continuous-Energy Monte Carlo. *Nuclear Science and Engineering*, 168(3):226–241, 2011.
- [76] T. Kitada and T. Takeda. Effective convergence of fission source distribution in Monte Carlo simulation. *Nuclear Science and Technology*, 38(5):324–329, 2001.
- [77] M. Knebel, L. Mercatali, V. Sanchez, R. Stieglitz, and R. Macian-Juan. Validation of the Serpent 2-DYNSUB code sequence using the Special Power Excursion Reactor Test III (SPERT III). *Annals of Nuclear Energy*, 91:79–91, 2016.
- [78] K. Kobayashi. A relation of the coupling coefficient to the eigenvalue separation in the coupled reactors theory. *Annals of Nuclear Energy*, 25:189–201, 1998.
- [79] J. Lappanen. Development of a Dynamic Simulation Mode in the Serpent 2 Monte Carlo Code. In *Proceedings of M&C conference 2013*, Sun Valley, USA, 2013.
- [80] E. W. Larsen. The spectrum of the multigroup neutron transport operator for bounded spatial domain. *Journal of Mathematical Physics*, 20:1776–1782, 1979.
- [81] E. W. Larsen. Physics, Fuels and Systems. In *Proceedings of Frédéric and Otto Hanh summer school*, 2011.
- [82] E. W. Larsen and P. F. Zweifel. On the spectrum of the linear transport operator. *Journal of Mathematical Physics*, 15:1987–1997, 1974.
- [83] K. Lassmann. TRANSURANUS: a fuel rod analysis code ready for use. *Journal of Nuclear Materials*, 188:295–302, 1992.
- [84] R. S. Laugesen. Spectral Theory of Partial Differential Equations. Technical report, University of Illinois,

- USA, 2012.
- [85] A. Laureau, M. Aufiero, P. Rubiolo, E. Merle-Lucotte, and D. Heuer. Transient fission matrix: kinetic calculation and kinetic parameters  $\beta_{eff}$  and  $\Lambda_{eff}$  calculation. *Annals of Nuclear Energy*, 85:1035–1044, 2015.
- [86] A. Laureau, L. Buiron, B. Fontaine, and V. Pascal. Fission Matrix Interpolation for the TFM approach based on a local correlated sampling technique for fast spectrum heterogeneous reactors. In *M&C2017*, Jeju, Korea, 16-20 April 2017.
- [87] A. Laureau, D. Heuer, E. Merle-Lucotte, P. Rubiolo, M. Allibert, and M. Aufiero. Transient coupled calculations of the Molten Salt Reactor using the Transient Fission Matrix approach. *Nuclear Engineering and Design*, 316:112–124, 2017.
- [88] D. Legrady and J. E. Hoogenboom. Scouting the feasibility of Monte Carlo reactor dynamics simulations. In *Proceedings of PHYSOR2008 conference*, Interlaken, Switzerland, 2008.
- [89] J. Lehner and G. M. Wing. On the spectrum of an unsymmetric operator arising in the transport theory of neutrons. *Communications of Pure and Applied Mathematics*, 8:217–234, 1955.
- [90] J. Lehner and G. M. Wing. Solution of the Linearized Boltzmann Transport Equation for the Slab Geometry. *Duke Mathematical Journal*, 23:125–142, 1956.
- [91] R. B. Lehoucq, D. C. Sorensen, and C. Yang. *ARPACK Users' Guide: Solution of Large Scale Eigenvalue Problems with Implicitly Restarted Arnoldi Methods*. Society for Industrial and Applied Mathematics, Philadelphia, Pennsylvania, 1998.
- [92] J. Leppänen. On the calculation of reactor time constants using the Monte Carlo method. In *Proceedings of IYNC 2008 conference*, Interlaken, Switzerland, 2008.
- [93] J. Leppänen, T. Viitanen, and V. Valtavirta. Multi-physics coupling scheme in the Serpent 2 Monte Carlo code. *Transactions of the American Nuclear Society*, 107:1165–1168, 2012.
- [94] J. Leppänen, M. Pusa, T. Viitanen, V. Valtavirta, and T. Kaltiaisenaho. The Serpent Monte Carlo code: Status, development and applications in 2013. *Annals of Nuclear Energy*, 82:142–150, 2015.
- [95] E. E. Lewis and W. F. J. Miller. *Computational Methods of Neutron Transport*. Wiley and sons, New York, 1984.
- [96] I. Lux and L. Koblinger. *Monte Carlo particle transport methods: Neutrons and photon calculations*. CRC Press, Boca Raton, 1991.
- [97] M. Maillot. Développement d'une Méthode d'Interprétation des essais de "Rod-Drop" dans TRIPOLI-4®: Application au réacteur CABRI. Technical Report NT SPRC/LPN/17-1740 ind .A, CEA Cadarache, 2017.
- [98] M. Maillot, J. Tommasi, and G. Rimpault. A search for theories enabling analyses of spatial effects in highly coupled SFR cores. In *Proceedings of PHYSOR 2016*, Sun valley, USA, 2016.
- [99] D. Mancusi and A. Zoia. Chaos in eigenvalue search methods. *Annals of Nuclear Energy*, 112:354–363, 2018.
- [100] D. Mancusi and A. Zoia. Zero-variance schemes for kinetic Monte Carlo simulations. *The European Physical Journal Plus*, 135:401, 2020.
- [101] MATLAB. *version 9.6.0 (R2019a)*. The MathWorks Inc., Natick, Massachusetts, 2019.
- [102] V. McLane. *Data Formats and Procedures for the Evaluated Nuclear Data File, ENDF-6*. Brookhaven National Laboratory, 2001.
- [103] C. B. Moler and G. W. Stewart. An Algorithm for Generalized Matrix Eigenvalue Problems. *Journal on Numerical Analysis*, 10:241–256, 1971.
- [104] B. Montagnini and V. Pierpaoli. The time-dependent rectilinear transport equation. *Transport Theory and Statistical Physics*, 1:59–75, 1971.
- [105] K. W. Morton. Criticality Calculations by Monte Carlo Methods. Technical Report Report T/R-1903, United Kingdom Atomic Energy Research Establishment, Harwell, 1956.
- [106] A. G. Mylonakis, M. Varvayanni, N. Catsaros, P. Savva, and D. G. E. Grigoriadis. Multi-physics and multi-

- scale methods used in nuclear reactor analysis. *Annals of Nuclear Energy*, 72:104–119, 2014.
- [107] A. G. Mylonakis, M. Varvayanni, D. G. E. Grigoriadis, and N. Catsaros. Developing and investigating a pure Monte-Carlo module for transient neutron transport analysis. *Annals of Nuclear Energy*, 104:103–112, 2017.
- [108] Y. Nauchi. Attempt to estimate reactor period by natural mode eigenvalue calculation. In *Proceedings of SNA+MC 2013*, Paris, France, 2013.
- [109] Y. Nauchi and T. Kameyama. Proposal of direct calculation of kinetic parameters  $\beta_{\text{eff}}$  and  $\Lambda_{\text{eff}}$  based on continuous energy Monte Carlo method. *Nuclear Science and Technology*, 42:503–514, 2005.
- [110] Y. Nauchi and T. Kameyama. Development of Calculation Technique for Iterated Fission Probability and Reactor Kinetic Parameters Using Continuous-Energy Monte Carlo Method. *Journal of Nuclear Science and Technology*, 47:977–990, 2010.
- [111] Y. Nauchi, A. Jinaphanh, and A. Zoia. Verification of adjoint functions of natural mode equation by Generalized Iterated Fission Probability method and by analog Monte Carlo. Proceedings of M&C 2019 conference, 2019.
- [112] Y. Nauchi, A. Zoia, and A. Jinaphanh. Analysis of time-eigenvalue and eigenfunctions in the CROCUS benchmark. In *Proceedings of PHYSOR 2020*, Cambridge, United Kingdom, 2020.
- [113] K. Nishina and M. Tokashiki. Verification of more general correspondence between eigenvalue separation and coupling coefficient. *Progress in Nuclear Energy*, 30:277–286, 1996.
- [114] B. Noble. *Applied Linear Algebra*. Prentice Hall, 1969.
- [115] S. D. Nolen, T. R. Adams, and J. E. Sweezy. Integral Criticality Estimators in MCATK(U). Technical Report LA-UR-12-25458, Los Alamos National Laboratory, 2012.
- [116] OECD/NEA. Benchmark on the kinetics parameters of the CROCUS reactor. Technical Report Plutonium recycling, NEA 4440, 2007.
- [117] R. K. Osborn and S. Yip. *The foundations of neutron transport theory*. Gordon and Breach, New York, 1966.
- [118] P. Reuss. *Précis de neutronique*. EDP Sciences/INSTN, Les Ulis, 2003.
- [119] J. M. Paratte, R. Früh, U. Kasemeyer, M. A. Kalugin, W. Timm, and R. Chawla. A benchmark on the calculation of kinetic parameters based on reactivity effect experiments in the CROCUS reactor. *Annals of Nuclear Energy*, 33:739–748, 2006.
- [120] I. Pázsit and V. Dykin. The role of the eigenvalue separation in reactor dynamics and neutron noise theory. *Journal of Nuclear Science and Technology*, 55(5):484–495, 2018.
- [121] I. Pázsit and L. Pál. *Neutron Fluctuations: A Treatise on the Physics of Branching Processes*. Elsevier, Oxford, UK, 2008.
- [122] C. M. Persson. Pulsed neutron source measurements in the subcritical ADS experiment YALINA-Booster. *Annals of Nuclear Energy*, 35:2357–2364, 2008.
- [123] W. Pfeiffer, J. R. Brown, and A. C. Marshall. Fort St. Vrain startup test A-3: Pulsed-Neutron experiments. Technical Report GA-A13079, General Atomic, 1974.
- [124] G. Pimbley. Solution of an Initial Value Problem for the Multi-Velocity Neutron Transport Equation with a Slab Geometry. *Journal of Mathematics and Mechanics*, 8:837–865, 1959.
- [125] R. G. Pinsky. Comparison theorems for the spectral gap of diffusion processes and Schrödinger operators on a interval. *Journal of the London Mathematical Society*, 72:621, 2005.
- [126] I. Pázsit, C. Demazière, and D. G. Cacuci. Noise techniques in nuclear systems. *Handbook of nuclear engineering*, 3:1631–1737, 2010.
- [127] R. Y. Rubinstein and D. P. Kroese. *Simulation and the Monte Carlo Method*. J. Wiley and sons, New York, 2007.
- [128] R. A. Rydin, A. Burke, and W. E. Moore. Noise and transient kinetics experiments and calculations for loosely coupled cores. *Nuclear Science and Engineering*, 46:179–196, 1971.

- [129] D. C. Sahni. Some new results pertaining to criticality and time eigenvalue of one speed neutron transport equation. *Progress in Nuclear Energy*, 30:305–320, 1996.
- [130] D. C. Sahni and N. G. Sjöstrand. Criticality and Time Eigenvalues in One-Speed Neutron Transport. *Progress in Nuclear Energy*, 23:241–289, 1990.
- [131] R. Sanchez and P. Jaegers. Prompt neutron decay constants and subcritical measurements for material control and accountability in SHEBA. In *International conference on the physics of nuclear science and technology*, Long Island, New York, United States, 5-8 October 1998.
- [132] R. Sanchez and D. Tomatis. Analysis of alpha modes in multigroup transport. In *Proceedings of the M&C 2019 conference*, Portland, USA, 2019.
- [133] R. Sanchez, D. Tomatis, I. Zmijarevic, and H. G. Joo. Analysis of alpha modes in multigroup diffusion. *Nuclear Engineering and Technology*, 49:1259–1268, 2017.
- [134] A. Santamarina, D. Bernard, P. Blaise, M. Coste, A. Courcelle, T. D. Huynh, C. Jouanne, P. Leconte, O. Litaize, S. Mengelle, G. Noguère, J. M. Ruggiéri, O. Sérot, J. Tommasi, C. Vaglio, and J. F. Vidal. The JEFF-3.1.1 Nuclear Data Library. Technical Report JEFF Report 22, OECD-NEA Data Bank, 2009.
- [135] A. Sargeni, K. W. Burn, and G. B. Bruna. Coupling effects in large reactors cores: The Impact of Heavy and Conventional Reflectors on Power Distribution Perturbations. In *Proceedings of Physor2014 : International Conference on the Physics of Reactors*, Kyoto, Japan, 2014.
- [136] B. Shi and B. Petrovic. Analysis of the Higher Eigenfunction Calculation Using a Modified Power Iteration Method. In *Physor 2010*, Pittsburgh, Pennsylvania, 2010.
- [137] B. Shi and B. Petrovic. Calculating the Second Eigenpair in Criticality Calculations Using the Monte Carlo Method with Source Points Pairing as an Efficient Net-Weight (Cancellation) Algorithm. *Nuclear Science and Engineering*, 172:138–150, 2012.
- [138] H. J. Shim, S. H. Jang, and S. M. Kang. Monte Carlo Alpha Iteration Algorithm for a Subcritical System Analysis. *Science and Technology of Nuclear Installations*, 2015:859242 (7 pages), 2015.
- [139] K. P. Singh, S. B. Degweker, R. S. Modak, and K. Singh. Iterative method for obtaining the prompt and the delayed  $\alpha$ -modes of the diffusion equation. *Annals of Nuclear Energy*, 38:1996–2004, 2011.
- [140] B. L. Sjenitzer and J. E. Hoogenboom. A Monte Carlo method for the calculation of the dynamic behaviour of nuclear reactors. *Progress in Nuclear Science and Technology*, 2:716–721, 2011.
- [141] B. L. Sjenitzer and J. E. Hoogenboom. Dynamic Monte Carlo Method for Nuclear Reactor Kinetics Calculations. *Nuclear Science and Engineering*, 175:94–107, 2013.
- [142] B. L. Sjenitzer, J. E. Hoogenboom, J. J. Escalante, and V. Sanchez. Coupling of dynamic Monte Carlo with thermal-hydraulic feedback. *Annals of Nuclear Energy*, 76:27–29, 2015.
- [143] J. Spanier and E. M. Gelbard. *Monte Carlo principles and neutron transport problems*. Addison-Wesley, Reading, 1969.
- [144] W. M. Stacey. *Space-Time Nuclear Reactor Kinetics*. Academic Press, New York, USA, 1969.
- [145] G. W. Stewart. A Krylov-Schur Algorithm for Large Eigenproblems. *SIAM Journal of Matrix Analysis and Applications*, 23:601–614, 2001.
- [146] V. Sánchez, L. Mercatali, F. Malvagi, P. Smith, J. Dufek, M. Seidl, L. Milisdorfer, J. Leppanen, E. Hoogenboom, R. Vocka, S. Kliem, P. V. Uffelen, and N. Kerkar. McSAFE - High Performance Monte Carlo Methods for Safety Demonstration. In *28th Symposium of AER on VVER Reactor Physics and Reactor Safety*, Olomouc, Czech Republic, 2018.
- [147] N. Terranova and A. Zoia. Generalized Iterated Fission Probability for Monte Carlo eigenvalue calculations. *Annals of Nuclear Energy*, 108:57–66, 2017.
- [148] N. Terranova, D. Mancusi, and A. Zoia. New perturbation and sensitivity capabilities in TRIPOLI-4<sup>®</sup>. *Annals of Nuclear Energy*, 121:335–349, 2018.
- [149] N. Terranova, G. Truchet, I. Zmijarevic, and A. Zoia. Adjoint neutron flux calculations with TRIPOLI-4<sup>®</sup>: Verification and comparison to deterministic codes. *Annals of Nuclear Energy*, 114:136–148, 2018.

- [150] G. Truchet, P. Leconte, A. Santamarina, E. Brun, F. Damian, and A. Zoia. Computing adjoint-weighted kinetics parameters in TRIPOLI-4<sup>®</sup>. *Annals of Nuclear Energy*, 85:17–26, 2015.
- [151] R. Tuominen, V. Valtavirta, J. Peltola, and J. Lappänen. Coupling Serpent and OpenFOAM for neutronics-CFD multiphysics calculations. In *Proceedings of PHYSOR 2016*, Sun Valley, Idaho, USA, 2016.
- [152] T. Urbatsch. Fission Matrix Capabilities in MCNP. Technical Report TJU-92-557, Transaction of the American Nuclear Society, 1992.
- [153] I. Variansyah, B. R. Betzler, and W. R. Martin. Alpha-weighted transition rate matrix method. In *M&C 2019*, Portland, Oregon, USA, 2019.
- [154] G. Velarde, C. Ahnert, and J. M. Aragonés. A comparison of the eigenvalue equations in  $\kappa$ ,  $\alpha$ ,  $\lambda$  and  $\gamma$  in reactor theory. Application to fast and thermal systems in unreflected and reflected configurations. *JEN-392*, 9:49, 1977.
- [155] A. M. Weinberg. Current Status on Nuclear Reactor Theory. *American Journal of Physics*, 20:401–412, 1952.
- [156] M. Wenner and A. Haghghat. A fission matrix based methodology for achieving an unbiased Solution for eigenvalue Monte Carlo simulations. *Progress in Nuclear Science and Technology*, 2:886–892, 2011.
- [157] M. M. R. Williams. *Mathematical Methods in Particle Transport Theory*. Butterworth, 1971.
- [158] M. M. R. Williams. *Random processes in nuclear reactors*. Pergamon Press, Oxford, 1974.
- [159] G. M. Wing. *An introduction to transport theory*. Wiley and sons, New York, 1962.
- [160] E. R. Woodcock, T. Murphy, P. J. Hemmings, and T. C. Longworth. Techniques used in the GEM code for Monte Carlo neutronics calculations in reactors and other systems of complex geometry. Technical Report ANL-7050, Argonne National Laboratory, 2018.
- [161] T. Yamamoto. Convergence of the second eigenfunction in Monte Carlo power iteration. *Annals of Nuclear Energy*, 36:7–14, 2009.
- [162] T. Yamamoto. Higher order alpha mode eigenvalue calculation by Monte Carlo power iteration. *Progress in Nuclear Science and Technology*, 2:826–835, 2011.
- [163] T. Yamamoto and H. Sakamoto. Two-step Monte Carlo sensitivity analysis of alpha- and gamma- eigenvalues with the differential operator sampling method. *Annals of Nuclear Energy*, 133:100–109, 2019.
- [164] T. Yamamoto and H. Sakamoto. A Monte Carlo technique for sensitivity analysis of alpha-eigenvalue with the differential operator sampling method. *Annals of Nuclear Energy*, 127:178–187, 2019.
- [165] T. Y. Yamamoto and Y. Nomura. Source Convergence Benchmark 3: Three thick one-dimensional slabs. Technical report, OECD/NEA, 2001.
- [166] T. Ye, C. Chen, W. Sun, B. Zhang, and D. Tian. Prompt Time Constants of a Reflected Reactor. In *Proceedings of the 2006 Symposium on nuclear data*, Tokaimura, Japan, 2006.
- [167] A. Zoia and E. Brun. Reactor physics analysis of the SPERT III E-core with TRIPOLI-4<sup>®</sup>. *Annals of Nuclear Energy*, 90:71–82, 2016.
- [168] A. Zoia, E. Dumonteil, and A. Mazzolo. Properties of branching exponential flights in bounded domains. *EPL*, 100:40002, 2012.
- [169] A. Zoia, E. Brun, and F. Malvagi. Alpha eigenvalue calculations with TRIPOLI-4<sup>®</sup>. *Annals of Nuclear Energy*, 63:276–284, 2014.
- [170] A. Zoia, E. Brun, F. Damian, and F. Malvagi. Monte Carlo methods for reactor period calculations. *Annals of Nuclear Energy*, 75:627–634, 2015.
- [171] A. Zoia, Y. Nauchi, E. Brun, and C. Jouanne. Monte Carlo analysis of the CROCUS benchmark on kinetics parameters calculation. *Annals of Nuclear Energy*, 96:377–388, 2016.
- [172] A. Zoia, C. Jouanne, P. Sireta, P. Leconte, G. Braoudakis, and L. Wong. Analysis of dynamic reactivity by Monte Carlo methods: The impact of nuclear data. *Annals of Nuclear Energy*, 110:11–24, 2017.

**Titre:** Analyse des effets d'hétérogénéité et de découplage sur la cinétique des cœurs: Application à la maquette EOLE

**Mots clés:** Monte-Carlo, analyse spectrale, Eole, maquette, cinétique

**Résumé:** L'analyse de la cinétique du réacteur est un élément clé pour la caractérisation du comportement non-stationnaire de la population neutronique lors de transitoires opérationnels ou accidentels. La dérivation des équations de la cinétique ponctuelle est intrinsèquement fondée sur le collapse de l'espace de phases associé à l'équation de Boltzmann (décrivant le transport des neutrons) en quelques paramètres efficaces permettant de représenter le réacteur comme un "point", pourvu que la population neutronique obéisse au mode propre fondamental. La cinétique ponctuelle est très largement adoptée dans la communauté de la physique des réacteurs en tant qu'outil fiable et rapide pour l'analyse de la cinétique des cœurs. Toutefois, il est connu que l'utilisation des équations de la cinétique ponctuelle est perti-

nente seulement si le cœur est suffisamment homogène (pour que le collapse en un point soit une approximation raisonnable) et si le mode propre fondamental est suffisamment séparé des harmoniques supérieures (pour que la réduction au mode fondamental soit bien posée). L'objectif de cette thèse est de maîtriser l'impact de la géométrie et des compositions matérielles du cœur sur la cinétique, en vue de la possibilité d'interpréter des données issues de l'expérience EPILOGUE (qui sera réalisée dans la maquette EOLE du CEA/Cadarache). A cette fin, une analyse spectrale par méthodes de Monte Carlo sera mise en place dans le code TRIPOLI-4 développé au SERMA, pour déterminer la séparation des modes propres et des valeurs propres du réacteur en fonction des caractéristiques du cœur.

**Title:** Monte Carlo analysis of heterogeneity and core decoupling effects on reactor kinetics: Application to the EOLE critical facility

**Keywords:** Monte Carlo, spectral decomposition, Eole, experimental facility, kinetics

**Abstract:** The analysis of the reactor core kinetics is key for the characterization of the non-stationary neutron population behavior during operational or accidental transients. Point-kinetics equations, whose derivation is intrinsically based on collapsing the full phase space of the Boltzmann equation into a few effective parameters (representing the whole reactor as a "point", provided that the entire neutron population obeys the fundamental eigen-mode), are widely used in the reactor physics community as a reliable and fast tool for the analysis of core kinetics. However, their use is deemed to be appropriate only when the core is sufficiently homogeneous (for the collapsing to a point to be a realistic approximation), and when the fundamental mode of the neutron population is

sufficiently separated from higher harmonics (for the reduction to the fundamental mode to be meaningful). The goal of this thesis is to investigate the impact of system geometry and material compositions on the reactor kinetics, via an eigen-mode decomposition, in view of interpreting experimental data coming from the EPILOGUE experiments carried out at the EOLE critical facility (CEA/Cadarache). To this aim, spectral analysis techniques based on Monte Carlo methods will be implemented in the Monte Carlo code TRIPOLI-4 (developed at SERMA), so as to determine the separation between reactor eigen-modes and eigen-values as a function of the core features.

